FINAL REPORT

Design Standards for Offshore Wind Farms

September 2011

Prepared by

American Bureau of Shipping
Corporate Offshore Technology, Renewables
16855 Northchase Drive
Houston, Texas 77060
www.eagle.org

Submitted to

U.S. Department of the Interior
Bureau of Ocean Energy Management, Regulation, and Enforcement
381 Elden Street
Herndon, Virginia 20170-4817

Acknowledgement of Sponsorship: This study was funded by the Bureau of Ocean Energy Management, Regulation, and Enforcement, U.S. Department of the Interior, Washington, D.C. under Contract Number M10PC00105.

Disclaimer: This report has been reviewed by the Bureau of Ocean Energy Management, Regulation, and Enforcement and approved for publication. Approval does not signify that the contents necessarily reflect the views and policies of the Service, nor does mention of the trade names or commercial products constitute endorsement or recommendation for use.

Acknowledgement

This study was funded by the Technology Assessment and Research Program (TA&R Project No. 670), Bureau of Ocean Energy Management, Regulation, and Enforcement (BOEMRE), U.S. Department of the Interior, Washington, D.C.

The wind turbine simulation programs used in this project, including FAST, AeroDyn and TurbSim, are developed and maintained by the National Renewable Energy Laboratory (NREL) of the U.S. Department of Energy.

Technical supports from Carl Stansberg, Casba Pakozdi and Sebastien Fouques at Marintek, Bingbin Yu at the University of Michigan, Jason Jonkman at the National Renewable Energy Laboratory, and John Conlon are gratefully acknowledged.

This report is prepared by Qing Yu (qyu@eagle.org), Kunho Kim and Tzu-Wei Lo at ABS Corporate Offshore Technology, Renewables Group. The project coordinator is Lars Samuelsson at ABSG Consulting.

Table of Contents

List of Tables ..... **iv**

List of Figures ..... **vi**

Executive Summary ..... **x**

1 Introduction **1**

2 Design of Offshore Wind Turbines Subjected to Hurricanes on the US OCS **4**

2.1 State-of-the-Art Review 6

2.1.1 Hurricane Wind 6

2.1.2 Hurricane Generated Waves 14

2.1.3 Design Load Case for Hurricane Conditions 19

2.1.4 Existing Design Standards and Their Applicability to Hurricane Conditions 22

2.1.5 Simulation Software 25

2.2 Technical Approach for Case Studies 27

2.2.1 Problem Definition 27

2.2.2 Modeling and Analysis Procedures 29

2.3 Case Study Models 41

2.3.1 Site Conditions 41

2.3.2 Wind Turbine RNA and Tower Specifications 45

2.3.3 Support Structure Configurations 47

2.3.4 Sensitivity Study to Determine Modeling Parameters 60

2.4 Comparison of API and IEC Wind Models 63

2.4.1 API and IEC Wind Model Definitions 64

2.4.2 Effect of Using IEC and API Wind Models on Turbine Responses 72

2.4.3 Summary 73

2.5 Effect of Fault in Turbine's Yaw and Pitch Control 75

2.5.1 Nacelle Yaw Misalignment 76

2.5.2 Blade Pitch Angle Locking 77

2.5.3 Summary 79

2.6 Case Studies – Monopile Support Structure 81

2.6.1 Summary of Model Parameters 81
2.6.2 Monopile Case Study Results 86
2.7 Case Studies – Tripod Support Structure 91
2.7.1 Summary of Model Parameters 91
2.7.2 Tripod Case Study Results 96
2.8 Case Studies – Jacket Support Structure 100
2.8.1 Summary of Model Parameters 100
2.8.2 Jacket Case Study Results 103
2.9 Parametric Comparisons of Case Study Results 107
2.9.1 Return Period of Environmental Conditions 107
2.9.2 Normal and Abnormal Turbine Operating Conditions 114
2.9.3 Wind and Wave Misalignment 118
2.9.4 Type of Support Structures 125
2.10 Conclusions and Recommendations 129
2.10.1 Hurricane Wind Models 129
2.10.2 Design Criteria for Offshore Wind Turbines in Hurricane-Prone Regions 129
2.10.3 Recommendations 133

3 Breaking Wave Slamming Loads 135
3.1 State-of-the-Art Review 136
3.1.1 Breaking Waves 136
3.1.2 Analytical Slamming Load Models 140
3.1.3 Numerical Methods 149
3.1.4 Slamming Experiments 157
3.1.5 Existing Design Guidelines 165
3.2 Parameter Study 168
3.2.1 Wave Related Parameters 168
3.2.2 Structure Related Parameters 170
3.2.3 Some Important Physical Relationships 171
3.3 Comparative Study of Analytical Breaking Wave Slamming Load Models 173
3.3.1 Analytical Models Used in the Comparative Study 173
3.3.2 Comparative Study Results 176
3.4 Conclusions and Recommendations 183

4 Summary 187

References for Section 2 190

References for Section 3 198

Appendix A Abbreviations 208

Appendix B Terms and Definitions 209

List of Tables

Table 2.1 Commonly Referenced Design Standards/Regulations for Offshore Wind Turbines 23
Table 2.2 General Load Cases Descriptions for the Case Studies 28
Table 2.3 50-Year Return Water Depth, Current Speed and Wind Speed 42
Table 2.4 50-Year Return Wave Condition 42
Table 2.5 100-Year Return Water Depth, Current Speed and Wind Speed 43
Table 2.6 100-Year Return Wave Conditions 43
Table 2.7 Properties of the RNA of NREL 5-MW Baseline Offshore Wind Turbine (Jonkman et al., 2009) 46
Table 2.8 Undistributed Blade Properties (Jonkman et al., 2009) 46
Table 2.9 Turbine Tower Properties (Fabian et al, 2011) 46
Table 2.10 Properties of the Grouted TP and Pile 49
Table 2.11 Monopile Support Structure Geometric Properties 49
Table 2.12 Monopile Support Structure Mass Properties (with Marine Growth) 49
Table 2.13 Properties of Equivalent Fixity of Equivalent Monopile 50
Table 2.14 Uniform C_d and C_m of Equivalent Monopile Used in the FAST Analysis 50
Table 2.15 Monopile Natural Frequencies 50
Table 2.16 Properties of the Equivalent Pile Simulating the Leg Sleeve and Pile 53
Table 2.17 Tripod Support Structure Geometric Properties 53
Table 2.18 Tripod Mass Properties (with Marine Growth) 53
Table 2.19 Properties of Equivalent Fixity of the Tripod Equivalent Monopile 54
Table 2.20 Uniform C_d and C_m of the Tripod's Equivalent Monopile Used in the FAST Analysis 54
Table 2.21 Tripod Natural Frequencies 54
Table 2.22 Properties of the Equivalent Pile Simulating the Grouted Leg and Pile 57
Table 2.23 Jacket Support Structure Geometric Properties 58
Table 2.24 Jacket Mass Properties (with Marine Growth and Sea Water in Flooded Legs) 58
Table 2.25 Uniform C_d and C_m of the Jacket's Equivalent Monopile Used in the FAST Analysis 58
Table 2.26 Properties of Equivalent Fixity of Jacket Equivalent Monopile 59
Table 2.27 Jacket Natural Frequencies 59
Table 2.28 Input Parameters for Wind Model Comparison Study 64

Table 2.29 Spectral Parameters for the Kaimal Model 66
Table 2.30 Turbulence Properties at Hub Height Based on the API Wind Model 69
Table 2.31 Turbulence Properties at Hub Height Based on the IEC Wind Model 69
Table 2.32 Coefficients and Distances for the Coherence Function (API Bulletin 2INT-MET, 2007) 70
Table 2.33 Static Wind Forces on the Monopile Support Structure 82
Table 2.34 Mudline Base Shear and Overturning Moment Due to Wave Slamming on the Monopile 84
Table 2.35 Summary of Structural Loads for the Monopile Case Studies 85
Table 2.36 Structural Reponses and Utilization Check Results for the Monopile Support Structure 89
Table 2.37 Monopile Case L12 Member Utilization Ratio Check 90
Table 2.38 Static Wind Forces on the Tripod Support Structure 92
Table 2.39 Mudline Base Shear and Overturning Moment Due to Wave Slamming on the Monopile 94
Table 2.40 Summary of Structural Loads for the Tripod Case Studies 95
Table 2.41 Structural Reponses and Utilization Check Results for the Tripod Support Structure 98
Table 2.42 Tripod Case L16 Member Utilization Ratio Check 99
Table 2.43 Static Wind Forces on the Jacket Support Structure 101
Table 2.44 Summary of Structural Loads for the Jacket Case Studies 102
Table 2.45 Structural Reponses and Utilization Check Results for the Jacket Support Structure 105
Table 2.46 Jacket Case L28 Member Utilization Ratio Check 106
Table 2.47 Occurrence of Breaking Wave Slamming 108
Table 3.1 Breaking Wave Types 139
Table 3.2 Commonly Used Design Guidelines for Wave Slamming Loads 167
Table 3.3 Load Case Definition for the Wave Slamming Comparison 180
Table 3.4 Maximum Slamming Responses at the Mudline Calculated Using the Wienke Model and the Truncated Campbell-Weynberg Model 180

List of Figures

Figure 2.1 Hurricane (Tropical Cyclone) Generated Wave Field (Young, 2003) 16
Figure 2.2 Wind and Primary Wave Field of 1998 Hurricane Bonnie 16
Figure 2.3 Reliability Index for Normal Conditions under Wind or Wave Loads (Yu et al., 2011) 24
Figure 2.4 Reliability Index for Abnormal Conditions under Wind or Wave Loads (Yu et al., 2011) 25
Figure 2.5 Modeling and Dynamic Analysis Procedure 31
Figure 2.6 Regional Wind Conditions in the US Atlantic Coast 33
Figure 2.7 Gulf of Mexico West Central Region 33
Figure 2.8 Site Location in the GOM (NOAA NDBC Station 42035) 33
Figure 2.9 Gumbel Curve Fitting for the Buoy Wind Data in Hurricane Seasons 34
Figure 2.10 Gumbel Curve Fitting for the Buoy Wave Data in Hurricane Seasons 34
Figure 2.11 Correlation of T_p and H_s Using the Binned Buoy Data in Hurricane Seasons 35
Figure 2.12 Verification of Modal Shapes of Equivalent Monopile for FAST Input 38
Figure 2.13 Verification of C_d and C_m of Equivalent Monopile for FAST Input 38
Figure 2.14 Wave Profile of 50-Year Return Waves 44
Figure 2.15 Wave Profile of 100-Year Return Waves 44
Figure 2.16 Undrained Shear Strength of Undisturbed Clay 45
Figure 2.17 RNA of NREL 5-MW Baseline Offshore Wind Turbine (Jonkman et al., 2009) 45
Figure 2.18 Campbell Diagram of NREL 5-MW Baseline Offshore Wind 47
Figure 2.19 Monopile Support Structure and Its Equivalent Monopile 48
Figure 2.20 Modal Shapes of the Monopile Support Structure 51
Figure 2.21 Tripod Support Structure and Its Equivalent Monopile 52
Figure 2.22 Modal Shapes of the Tripod Support Structure 55
Figure 2.23 Jacket Support Structure and Its Equivalent Monopile 57
Figure 2.24 Modal Shapes of the Jacket Support Structure 59
Figure 2.25 Mudline Shear Force (Fore-Aft Direction) Averaged over Multiple Realizations 61
Figure 2.26 Mudline Overturning Moment Averaged over Multiple Realizations 61
Figure 2.27 Comparison of Mudline Shear Force and Overturning Moment Calculated Using the Two Different Domain Sizes 62

Figure 2.28 Sensitivity of Mudline Shear Force and Overturning Moment to the Grid Resolution 62
Figure 2.29 Comparison of Wind Shear for the GOM West Central 100-yr Return Wind Condition 65
Figure 2.30 Comparison of Wind Spectra for the GOM West Central 100-yr Return Wind Condition 67
Figure 2.31 Standard Deviation and Reynolds Stress for the GOM West Central 100-yr Return Wind Condition 69
Figure 2.32 Time Series of the Wind Speed at Hub Height for the GOM West Central 100-yr Return Wind Condition 69
Figure 2.33 Coherence IEC and API Wind Model at f=0.004Hz 71
Figure 2.34 Coherence IEC and API Wind Model at f=0.01Hz 71
Figure 2.35 Coherence IEC and API Wind Model at f=0.1Hz 71
Figure 2.36 Comparison of the Maximum Shear Force and Overturning Moment at the Mudline 72
Figure 2.37 Time Series and Amplitude Spectrum of the Shear force at the Mudline 73
Figure 2.38 Sensitivity of Mudline Shear Force to Nacelle Yaw Angle for the GOM West Central 100-yr Return Wind Condition 77
Figure 2.39 Sensitivity of Mudline Overturning Moment to Nacelle Yaw Angle for the GOM West Central 100-yr Return Wind Condition 77
Figure 2.40 Sensitivity of Mudline Shear Force to the Blade Pitch Angle for the GOM West Central 100-yr Return Wind Condition 78
Figure 2.41 Sensitivity of Mudline Overturning Moment to the Blade Pitch Angle for the GOM West Central 100-yr Return Wind Condition 79
Figure 2.42 Static Wind Forces on the Monopile Support Structure 82
Figure 2.43 Time History of Breaking Wave Slamming Loads on the Monopile 83
Figure 2.44 Mudline Base Shear Forces Due to Wave Slamming on the Monopile 83
Figure 2.45 Mudline Overturning Moments Due to Wave Slamming on the Monopile 84
Figure 2.46 Monopile Member Size and Location for Utilization Ratio Calculation 88
Figure 2.47 Static Wind Forces on the Tripod Support Structure 92
Figure 2.48 Time History of Breaking Wave Slamming Loads on the Tripod 93
Figure 2.49 Mudline Base Shear Forces Due to Wave Slamming on the Tripod 93
Figure 2.50 Mudline Overturning Moments Due to Wave Slamming on the Tripod 94

Figure 2.51 Tripod Member Size and Location for Utilization Ratio Calculation 97
Figure 2.52 Static Wind Forces on the Jacket Support Structure 101
Figure 2.53 Jacket Member Size and Location for Utilization Ratio Calculation 104
Figure 2.54 Ratio of 100-yr Return to 50-yr Return Mudline Shear Forces 110
Figure 2.55 Ratio of 100-yr Return to 50-yr Return Mudline Overturning Moments 110
Figure 2.56 Ratio of 100-yr Return to 50-yr Return Maximum Utilization Ratios 110
Figure 2.57 Mudline Shear Forces and Overturning Moments (50-yr vs. 100-yr) in the ATL2 Region 111
Figure 2.58 Mudline Shear Forces and Overturning Moments (50-yr vs. 100-yr) in the GOM Region 112
Figure 2.59 Utilization Ratios (50-yr vs. 100-yr) at the ATL2 and GOM Regions 113
Figure 2.60 Mudline Shear Forces and Overturning Moments (Normal vs. Abnormal) under the 50-Year Return Conditions 115
Figure 2.61 Mudline Shear Forces and Overturning Moments (Normal vs. Abnormal) under the 100-Year Return Conditions 116
Figure 2.62 Member Utilization Ratios (Normal vs. Abnormal) 117
Figure 2.63 Turbine Tower Base Shear and Overturning Moment for the Monopile Case 119
Figure 2.64 Turbine Tower Base Shear and Overturning Moment for the Tripod Case 120
Figure 2.65 Turbine Tower Base Shear and Overturning Moment for the Jacket Case 121
Figure 2.66 Mudline Shear Forces and Overturning Moments vs. Wind-Wave Misalignment (under the 50-Year Return Conditions in the GOM West Central Region) 122
Figure 2.67 Mudline Shear Forces and Overturning Moments vs. Wind-Wave Misalignment (under the 100-Year Return Conditions in the GOM West Central Region) 123
Figure 2.68 Member Utilization Ratios vs. Wind-Wave Misalignment (GOM West Central Region) 124
Figure 2.69 Mudline Shear Forces and Overturning Moments (All Structures in ATL2) 127
Figure 2.70 Mudline Shear Forces and Overturning Moments (All Structures in GOM) 127
Figure 2.71 Mudline Shear Forces and Overturning Moments (All Structures under the 100-Year Return Conditions in the GOM with Various Wind-Wave Misalignments) .. 128
Figure 3.1 Definition of Parameters for Calculating Wave Slamming Forces 142
Figure 3.2 Splashing Pattern of Plunging Breaking Wave (IEC61400-3 Annex D) 145
Figure 3.3 Breaking Wave Slamming Load on a Circular Cylinder (IEC 61400-3, 2009) 174
Figure 3.4 Wave Slamming Load of Four Different Models 177

Figure 3.5 Time History of Mudline Shear Forces 178
Figure 3.6 Time History of Mudline Bending Moments 178
Figure 3.7 Undrained Shear Strength for Stiff and Soft Soil 180
Figure 3.8 Mudline Shear Forces Calculated Using the Wienke Model..... 181
Figure 3.9 Mudline Shear Forces Calculated Using the Truncated Campbell-Weynberg Model 181
Figure 3.10 Mudline Bending Moments Calculated Using the Wienke Model..... 182
Figure 3.11 Mudline Bending Moments Calculated Using the Truncated Campbell-Weynberg Model..... 182

Executive Summary

The main objectives of this project, as outlined in the BOEMRE Contract M10PC00105, are to:

- Study the governing load cases and load effects of bottom-founded offshore wind turbines subjected to the hurricanes on the US Outer Continental Shelf (OCS)
- Review and evaluate the existing methods of calculating the breaking wave slamming load exerted on an offshore wind turbine support structure
- Provide recommendations to support the future enhancement to the relevant design criteria for offshore wind turbines

This report presents the results of the state-of-the-art review, the case study results for the characteristic responses of bottom-founded offshore wind turbines assumed as being installed in hurricane-prone regions on the US OCS, the research findings of modeling breaking wave slamming loads, and the recommended design methods.

The study starts with a review of the existing knowledge applicable to offshore wind turbines to be deployed on the US OCS. Case studies, primarily involving bottom-founded wind turbines subjected to tropical hurricane conditions in US waters, are carried out to evaluate governing load cases and load effects. Emphasis is given to both the relevant load cases specified in IEC 61400-3 and those that are not specified in the IEC standards but considered critical to hurricane-prone regions. Three typical configurations of turbine support structure, including monopile, tripod and jacket assumed as being installed at locations in the Mid-Atlantic, South Atlantic and Gulf of Mexico coastal regions on the US OCS, are selected for the case studies. Hurricane conditions with various combinations of other site conditions such as water depth and return periods are considered. The well-documented 5MW baseline offshore wind turbine developed by National Renewable Energy Laboratory (NREL) is employed in the case studies. The effect of fault conditions in the turbine's control system for nacelle yaw and blade pitch is evaluated. The recommendations on the design environmental conditions, design load cases and strength criteria are made based upon the findings from the literature review, comparative studies and case studies.

The state-of-the-art review is also performed to study the existing design methods for offshore wind turbine support structures subjected to breaking wave slamming loads. Various analytical

and numerical methods for predicting wave slamming loads are reviewed. An assessment is also performed to identify the relative importance of the parameters that affect the calculation of wave slamming loads. Nonlinear dynamic analyses are carried out to examine the response of a typical offshore monopile support structure under the wave slamming forces, which are estimated using the four representative slamming load models. The combined effect of soil conditions and structural damping is evaluated. Based on the results of the literature review and numerical analyses, recommendations are given for the design of cylindrical structural members subjected to the breaking wave slamming (impact) loads.

Four technical areas are considered of great importance and recommended for further studies. They include turbulent hurricane wind modeling, foundation soil-structure interaction models, offshore wind turbine analysis procedures and software tools, and validation of slamming load models.

1 Introduction

The US offshore oil and gas industry and the Bureau of Ocean Energy Management, Regulation, and Enforcement (BOEMRE) have extensive experience with hydrocarbon-related offshore structures installed on the US Outer Continental Shelf (OCS). A series of Recommended Practices has been published through American Petroleum Institute (API) under their Subcommittee on Offshore Structures. The primary document is API RP 2A-WSD, which provides a comprehensive basis for the design of offshore structures located on the US OCS and subjected to wave, wind, current and earthquake loads. What is not available from API RP 2A-WSD, however, is the definition of design environmental conditions and design load conditions that can capture the unique response characteristics of offshore wind turbines.

Several design and certification guidelines for offshore wind turbines have been developed in the past ten years. Most of them are based on the experience from offshore wind turbines installed in European coastal areas. Of these guidelines, the International Electrotechnical Commission (IEC) 61400-3 (2009) *Wind turbines – Part 3: Design Requirements for Offshore Wind Turbines* represents industry's "state-of-the-art" knowledge of offshore wind turbines by the time this IEC standard was published. Although a framework of defining the site-specific Class S wind turbines is included in IEC 61400-1 (2005) *Wind turbines – Part 1: Design Requirements* and further referred to by IEC 61400-3 (2009), the applicability of IEC standards to the offshore areas subjected to the risk of hurricane remains unanswered.

The latest guideline for bottom-founded offshore wind turbines – ABS *Guide for Building and Classing Offshore Wind Turbine Installations* – was published in 2010. The ABS Guide established a set of design criteria that takes into account the risk of tropical storms on the US OCS. Calibrations have been carried out to demonstrate that an offshore wind turbine support structure in US waters designed to ABS criteria is at least as safe as those designed to IEC 61400-3 (2009) under European offshore conditions. The current project is partially based on the experience that the ABS project team has garnered during the development of the ABS Guide.

Existing offshore wind turbines in commercial operation are dominated by bottom-founded designs installed in waters less than 30 m deep. In this relatively shallow water, the progressive waves have high possibility of reaching its breaking limit due to bathymetry effects and will interact with the wind turbine support structure. The expected loads exerted by breaking waves

are of transient nature and can be significantly higher than the loads from non-breaking waves. Breaking waves in shallow waters can also potentially result in other issues such as foundation scouring and slamming load induced vibrations of the turbine support structure.

Wave slamming is a strongly nonlinear phenomenon that exhibits significant statistical scattering. Hence, the development of a robust model for predicting wave slamming loads is a very challenging subject. There are a few existing guidelines, such as the one provided in IEC 61400-3 (2007) Annex D, which can be used to determine the breaking wave load for design. This project is aimed to evaluate the existing design methods and perform comparative studies using the published analytical slamming load models. Based on the findings from the literature review and numerical analyses, recommendations are made for the design of offshore wind turbine support structures subjected to breaking wave slamming loads.

This report is organized around the two main subjects studied in this project. The first is the governing load cases and load effects of offshore wind turbines subjected to hurricane environmental conditions on the US OCS. The second is the evaluation of the existing methods of calculating the breaking wave slamming loads on offshore wind turbine support structures.

Section 2 presents the research findings on the design load cases for offshore wind turbines to be deployed in hurricane-prone regions on the US OCS. The section starts with the discussion of the outcome of the state-of-the-art review of subjects relevant to the hurricane design load cases. The results of comparative study of two representative turbulent wind models and the study of the effect of failure of turbine's yaw and pitch control systems are then reported. Extensive case studies using three typical configurations of offshore wind turbine support structures are carried out to explore characteristic responses of offshore wind turbines subjected to hurricane environmental conditions. The correlations of the support structure responses with various design parameters, including the environmental conditions, support structure configurations, site conditions and turbine operating conditions are evaluated in the study and reported in this section. This section concludes with the recommended strength design criteria for bottom-founded offshore wind turbines to be installed in hurricane-prone regions.

Section 3 is dedicated to the review and evaluation of existing breaking wave slamming load models. The outcome of the state-of-the-art review, which covers various analytical and numerical wave slamming force calculation methods as well as the slamming experiments, are first reported in this section. An evaluation is performed to identify the relative importance of

various parameters affecting the calculation of wave slamming forces. This is followed by parametric analyses of four representative analytical slamming load models as well as the resultant dynamic responses of a monopile support structure. The combined effect of soil conditions and structural damping ratios is evaluated. Based on the results of the literature review and numerical analyses, recommendations are made for the design of an offshore wind turbine for which the breaking wave slamming is a matter of concern.

Main conclusions and recommendations for future research are provided in Section 4.

2 Design of Offshore Wind Turbines Subjected to Hurricanes on the US OCS

A number of studies have been undertaken from various perspectives to examine the gaps between existing offshore wind turbine design standards and the established practices for designing offshore oil and gas platforms on the US OCS. Some of those studies explored the means of extending the coverage of IEC 61400-3 (2009), which is primarily developed based on the experience from Europe, to hurricane-prone regions. Efforts have also been made to adapt the design criteria in API RP 2A-WSD (2007) for the design of offshore wind turbines subjected to hurricane risks.

The study reported in this section expanded the scopes of previous studies, particularly those carried out during the development of the ABS *Guide for Building and Classing Offshore Wind Turbine Installations* (2010). The following summarizes the scope of work of the present study.

- State-of-the-art review of the modeling of hurricane winds and waves, the definition of design load cases for hurricane conditions, applicability of existing design standards and regulations, and simulation software.

- Comparative study of the effect of using the Kaimal wind model referred to in IEC 61400-3 (2009), and the NPD (Frøya) wind model recommended by API RP 2A-WSD (2007).

- Comparative study of the effect of failure of nacelle yaw and blade pitch control systems due to a control system fault or loss of electric power supply.

- Case studies for the three typical support structure configurations *viz.* monopile, tripod and jacket. One conceptual design for each type of support structure is defined for the case studies. Regional site conditions in the Gulf of Mexico as well as the Mid-Atlantic and South Atlantic sections of the US East Coast are used in the case studies. Site conditions at one specific location near the Texas coastline in the Gulf of Mexico are also included.

- Parametric study of the correlations between the global and local responses of turbine support structures and the main design parameters including return period of design environmental conditions, normal and abnormal turbine operating modes, misalignment between wind and wave directions, type of support structures and site variations.

- Conclusions and recommendations drawn based on the findings obtained in this study.

Section 2.1 presents the results of the state-of-the-art review. The technical approaches and software employed in the case studies are summarized in Section 2.2. The case study models, environmental conditions, foundation properties and load case definitions are described in Section 2.3. Section 2.4 presents the results of comparative study using the IEC and API wind models, while Section 2.5 is dedicated to the comparative study of turbine responses under various scenarios of nacelle yaw misalignment and blade pitch angle locking. Detailed case study results for the three conceptual designs are presented in Section 2.6, 2.7 and 2.8, respectively. Section 2.9 summarizes the findings from the parametric evaluation of the effect of various design parameters on global and local responses of offshore wind turbine support structures. Conclusions and recommendations are discussed in Section 2.10.

2.1 State-of-the-Art Review

The state-of-the-art review is focused on following subjects that are considered relevant to the objectives of this project.

- Hurricane conditions and relevant wind and wave models applicable to the US OCS
- Technical basis employed to define the design load cases and strength criteria in the existing offshore wind turbine design guidelines and its applicability to hurricane-prone regions
- Available offshore wind turbine analysis tools

2.1.1 Hurricane Wind

The extreme wind condition is one of the most important external conditions that need to be considered in the design of offshore wind turbines. On the US Atlantic Coast and the Gulf of Mexico, this extreme wind condition is mostly characterized by hurricanes. A similar type of strong weather condition is also referred to by names such as tropical cyclones or typhoons in other parts of the world. This review is focused on the surface level hurricane wind modeling and data collection. Information on mean wind profiles, gust factors, turbulence intensity, integral scale, and turbulence spectra and coherence is essential for developing a realistic wind model.

2.1.1.1 Wind Data

Wind data measurement provides statistical wind characteristics that can be used as input to the theoretical wind models for hurricane forecast. Historical wind data are also commonly used to calibrate wind models.

Wind data are mainly measured by surface wind measuring stations. Automated Surface Observing System (ASOS) operated by National Weather Service (NWS) is one of the primary sources for surface wind measurements. Nearly all ASOS stations are located at airports. At offshore and coastal sites, National Data Buoy Center (NDBC) of National Oceanic and Atmospheric Administration (NOAA) manages the data buoys and the Coastal Marine Automated Network (C-MAN) to measure near surface wind conditions.

In addition to the surface wind measuring stations, the surface wind speed can also be inferred from other data sources including satellite images, reconnaissance aircrafts, and radar and radiosonde observations [2.60]. Some of the latest wind field measurement devices include Sonic Detection and Ranging (SODAR), Light Detection and Ranging (LIDAR) and Satellite based SAR (Synthetic Aperture Radar) [2.51].

There are several hindcast databases that have been developed for the areas subjected to the risk of hurricanes. The Wave Information Studies (WIS) Project [2.72] sponsored by the US Army Corps of Engineers (USACE) maintains more than 20 years of hourly wind speed, wind direction and wave data along all US coastlines, including the Great Lakes and US island territories. The database is available for the public access through USACE's website.

Another useful database is developed by the U.S. National Centers for Environmental Prediction (NCEP) and the National Center for Atmospheric Research (NCAR) [2.54]. The NCEP/NCAR database covers about 50 years of wind data worldwide derived through an analysis of global weather observations using a numerical weather analysis and modeling system. The database provides a useful data source for estimating extreme wind speeds at a given location worldwide. However, as indicated by Mann, et al. (2002) [2.50], the low resolution of the reanalysis model and the coarse temporal resolution of 6 hours could result in an underestimation of the actual extreme wind speed.

One of the commercially available sources is from Oceanweather, Inc. [2.56]. For the Gulf of Mexico, Oceanweather's GOMOS (Gulf of Mexico Oceanographic Study) database includes 29 years of continuous wind and wave hindcast data for the period between 1980 and 2008, 379 tropical events (hurricanes) for the period between 1900 and 2008, and 68 extra-tropical events (winter storms) for the period between 1950 and 2008. The GOMOS database was used in support of the development of API Bulletin 2INT-MET (2007) [2.11]. Hindcast wind and wave data that include the historical tropical and extra-tropical storms in the near-shore regions along part of the US East Coast and West Coast are also available from Oceanweather, Inc.

For the western North Pacific region, the best track data are derived by Japanese Meteorological Agency (JMA) and Joint Typhoon Warning Center (JTWC) using the hindcast technique and the available measurement of typhoons [2.60] [2.18]. The data sets contain the center position and the central pressure (at sea level) at 6 hours intervals. Other information contained in the best track data varies at different sites.

Other than the above hindcast or reanalysis data, measured data of a single hurricane or typhoon (e.g. [2.33], [2.43], [2.80] and [2.85]) may also be used to verify the physical models. The high resolution hurricane wind data measured on land near coastline are available through Texas Tech Hurricane Research Team (e.g. [2.33]) and Florida Coastal Monitoring Program (FCMP) [2.73]. Multi-level measurement on a mobile tower makes it possible to investigate the variations of some wind parameters with the height above surface. In addition, simultaneous measurements from three or four towers during the same hurricane passage can be used to analyze spatial correlations.

The extreme wind speeds for particular return periods are specified in number of design guidelines. Regional averaged extreme wind speeds in the GOM can be found in API Bulletin 2INT-MET (2007) [2.4]. API RP 2A-WSD (2007) [2.5] covers a number of other locations on the US OCS, but only provides 100-year return wind speeds. Recently published ASCE-7 (2010) [2.6] includes the updated wind speed contour maps with various return periods for both on-land and coastal regions in the US. BOEMRE TA&R Project No.672, which is expected to be completed in 2012, is meant to provide a comprehensive metocean data set for the offshore US Mid-Atlantic Coast.

2.1.1.2 Hurricane Wind Field Model

Hurricane wind field modeling has been the subject of considerable research over many years [2.76]. Dvorak (1975) [2.23] developed a hurricane ranking scale by assigning the *T* scale numbers to hurricanes recorded by satellite imaging. Each *T* number, which ranges on a scale from 1 to 8, is associated with the level of estimated central pressure and maximum sustained wind. This method is a purely empirical approach because it solely relies on the recognition of the shapes and patterns of satellite images of hurricanes. To some extent, it also depends on the absolute sizes of the satellite images.

Holland (1980) [2.35] proposes a theoretical hurricane model that uses an exponential formulation to define the relationship between wind speed and the radius from hurricane center. The parameters of this model can be calculated from best track data. This method has been validated by comparing to the measurement of wind field of many tropical cyclones and hurricanes, mostly in the central parts of the cyclone and within about 3-4 times the radius of the maximum wind speed (R_w) (see e.g. [2.81]). Applications and validity of this model are also

discussed in Black et al., (1999) [2.12], Ochi (2003) [2.58], Ott (2006) [2.60], and Vickery et al. (2007) [2.76].

A hurricane wind field model developed by Vickery et al. (2004) [2.77] has shown some advantages in comparison to other models developed in previous studies. Rather than using the spectral model, a fully nonlinear solution to the equations of motion of a translating hurricane is derived. This model appears to be able to predict accurately the asymmetries in fast moving hurricanes as well as the effect of the sea surface roughness. Over 90 full-scale hurricane wind speed measurements are used to evaluate the validity of the hurricane wind field model. The evaluation shows that the model provides a good representation of the hurricane wind field. It is noted that the basis of this approach is the assumption that the large-scale structure of the hurricane wind fields changes relatively slowly over time.

As indicated by Vickery et al. (2007) [2.76], an important step in the entire hurricane modeling process is the ability of the wind field model used in the simulation procedure to reproduce measured wind speeds as well as the pressure field. Validation methods include comparison to the observation of past hurricanes [2.60] [2.59] [2.36] and wind tunnel experiment [2.50].

2.1.1.3 Gust Factor

The gust factor is defined as the ratio of the peak wind speed averaged over a short period (e.g., 3 second) to the mean wind speed averaged over a relatively long reference period (e.g., one hour). The gust factor depends on many characteristics of a wind field, such as the roughness length, the transitional flow regimes (change in terrain, distance from upstream terrain, etc.), the anemometer height, the stability of boundary layer and the presence of deep convection.

A technical report prepared by Harper et al. (2009) [2.34] and sponsored by the World Meteorological Organization (WMO) provides a guideline for converting between wind speeds having different time averaging periods under tropical cyclone conditions. The gust factors are defined for the different surface conditions and origins of cyclone, i.e. “In-Land: Roughly open terrain”, “Off-Land: Offshore wind at a coastline”, “Off-Sea: Onshore wind at a coastline” and “At-Sea: Beyond 20 km offshore”. An extensive review is performed of the theoretical and numerical models and the existing recommended practices as documented in the five WMO tropical cyclone regional associations. Discussions are also directed to the two primary

assumptions made in theoretical models, i.e. the steady mean wind speed and turbulent boundary layer in equilibrium with the underlying surface roughness.

In a review paper by Vickery and Skerlj (2005) [2.75], the gust factors obtained using the ESDU model (1982, 1983) [2.25] [2.26] are compared to the observed data and those calculated by the Krayer–Marshall method, which assumes that in a given hour, the deviation of a short-duration mean wind speed from the one hour mean wind speed follows the Gaussian distribution. The study concludes that the ESDU model provides adequate accuracy for describing the hurricane gust factors over both water and land. The study also confirms that gust factor is very sensitive to the local surface roughness.

Argyriadis (2003) [2.8] concludes that the peak wind speeds and gust factors may be calculated using the ESDU-spectra and the Charnock equation for roughness length over open sea. It is also stated that this approach is only valid for fully developed seas.

Gust factors can also be calculated directly from wind speed data. Based on the high-resolution measurement data, Paulsen and Schroeder (2005) [2.61] divides the time histories of recorded wind speed into 10-minute segments, which are then used to calculate the gust factors. The mean gust factor is found to increase with increasing upstream surface roughness. The gust factor also appears to include increasing amounts of scatter with decreasing wind speed. Some differences are observed between data from the tropical storms and the extra-tropical storms.

In Yu (2007) [2.85], the gust factor is estimated using the measurements of surface hurricane wind speeds over the sea surface and open flat terrain in Florida coastal areas. This research shows that the Durst model used in US design standards and codes underestimates the gust factors of hurricane winds for gust durations of less than 20 seconds. The dependence of the estimation of gust factors on upstream surface roughness conditions appears approximately in agreement with the results of other studies (e.g. Paulsen and Schroeder [2.61]).

For hurricane wind conditions, Hsu (2008) [2.36] proposes a formula for estimating the 3-second gust from a 1-minute mean wind speed. The formula is developed based on the models developed for standard neutral boundary layer flow conditions. Conversion factors for the hurricane winds with different averaging time durations are also referred in Stewart (2010) [2.65], where the conversion factor between the 10 minute mean wind and 3 second gust is related to the exponent of the power law wind profile.

Cautions are raised by Buchan et al. (1999) [2.14] and Black et al. (1999) [2.12] when applying the generic values of gust factors to tropical cyclone wind near the eye wall, where the maximum wind speed occurs. The measurement recorded during the passage of tropical cyclone Olivia shows that the gust factor (3 second gust to 10 minute mean wind speed) can reach as high as 2.75, which is much higher than the gust factor commonly referred in the existing design guidelines for offshore platforms and offshore wind turbines. It should be noted, however, that the observations in these studies are made from the wind speed measurement of a single cyclone. The statistical scattering of gust factors may play a big role in this case such that the conclusion may not have general implications.

2.1.1.4 Mean Wind Speed and Profiles

The most commonly used averaging period is 10 minutes. According to Harper et al. (2009) [2.34] and Barth and Peinke (2007) [2.10], the intermittent behavior of turbulent wind can be found especially on small scales, while the statistics on larger scales are close to pure Gaussian behavior. A separation of very intermittent and intermittent behavior seems to take place at about 10 minutes. This has given support to the common procedure of using 10 minutes averages in order to neglect small-scale turbulence. However, since the fluctuations on smaller time scales are responsible for the extreme loads on wind turbines, the non-Gaussian behavior has to be taken into account.

The time averaging period for mean wind speed may vary due to different data collecting methods and conditions. In a WMO report by Harper et al. (2009) [2.34], the conversion factors are recommended between the WMO standard 10 minute average wind speed at 10 m above water and 1-minute, 2-minute and 3-minute "sustained" gust winds, respectively, in tropical cyclone conditions. The report indicates that an at-sea conversion factor between the 1-minute sustained estimate of peak storm intensity and the 10-minute average wind speed should be 0.93, rather than the traditional value of 0.88, which is shown to be associated more with an off-land exposure.

The variation of mean wind speed with the height above surface is described by the so-called "wind shear law". The logarithmic law, which is defined as a function of the surface roughness, has been used in most cases to describe the relationship between the wind speed and the height above surface [2.24] [2.85] [2.8] [2.65]. A relatively simple empirical format of exponential model has also been widely used in the wind turbine design standards such as IEC 61400-3 [2.40].

As observed by Argyriadis (2003) [2.8], the distribution of mean wind speed recommended in most of wind turbine related standards follows the Weibull distribution or, with some limitations, the Rayleigh distribution.

2.1.1.5 Turbulence Intensity

The turbulence intensity is the ratio of the wind speed standard deviation to the mean wind speed. Both the wind standard deviation and mean wind speed should be determined from the same set of measured data samples of wind speed taken over a specified period of time (usually 10 minutes). The turbulence intensity is dependent on the stability of the atmosphere and the surface roughness length.

Dynamic wind loading caused by the atmospheric turbulence is one of the most important wind turbine design parameters. Simulations of three-dimensional fields of all three components of the wind velocity fluctuations are particularly important for the time domain simulations of gust loading on turbines.

A survey report by Argyriadis (2003) [2.8] provides a comparison of different models of the longitudinal turbulence intensity near the ground. References are made to the design guidelines developed by ESDU, Danish standard DS472, Germanischer Lloyd, ISO, NORSOK and API.

In Mann et al. (2000) [2.50], a spectral tensor model of turbulence over flat terrain is discussed in detail, along with experimental verification and comparison with other commonly referenced wind spectra. The model is further generalized to cover moderately complex terrains that take into account the influence of roughness changes and gentle hills on the turbulence statistics. The tensor model described in this study is used as a basis of the simulation of turbulent fields implemented in Riso's WAsP Engineering software.

Yu (2007) [2.85] calculates the turbulence intensity based on the normalized standard deviation of wind speed data estimates for very short averaging periods. The research shows that the estimated values of turbulence intensities of longitudinal and vertical wind components increase as the terrain roughness increases.

2.1.1.6 Wind Power (Turbulence) Spectra

Turbulence spectra represent the frequency distribution of the turbulent kinetic energy of fluctuating wind velocity components. Since turbulent fluctuations in the surface layer of the

atmosphere have a significant effect on wind loads as well as the losses they produce in high winds, the research of turbulence spectra at the surface layer is of great interest to wind turbine designers.

IEC 61400-3 [2.40] recommends using Mann's spectrum, but also makes a reference to Kaimal spectrum, for application to offshore wind turbine design. Argyriadis (2003) [2.8] states that the information on the spectral characteristics of offshore wind is scarce although there is some evidence that standard spectral models are adequate with some discrepancies at low frequencies, particularly in stable and unstable atmospheric conditions. GL [2.32] and the Danish [2.19] standards recommend that the spectra used for the onshore wind turbines may be used for offshore applications.

Ochi and Shin (1988) [2.57] perform a study of the turbulent wind spectrum over a seaway. The measured hurricane wind data at various locations are used to construct the spectral density data set. The comparison of the measurements with those predicted by existing wind spectra, which are developed based on the measurements on land, reveals a significant discrepancy in the low frequency range. For applications to the design of offshore structures, a new spectral formulation is proposed in the paper to address this discrepancy.

Based on the wind turbulence measurements (Frøya database) obtained at the exposed sites on the western coast of Norway, Andersena and Løvsethlow (2006) [2.7] reach a conclusion similar to the one by Ochi and Shin (1988) [2.57] that the low frequency range (<0.01 Hz) is significantly more energetic than what can be predicted using the wind spectral formulations derived from land based wind data. The paper also indicates that coherence for lateral separation is much lower than that obtained from some land-based wind models.

The wind spectrum and coherence model recommended by API RP 2A-WSD (2007) [2.5], API Bulletin 2INT-MET (2007) [2.4] and ISO 19901-1 [2.41] are intended for the design of offshore structures and structural elements for which the wind load induced dynamic responses need to be considered. The turbulent wind is represented by the NPD wind spectrum (also known as the Frøya wind model) and the two-point coherence function in conjunction with the logarithmic wind shear law.

Comparison of various existing wind spectra is also performed by Mann et al. (2000) [2.50] and Ochi (2003) [2.58]. A summary of commonly used wind spectra can be found in DNV [2.22].

2.1.1.7 Roughness Length

Roughness length is an important parameter in the logarithmic law of wind speed profile. It represents the surface roughness, which correlates with many wind field characteristics, such as gust factor [2.61], turbulent intensity [2.85], etc. In the case of wind over water, the surface roughness is also related to the wind speed itself, where wind driven ripples and increasingly larger surface waves may be generated, depending on the water depth, fetch and wave age.

The roughness length can be calculated directly from wind speeds measured at two heights [2.24], while other modeling methods are also used (e.g. [2.61] [2.85]). The representative terrain classes and roughness length classifications for tropical cyclone applications are provided in Harper et al. (2009) [2.34].

2.1.2 Hurricane Generated Waves

The severity of the sea, including the magnitude and the spatial distribution of those waves generated by hurricane winds, depends on the magnitude of maximum sustained wind speed, minimum surface pressure in the hurricane eye, forward velocity of the hurricane center and radius of maximum wind speed [2.83] [2.58]. In this regard, the wind field model provides parameters for modeling hurricane generated waves.

On the other hand, the wave field can also influence the wind field through the variation of the surface roughness. In general, hurricane generated waves will drive up surface roughness and lead to a steeper wind profile. IEC 61400-3 [2.40] refers to the Charnock relation for calculating surface roughness length over the sea.

There have been numerous studies carried out on hurricane wind generated waves. Two relatively recent publications by Young (1999) [2.81] and Ochi (2003) [2.58], respectively, provide an excellent overview of the mechanism and theoretical models of hurricane generated waves.

2.1.2.1 Wave Data

The primary source of wave measurements is National Data Buoy Center (NDBC) of the National Oceanic and Atmospheric Administration (NOAA), which manages data buoys deployed on the

US OCS. There are also a number of regional wave measurement programs run by local research institutions.

As summarized in Section 2.1.1.1, several metocean hindcast databases have been developed for the hurricanes-prone regions on the US OCS. Three primary sources for wave data available in the public domain are

- Wave Information Studies (WIS) project sponsored by the US Army Corps of Engineers (USACE) [2.72]
- Database developed by the U.S. National Centers for Environmental Prediction (NCEP) and the National Center for Atmospheric Research (NCAR) [2.54]
- NOAA WAVEWATCH III model data [2.55]

One of the commercially available hindcast databases is developed and maintained by Oceanweather, Inc. [2.56], which has been providing metocean data services to the offshore oil and gas industry for years. For the Gulf of Mexico, Oceanweather's GOMOS (Gulf of Mexico Oceanographic Study) database was used in support of the development of API Bulletin 2INT-MET (2007) [2.11]. Hindcast wind and wave data that include the historical tropical and extra-tropical storms in near shore regions of the US East Coast and West Coast are also available from Oceanweather, Inc.

Along with the extreme wind, the parameters of extreme wave with various return periods are specified in API Bulletin 2INT-MET (2007) [2.4] and API RP 2A-WSD (2007) [2.5] for selected offshore sites on the US OCS.

BOEMRE TA&R Project No.672, which is expected to be completed in 2012, aims to develop a comprehensive metocean data set for the regions offshore US Mid-Atlantic Coast.

2.1.2.2 Hurricane Wind Generated Wave Field

A hurricane generated wave field shows a unique spatial pattern and directional characteristics. Young (2003) [2.84] studies the wave fields generated by tropical cyclones in the northern hemisphere. It is found that the wave field is more asymmetric than the corresponding wind field, mainly due to the extended fetch to the right of a translating cyclone (see Figure 2.1).

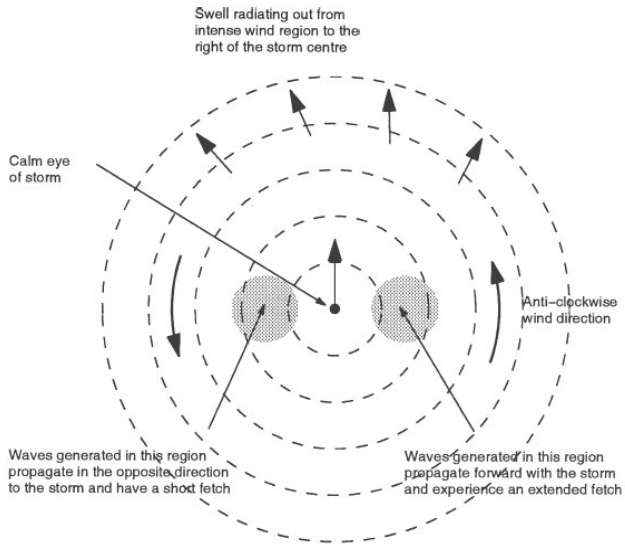

Figure 2.1 Hurricane (Tropical Cyclone) Generated Wave Field (Young, 2003)

Source: http://www.class.noaa.gov/

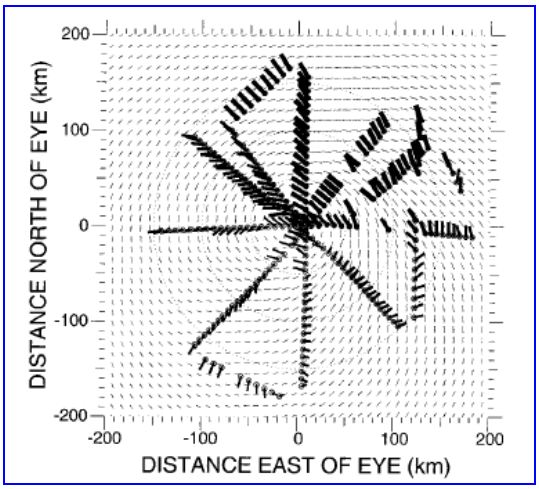

Source: Wright et al. (2001)

Figure 2.2 Wind and Primary Wave Field of 1998 Hurricane Bonnie

Valuable information about the directionality of hurricane generated waves on the US OCS has been collected through NOAA's airborne radars or computer simulations such as NOAA's WAEWATCH III (see e.g. [2.79] [2.78]).

Figure 2.2 shows the satellite hurricane wind field image of the 1998 Hurricane Bonnie as well as the plot of the primary wave field created using the airborne radar observations (Wright et al., 2001 [2.78]). The radial length in the plot is proportional to the wave length and the radial width

is proportional to the significant wave height. The aspect ratio of a radial stands for the wave steepness so that a wide rectangle represents steep waves. The radials start from the circles denoting the data point locations and extend toward the wave propagation directions. The light narrow lines show the surface wind orientations. It can be seen from the plot that the large waves mostly occur in the upper right (northeast) quadrant.

As summarized by Ochi (2003) [2.58], the following features of hurricane-generated wave field have been observed:

- Around the area having maximum wind speed (R_{max}), the wave direction generally follows the wind direction.
- Waves within the eye appear to be the local wind generated short crested waves.
- Waves in the region in front of the hurricane eye appear to be propagating in a radial direction and roughly perpendicular to the local wind direction. Both wave length and height are large in this region. These large waves propagate ahead of the hurricane as swells.
- Waves in the rear half area behind the hurricane eye mostly have shorter length and smaller steepness.

2.1.2.3 Hurricane Wave Spectrum

The severity of wind generated storm seas is typically described by a wave spectrum representing the distribution of time averaged wave energy with respect to frequencies and directions. A wave spectrum may be given as a measured spectrum or in a parameterized form with empirically fitted wave characteristic parameters. Parameters required for defining a parameterized wave spectrum normally include the significant wave height and a representative frequency or period. The two most frequently referenced standard formulations of a wave frequency spectrum in marine applications are the Pierson-Moskowitz spectrum for a fully developed sea and the JONSWAP spectrum for a developing sea state under a fetch limited condition. JONSWAP spectrum has been applied and modified in many studies on hurricanes, or tropical cyclones.

Young (1988) [2.83] develops a spectral wave model based on numerical solution of the radiative transfer equation and uses this wave spectrum to create a synthetic database for hurricane wave conditions. This model is based on the concept of equivalent fetch and the standard JONSWAP fetch-limited growth relationships. A simple parametric model has been developed for the maximum significant wave height within the storm and its associated peak spectral frequency.

In Wu et al. (2003) [2.79], wave heights and periods from Young's wave model are compared with ocean wave observations. For six major hurricanes in the U.S. East Coast and the Gulf of Mexico where a wave buoy is close to the storm center, the parametric model gives wave height predictions that are within 5% error compared with the buoy-measured wave data. The swell period and thus wave steepness are also favorably verified with the wave data.

Young (1999, 2003) [2.81] [2.84] concludes that the wave spectra recorded within tropical cyclones shows significant similarity to fetch limited forms. Such similarity is considered to be caused by the shape stabilizing effect of nonlinear wave interactions, which continually reshape the spectrum to conform to the standard JONSWAP form. The observed data indicates that the scale parameter α of JONSWAP spectrum is a function of the wave age, and the peak enhancement parameter $\gamma$is somewhat lower than the mean value in the original JONSWAP spectrum. The latter implies that much of the energy is from swell. For slowly moving tropical cyclones, waves generated in the intense wind regions to the right of the storm could propagate ahead of the storm.

The wave spectral shape with the consideration of the wave directionality is further developed by Young (2006) [2.82] based on tropical cyclone data near Australian offshore. A review is also made about other studies on using modified JONSWAP spectrum to model hurricane waves.

Ochi (2003) [2.58] proposes a modified JONSWAP spectrum for hurricane seas as a function of the predicted significant wave height and the peak frequency. This spectrum considers the incoming wave from the ocean to shallow water. The spectrum parameters are also derived based on observed hurricane wave data.

For finite water depth, the shape of the wave spectrum tends to be flattened with more wave energy shifting from the peak frequency to both higher and lower frequencies (see e.g. Costal Engineering Manual (2008) [2.71]). A commonly used wave spectral formulation for non-breaking waves in shallow/finite water is the TMA spectrum, which is defined as the JONSWAP spectrum multiplied by a frequency and water depth dependent transformation factor (see e.g. Bouws et al., 1985 [2.13]). In IEC 61400-3 (2009) [2.39], another wave spectrum is referred to for the shallow water waves with the consideration of the slope and water depth of local seabed. However, its application to hurricane generated waves has not yet been validated. In Buchan et al. (1999) [2.14], a refined Young's shallow water directional spectral model is applied to estimate the wave parameters in tropical cyclone Olivia passing Australian offshore.

2.1.3 Design Load Case for Hurricane Conditions

For the design of an offshore wind turbine support structure, design environmental loadings are represented by a set of Design Load Cases (DLCs), which are defined by the combinations of turbine operational modes, site-specific environmental conditions, electrical network conditions and other applicable design conditions, such as specific transportation, assembly, maintenance or repair conditions. Since the turbine's operating modes could have a significant impact on the loads inflicted on the turbine support structure, the DLCs for the hurricane conditions must also take into account of the effects of the turbine's operations during the hurricane's passage (Yu et al., 2011 [2.86]).

In a review paper by Manwell et al. (2004) [2.51], the US offshore environmental conditions and data sources are discussed. It is recognized that the hurricane conditions on the US OCS and fresh water ice conditions in the Great Lakes may impose unique design requirements.

Tarp-Johansen et al., (2006) [2.68] provide a summary of the relevant methods and recommendations specified in IEC 61400-3, and discuss the development of offshore wind turbines in the US in terms of external conditions and design requirements. The level of structural reliability implied by IEC 61400-3 and its application to the US are also studied. It is concluded that the uncertainty model is different for hurricane conditions. An increased load factor will have to be established if the same return period, i.e. 50-yr, and the same level of safety as required by IEC 61400-3 are to be maintained. The load factors proposed in IEC 61400-3 are not calibrated for various climatic regions, but mainly reflect North European conditions. With the consideration of the low consequences to human life and environment, the authors suggest that for hurricane-prone regions like the Gulf of Mexico, the economically sound approach may simply be to accept that offshore wind turbines cannot survive hurricanes. Or otherwise, the authors claim that the load safety factors will have to be increased, possibly making the exploitation of wind power in the Gulf Mexico economically infeasible. The authors also cast doubt on whether using the API RP 2A 100-year criteria for the design of offshore wind turbines could actually result in higher reliability than the use of the IEC 61400-3 recommendations.

A recent report issued by Transportation Research Board (2011) [2.70] introduces a new consequence regime termed the "policy risk", which is traditionally not considered in the design of offshore oil and gas platforms in the US. The report calls for a goal-based regulation that

should take into account the policy risk in addition to the risk of loss of human life and environmental pollutions.

A joint industry project report (MMI, 2009) [2.53] by MMI Engineering and sponsored by MMS/BOEMRE, NREL and other partners presents the results of comparative study of IEC 61400-3 and API RP 2A-WSD and their applicability to US waters. Part of the findings of this study is also reported by Saigal et al. (2007) [2.62] and Jha et al. (2009) [2.44]. The nominal and structural reliability analyses are performed to examine the level of safety of two different design approaches, or so-called “design recipe”, namely IEC 61400-3 in combination with ISO 19902 versus API RP 2A-WSD. A monopile and a tripod type of turbine support structures are considered in the case studies. Metocean conditions of a site offshore Massachusetts and a site near Texas GOM coast are derived and used for the monopile and tripod supported turbines, respectively. A component level structural strength check is performed based on the requirement of two different design standards. The conclusion is that support structure designs based on the API 100-year conditions in conjunction with the API safety factors yield a reliability level comparable to that for designs based on IEC 61400-3 and ISO 19902. It should be noted that the study is limited to "normal" turbine operating conditions; those “abnormal” design load cases as defined in IEC 61400-3 addressing the faults in safety and control systems as well as the consequences of loss of power supply are not covered. The comparison results essentially imply that the “normal” and “abnormal” conditions defined in IEC 61400-3 may be considered equivalent to the “operational” and “extreme” conditions defined in API RP 2A-WSD.

Yu et al. (2011) [2.86] present the technical background of the design criteria recently published in *ABS Guide for Building and Classing Offshore Wind Turbine Installations*, where the design requirement for offshore wind turbine support structures in hurricane-prone regions is specifically defined. The paper discusses unique design considerations for the support structure of an offshore wind turbine in US waters and how the Working Stress Design (WSD) approach can be applied. The applicability of IEC 61400-3 and API RP 2A-WSD to offshore wind turbines in the US is also evaluated. The paper concludes that the definition of “Operating” and “Extreme” design conditions in API RP 2A-WSD (2007) is not directly applicable to offshore wind turbines because of the unique load characteristic of offshore wind turbines. In addition, the paper argues that due to the higher variability of the wind and wave climate in hurricane-prone areas, offshore wind turbines in US waters would not achieve the same level of safety as those in European waters if the existing IEC Ultimate Limit State (ULS) design criteria were applied without any

modification. It is noted that the ULS design criteria specified in IEC 61400-3 are primarily developed based on the experience from designing offshore wind turbines for European coastal areas. The results of calibrations, which are carried out to verify the adequacy of design load conditions and structural design requirements of the ABS WSD-based design criteria, are presented in the paper. Metocean conditions in the US Gulf of Mexico and Atlantic Coast are used to calculate the aerodynamic and hydrodynamic loads as well as the structural responses of a typical design of offshore wind turbine support structure. The effect of the failure of turbine's active yaw control, which is considered as a part of the "abnormal" conditions, is taken into account.

Sharples (2010) [2.63], under sponsorship from BOEMRE, conducts a comprehensive review of various design guidelines and their application to US waters. The potential impact of hurricanes in the US is assessed, emphasizing the social risk of collective damage/failure of multiple wind farms in the track of a single hurricane, the application of design criteria addressing backup battery power supply to maintain the proper functioning of yaw control when the grid connection is lost, and the possibility of establishing an alternative set of design criteria for offshore wind turbines in the US.

A number of studies have also been carried out to develop the design criteria for land-based wind turbines installed in the regions subjected to the risk of typhoons. Assuming that the return period is 50 years for the extreme storm condition and the turbine support structure is targeted to be designed to the same safety level as those in Europe, Clausen, et al. (2006a, 2006b, 2007) [2.16][2.17][2.18] indicate that the load factor of the LRFD-based criteria in IEC 61400-1 needs to be increased by approximately 25% to 50% for the regions subjected to typhoons in the Philippines. Garciano and Koike (2007) [2.29], on the other hand, propose to increase the resistance factor by as much as 74% for those turbine support structures designed for surviving typhoon winds while maintaining the same IEC load factors and 50-year return extreme storm condition. Garciano and Koike (2010) [2.30] further make an attempt to propose a typhoon class of wind turbines within the current IEC 61400 framework.

2.1.4 Existing Design Standards and Their Applicability to Hurricane Conditions

A number of design guidelines and regulations for offshore wind turbines have been developed over the last ten years. Table 2.1 lists some of the commonly referenced design standards and regulations. A brief description of each standard or regulation is also provided in the table.

Several attempts have been made to adapt IEC 61400-3 for application in US waters. One of the major concerns is whether the current IEC design criteria can adequately take into account the risk imposed by hurricane conditions on the US OCS.

IEC 61400-3, which represents the industry's state-of-the-art knowledge of offshore wind turbines, is developed primarily based on the experience from designing offshore wind turbines for European coastal areas. Although a framework to define the site-specific Class S wind turbines is included in IEC 61400-1 for land-based turbines and further referred to by IEC 61400-3 for offshore applications, the applicability of IEC standards to the hurricane-prone offshore sites remains unanswered. A statement is also made in the guides published by DNV (2010) [2.21] and GL (2005) [2.32], calling for the discretion of those using their guides to design offshore wind turbine in hurricane-prone regions.

The study carried out by MMI Engineering (2009) [2.53] concludes that the turbine support structure designed using IEC 61400-3 and ISO 19902 are comparable in terms of strength to those designed to API RP 2A-WSD. It also implies that the "normal" and "abnormal" turbine operating conditions defined in IEC 61400-3 may be considered equivalent to the "operational" and "extreme" conditions defined in API RP 2A-WSD. In their study, the IEC/ISO scheme is based on 50-year return environmental conditions with the load factors from IEC 61400-3 and the resistance factors from ISO 19902, while the API scheme is based on 100-year return conditions along with the safety factors defined in API RP 2A-WSD.

Table 2.1 Commonly Referenced Design Standards/Regulations for Offshore Wind Turbines

Standards / Regulations	*Brief Descriptions*
The International Electrotechnical Commission (IEC), 2005. IEC 61400-1 Ed.3: Wind turbines – Part 1: Design Requirements.	• International standard for land based turbines. Many contents, and most importantly, the design philosophy, are adopted by IEC 61400-3 for offshore wind turbines. • Requirements for environmental conditions, design load cases, structural and foundation design criteria are specified. • References are made to other standards within the IEC 61400 series for the turbine and rotor design requirements.
The International Electrotechnical Commission (IEC), 2009. IEC 61400-3 Ed.1: Wind turbines – Part 3: Design Requirements for Offshore Wind Turbines.	• International standard, but mainly based on the experience from designing offshore wind turbines for North European shallow waters. • Significant amount of references are made to IEC 61400-1, which is for land based turbines. • Requirements for environmental conditions and design load cases are specified. • Refer to other recognized standards for offshore oil and gas platforms for structural or foundation design criteria
American Bureau of Shipping (ABS), 2010. Guide for Building and Classing Offshore Wind Turbine Installations.	• Environmental conditions and load cases are based on IEC 61400-3 but with additional requirements to account for hurricane/tropical cyclone conditions • Working Stress Design (WSD) based criteria are specified in addition to Load and Resistance Design (LRFD) based criteria • Also include criteria for material selection, fabrication, installation and inspections during service life • Applicable to offshore wind turbine support structures including tower, substructure and foundation.
Germanischer Lloyd (GL), 2005. Guideline for the Certification of Offshore Wind Turbines.	• Environmental conditions and load cases are similar to those in IEC 61400-3 with some modifications • Structural design criteria and inspection requirements are specified. • Both turbines (rotor nacelle assembly) and turbine support structures are covered.
Det Norske Veritas (DNV), 2010. Design of Offshore Wind Turbine Structures.	• IEC environmental conditions and load cases are adopted with minor modifications • Structural and foundation design criteria mostly refer to other DNV design guidelines for offshore structures. • Applicable to offshore wind turbine support structures including tower, substructure and foundation.
US Department of Interior, 30 CFR Part 285, 2009. Renewable Energy Alternate Uses of Existing Facilities on the Outer Continental Shelf.	• US regulation • Reference is made to API RP 2A-WSD for the design and inspection • Environmental conditions and design load cases for offshore wind turbines are not specifically covered.
German Federal Maritime and Hydrographic Agency (BSH), 2007. Standard Design of Offshore Wind Turbines.	• German regulation on design, certification and operation
Danish Energy Agency, 2001. Recommendation for Technical Approval of Offshore Wind Turbines.	• Annex to Danish regulation for land-based turbines. • Covers environmental conditions, loads and structural design requirements

As a part of the recent calibration study carried out by ABS (Yu et al., 2011 [2.86]), the nominal reliability analysis is performed using a formulation similar to Tarp-Johansen's model (2005) [2.67] and environmental conditions for several locations on the US Atlantic Coast and Gulf Coast. Both "normal" and "abnormal" turbine operating conditions are considered in the study. The results for the "normal" load cases agree well with MMI's results, but are interpreted in a different way. In addition to comparing the ABS and IEC design guides, the focus is also placed on whether the direct application of IEC 61400-3 to the US OCS can result in the comparable level of safety that can be anticipated from a design in European waters. The results are presented in Figure 2.3 and Figure 2.4, which are adapted from Yu et al. (2011) [2.86]. The blue "benchmark" lines represent the values of reliability index obtained using IEC 61400-3 design criteria and the North Sea wind or wave conditions. The purple squares are the values of reliability index obtained using IEC 61400-3 design criteria and the wind or wave data at different US offshore locations, while the green diamonds are those obtained using ABS design criteria. The effect of wave slamming (impact) is not taken into account. It is shown in these plots that applying IEC 61400-3 strength design criteria in combination with the US metocean conditions could result in a design having much lower reliability than what is anticipated from a design in European waters, assuming that the design of turbine support structure is governed by the strength criteria. It is also likely that other design considerations such as resonance avoidance, wave slamming, and fatigue resistance may dominate and thus determine the actual structural reliability level.

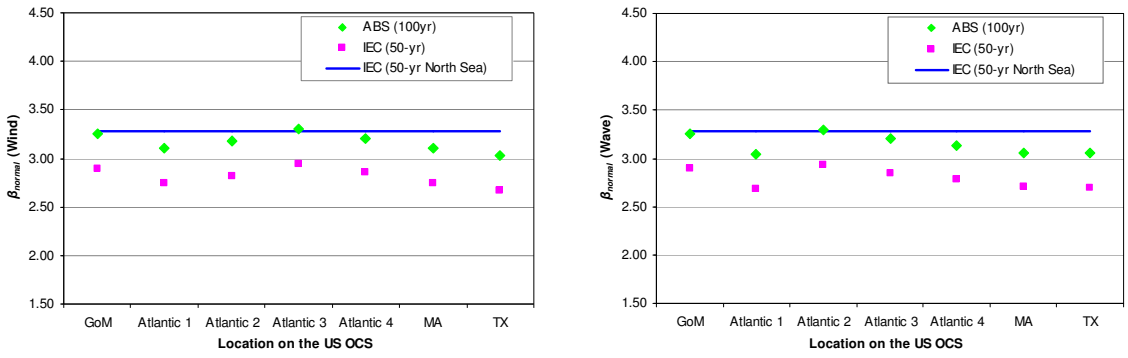

Figure 2.3 Reliability Index for Normal Conditions under Wind or Wave Loads (Yu et al., 2011)

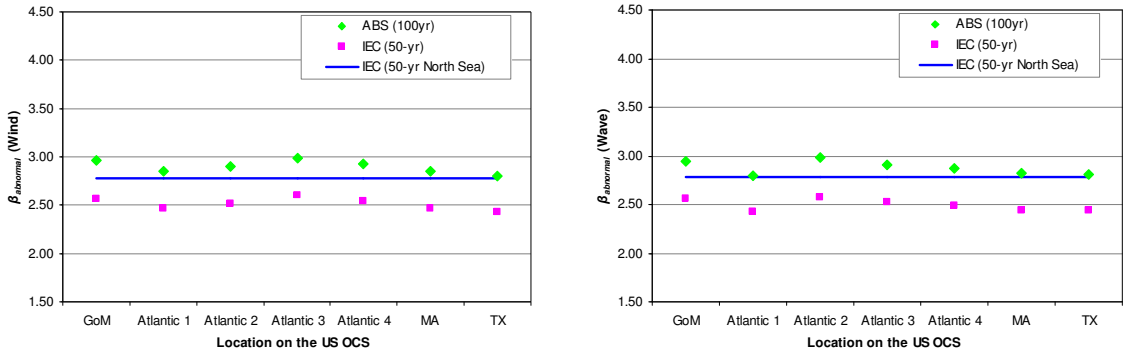

Figure 2.4 Reliability Index for Abnormal Conditions under Wind or Wave Loads (Yu et al., 2011)

Yu et al. (2011) [2.86] also present the case study results for a tripod supported reference offshore wind turbine subjected to the site specific environmental conditions in the GOM offshore Texas. The consequence of the failure of yaw control system is considered by assuming omni-directional hurricane winds. It is shown that the magnitude of relative increase in structural response due to the change of return period from 50-year to 100-year is approximately 60%, which is in contrast to a typical 20%~30% increase for an fixed offshore platform designed to API RP 2A-WSD in the GOM. It appears that the combined effect of strong hurricane wind and most unfavorable yaw misalignment could amplify the level of load increase. Such a relative magnitude of load increase becomes less significant when the wind condition turns weaker. This observation highlights the importance of including the turbine operating conditions in the design load case definition and taking this into account when establishing the design criteria.

2.1.5 Simulation Software

Modern wind turbine analysis software provides capabilities of modeling aerodynamic (aero), control system (servo), and structural-dynamic (elastic) behavior of a wind turbine in the time domain. Numerous wind tunnel tests and field measurements have been performed for land-based turbines. The collected data have been used to calibrate and enhance the simulation tools. In recent years, some of these simulation tools are extended to include the additional dynamics, such as responses due to hydrodynamic loads and foundation dynamics, pertinent to offshore wind turbines. A brief survey of available offshore wind turbine design tools can be found in Ashuri and Zaaijer (2007) [2.9].

The sophistication of these aero-hydro-servo-elastic simulation tools and the fact that there are limited data available for verification prompted the researchers to launch an international

collaborative project, “The Offshore Code Comparison Collaboration” (OC3), which operates under Subtask 2 of the International Energy Agency (IEA) Wind Task 23. The primary focus is to verify the accuracy and correctness of participating simulation software through code-to-code comparisons. The final report (Jonkman and Musial, 2010 [2.45]), as well as the publications referred in the report, provides a valuable source of information about the background and performance of the simulation software. In the new IEA Wind Task 30 initiated in 2010 as an extension of OC3, more simulation tools are involved and model test data will be used in the software verification.

2.2 Technical Approach for Case Studies

In addition to the design standard gap analysis, which has been conducted in a number of studies, it is believed that case studies using typical designs and latest simulation technologies will provide more insights into the actual behavior of offshore wind turbines subjected to hurricanes on the US OCS. Several case studies have been performed to assess a hurricane's effects on the design of offshore wind turbine support structures (see e.g. Yu et al. [2.86], 2010; MMI, 2008 [2.53]). This project extends the scope and the level of detail of previous studies, with the aim of providing a thorough understanding of the effects of various design parameters that are potentially important to the design of offshore wind turbines for hurricane-prone regions on the US OCS.

2.2.1 Problem Definition

The objective of the case studies is to assess the applicability of relevant load cases originally defined in IEC 61400-3 for bottom-founded offshore wind turbines and explore other potentially critical load cases for offshore wind turbines in the hurricane prone areas on the US OCS. The characteristic global and local responses of offshore wind turbines under hurricane environmental conditions are calculated with the consideration of the dynamic interaction among the turbine's Rotor Nacelle Assembly (RNA), support structure and foundation. The correlations between those responses and various design parameters are of particular interest. The design parameters considered in the studies are listed as follows:

- Wind models
- Normal and abnormal turbine operating modes
- Design environmental conditions
- Site conditions
- Support structure configurations

To assess the characteristic responses for different configurations of turbine support structure, the conceptual designs of a monopile, a tripod and a jacket type support structure, respectively, are selected in the case studies. Efforts have been made to keep these conceptual designs as realistic as possible. It is not, however, the focus of the case studies to produce optimized designs.

The turbine is selected based on the data available in the public domain. The same turbine is used for the all three different types of support structures.

Regional site conditions in the West Central region of the Gulf of Mexico as well as the Mid-Atlantic and South Atlantic regions of the US East Coast are used in the case studies. Site conditions at one specific location near the Texas coastline in the Gulf of Mexico are also selected for the monopile case studies.

A general description of the load cases considered in the case studies is summarized in Table 2.2 below. Detailed summaries of the analysis load cases for each conceptual design are listed in Section 2.6 for the monopile, Section 2.7 for the tripod and Section 2.8 for the jacket.

Table 2.2 General Load Cases Descriptions for the Case Studies

Wind condition	*Wave*	*Wind and wave directionality*	*Current*	*Water level*	*Yaw Control*	*Turbine Operating Mode*
Extreme turbulent wind $V_{hub} = V_{10min,50\text{-}yr}$	50-yr return wave	Collinear $\pm 30^0$ cross waves $\pm 90^0$ cross waves	50-yr Currents	50-yr Water Level	Yaw misalignment $\varphi = \pm 8^0$	Normal
Extreme turbulent wind $V_{hub} = V_{10min,100\text{-}yr}$	100-yr return wave	Collinear $\pm 30^0$ cross waves $\pm 90^0$ cross waves	100-yr Currents	100-yr Water Level	Yaw misalignment $\varphi = \pm 8^0$	Normal
Extreme turbulent wind $V_{hub} = V_{10min,50\text{-}yr}$	50-yr return wave	Collinear $\pm 30^0$ cross waves $\pm 90^0$ cross waves	50-yr Currents	50-yr Water Level	Yaw misalignment $-180^0 \leq \varphi < 180^0$	Abnormal
Extreme turbulent wind $V_{hub} = V_{10min,100\text{-}yr}$	100-yr return wave	Collinear $\pm 30^0$ cross waves $\pm 90^0$ cross waves	100-yr Currents	100-yr Water Level	Yaw misalignment $-180^0 \leq \varphi < 180^0$	Abnormal

Notes:

1. V_{hub} is the mean wind speed at hub height
2. $V_{10min,50\text{-}yr}$ is the 50-year return 10-minute average wind speed at hub height.
3. $V_{10min,100\text{-}yr}$ is the 100-year return 10-minute average wind speed at hub height.
4. The normal and abnormal turbine operating modes correspond to the different safety factors as defined in IEC 61400-3 (2009) for the LRFD design approach and the ABS Guide (2010) for the WSD design approach.

2.2.2 Modeling and Analysis Procedures

2.2.2.1 Overall Approach and Analysis Tools

Figure 2.5 shows a schematic plot of the overall modeling and dynamic analysis procedure. Structural responses due to the static wind drag loads on the nacelle and support structure as well as the wave slamming loads, where applicable, are computed in separate structural analyses and then superimposed on those calculated following the procedure depicted in Figure 2.5. More details on the load and structural analysis methods can be found in Section 2.2.2.3 and Section 2.2.2.4.

To perform the coupled aerodynamic and hydrodynamic load analyses, the FAST program suite (v7.00.01a-bjj), which includes the aerodynamic load analysis program AeroDyn and the hydrodynamic load analysis program HydroDyn, is employed along with the turbulent wind field simulator TurbSim (v1.5). Both the FAST and TurbSim programs are developed and maintained by the National Renewable Energy Laboratory (NREL) (Jonkman and Buhl, 2005 [2.46]). Modifications have been made to the NREL's TurbSim program to include the wind models recommended in API RP-2A-WSD (2007).

For the structural analysis, the general purpose finite element program ANSYS (R11) is used for both static and dynamic analysis.

A number of in-house tools, including the stream function wave generator, which is based on the subroutines developed by Dalrymple at the University of Delaware, are also used to derive the input data and post process the analysis results.

The case studies include the evaluation of loads on the wind turbine support structure for a range of yaw misalignment angles with respect to the incoming wind direction. Yaw misalignment may occur on various occasions such as

- Fault in yaw control system
- Loss of grid connection and lack of sufficient back-up battery power supply
- Rapid change of local hurricane wind direction

The effect of blade pitch angle locking on the loads on turbine support structure is evaluated in the case studies, although the pitch control failure and angle locking are not specifically included in the IEC abnormal load cases. The direct consequence of a malfunction of pitch angle control is

over-speeding of the rotor under strong winds that can potentially cause damage to turbine blades and power drive trains. The turbine blades are normally feathered during the storm condition to minimize the load. Since the pitch control for each blade normally operates independently, the possibility of having failure in all pitch controllers is very low.

Main assumptions made in the case studies are summarized as follows:

- The wind turbine selected for the case studies is the NREL 5-MW baseline offshore wind turbine (see Section 2.3.2), which is a three-blade horizontal axis wind turbine. Note that all existing design guidelines are developed for horizontal axis wind turbines and may not be applicable to other turbine configurations.

- The FAST program is limited to modeling monopiles. In order to solve for the loads on a tripod or jacket support structure, an "equivalent" monopile design is derived to simulate the structural properties (natural period, mass, stiffness, wave load) of the actual tripod or jacket design. While the wind and wave misalignment are considered in the case studies, it is assumed that the damping ratios employed in the FAST program analysis model are not sensitive to the misalignment of wind and wave directions. See Section 2.3.3 for details.

- Multiple realizations are calculated in the load analysis for each load case involving turbulent wind conditions. The maximum tower base shear and overturning moment of the equivalent monopile are obtained from their time histories for each realization. The mean of these maxima is calculated over the multiple realizations and used in the subsequent structural finite element analysis. See Section 2.3.4 for more details.

- The mean maximum tower base shear and overturning moment calculated by the FAST program are applied as quasi-static loads to the same location in the finite element model. The time history of non-linear regular wave generated based on the stream function theory is applied to the finite element model at the same time. The maximum responses from the dynamic structural finite element analysis under this combined loading are calculated as an approximation of the maximum responses to aerodynamic and hydrodynamic loading. See Section 2.2.2.4 for more details.

- Structural analysis results for individual members are processed and presented in terms of unity check results. See Section 2.2.2.5 for more details.

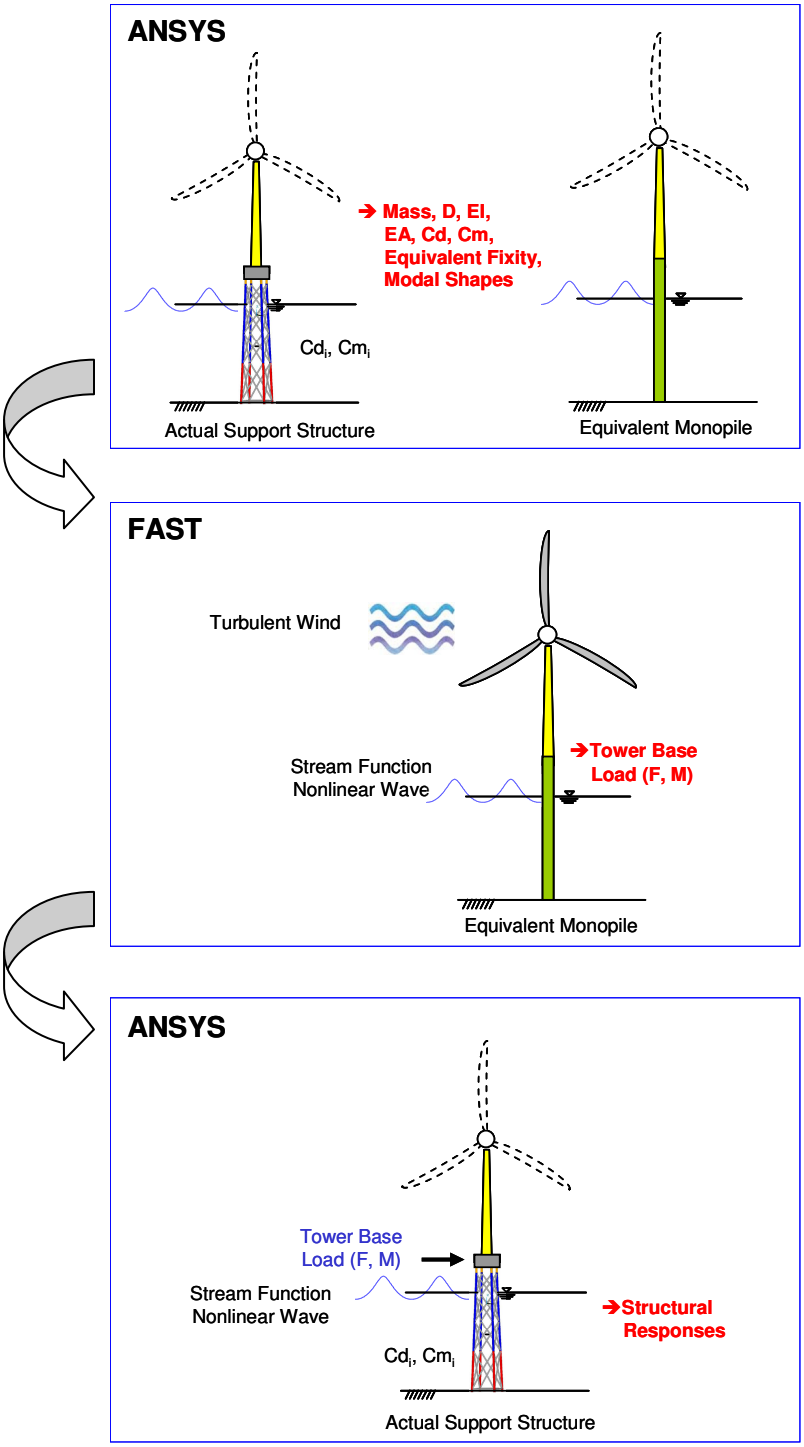

(Note: Structural responses to the static wind drag load on the nacelle and support structure as well as the wave slamming load where applicable are computed in separate analyses and then superimposed on those responses calculated following the procedure shown above.)

Figure 2.5 Modeling and Dynamic Analysis Procedure

2.2.2.2 Site Conditions

The regional metocean data for the US Atlantic Coast and the Gulf of Mexico are applied in the case studies. Three different water depths are assumed for each site location to accommodate the conceptual designs of monopile, tripod and jacket, respectively.

For the US Atlantic Coast, a gridded wind map was acquired by ABS to support its internal research projects. The site assessment for the US Atlantic Coast is performed for the purpose of providing a set of "indicative" metocean data for the calibration of design standards. The effect of water depth on the significant wave height is not included. Although this set of metocean data has shown reasonably good agreement with other metocean data available in the public domain, including API standards, ASCE-7 (2010), and NOAA NDBC buoy database, it is not meant to be used in the actual design of an offshore wind farm. Instead, a site assessment should always be carried out to establish site specific design environmental conditions.

The wind map is derived using NOAA North Atlantic Basin Tropical Storm and Hurricane Database (HURDAT), also known as the "best-track" hurricane database, and covers about 30 miles offshore Atlantic Coast. The target area is discretized into small cells each with size of 4 km by 4 km. In the simulation of each hurricane wind field, all information is stored cell by cell and finally used to derive the wind map. The 1-minute mean wind speeds at 10 m above surface with 10-year, 50-year and 100-year return periods are calculated in each cell. The Atlantic Coast is then divided into four regions based on the four-scale magnitudes of 100-year return wind speeds as shown in Figure 2.6. The associated significant wave height in each cell is calculated using the parametric model developed by Young (1988) [2.83] for the hurricane generated waves (see also Section 2.1.2.3). Surface current is roughly estimated to be 2 to 3 % of the one-hour sustained wind speed during a tropical storm according to API RP 2A-WSD (2007). Storm surge heights are derived using the SLOSH program, which is developed by the Federal Emergency Management Agency (FEMA), United States Army Corps of Engineers (USACE), and the National Weather Service (NWS). Using the metocean data in each cell, the exceedance probability curves for the wind speed, significant wave height, current speed and surge height are also developed for four regions along the US Atlantic Coast. See Figure 2.6 for an example.

For the Gulf of Mexico, the regional metocean data are extracted from API Bulletin 2INT-MET (2007) for the West Central region (Figure 2.7).

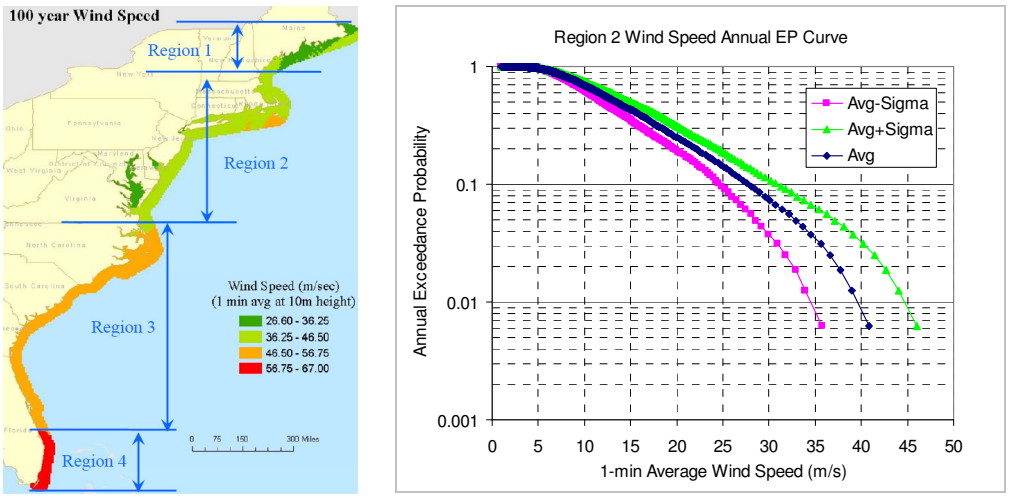

Figure 2.6 Regional Wind Conditions in the US Atlantic Coast

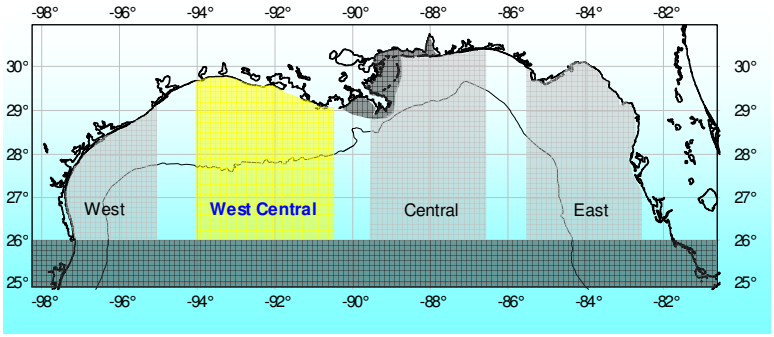

Figure 2.7 Gulf of Mexico West Central Region

Figure 2.8 Site Location in the GOM (NOAA NDBC Station 42035)

A site location near Galveston Bay is also selected for the site specific assessment. The NOAA NDBC buoy station 42035 as shown in Figure 2.8 is located about 22 nautical miles east of Galveston. The extreme wind speed and significant wave height at the site are derived using the buoy measurements between 1993 and 2010. The annual maxima of 8-minute wind speeds at 5 m above the water surface and the significant wave height during the hurricane season are extracted from the measurements. Gumbel curve fitting is used to determine the 50-year and 100-year return wind speeds and wave height as shown in Figure 2.9 and Figure 2.10. The correlation between wave spectrum peak period and significant wave height is derived using the binned buoy data as shown in Figure 2.11. The current speed and surge height at this site are calculated based on the recommendations in API Bulletin 2INT-MET (2007).

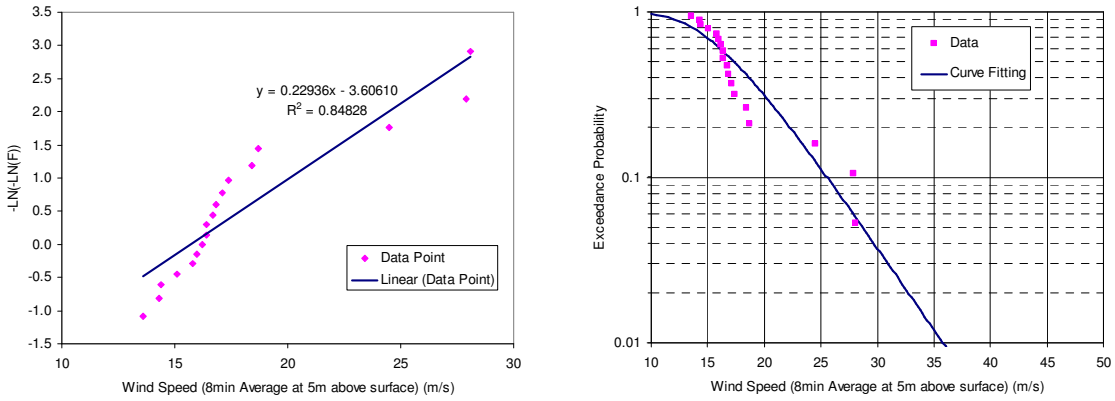

Figure 2.9 Gumbel Curve Fitting for the Buoy Wind Data in Hurricane Seasons

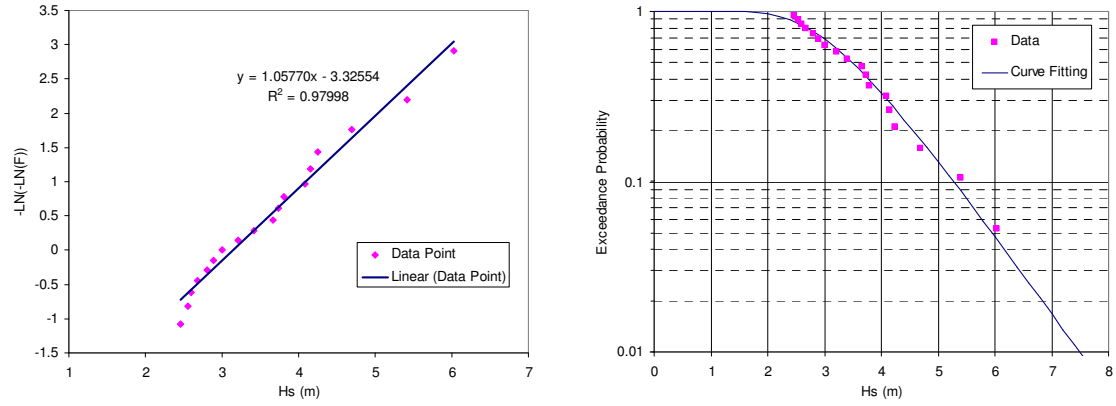

Figure 2.10 Gumbel Curve Fitting for the Buoy Wave Data in Hurricane Seasons

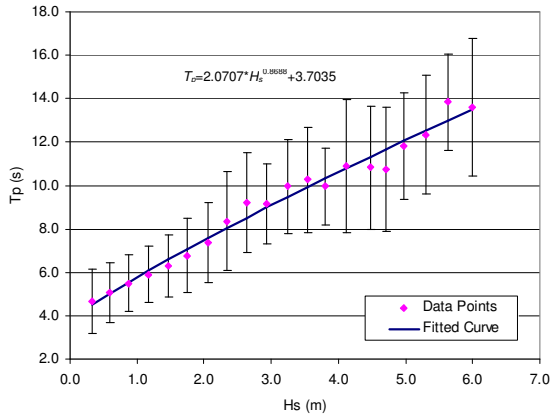

Figure 2.11 Correlation of T_p and H_s Using the Binned Buoy Data in Hurricane Seasons

2.2.2.3 Load Analysis

The coupled aero-hydro-servo-elastic analyses are carried out using the FAST program developed by NREL. The theory background and user's guide for the FAST program and other relevant references can be found in Jonkman and Buhl (2005) [2.46].

Both turbine rotor-nacelle-assembly (RNA) and its support structure are modeled in the FAST model. Since the modeling capability in the FAST program is currently limited to the monopile type of turbine support structure with a clamped foundation and constant drag and inertia coefficients, an equivalent monopile emulating the first four natural frequencies and mode shapes as well as the mass, stiffness and wave drag and inertial loads of the actual structure is derived for the load analysis using the FAST program.

The flexible foundation, which is characterized by the nonlinear soil-structure interaction, is approximated in the FAST model as an extended section of equivalent monopile beyond the mudline. The end of this extended section is clamped while its length is determined in such a way that the displacements at the mudline under a given lateral force match those obtained from the finite element analysis of the full model. This approach is also referred to as the "equivalent fixity" approach.

The 3D turbulent wind field is generated using the TurbSim program. The Kaimal wind spectrum and the exponential coherence function referred in IEC 61400-1 (2005) are applied to all the site locations. Sensitivity analyses are also performed to find the optimal domain and grid size for the

wind field simulation. The applicability of the wind model recommended in API Bulletin 2INT-MET (2007) is also evaluated.

The nonlinear shallow water waves are defined through the user defined wave option in the FAST program. The wave profile and kinematics for each site condition are calculated using an ABS in-house program, which is partially based on the work at the University of Delaware on the stream function theory and numerical algorithm. This in-house program is capable of generating the stream function waves up to the wave breaking.

The combination of various environmental parameters as well as the turbine operating modes used in the FAST simulation is on the basis of the load case definitions. Multiple realizations with different random seeds are calculated in the load analysis for each load case involving turbulent wind conditions. The output of the FAST simulation used in the structural analysis is the forces and moments at the interface between the tower and substructure, which is also called tower base loads, as well as the forces and moments at the mudline. The time series of load components (F_x, F_y, M_x and M_y) at the tower base and the mudline are calculated.

Four global responses, which include the shear force, $(F_x^2+F_y^2)^{1/2}$, and overturning moment, $(M_x^2+M_y^2)^{1/2}$, at the tower base and the mudline, are used to define the design loads in the case studies. For each realization, the moment when a global response reaches its maximum is identified from its time history, and the values of the concurrent load components F_x, F_y, M_x and M_y at the tower base and the mudline are also recorded at that moment. The same process is applied to each global response and finally each resultant load component set is averaged over multiple realizations. The final output of this process yields four load combinations consisting of both the tower base and mudline load components. These four load combinations are used to determine the load set applied in the subsequent structural finite element analysis using the full support structure model in ANSYS.

The static wind drag load on the nacelle and the support structure above the still water level is calculated by $F_{d-wind} = 1/2\,\rho\, C_{d-wind}\, A V^2$, where $F_{d\text{-}wind}$ is the wind drag force per unit length, ρ is the air density, $C_{d\text{-}wind}$ is the wind drag coefficient, A is the projected area normal to the wind direction, and V is the wind speed.

When applicable, the breaking wave slamming load is also considered. The slamming load calculation follows the guidance given in IEC 61400-3 Annex D. The formulation is referenced in Section 3.3.1.1.

2.2.2.4 Structural Analysis

The static and dynamic structural analyses as well as the modal analysis are carried out using the general purpose finite element software ANSYS.

- Structural Model

The turbine RNA is modeled as a lumped mass element (MASS21 element) placed at its center of gravity. The mass inertia of turbine RNA is also defined as mass element property. The support structure subjected to hydrodynamic loads is modeled using the PIPE59 element, which is capable of accounting for the wave drag and inertia loads (Morison forces), the marine growth and the internal fluid content of flooded members. The stream function wave under a given site condition is calculated by an ABS in-house program and used as input to the dynamic structural analysis. The soil-structure interaction is simulated by the lateral bearing (p-y), shaft friction (t-z) and end bearing (Q-z) relationships. The nonlinear spring element COMBIN39 in ANSYS is used to model these soil-pile interactions.

- Modal Analysis – For calculating modal shapes to be used as the input to the FAST simulation

The modal analysis is carried out to calculate the modal shapes and natural frequencies of each offshore wind turbine at a specific site. The natural frequencies are compared against the turbine Campbell chart in order to verify that there is no resonance between the turbine RNA and turbine's support structure. The mode shapes are used as part of the input to the FAST analysis. They are also employed to verify the equivalent monopile model for the FAST simulation. Figure 2.12 shows an example of the comparison of the first four modal shapes of a jacket-type support structure with those of the equivalent monopile.

- Dynamic Analysis #1 – For calculating the equivalent monopile properties to be used as the input to the FAST simulation

The dynamic analysis is performed using the finite element model of both the actual support structure and its equivalent monopile to determine the uniform drag and inertia coefficients, i.e. C_d and C_m, of the equivalent monopile. As indicated in Section 2.2.2.3, the FAST program currently only accepts the uniform C_d and C_m of the equivalent monopile as inputs, while an actual support structure could have different configurations, such as a tripod or a jacket, and varying C_d and C_m values for different locations on the structure. Figure 2.13 depicts a verification example showing that under the same wave condition, the base shear and overturning moment at the mudline of an actual turbine support structure are comparable to those of its equivalent monopile.

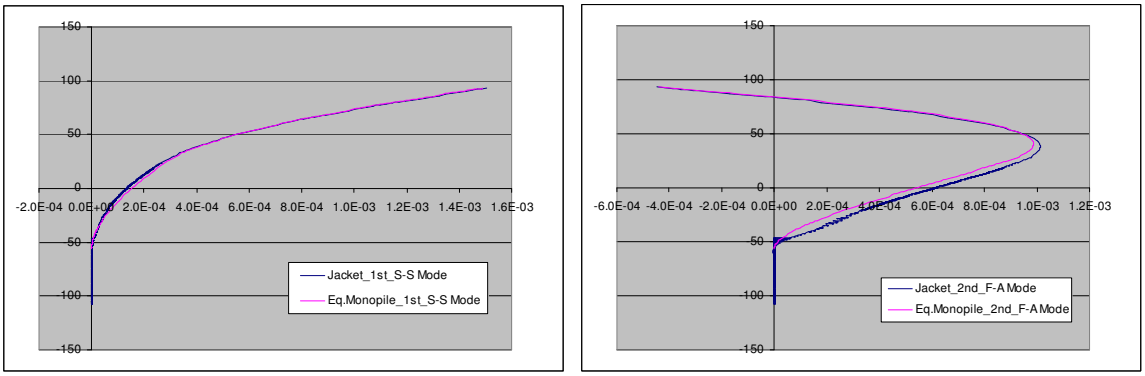

Figure 2.12 Verification of Modal Shapes of Equivalent Monopile for FAST Input

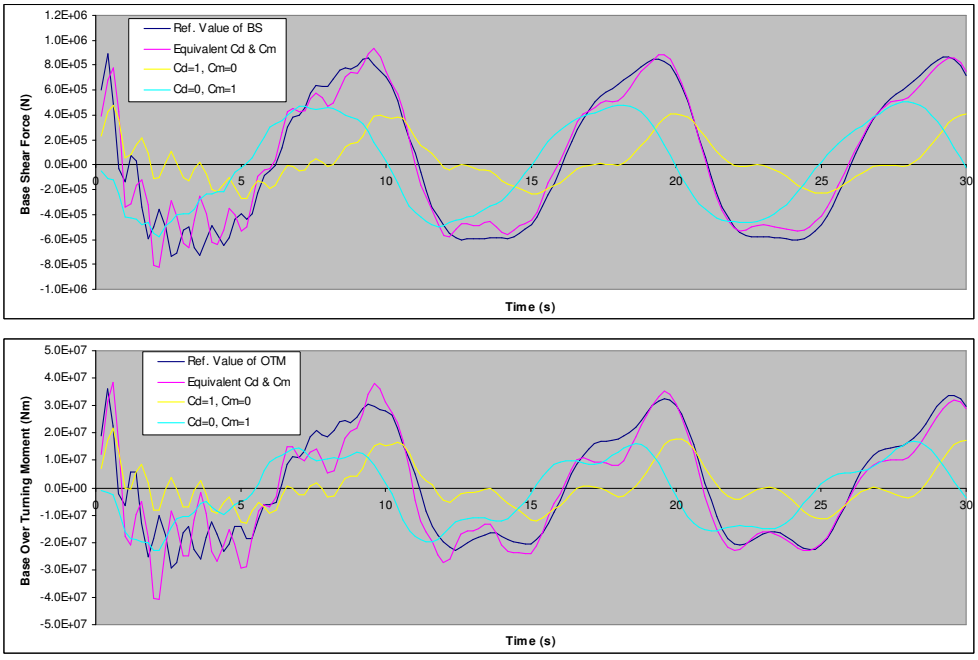

Figure 2.13 Verification of C_d and C_m of Equivalent Monopile for FAST Input

- Dynamic Analysis #2 – For calculating the responses of a support structure subjected to the passing stream function wave and the quasi-static tower base loads obtained from the FAST simulation

From the results of the FAST simulation, the four combinations of load components at the tower base and the mudline are derived according to Section 2.2.2.3. Ideally, the dynamic structural analysis should be performed for all these load combinations and then the maximum responses in each structural member are identified. To limit the total number of time domain structural analyses to a manageable level for these case studies, tower base loads for one load combination that is expected to generate the maximum structural responses is first determined so that only that load combination is applied in the structural dynamic analysis. In conjunction with the selected load combination of tower base loads, the time history of stream function wave under a given site condition is also applied to the support structure. This process is demonstrated in the third step shown in Figure 2.5. It is assumed that

- Since all the inertia effects have been taken into account in the FAST simulation and therefore in the quasi-static tower base loads, the inertia effect does not need to be considered in the structural dynamic analysis subjected to the passing waves. This assumption could potentially underestimate the mudline shear force and overturning moment, although the first natural period of the support structure is about 3.5 seconds and therefore the inertial load effect of the support structure due to incident waves is relatively small.

- The maximum structural responses obtained through the time domain dynamic analysis are used to combine with the responses due to other static and quasi-static loads as described in the latter part of this subsection on performing code checks. Note that the maximum tower base loads may not occur at the same moment when the wave load reaches its peak. Simply choosing the maximum response of the support structure subjected to the quasi-static tower base loads and passing waves may yield conservative results.

A verification study has been carried out to compare the maximum mudline shear force and overturning moment obtained from the ANSYS dynamic analysis to those obtained from FAST simulation, where the above two assumptions are not applied. The differences are found to be mostly on the conservative side with approximately the magnitude between -5% and +10%, which indicates that the above two assumptions introduce insignificant modeling errors into the calculation and therefore are considered acceptable for the purpose of the case studies.

- Dynamic Analysis #3 – For calculating maximum transient responses of the support structure subjected to the wave slamming load

When the breaking wave slamming load needs to be considered, a separate dynamic analysis is performed to calculate the transient response of the support structure subjected to the slamming load. The time varying slamming forces are calculated according to Section 2.2.2.3. The output of this dynamic analysis is the time history of the base shear and bending moment at mudline. The quasi-static tower base force and moment that balance the maximum bending moment and the associated shear force at the mudline are computed.

- Static Analysis – For calculating the response of structural member subjected to the static wind drag load and quasi-static maximum wave slamming load

With the static wind drag loads on the nacelle and support structure as well as the quasi-static tower base force and moment due to the wave slamming where applicable, a separate static finite element analysis is performed. The resultant responses of each member are superimposed on those obtained from the "Dynamic Analysis #2", described above.

2.2.2.5 Code Check

There are two strength design approaches currently available for the design of offshore wind turbine support structures. One is the load and resistance factor design (LRFD) strength criteria specified by IEC 61400-3 (2009) in conjunction with ISO 19902 (2007). Another is the working stress design (WSD) strength criteria defined in the ABS Guide (2011). In the case studies, the structural analysis results for the selected structural members are processed and presented in terms of unity check results, or the utilization ratios. When the ABS WSD-based criteria are followed, a utilization ratio is defined as the ratio of structural response times the safety factor to the strength capacity. For the IEC LRFD-based criteria, a utilization ratio is defined as the ratio of the factored structural response to the factored strength capacity. The strength criteria specified in API RP 2A-WSD (2007) for the extreme design condition are also applied for the comparison.

It should be noted that IEC 61400-3 (2009) defines the extreme condition as a 50-year return event. In the present study, both 50-year and 100-year return conditions are considered. The strength criteria, particularly the load factors, specified in IEC 61400-3 are used in the unity check using the IEC LRFD-based approach. These load factors are applied to the load cases for both the 50-year and the 100-year return conditions.

2.3 Case Study Models

2.3.1 Site Conditions

The 50-year and 100-year return metocean conditions are listed in Table 2.3 through Table 2.6. Section 2.2.2.2 provides the technical background and methods used in the determination of these metocean data. The locations of two regions along US Atlantic Coast and the West Central region of Gulf of Mexico can be found in Figure 2.6 and Figure 2.7, respectively. The site location represented by NOAA NDBC Station 42035 is shown in Figure 2.8.

The mean water depth for each type of support structure is assumed the same at different site locations, where the storm surge and tide heights may vary.

The maximum wave height H_{max} highlighted in yellow in these tables indicates that the breaking limit has been reached and therefore, the wave slamming load and the relevant dynamic structural analysis need to be performed.

For the GOM Site condition, the 50-year and 100-year return significant wave heights (H_s) are derived based on the buoy measurements as described in Section 2.2.2.2. The wave spectrum peak period T_p is calculated using the H_s and T_p relation T_p=2.0707*$H_s^{0.8688}$+3.7035 as shown in Figure 2.11. Note that the wind speed given in the table is the 1-hour mean wind speed at 10 m above the water surface, while the buoy measurement gives the 8-minute mean wind speed at 5 m above the water surface (see Figure 2.9 and Section 2.2.2.2). The logarithmic wind shear equation referred in API RP 2A-WSD (2007) is employed to convert the prediction based on the buoy data to what are listed in the tables. This logarithmic wind shear equation is also shown in Section 2.4.1. The current speed, surge height and wave period of maximum wave height (T_{max}) are approximately taken as the regional data for the GOM West Central at the water depth of 13.7 m as recommend in API Bulletin 2INT-MET (2007).

The wave profiles associated with the wave conditions defined in Table 2.4 and Table 2.6 are plotted in Figure 2.14 and Figure 2.15, respectively, calculated following the stream function wave theory. It can be seen that the steep waves are generated for the monopile and tripod cases with shallow water depth. The wave kinematics of these nonlinear waves are also derived based on the stream function wave theory and used as input in the integrated turbine aerodynamic-hydrodynamic load analysis using FAST and the structural finite element analysis using ANSYS.

Table 2.3 50-Year Return Water Depth, Current Speed and Wind Speed

Location	*Support Structure*	*Water Depth (d)*	*Surge+Tide Height*	*Effective Water Depth (d_{eff})*	*Wind Speed (1hr @ 10m)*	*Current Speed*
		(m)	(m)	(m)	(m/s)	(m/s)
Atlantic Region 2	Monopile	13.70	1.60	15.30	30.35	0.90
	Tripod	24.00	1.60	25.60	30.35	0.90
	Jacket	47.00	1.60	48.60	30.35	0.90
Atlantic Region 3	Monopile	13.70	2.40	16.10	36.60	1.10
	Tripod	24.00	2.40	26.40	36.60	1.10
	Jacket	47.00	2.40	49.40	36.60	1.10
GOM West Central	Monopile	13.70	2.60	16.30	34.30	1.48
	Tripod	24.00	1.98	25.98	34.30	1.41
	Jacket	47.00	1.46	48.46	34.30	1.21
TX Site in GOM	Monopile	13.70	2.60	16.30	31.88	1.48

Notes:

1. The 1-hour mean wind speed at 10 m above the mean water level for the TX Site in the GOM is obtained from the buoy data analysis and converted using the logarithmic wind shear equation defined in API RP 2A-WSD (2007)
2. 10-min mean wind speed at 10m above the mean water level is derived using the 1-hr mean wind speed at 10m above the mean water level given in this table and the conversion equation specified in API RP 2A-WSD (2007).

Table 2.4 50-Year Return Wave Condition

Location	*Support Structure*	H_s	T_z	T_p	H_{max0}	T_{max}	L_0	H_b/L_0	$H_{max} \leq H_b$	*Celerity*
		(m)	(s)	(s)	(m)	(s)	(m)		(m)	(m/s)
Atlantic Region 2	Monopile	9.00	9.63	-	16.86	10.90	185.51	0.0612	11.35	11.75
	Tripod	9.00	9.63	-	16.86	10.90	185.51	0.0926	16.86	14.24
	Jacket	9.00	9.63	-	16.86	10.90	185.51	0.1430	16.86	16.40
Atlantic Region 3	Monopile	11.40	10.84	-	21.18	12.76	254.17	0.0481	12.23	12.25
	Tripod	11.40	10.84	-	21.18	12.76	254.17	0.0750	19.07	15.09
	Jacket	11.40	10.84	-	21.18	12.76	254.17	0.1216	21.18	18.26
GOM West Central	Monopile	6.90	-	14.20	12.30	12.80	255.93	0.0484	12.30	12.32
	Tripod	8.10	-	14.20	14.30	12.80	255.93	0.0738	14.30	15.01
	Jacket	9.40	-	14.20	16.60	12.80	255.93	0.1190	16.60	18.22
TX Site in GOM	Monopile	6.84	-	14.71	12.72	12.80	255.93	0.0484	12.38	12.32

Notes:

1. H_s, T_z and T_p are the significant wave height, the zero up-crossing wave period and the peak period of wave spectrum
2. H_{max0} is the maximum wave height in the intermediate water depth without considering the breaking limit
3. H_{max} is the maximum wave height capped by the breaking limit
4. T_{max} is the period of maximum wave height
5. L_0 is the wave length determined using the dispersion equation ($L_0 = gT_{max}^2/2\pi$, where g is the acceleration of gravity)
6. H_b is the breaking wave height. H_b/L_0 is determined according to Dean (1974) [2.20]
7. The wave height H_{max} highlighted in yellow indicates that the breaking limit has been reached and the wave slamming load needs to be taken into account.

Table 2.5 100-Year Return Water Depth, Current Speed and Wind Speed

Location	*Support Structure*	*Water Depth (d)*	*Surge+Tide Height*	*Effective Water Depth (d_{eff})*	*Wind Speed (1hr @ 10m)*	*Current Speed*
		(m)	(m)	(m)	(m/s)	(m/s)
Atlantic Region 2	Monopile	13.70	1.90	15.60	32.90	1.25
	Tripod	24.00	1.90	25.90	32.90	1.25
	Jacket	47.00	1.90	48.90	32.90	1.25
Atlantic Region 3	Monopile	13.70	2.90	16.60	40.15	1.55
	Tripod	24.00	2.90	26.90	40.15	1.55
	Jacket	47.00	2.90	49.90	40.15	1.55
GOM West Central	Monopile	13.70	3.08	16.78	38.10	1.84
	Tripod	24.00	2.32	26.32	38.10	1.74
	Jacket	47.00	1.68	48.68	38.10	1.50
TX Site in GOM	Monopile	13.70	3.08	16.78	34.73	1.84

Notes:

1. The 1-hour mean wind speed at 10 m above the mean water level for the TX Site in the GOM is obtained from the buoy data analysis and converted using the logarithmic wind shear equation defined in API RP 2A-WSD (2007)
2. 10-min mean wind speed at 10m above the mean water level is derived using the 1-hr mean wind speed at 10m above the mean water level given in this table and the conversion equation specified in API RP 2A-WSD (2007).

Table 2.6 100-Year Return Wave Conditions

Location	*Support Structure*	H_s	T_z	T_p	H_{max0}	T_{max}	L_0	H_b/L_0	$H_{max} \leq H_b$	*Celerity*
		(m)	(s)	(s)	(m)	(s)	(m)		(m)	(m/s)
Atlantic Region 2	Monopile	9.75	10.01	-	18.22	11.33	200.41	0.0778	11.62	11.91
	Tripod	9.75	10.01	-	18.22	11.33	200.41	0.1292	17.65	14.49
	Jacket	9.75	10.01	-	18.22	11.33	200.41	0.2440	18.22	16.89
Atlantic Region 3	Monopile	12.25	11.26	-	22.70	13.20	272.37	0.0609	12.66	12.46
	Tripod	12.25	11.26	-	22.70	13.20	272.37	0.0988	19.68	15.32
	Jacket	12.25	11.26	-	22.70	13.20	272.37	0.1832	22.70	18.65
GOM West Central	Monopile	7.40	-	14.40	12.90	13.00	264.00	0.0636	12.75	12.51
	Tripod	8.70	-	14.40	15.30	13.00	264.00	0.0997	15.30	15.13
	Jacket	10.10	-	14.40	17.80	13.00	264.00	0.1844	17.80	18.39
TX Site in GOM	Monopile	7.50	-	15.63	13.95	13.00	264.00	0.0636	12.75	12.51

Notes:

1. H_s, T_z and T_p are the significant wave height, the zero up-crossing wave period and the peak period of wave spectrum
2. H_{max0} is the maximum wave height in the intermediate water depth without considering the breaking limit
3. H_{max} is the maximum wave height capped by the breaking limit
4. T_{max} is the period of maximum wave height
5. L_0 is the wave length determined using the dispersion equation ($L_0 = gT_{max}^2/2\pi$, where g is the acceleration of gravity)
6. H_b is the breaking wave height. H_b/L_0 is determined according to Dean (1974) [2.20]
7. The wave height H_{max} highlighted in yellow indicates that the breaking limit has been reached and the wave slamming load needs to be taken into account.

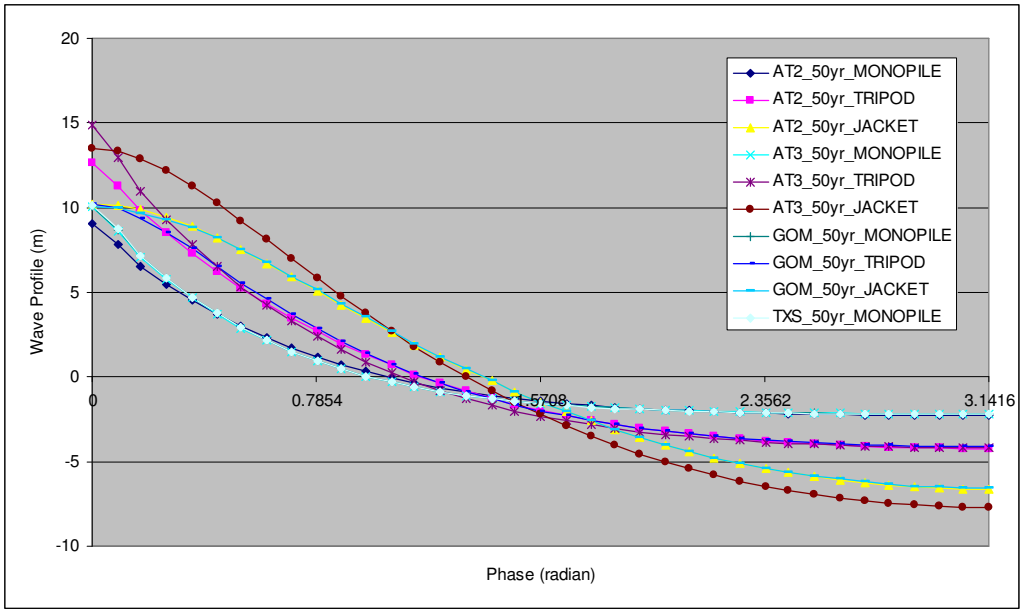

Figure 2.14 Wave Profile of 50-Year Return Waves

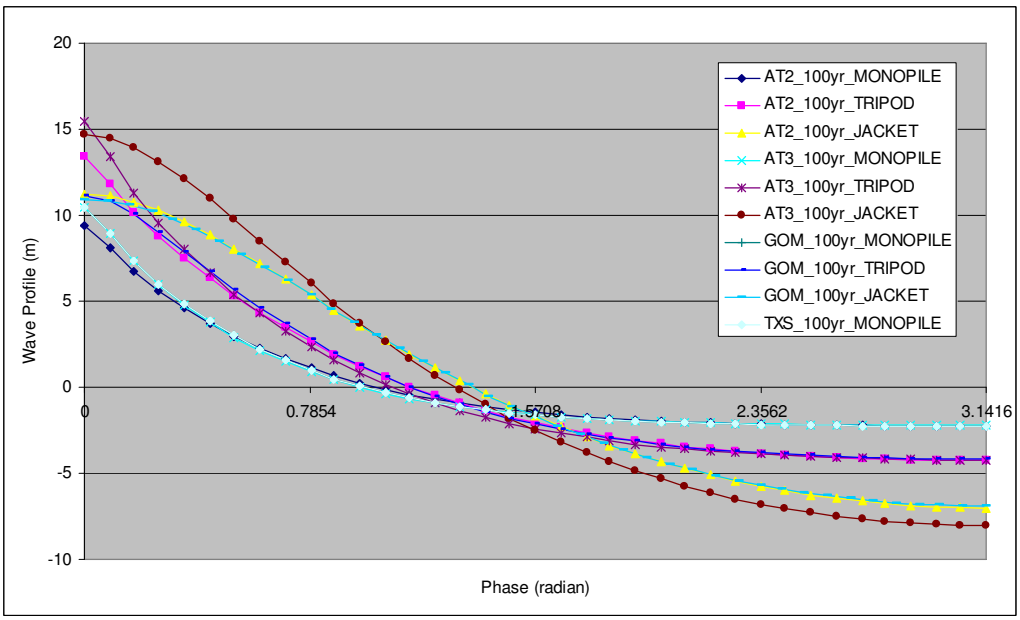

Figure 2.15 Wave Profile of 100-Year Return Waves

It is assumed that, at all site locations, the soil is composed of stiff clays whose undrained shear strength (c_u) as a function of the depth (z) below the mudline is depicted in Figure 2.16. The effective unit weight is taken as 8 kN/m^3. The effect of sea floor slope and scour is not considered in the case studies.

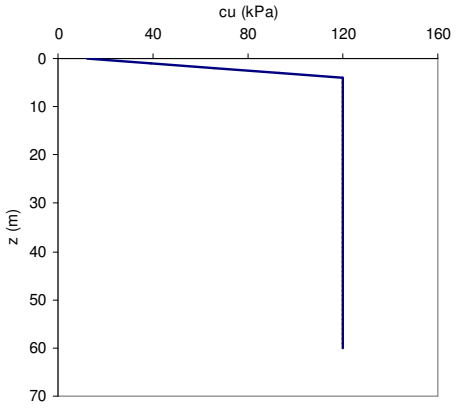

Figure 2.16 Undrained Shear Strength of Undisturbed Clay

2.3.2 Wind Turbine RNA and Tower Specifications

The wind turbine rotor-nacelle assembly (RNA) selected for the case studies is the NREL 5-MW baseline offshore wind turbine (Jonkman et al., 2009 [2.47]), which is a three-blade, pitch regulated and variable speed horizontal axis wind turbine. Figure 2.17 illustrates the main dimensions (in meters) of the turbine RNA. The main properties of turbine RNA and blades are listed in Table 2.7 and Table 2.8. The properties of turbine tower, which are adapted from Fabian et al. (2011), are summarized in Table 2.9.

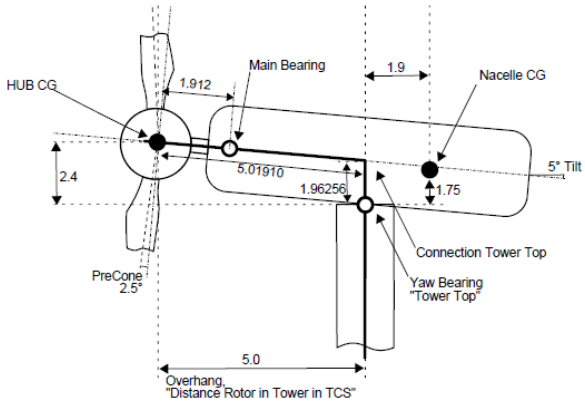

Figure 2.17 RNA of NREL 5-MW Baseline Offshore Wind Turbine (Jonkman et al., 2009)

Table 2.7 Properties of the RNA of NREL 5-MW Baseline Offshore Wind Turbine (Jonkman et al., 2009)

Rating	5 MW
Rotor Orientation, Configuration	Upwind, 3 Blades
Control	Variable Speed, Collective Pitch
Drive train	High Speed, Multiple-Stage Gearbox
Rotor, Hub Diameter	126 m, 3 m
Cut-In, Rated, Cut-Out Wind Speed	3 m/s, 11.4 m/s, 25 m/s (10-minute average, at hub height)
Cut-In, Rated Rotor Speed	6.9 rpm, 12.1 rpm
Rated Tip Speed	80 m/s
Rotor Mass	110000 kg
Nacelle Mass	240000 kg

Table 2.8 Undistributed Blade Properties (Jonkman et al., 2009)

Length	61.5 m
Mass	17740 kg
Second Mass Moment of Inertia (w.r.t. Root)	11776047 kg-m2
First Mass Moment of Inertia (w.r.t. Root)	363231 kg-m
CM Location (w.r.t. Root along Preconed Axis)	20.475 m
Structural Damping Ratio (All Modes)	2.5 %

Table 2.9 Turbine Tower Properties (Fabian et al, 2011)

Elevation	*Outer Diameter*	*Thickness*	*Point Mass*
(m)	(m)	(m)	(kg)
0 (tower base)	5.600	0.032	1900
1	5.577	0.032	-
12	5.318	0.030	-
22	5.082	0.028	-
34	4.800	0.024	1400
44	4.550	0.022	-
54	4.329	0.020	-
63	4.118	0.030	-
68 (Yaw Bearing)	4.000	0.030	1000

The Campbell diagram of the NREL 5-MW baseline offshore wind turbine, as depicted in Figure 2.18, shows that the resonance of the support structure and the rotor can be avoided when the the structural frequency lies between 0.20 Hz and 0.34 Hz, which is the frequency gap

between the blade passing frequency at the cut-in rotor speed and the rotor rotating frequency at the cut-out rotor speed (shaded area in the plot).

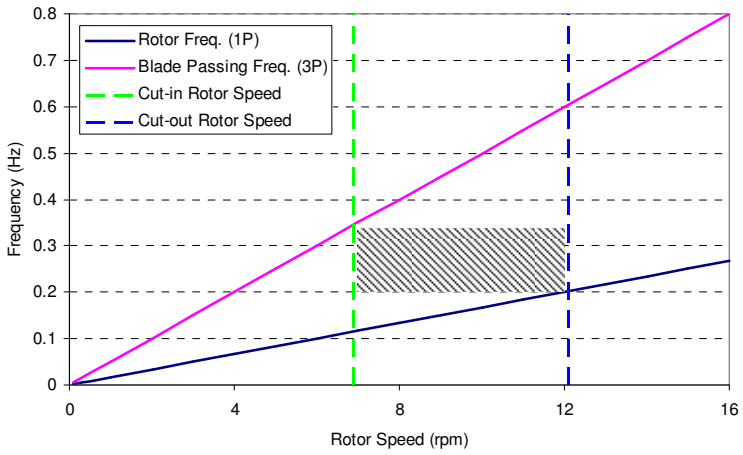

Figure 2.18 Campbell Diagram of NREL 5-MW Baseline Offshore Wind

2.3.3 Support Structure Configurations

The conceptual designs of a monopile, a tripod and a jacket type support structure, respectively, are selected in the case studies. Efforts have been made to keep these conceptual designs as realistic as possible, although only limited design modification or optimization is performed before launching the full-blown numerical analysis.

2.3.3.1 Monopile Support Structure

Figure 2.19 illustrates the geometry of the monopile support structure for the structural analysis in ANSYS and its equivalent monopile used in the FAST load analysis. The monopile support structure is composed of a tower, a transition piece welded to the tower and grouted to the pile, a submerged pile and a foundation pile. The hub height of monopile supported wind turbine is 86.9 m. The mean still water level is 13.7 m above the mudline.

The properties of the grouted transition piece and pile as well as an equivalent pile simulating this grouted connection in the finite element model are shown in Table 2.10. The geometry and mass properties of the monopile support structure are listed in Table 2.11 and Table 2.12, respectively.

Table 2.13 presents the properties of the equivalent fixity extension (see Section 2.2.2.3) of the equivalent monopile. This equivalent fixity extension below the mudline level is derived to approximate the effect of foundation stiffness due to soil-structure interactions so that a more accurate representation of structural dynamic characteristics, i.e. natural frequencies and modal shapes, can be applied to the FAST load analysis.

Table 2.14 lists the uniform C_d and C_m coefficients of the equivalent monopile model for the FAST load analysis. These coefficients are calculated in the manner described in Section 2.2.2.4 such that under the same wave condition, the resultant shear force and overturning moment at the mudline of the equivalent monopile are comparable to those of the actual monopile support structure calculated using the actual C_d and C_m coefficients.

The natural frequencies and modal shapes of the four eigen-modes required as the input to the FAST analysis are presented in Table 2.15 and Figure 2.20, respectively. The comparison of these structural dynamic characteristics between the actual monopile, which serves as the reference, and the equivalent monopile model used in the FAST load analysis shows a very good agreement.

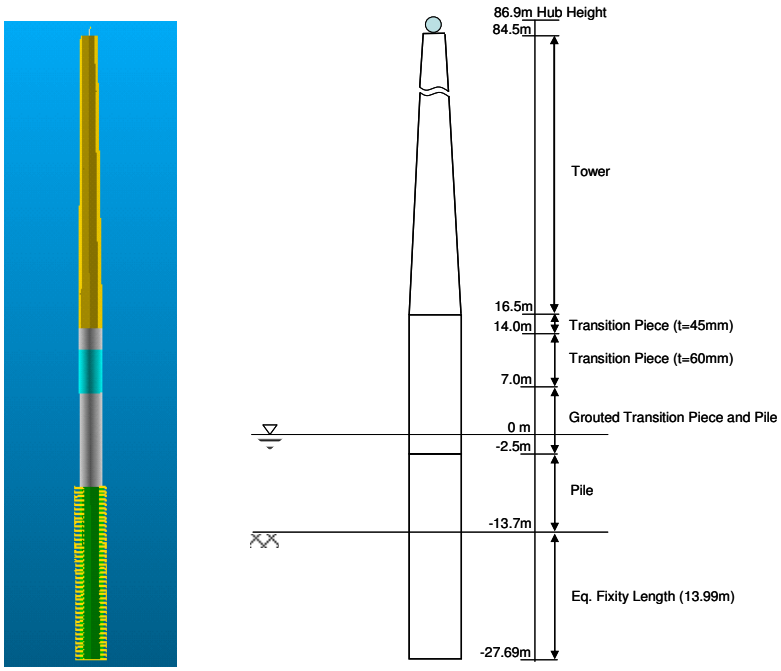

Figure 2.19 Monopile Support Structure and Its Equivalent Monopile

Table 2.10 Properties of the Grouted TP and Pile

Components	*Outer Diameter*	*Thickness*	*Young's Modulus*	*Flexural Stiffness*	*Axial Stiffness*	*Poisson's Ratio*	*Density*
	OD	*t*	*E*	*EI*	*EA*	*ν*	*ρ*
	(m)	(m)	(Pa)	(N-m^2)	(N)		(kg/m^3)
Transition Piece (TP)	5.6	0.06	2.10E+11	8.41E+11	2.19E+11	0.3	7850
Pile	5.3	0.07	2.10E+11	8.26E+11	2.42E+11	0.3	7850
Grout	5.4	0.09	5.50E+10	3.04E+11	8.38E+10	0.19	2440
Equivalent Pile	5.6	0.22	1.46E+11	1.97E+12	5.44E+11	0.2549	5632.7

Table 2.11 Monopile Support Structure Geometric Properties

Structural Components	*Elevation From*	*Elevation To*	*Length*	*Outer Diameter*	*Thickness*
	(m)	(m)	(m)	(m)	(m)
Penetrated Pile	-53.7	-13.7	40	5.3	0.07
Submerged Pile	-13.7	-2.5	11.2	5.3	0.07
Submerged Grouted TP and Pile	-2.5	0	2.5	5.6	0.22
Grouted TP and Pile	0	7	7	5.6	0.22
Transition Piece (TP)	7	14	7	5.6	0.06
Transition Piece (TP)	14	16.5	2.5	5.6	0.045
Tower (Table 2.9)	16.5	84.5	68	5.6-4.0	variable
From the tower top to the hub CG (Hub Height)	84.5	86.9	2.4	-	-

Table 2.12 Monopile Support Structure Mass Properties (with Marine Growth)

Structural Components	*Elevation from*	*Elevation to*	*Mass*
	(m)	(m)	(kg)
Pile below the Mudline	-53.70	-13.70	361135
Submerged Pile	-13.70	-2.5	108880
Submerged Grouted TP & Pile	-2.5	0	54500
Grouted TP and Pile	0	7.0	146612
TP (*t*=60mm)	7.0	14.0	57383
TP (*t*=45mm)	14.0	16.5	15412
Tower	16.5	84.5	212149
Point Mass on Tower	16.5	16.5	1900
Point Mass on Tower	50.5	50.5	1400
Point Mass on Tower	84.5	84.5	1000

Table 2.13 Properties of Equivalent Fixity of Equivalent Monopile

Equivalent Fixity Length	13.9903	m
Outer Diameter	5.3	m
Thickness	0.0772	m
Density	20380	kg/m^3
Young's Modulus	2.1E+11	N/m^2
Poisson's Ratio	0.3	

Table 2.14 Uniform C_d and C_m of Equivalent Monopile Used in the FAST Analysis

Locations	*50-Year Return*		*100-Year Return*	
	C_d	C_m	C_d	C_m
Atlantic Region 2	0.911	1.832	0.917	1.831
Atlantic Region 3	0.890	1.823	0.898	1.821
GOM West Central	0.906	1.824	0.898	1.828
TX site in GOM	0.903	1.824	0.901	1.820

Table 2.15 Monopile Natural Frequencies

Modes	*Natural Frequency (Hz)*		
	Actual Monopile	*Equivalent Monopile*	*Error*
1st Side-Side	0.2782	0.2774	-0.27%
1st Fore-Aft	0.2802	0.2794	-0.27%
2nd Side-Side	1.5148	1.4940	-1.37%
2nd Fore-Aft	1.6751	1.6446	-1.82%

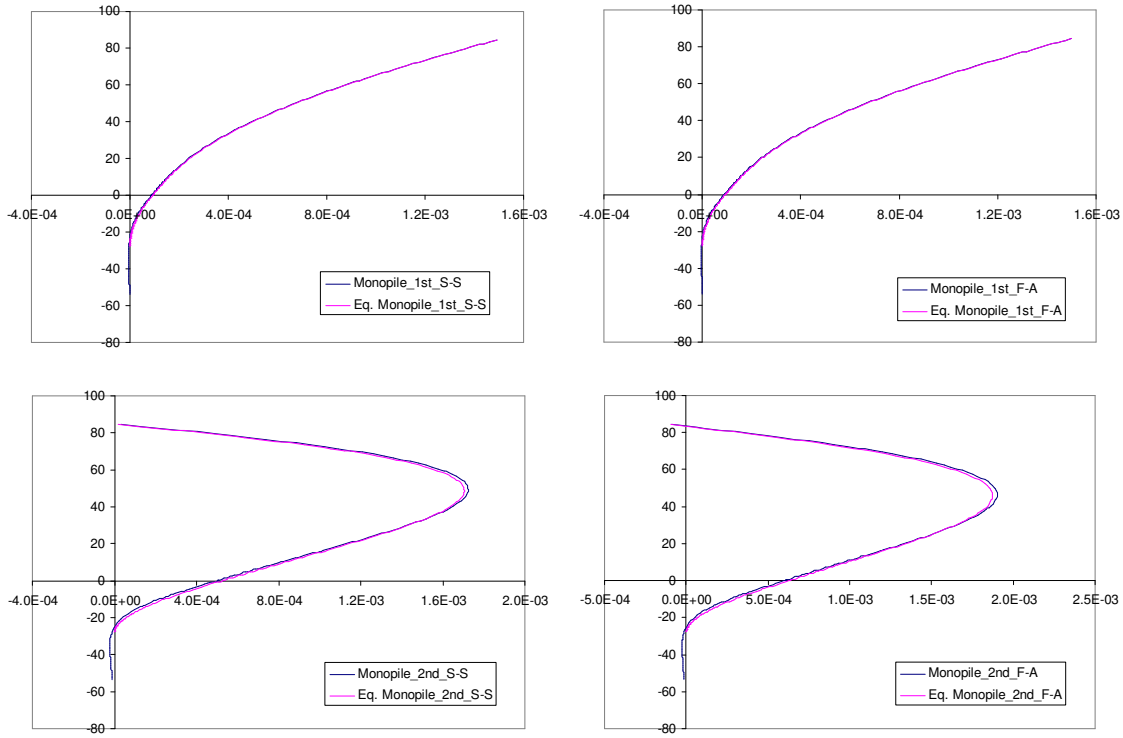

Figure 2.20 Modal Shapes of the Monopile Support Structure

2.3.3.2 Tripod Support Structure

The geometry of the tripod support structure for the structural analysis in ANSYS and its equivalent monopile used in the FAST load analysis is plotted in Figure 2.21. The tripod model developed in the previous study (MMI, 2009 [2.53]) is adapted with some modifications. The tripod support structure is composed of a tower, a transition piece welded to the tower and the center column of the tripod, a center column with tapered end, brace members, tripod legs and foundation piles. The turbine hub height is 93.55 m. The mean still water level is 24 m above the mudline.

The properties of the leg sleeve and pile as well as an equivalent leg simulating this sleeve weld connection in the finite element model are shown in Table 2.16. The geometry and mass properties of the tripod support structure are listed in Table 2.17 and Table 2.18, respectively.

Table 2.19 shows the properties of the equivalent fixity extension (see Section 2.2.2.3) of the equivalent monopile. This equivalent fixity extension below the mudline level is derived to approximate the effect of foundation stiffness due to the interaction of soil and foundation piles.

Table 2.20 lists the uniform C_d and C_m coefficients of the equivalent monopile model for the FAST load analysis. These coefficients are calculated in the manner described in Section 2.2.2.4 such that under the same wave condition, the resultant shear force and overturning moment at the mudline of the equivalent monopile are comparable to those of the tripod support structure calculated using the actual C_d and C_m coefficients.

The natural frequencies and modal shapes of the four eigen-modes required as the input to the FAST analysis are presented in Table 2.21 and Figure 2.22, respectively. It is shown that the structural dynamic characteristics of the equivalent monopile model used in the FAST load analysis agree well with those of the tripod support structure.

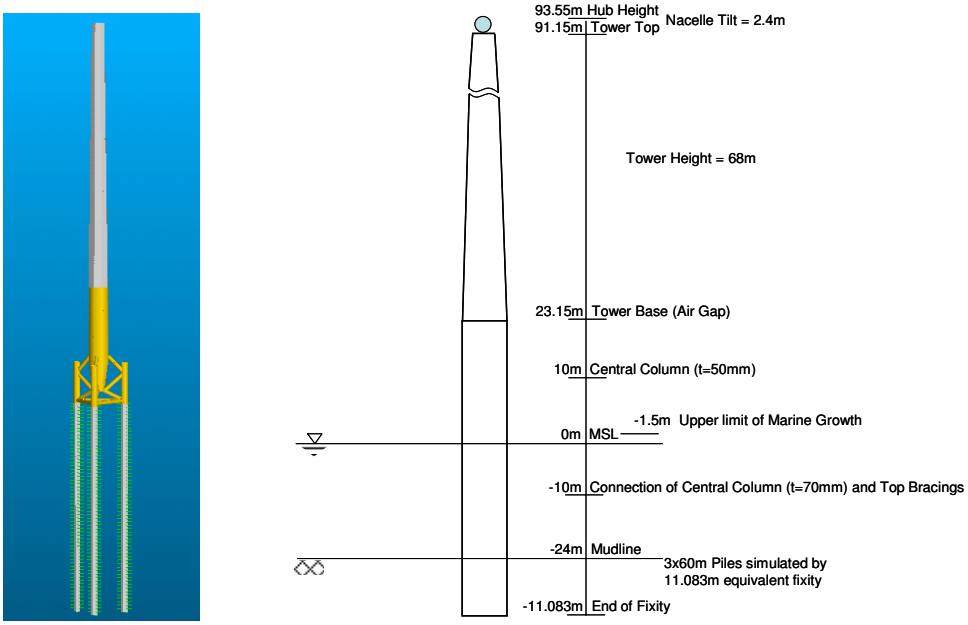

Figure 2.21 Tripod Support Structure and Its Equivalent Monopile

Table 2.16 Properties of the Equivalent Pile Simulating the Leg Sleeve and Pile

Components	*Outer Diameter*	*Thickness*	*Young's Modulus*	*Flexural Stiffness*	*Axial Stiffness*	*Poisson's Ratio*	*Density*
	OD	*t*	*E*	*EI*	*EA*	*ν*	*ρ*
	(m)	(m)	(Pa)	(N-m^2)	(N)		(kg/m^3)
Leg Sleeve	2.10000	0.02100	2.10E+11	1.56E+10	2.88E+10	0.3	7850
Pile	2.00000	0.05000	2.10E+11	3.06E+10	6.43E+10	0.3	7850
Equivalent Pile	2.10000	0.07100	1.98E+11	4.62E+10	8.96E+10	0.294	7692

Table 2.17 Tripod Support Structure Geometric Properties

Structural Components	*Elevation From*	*Elevation To*	*Length*	*Outer Diameter*	*Thickness*
	(m)	(m)	(m)	(m)	(m)
Pile under the mudline (x3)	-84	-54	30	2	0.03
Pile under the mudline (x3)	-54	-24	30	2	0.05
Submerged lower central column (tapered)	-20	-12	8	5.6-3.6	0.07-0.04
Submerged central column	-12	1.5	13.5	5.6	0.07
Top Brace (x3)	-11	-16	7.2	1.8	0.07
Middle Brace (x3)	-16	-21	8	1.8	0.03
Bottom Brace (x3)	-21	-24	6.9	1.8	0.02
Leg (x3)	-13	-24	11	2.1	0.021
Central column above MSL	1.5	10	8.5	5.6	0.07
Transition piece	10	23.15	13.15	5.6	0.05
Tapered tower sections (Table 2.9)	23.15	91.15	68	5.6-4.0	variable
From the tower top to the hub CG (Hub Height)	91.15	93.55	2.4	-	-

Table 2.18 Tripod Mass Properties (with Marine Growth)

Structural Components	*Elevation from*	*Elevation to*	*Mass*
	(m)	(m)	(kg)
Pile below the Mudline	-84.00	-54.00	131175
Pile below the Mudline	-54.00	-24.00	216405
Tripod Structure	-24.00	-10.00	385694
	-10.00	1.50	118321
	1.50	10.00	81145
	10.00	23.15	89993
Tower	23.15	91.15	212149
Point Mass on Tower	23.15	23.15	1900
Point Mass on Tower	57.15	57.15	1400
Point Mass on Tower	91.15	91.15	1000

Table 2.19 Properties of Equivalent Fixity of the Tripod Equivalent Monopile

Equivalent Fixity Length	11.0825	m
Outer Diameter	5.6	m
Thickness	0.1382	m
Density	13230	kg/m^3
Young's Modulus	2.1E+11	N/m^2
Poisson's Ratio	0.3	

Table 2.20 Uniform C_d and C_m of the Tripod's Equivalent Monopile Used in the FAST Analysis

Locations	*50-Year Return*		*100-Year Return*	
	C_d	C_m	C_d	C_m
Atlantic Region 2	1.00	1.83	1.01	1.74
Atlantic Region 3	0.98	1.86	0.97	1.89
GOM West Central	1.19	1.89	1.14	1.90

Table 2.21 Tripod Natural Frequencies

Modes	*Natural Frequency (Hz)*		
	Actual Monopile	*Equivalent Monopile*	*Error*
1st Side-Side	0.2723	0.2776	1.95%
1st Fore-Aft	0.2742	0.2796	1.98%
2nd Side-Side	1.4768	1.5014	1.67%
2nd Fore-Aft	1.6177	1.6524	2.15%

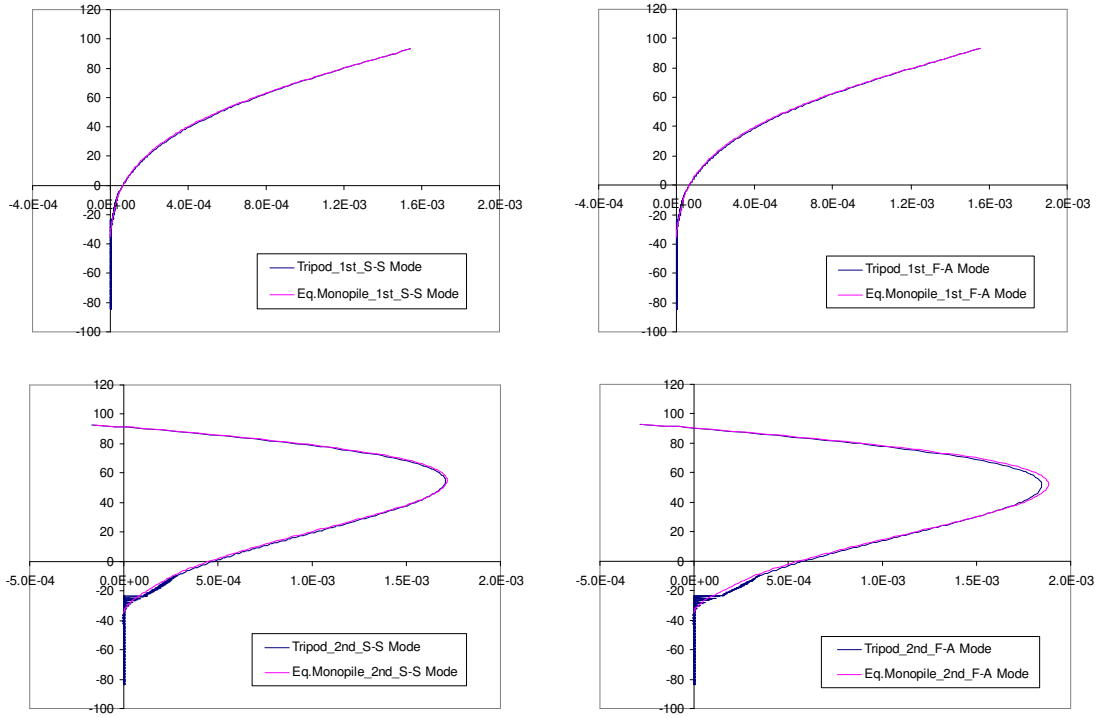

Figure 2.22 Modal Shapes of the Tripod Support Structure

2.3.3.3 Jacket Support Structure

The jacket support structure is defined based on the model used in IEA-OC4 study (OC4-Jacket) (Fabian et al., 2011 [2.27]). The modifications introduced in the model for the present case studies include:

- Water depth is adjusted from 50 m to 47 m to provide a sufficient air gap. As a result, the hub height is elevated from 90.55 m to 93.55 m above the mean still water level.
- Pile foundation is defined in the revised model, while the original OC4 jacket assumes being fixed at the mudline.
- The outer diameter of the leg is changed from 2.082 m to 2.1 m.

The geometry of the jacket support structure for the structural analysis in ANSYS and its equivalent monopile used in the FAST load analysis is plotted in Figure 2.23. The jacket support structure is composed of a tower, a concrete transition piece connected to the tower base and

embedded with the extensions of the jacket legs, a jacket structure, and foundation piles. Each of the jacket legs is grouted to the foundation pile near the mudline. The mass of the rigid concrete transition piece is 666,000 kg (the mass of embedded jacket leg extensions are not included). The outer dimension of the transitions piece is 4 m x 9.6 m x 9.6 m. In the finite element model, this concrete transition piece is modeled as a mass point with rigid connections to the tower base and the portion of the jacket legs, which are extended and grouted into in the concrete transition piece in the actual design. The turbine hub height is 93.55 m. The mean still water level is 47 m above the mudline.

The properties of the grouted leg and pile as well as an equivalent leg simulating this connection in the finite element model are shown in Table 2.22. The geometry and mass properties of the jacket support structure are given in Table 2.23 and Table 2.24, respectively.

Table 2.25 shows the properties of the equivalent fixity extension (see Section 2.2.2.3) of the equivalent monopile. This equivalent fixity extension below the mudline level is derived to approximate the effect of the foundation stiffness due to the interaction of soil and foundation piles.

Table 2.26 lists the uniform C_d and C_m coefficients of the equivalent monopile model for the FAST load analysis. These coefficients are calculated in the manner described in Section 2.2.2.4 such that under the same wave condition, the resultant shear force and overturning moment at the mudline of the equivalent monopile are comparable to those of the jacket support structure calculated using the actual C_d and C_m coefficients.

The natural frequencies and modal shapes of the four eigen-modes required as the input to the FAST analysis are presented in Table 2.27 and Figure 2.24, respectively. It is shown that the structural dynamic characteristics of the equivalent monopile model used in the FAST load analysis agree well with those of the jacket support structure.

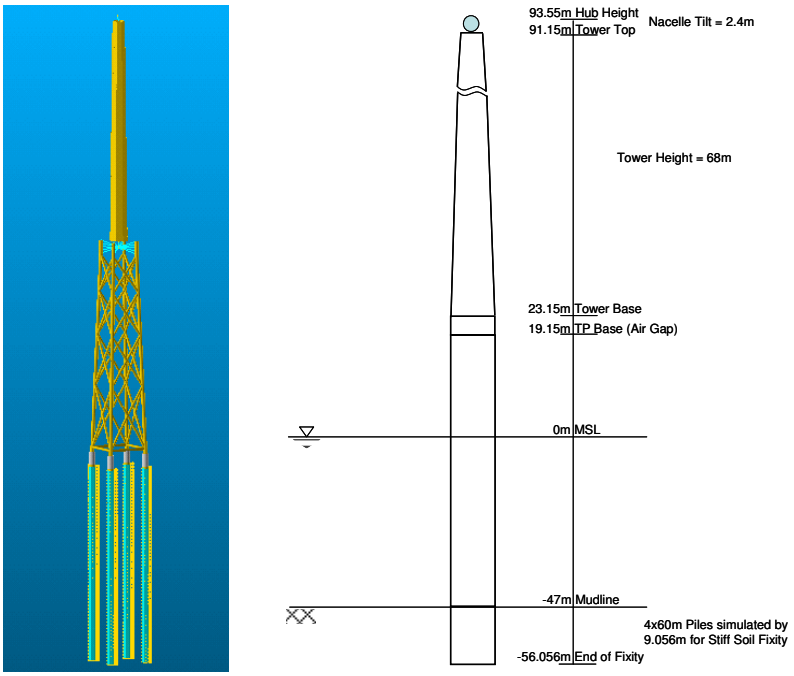

Figure 2.23 Jacket Support Structure and Its Equivalent Monopile

Table 2.22 Properties of the Equivalent Pile Simulating the Grouted Leg and Pile

Components	*Outer Diameter* *OD* (m)	*Thickness* *t* (m)	*Young's Modulus* *E* (Pa)	*Flexural Stiffness* *EI* (N-m^2)	*Axial Stiffness* *EA* (N)	*Poisson's Ratio* *ν*	*Density* *ρ* (kg/m^3)
Pile	2.10	0.06	2.10E+11	4.20E+10	8.08E+10	0.3	7850
Leg	1.20	0.05	2.10E+11	6.28E+09	3.79E+10	0.3	7850
Grout	1.98	0.39	5.50E+10	3.59E+10	1.07E+11	0.19	2000
Equivalent Pile	2.10	0.50	9.54E+10	8.42E+10	8.04E+21	0.215	3316

Table 2.23 Jacket Support Structure Geometric Properties

Structural Components	*Elevation From* (m)	*Elevation To* (m)	*Outer Diameter* (m)	*Thickness* (m)
Pile under the mudline (x4)	-107	-77	2.1	0.03
Pile under the mudline (x4)	-77	-47	2.1	0.06
Horizontal braces above the mudline (x4)	-41	-41	0.8	0.02
X-braces	-40.127	18.615	0.8	0.02
Legs below the 2nd level (x4)	-46.5	-21.615	1.2	0.05
Legs within the 2nd and 4th level (x4)	-21.615	18.615	1.2	0.035
Legs crossing TP (x4)	19.15	23.15	1.2	0.04
Tapered tower sections (Table 2.9)	23.15	91.15	5.6-4.0	variable
From the tower top to the hub CG (Hub Height)	91.15	93.55	-	-

Table 2.24 Jacket Mass Properties (with Marine Growth and Sea Water in Flooded Legs)

Structural Components	*Elevation from* (m)	*Elevation to* (m)	*Mass* (kg)
Pile below the Mudline	-107.00	-77.00	183778
Pile below the Mudline	-77.00	-47.00	362228
Jacket Structure and Transition Piece	-47.00	-41.00	178075
	-41.00	-21.61	295173
	-21.61	-5.92	199747
	-5.92	7.38	170325
	7.38	19.15	90686
	19.15	23.15	684309
Tower	23.15	91.15	212149
Point Mass on Tower	23.15	23.15	1900
Point Mass on Tower	57.15	57.15	1400
Point Mass on Tower	91.15	91.15	1000

Table 2.25 Uniform C_d and C_m of the Jacket's Equivalent Monopile Used in the FAST Analysis

Locations	*50-Year Return*		*100-Year Return*	
	C_d	C_m	C_d	C_m
Atlantic Region 2	1.41	1.00	1.44	1.00
Atlantic Region 3	1.43	1.00	1.44	1.00
GOM West Central	1.54	1.00	1.53	1.00

Table 2.26 Properties of Equivalent Fixity of Jacket Equivalent Monopile

Equivalent Fixity Length	9.0564	m
Outer Diameter	6	m
Thickness	0.1749	m
Density	18839	kg/m^3
Young's Modulus	2.1E+11	N/m^2
Poisson's Ratio	0.3	

Table 2.27 Jacket Natural Frequencies

Modes	*Natural Frequency (Hz)*		
	Actual Monopile	*Equivalent Monopile*	*Error*
1st Side-Side	0.2949	0.2992	1.47%
1st Fore-Aft	0.2974	0.3012	1.29%
2nd Side-Side	0.8964	0.8930	-0.38%
2nd Fore-Aft	0.9316	0.9146	-1.82%

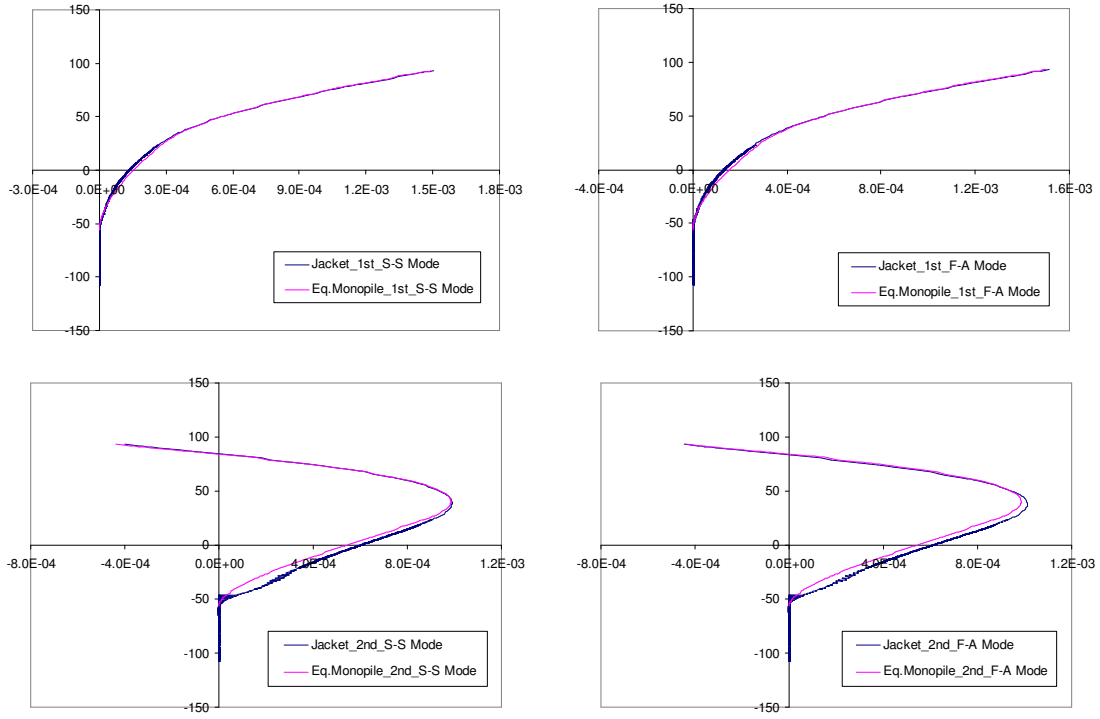

Figure 2.24 Modal Shapes of the Jacket Support Structure

2.3.4 Sensitivity Study to Determine Modeling Parameters

Sensitivity studies are carried out to determine the minimum number of realizations for turbulent (random) wind field and aerodynamic load simulation as well as the optimal size of wind field domain and grid resolution.

2.3.4.1 Number of Realizations

In the case studies where the turbulent wind condition is considered, the time series of wind speed in the three dimensional turbulent wind field needs to be calculated using a given wind spectral model and a spatial coherence model. Each wind speed time series, also called a "realization", is generated using a different random seed. Due to the random nature of the turbulent wind field, it is necessary to identify what is the minimum number of realizations that can result in statistically converged structural responses. In the convergence test, the global loads on the turbine support structure, including the base shear force and overturning moment at the mudline, are employed to determine the required number of realizations.

As shown in Figure 2.25 and Figure 2.26, the averaged maximum and minimum values of base shear and overturning moment, respectively, converge within at least 12 realizations. The base shear forces and overturning moments are obtained from the FAST simulations using the equivalent monopile of the jacket support structure fixed at the mudline. Only turbulent wind loads are applied in the analysis. The 10-minute mean wind speed is 42.5 m/s at 10 m above the mean sea level, which corresponds to the 100-year return wind speed in the GOM West Central region.

Based on the conclusion of this convergence study, the number of realizations of wind data and the resultant structural responses for each load case is chosen as 12.

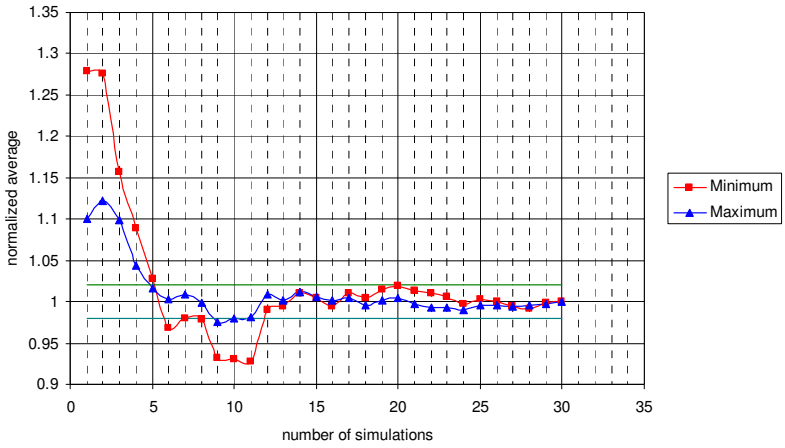

Figure 2.25 Mudline Shear Force (Fore-Aft Direction) Averaged over Multiple Realizations

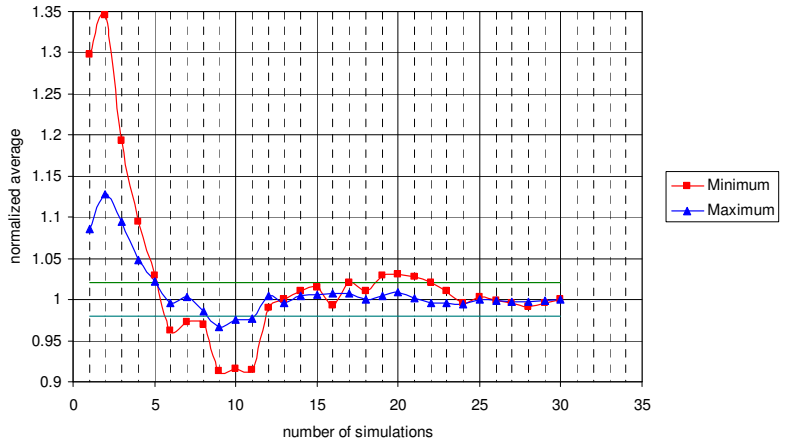

Figure 2.26 Mudline Overturning Moment Averaged over Multiple Realizations

2.3.4.2 Domain Size

The size of the domain where the wind data is calculated should be sufficiently large to cover the blade rotating plane with certain margins. Two sets of domain sizes are tested, i.e. 140 m x 140 m and 180 m x 180 m. The size of 140 m is about 10% larger than the rotor diameter, which is 126 m. For a bottom-founded wind turbine, the motion of the turbine is expected to be insignificant.

Figure 2.27 shows the shear force and the overturning moment at the mudline for 140 m x 140 m and 180 m x 180 m domains. It is found that the two domain sizes lead to very close results. It is

therefore decided to use the 140m x 140m domain size, which implies a finer wind data cell for a given number of grid points.

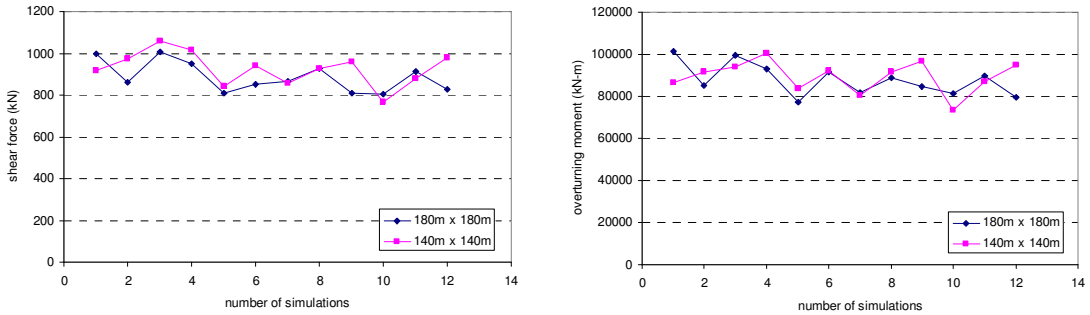

Figure 2.27 Comparison of Mudline Shear Force and Overturning Moment Calculated Using the Two Different Domain Sizes

2.3.4.3 Grid Resolution

Using a domain with a size of 140 m x 140 m, a grid dependency study is carried out to determine the number of cells in the domain that can result in converged global loads. Figure 2.28 depicts the average maximum shear forces and the average maximum overturning moments at the mudline calculated using different grid resolutions. It is shown that the 50 x 20 grid appears to be a reasonable choice and is therefore selected in the case studies for calculating the turbulent wind field data for the aerodynamic load analysis.

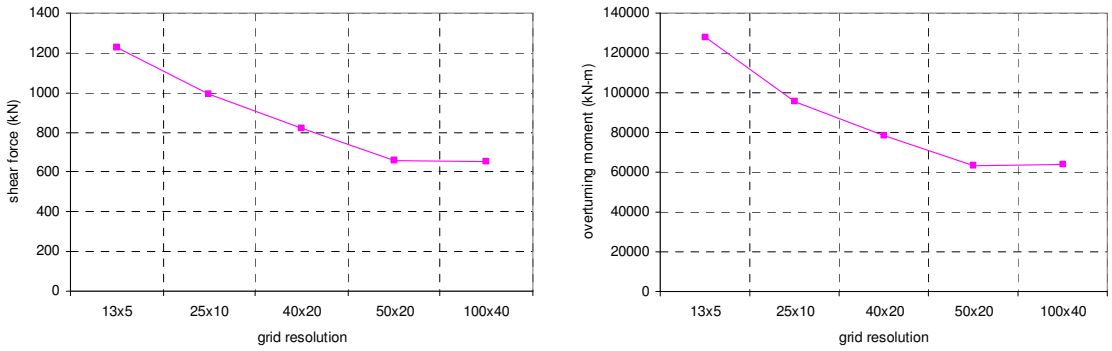

Figure 2.28 Sensitivity of Mudline Shear Force and Overturning Moment to the Grid Resolution

2.4 Comparison of API and IEC Wind Models

The wind spectrum and coherence model recommended by API RP 2A-WSD (2007) [2.5], as well as API Bulletin 2INT-MET (2007) [2.4] and ISO 19901-1 [2.41], are intended for the design of offshore oil/gas platform structures for which the wind load induced dynamic response needs to be considered. The turbulent wind is represented by the NPD wind spectrum (also known as the Frøya wind model) and the two-point coherence function in conjunction with the logarithmic wind shear law.

IEC 61400-3 (2009) makes reference to IEC 61400-1 (2005) for the definition of wind models, which are originally developed for application to land based turbines. There are two wind models, namely Kaimal's model and Mann's model, referred in IEC 61400-1. The wind shear law is formulated in a power law format.

The state-of-the-art review of hurricane wind modeling (see Section 2.1.1) described some differences between the wind models appropriate for the open ocean surface and those developed mainly based on the land or coast wind measurements. Some studies argue that for offshore wind turbines, the wind spectra verified by on-land wind measurement may also be applicable.

In addition to comparing the wind model formulations, the present study uses numerical simulations to further examine the wind turbine responses subjected to turbulent wind loads predicted using different wind models.

In the present study, the "API wind model" represents the model described in API Bulletin 2INT-MET (2007) [2.4]. The "IEC wind model" represents the extreme wind speed model (EWM) for wind shear and Kaimal's model for turbulence as described in IEC 61400-1 (2005) [2.38]. Section 2.4.1 summarizes the definition of the two wind models adapted from the references above.

The main input parameters used in the wind model comparison are summarized in Table 2.28.

Table 2.28 Input Parameters for Wind Model Comparison Study

1-hour mean wind speed at 10m above the mean sea level (GOM West Central 100-year return wind condition)	38.1	m/s
Hub height	93.55	m
Wind field domain height (center at the hub)	140	m
Wind field domain width (center at the hub)	140	m
Grid resolution	25 x 10	
Water depth	47.0	m
Simulation time duration	3600 (for the API model) 600 (for the IEC model)	s
Wave	no waves	

Notes:

A relative coarse grid (25 x 10) is applied to generate the wind fields for comparing the API and IEC wind models, while a much finer grid (50 x 20) as determined in Section 2.3.4.3 is used in the case studies.

2.4.1 API and IEC Wind Model Definitions

2.4.1.1 Wind Shear

In the API wind model, the wind speed $u(z,t)$ at height z above the mean sea level (MSL) and with an average time duration t is given as follows:

$$u(z,t) = U(z)\left[1 - 0.41 I_u(z) \ln(t/t_0)\right] \qquad \text{for } t < t_0 \tag{2.1}$$

where

$$U(z) = U_0\left[1 + C \ln\left(\frac{z}{10}\right)\right]$$

$$C = 0.0573\sqrt{1 + 0.15U_0}$$

$I_u = 0.06\left[1 + 0.043U_0\right]\left(\frac{z}{10}\right)^{-0.22}$, which defines the turbulence intensity

U_0 = 1-hour mean wind speed at 10 m above the MSL, in m/s

z = height above the MSL, in m

t = averaging time period shorter than t_0 =3600 s, in seconds

t_0 = 3600 seconds, which is the reference averaging time period (1 hour) in seconds

The wind shear law of IEC wind model is defined in IEC 61400-1 for the extreme wind speed model (EWM). The formulation is an empirical power law equation as shown below

$$V(z) = V_{ref}\left(z/z_{ref}\right)^{0.11} \tag{2.2}$$

where

V_{ref} = reference wind speed, which can be either a 50-year return or a 100-year return mean wind speed at the hub height in the present study

z_{ref} = reference (hub) height above the MSL

Figure 2.29 compares the wind shear profiles defined in the API and IEC model. The same 10-minute average wind speed of 42.5 m/s at 10 m above the MSL, representing 100-year GOM West Central wind conditions, is assumed in both profiles. As shown in the figure, the wind shears calculated using the two models agree each other very well except near the surface. The difference is found to be less than 1% at the hub height.

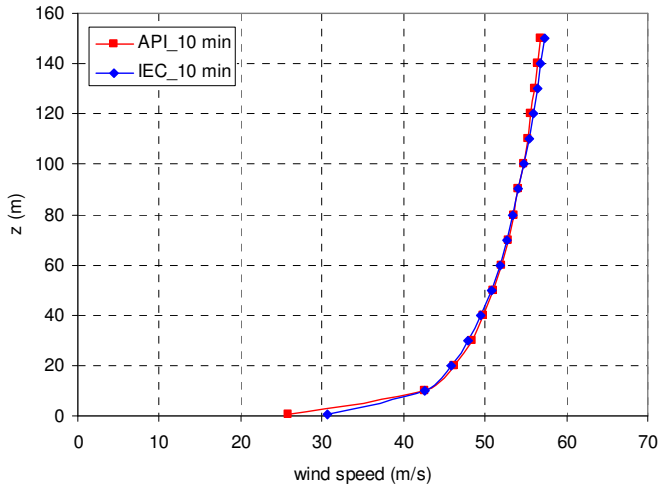

Figure 2.29 Comparison of Wind Shear for the GOM West Central 100-yr Return Wind Condition

2.4.1.2 Wind Spectrum

In the API model, the one-point spectrum is defined for the energy density of the longitudinal wind speed fluctuations

$$S(f) = \frac{320\left(\frac{U_0}{10}\right)^2\left(\frac{z}{10}\right)^{0.45}}{\left(1+\tilde{f}^{\,n}\right)^{(5/3n)}} \tag{2.3}$$

where

n = 0.468

$\tilde{f}$ = $172 f\left(\frac{z}{10}\right)^{2/3}\left(\frac{U_0}{10}\right)^{-0.75}$

U_0 = 1-hour mean wind speed at 10 m above the MSL, in m/s

f = frequency in Hz

A modified version of the Kaimal wind spectrum is provided in IEC 61400-1 (2005). The power spectral densities for the wind fluctuations in three dimensions are given as follows:

$$\frac{f \cdot S_k(f)}{\sigma_k^2} = \frac{4 f L_k / V_{hub}}{(1 + 6 f L_k / V_{hub})^{5/3}} \tag{2.4}$$

where

$S_k(f)$ = spectral energy density at frequency f, in m^2s^{-2}/Hz

f = frequency, in Hz

k = index referring to the direction of wind speed component (i.e., 1 = longitudinal, 2 = lateral, and 3 = upward)

σ_k = standard deviation of turbulent wind speed component (see Table 2.29)

L_k = integral parameter of turbulent wind speed component (see Table 2.29)

Table 2.29 Spectral Parameters for the Kaimal Model

	Wind Speed Direction		
	k=1 (longitudinal)	*k=2 (lateral)*	*k=3 (upward)*
Standard Deviation (σ_k)	σ_1	$0.8\sigma_1$	$0.5\sigma_1$
Integral Scale (L_k)	$8.1\Lambda_1$	$2.7\Lambda_1$	$0.66\Lambda_1$

Notes:

σ_1 = standard deviation of longitudinal turbulent wind speed

Λ_1 = scale parameter of the turbulence, $\Lambda_1 = 0.7z$ for $z \le 60$m; $\Lambda_1 = 42$, for $z \ge 60$m

Figure 2.30 compares the wind spectra from API and IEC models for the GOM West Central region100-year return wind condition. The 10-minute mean wind speed at 10m above the MSL is 42.5 m/s. The corresponding hub height 10-minute mean wind speed at 93.55m above the MSL is 54.4 m/s. It is shown that the API wind model has more energetic wind in the low frequency range. In the relatively higher frequency range, the IEC wind model results in power spectral densities with much higher values that those calculated using the API model. Under the same wind conditions, this difference implies that for bottom-founded wind turbine support structures,

which have relatively higher natural frequencies, the IEC wind spectral could excite large structural responses. On the other hand, for those turbine support structures with low natural frequency, such as floating wind turbines, the API wind model could lead to significantly higher responses than those for the IEC wind spectrum.

A similar observation is also made by Ochi and Shin (1988) [2.57] when they develop the wind spectrum for the open ocean (see also Section 2.1.1.6).

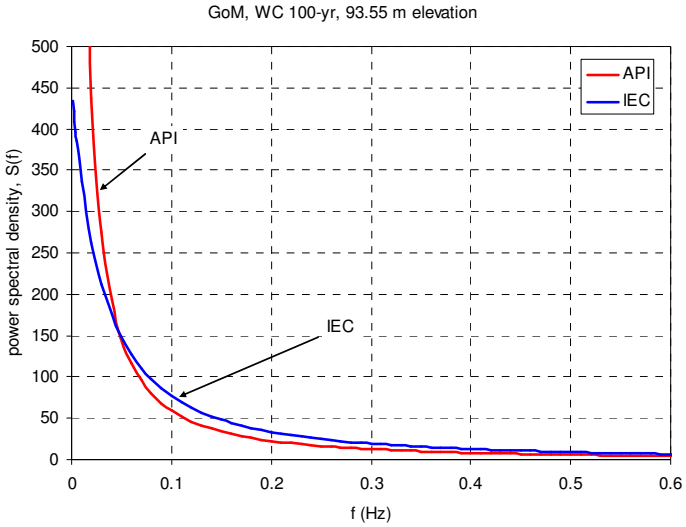

Figure 2.30 Comparison of Wind Spectra for the GOM West Central 100-yr Return Wind Condition

2.4.1.3 Standard Deviation and Reynolds Stress

In the API model, the turbulence intensity, which is the ratio of turbulence standard deviation to the mean wind speed, is defined by the following equation:

$$I_u = 0.06\left[1 + 0.043U_0\right]\left(\frac{z}{10}\right)^{-0.22} \tag{2.5}$$

where U_0 (in m/s) is the one-hour mean wind speed at 10 m above the MSL, while z (in m) is the height above the MSL. The longitudinal standard deviation with an averaging duration of one-hour can be obtained by multiplying the equation above with the one-hour mean wind speed at height z, $u(z, t)$ (in m/s), calculated by the wind shear law given in Equation (2.1). The standard

deviations for horizontal and vertical components are not defined in the API model, but can normally be assumed as 80% and 50%, respectively, of the standard deviation of longitudinal component for the offshore wind.

In the IEC model, the longitudinal turbulence standard deviation, σ_1, with the averaging duration of 10 minutes for the extreme wind model (EWM) is defined by

$$\sigma_1 = 0.11 V_{ref} \tag{2.6}$$

where V_{ref} is the 10-minute mean wind speed at hub height. The standard deviations of horizontal and vertical components are 80% and 50%, respectively, of the standard deviation of longitudinal components as specified in Table 2.29.

The turbulence properties calculated based on Equation (2.5) is listed in the "Intended" column in Table 2.30 for the API wind model. Table 2.31 provides the turbulence properties based on Equation (2.6) for the IEC wind model. Note that a different time scale is implied in the API and IEC wind models. Also presented in these two tables is the actually achieved turbulence properties estimated using the time series (see e.g. Figure 2.32) of wind speed generated using the API and IEC wind models. The difference between intended and actual turbulence properties is due to the statistical scattering, although the results are the average values of 12 realizations.

Figure 2.31 depicts the standard deviation and Reynolds stress at hub height calculated using the turbulent wind speed time series, which is generated using the API and IEC wind models. The wind data used in the comparison is the 100-year return wind condition in the GOM West Central region. Reynolds stress is a stress tensor due to the random turbulent fluctuations in the wind flow, which is averaged over these fluctuations. Both standard deviation and Reynolds stress represent the significance of turbulence intensity from the wind data.

It can be seen that the turbulence intensity, or the standard deviation, calculated using the API wind model is considerably lower than that based on the IEC wind model. This is partially because the API model is derived from the observations on the open ocean, while the IEC model is developed using the land based measurements where the surface roughness is relatively high.

Table 2.30 Turbulence Properties at Hub Height Based on the API Wind Model

API (*Time Scale = one hour*)	*Intended*			*Actual (TurbSim Output)*		
	V_{hub} (m/s)	σ (m/s)	*Turbulence Intensity*	V_{hub} (m/s)	σ (m/s)	*Turbulence Intensity*
u	50.75	4.91	9.7%	50.75	5.00	9.8%
v	0.00	3.93	7.7%	0.00	3.94	7.8%
w	0.00	2.46	4.8%	0.00	2.46	4.9%

Table 2.31 Turbulence Properties at Hub Height Based on the IEC Wind Model

IEC (*Time Scale = ten minutes*)	*Intended*			*Actual (TurbSim Output)*		
	V_{hub} (m/s)	σ (m/s)	*Turbulence Intensity*	V_{hub} (m/s)	σ (m/s)	*Turbulence Intensity*
u	54.39	5.98	11.0%	54.35	5.85	10.8%
v	0.00	4.79	8.8%	0.00	4.67	8.6%
w	0.00	2.99	5.5%	0.00	2.83	5.2%

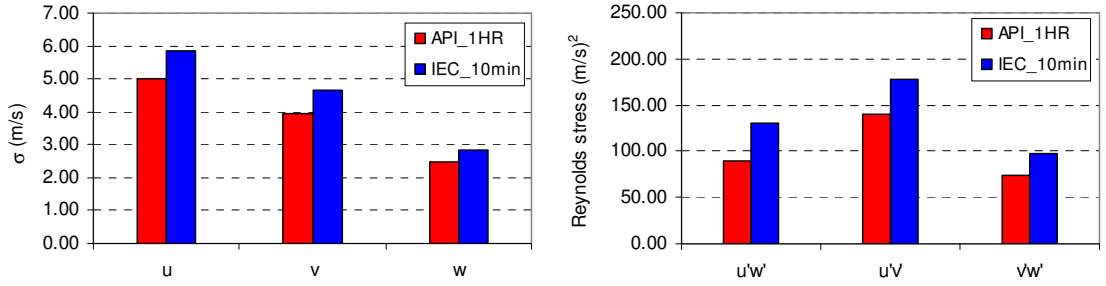

Figure 2.31 Standard Deviation and Reynolds Stress for the GOM West Central 100-yr Return Wind Condition

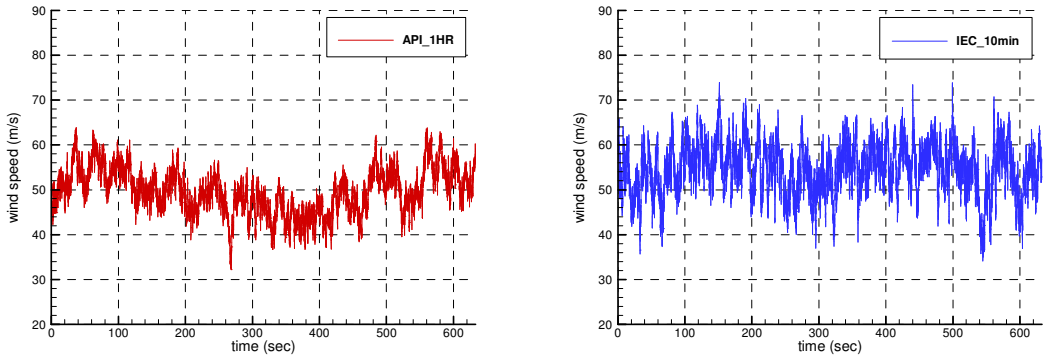

Figure 2.32 Time Series of the Wind Speed at Hub Height for the GOM West Central 100-yr Return Wind Condition

2.4.1.4 Wind Coherence

Wind coherence determines the correlation between two points in a wind field. Following API Bulletin 2INT-MET (2007), the squared correlation between the spectral energy densities $S(f)$ of the longitudinal wind speed fluctuations between two points (x_j, y_j, z_j), $j = 1, 2$, (in meter) in space is described by the two-point coherence function as follows:

$$\mathrm{Coh}(f) = \exp\left\{-\frac{1}{U_0}\left[\sum_{i=1}^{3} A_i^2\right]^{\frac{1}{2}}\right\} \tag{2.7}$$

where $A_i = \alpha_i f^{r_i} \Delta_i^{q_i} z_g^{-p_i}$ and $z_g = \frac{\sqrt{z_1 z_2}}{10}$, with α_i, r_i, q_i, p_i, and Δ_i defined in Table 2.32.

Table 2.32 Coefficients and Distances for the Coherence Function (API Bulletin 2INT-MET, 2007)

i	Δ_i	q_i	p_i	r_i	α_i
1	$\lvert x_2 - x_1 \rvert$	1.00	0.4	0.92	2.9
2	$\lvert y_2 - y_1 \rvert$	1.00	0.4	0.92	45.0
3	$\lvert z_2 - z_1 \rvert$	1.25	0.5	0.85	13.0

Along with the Kaimal spectrum, an exponential coherence model is provided in IEC 61400-1 (2005) to account for the spatial correlation of the longitudinal wind speed:

$$Coh(r,f) = \exp\left[-12\sqrt{(f \cdot r / V_{hub})^2 + (0.12 \cdot r / L_c)^2}\right] \tag{2.8}$$

where

$Coh(r,f)$ = coherence function at frequency f

f = frequency, in Hz

r = magnitude of the projection of the separation vector between the two points on to a plane normal to the average wind direction, in m

V_{hub} = 10-minute mean wind speed at hub height, in m/s

L_c = $8.1\Lambda_1$, coherence scale parameter, in m (see Table 2.29)

The shapes of the IEC (Kaimal model) and API (NPD model) coherence functions at different frequencies are plotted in Figure 2.33 through Figure 2.35. The wind data used in the comparison is the 100-year return wind condition in the GOM West Central region. It is shown that at the low

frequency, the API wind model has much lower spatial coherence than the IEC model. As the frequency increases, the discrepancy between the two models becomes less significant.

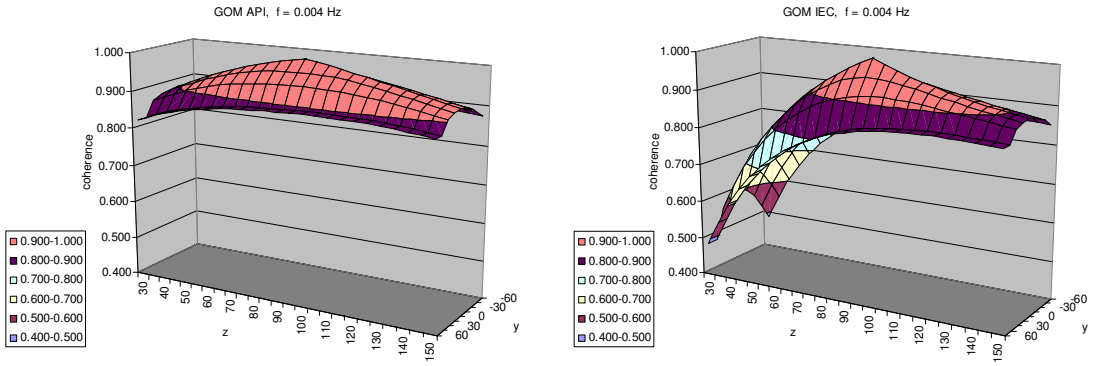

Figure 2.33 Coherence IEC and API Wind Model at f=0.004Hz

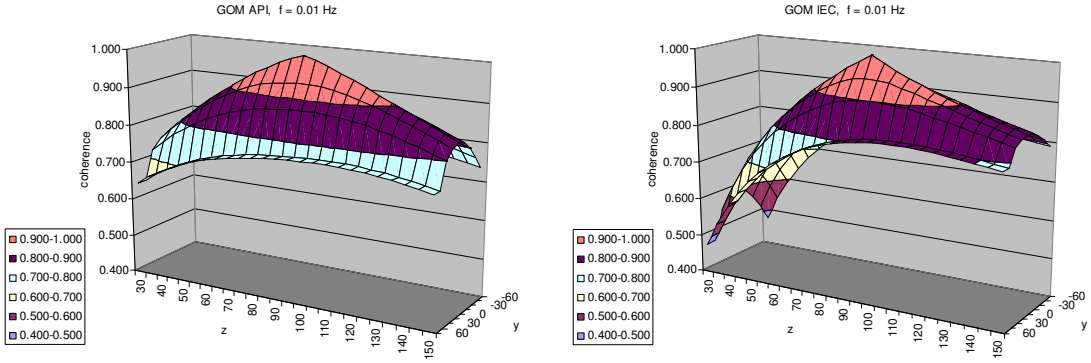

Figure 2.34 Coherence IEC and API Wind Model at f=0.01Hz

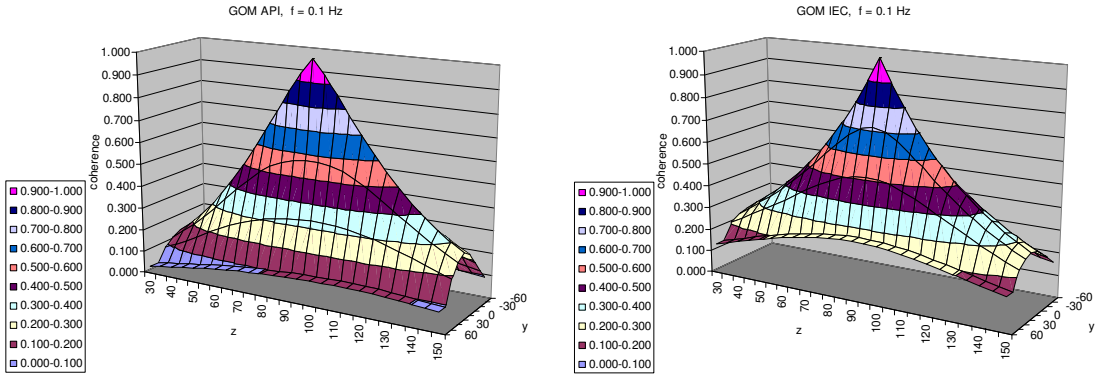

Figure 2.35 Coherence IEC and API Wind Model at f=0.1Hz

2.4.2 Effect of Using IEC and API Wind Models on Turbine Responses

Section 2.4.1 compares the wind models given in the API and IEC design guidelines. This section compares the structural responses of the jacket support structure (see Section 2.3.3.3) subjected to the turbulent wind field generated using the two wind models. The jacket support structure, without considering its foundation stiffness, is simulated as an equivalent monopile in the FAST load analysis. Only the wind load is applied in the analysis in order to filter out the effect of other environmental conditions. The same environmental condition as in the previous section, i.e. the 100-year return turbulent wind condition in the GOM West Central region, is employed. It is noted that the API wind model has a time scale of 1 hour, while the IEC wind model has a time scale of 10 minutes. The simulation time duration is chosen to reflect this difference.

Figure 2.36 plots the maximum shear force and overturning moment at the mudline calculated using the two different wind models. It is shown that the API wind model results in the considerably smaller values of the maximum mudline loads of the jacket support structure than those calculated using the wind field generated by the IEC wind model. This difference can be partially explained by Figure 2.37. The time series comparison shows the results within a 10-second time window. The actual simulation time duration for the case using the API wind model is one hour. The amplitude spectrum plot of the base shear force indicates that the peak is in the high frequency range, where the API wind spectrum yields much lower power density than that from the IEC wind spectrum (see Figure 2.30). Another reason, as indicated in Section 2.4.1.3, is that the API wind model predicts much lower turbulence intensity than the IEC wind model does.

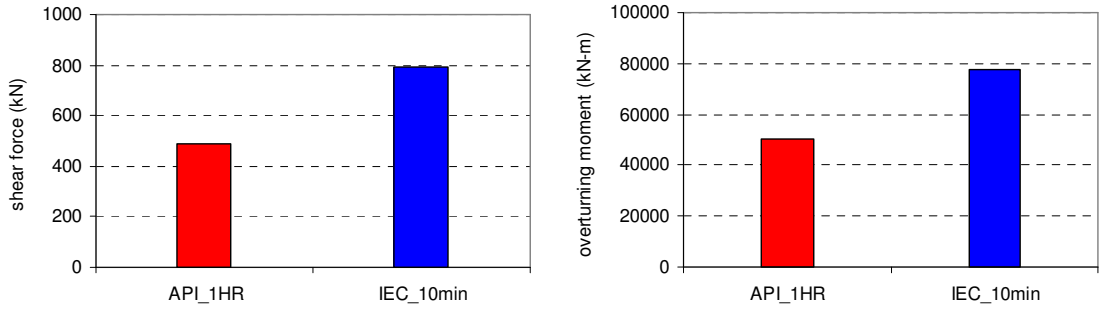

Figure 2.36 Comparison of the Maximum Shear Force and Overturning Moment at the Mudline

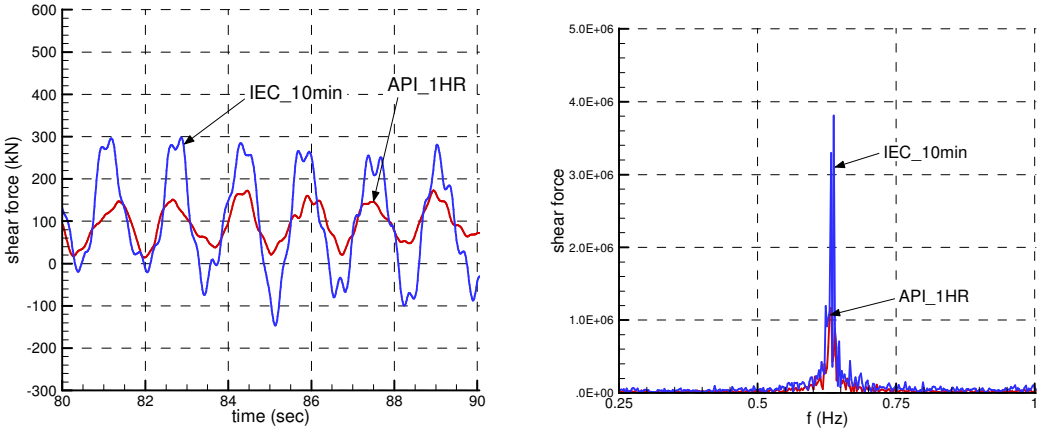

Figure 2.37 Time Series and Amplitude Spectrum of the Shear force at the Mudline

2.4.3 Summary

The following summarizes the observations and conclusions for the comparative study of the API and IEC wind models.

- Bottom-founded offshore wind turbines are mostly located near coastlines, where the shore topology and onshore roughness may still be influential. The API wind model, as well as the Ochi-Shin model (see 2.1.1.6), is primarily developed based on the observations on the open ocean.

- The high frequency range, i.e. the tail, of a wind spectrum, where the IEC wind model has a higher power density value than the API wind model, is more applicable to the bottom-founded offshore wind turbines.

- The API recommended wind model appears more suitable to those offshore floating wind turbine support structures where the low frequency responses could be of greater significance to dynamic stability, global motions, and the design of electric cables and mooring systems.

- The conservativeness of using the IEC model may be less significant than what is shown in Figure 2.36, when wave loads are taken into account. For those support structures where

wave forces and/or slamming forces are predominant, the total loads exerted on the support structure are less affected whether the API or IEC wind models are used.

- In the present case studies, the Kaimal model referenced in IEC 61400-1 (2005) and IEC 61400-3 (2009) is used to generated the turbulent wind data.

2.5 Effect of Fault in Turbine's Yaw and Pitch Control

Wind turbine's control and safety systems play a significant role in regulating aerodynamic loads by adjusting the blade pitch angle (angle of attack) and the nacelle yawing angle relative to the wind direction. Previous studies have shown that the yaw misalignment could lead to a significant overload in the turbine support structure (see e.g. Yu et al, 2011 [2.86]).

The design load cases (DLCs) specified in IEC 61400-3 (2009) for extreme wind conditions require the consideration of the yaw misalignment effect. In the DLC 6.1a for the normal turbine operating modes, ±8 degrees should be considered for the turbulent wind condition. In the companion load cases, DLC 6.1b and 6.1c, where the steady-state wind model is applied, ±15 degrees of yaw misalignment should be considered. The abnormal turbine operating mode associated with the loss of electrical grid connection is required in DLC 6.2a and 6.2b, where yaw misalignment up to ±180 degrees should be considered unless there are at least 6 hours of backup power supply to support the control and yaw systems.

In GL's guideline (2005) [2.32], a stricter requirement in terms of the capacity of backup power supply is imposed.

In the *ABS Guide for Building and Classing Offshore Wind Turbine Installations* (ABS Guide, 2010), the omni-directional wind and yaw misalignment up to ±180 degrees is in general required to be considered in the abnormal turbine operating mode as defined in DLC 6.2a and 6.2b. The following is quoted from the ABS Guide (2010).

> *For a site where the effect of tropical hurricanes, cyclones or typhoons needs to be considered, omni-directional wind and a yaw misalignment with ±180° is to be assumed for DLC 6.2a and 6.2b. Load calculations are to be based on the misalignment angle that results in the highest load acting on the Support Structure. The range of yaw misalignment assumed in the design of the Support Structure may be reduced to account for the contribution from an active or passive yaw control system, provided that the designer can justify that such a system is capable of achieving the assumed reduction of yaw misalignment under site specific conditions and an appropriate monitoring and maintenance program is implemented to maintain the effectiveness of yawing control during the service life of an offshore wind turbine.*

In this section, the effects of failure in nacelle yaw control and blade pitch control system are explored further, with the focus on the global responses. The jacket support structure (see Section 2.3.3.3), which is modeled as an equivalent monopile in the FAST load analysis, is employed in this study. The equivalent monopile is assumed to be fixed at the mudline without considering the actual foundation stiffness. The turbine is parked and subjected to the 100-year return turbulent wind condition in the GOM West Central region. Only the wind load is applied in the analysis in order to remove the effect of other environmental conditions. The resultant maximum shear force and overturning moment at the mudline are averaged over multiple realizations obtained through the FAST load analysis.

2.5.1 Nacelle Yaw Misalignment

Figure 2.38 and Figure 2.39 show the sensitivity of the maximum shear force and the overturning moment at the mudline, respectively, due to the yaw misalignment angle. A number of yaw misalignment angles ranging from -180 to 180 degrees relative to the incoming wind direction are selected in the simulation. All the blades are feathered, or turned to 90-degree pitch angle, to minimize the loads on turbine blades. It is found that

- The shear force and overturning moment follow a similar correlation with the yaw misalignment angle. The shear force and moment are close to the lowest at 0 degree, when the turbine's horizontal axis aligns with the incoming wind. The peak values occur approximately at a yaw angle of 30 degrees.

- When the yaw misalignment angle changes from 0 degree to 30 degrees, the mudline shear force approximately increases by a factor of 2, while the mudline overturning moment increases by roughly a factor of 2.5.

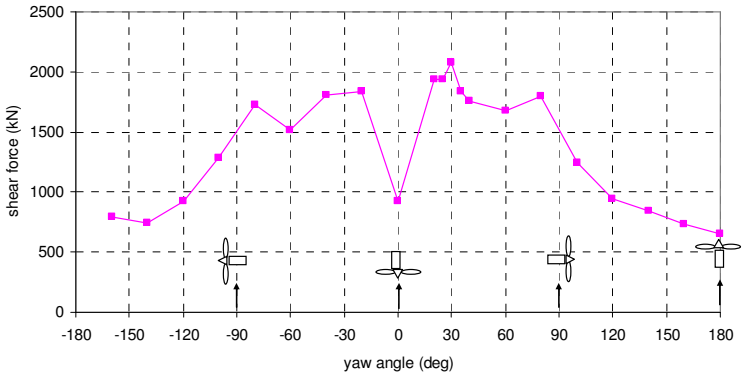

Figure 2.38 Sensitivity of Mudline Shear Force to Nacelle Yaw Angle for the GOM West Central 100-yr Return Wind Condition

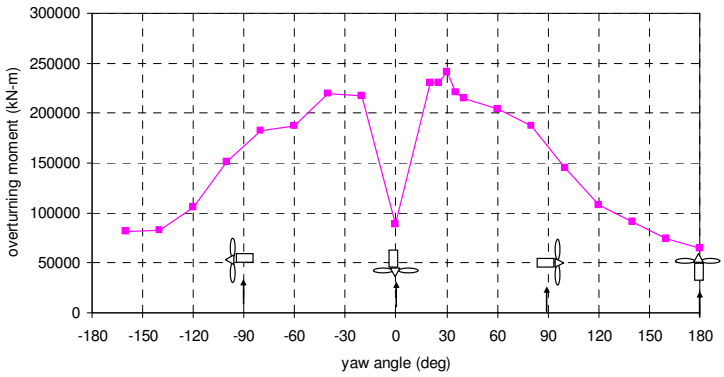

Figure 2.39 Sensitivity of Mudline Overturning Moment to Nacelle Yaw Angle for the GOM West Central 100-yr Return Wind Condition

2.5.2 Blade Pitch Angle Locking

Figure 2.40 and Figure 2.41 depict the sensitivity of the maximum shear force and overturning moment at the mudline to the blade pitch angle locked at various positions (angles).

The line with square marks represents the case in which all three blades are locked at the same pitch angle. The line with diamond marks is for the case in which only one blade is locked at a given angle ranging between 20 degrees to 90 degrees, while the other two are feathered to the 90-degree pitch angle as they are supposed to be if the pitch controller works correctly. In both cases, the nacelle yaw angle is at 0 degree, i.e. facing toward the wind.

The circle mark on each plot is for the further check of the effect of combined yaw misalignment and blade pitch locking. The blade pitch angles are selected from the one blade locking and two blade featured case (the line with diamond marks). The locked angle for one blade is set to be 60 degrees associated with the maximum mudline loads. The yaw misalignment is set to be a 30-degree angle, which corresponds to the peak mudline shear force and overturning moment, as shown in Figure 2.38 and Figure 2.39, when all three blades are feathered.

The following observations can be made based on the simulation results:

- In the all-blade locked case, the largest load is observed at the pitch angle of 45 degrees where the loads are approximately increased four times in comparison to those at the pitch angle of 90 degrees. It should be noted, however, that the pitch control for each blade typically operates independently, the possibility of having failure in all pitch controllers at the same time is considered very low.

- In the one-blade locked case, the maximum loads occur at the pitch angle of 60 degrees. The magnitude of relative load increases from those at all-feathered blade position is about a factor of 2 for the mudline shear force and 2.5 for the mudline overturning moment. This observation is comparable to the one drawn in Section 2.5.1 for the effect of yaw misalignment.

- With an additional nacelle yaw misalignment angle of 30 degrees applied to the one-blade locked case, the increase of mudline loads is about 10 %, which does not appear significant.

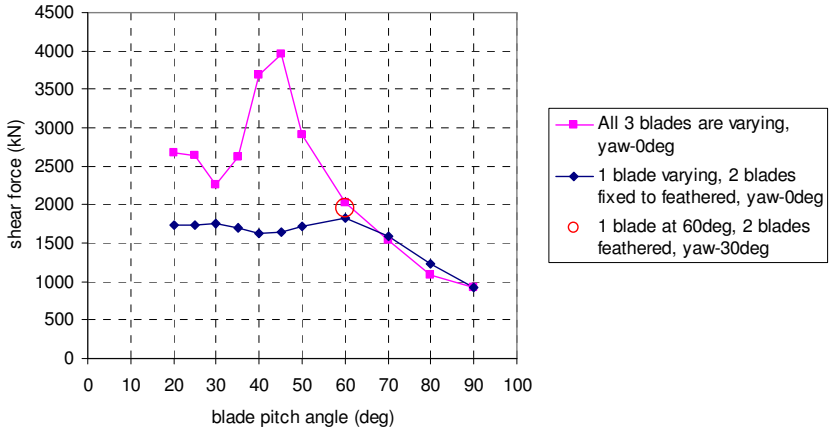

Figure 2.40 Sensitivity of Mudline Shear Force to the Blade Pitch Angle for the GOM West Central 100-yr Return Wind Condition

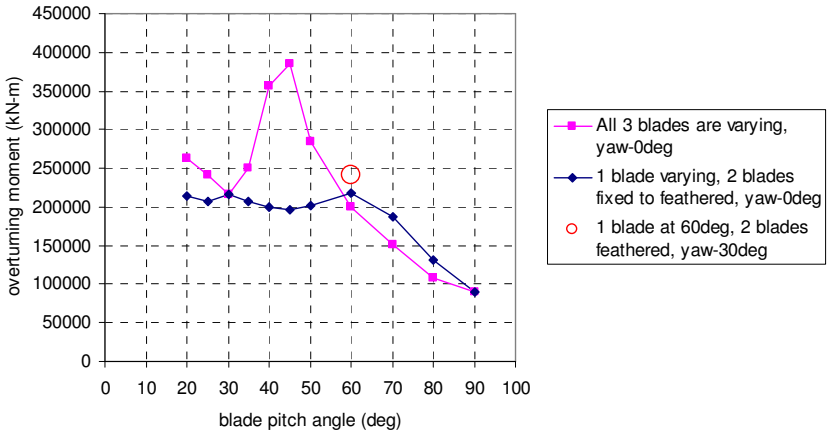

Figure 2.41 Sensitivity of Mudline Overturning Moment to the Blade Pitch Angle for the GOM West Central 100-yr Return Wind Condition

2.5.3 Summary

The following conclusions can be drawn based on the results presented in this subsection.

- The nacelle yaw misalignment could significantly increase the aerodynamic load exerted on an offshore wind turbine support structure. IEC 61400-3 (2009) allows to account for up to ±8 degrees of yaw misalignment in the extreme storm design load case where the turbulent wind model is used in the design, provided that there are at least 6 hours of capacity of back-up power supply to the safety and control systems. As shown in this study, the ratio of the peak aerodynamic loads obtained at the most unfavorable yaw misalignment angle to the wind loads at ±8 degrees of yaw misalignment is about a factor of 2 under the 100-year return turbulent wind conditions in the GOM West Central region. Relying solely on the 6-hour capacity of back-up power supply to mitigate this magnitude of load increase requires a thorough risk assessment, particularly for the area that prolonged black-out could occur during and after a major hurricane. As an alternative, a turbine support structure can be designed to accommodate the most unfavorable load conditions due to the yaw misalignment. The latter approach has recently been used in a few offshore wind farm projects on the US OCS.

- The effect of pitch angle locking on the loads on turbine support structure is evaluated in this study, although the pitch control failure and angle locking are normally not considered

during the design of turbine support structure and thus not included in the IEC abnormal load cases. The turbine blades are normally feathered during the storm condition to minimize the load. The direct consequence of malfunction of pitch angle control is over-speeding of rotor under strong wind that can potentially cause damage to turbine blades and power drive trains before the support structure collapses. Since the pitch control for each blade normally operates independently, the possibility of having failure in all pitch controllers at the same time is very low and therefore, it may not be necessary to consider this scenario as a design load case. Meanwhile, a concurrent failure in the nacelle yaw controller and the single blade pitch controller does not appear to noticeably increase the peak loads obtained from the yaw controller failure only case.

- It should be noted that the observations and conclusion made in this subsection are based on the FAST load analysis with the consideration of wind-induced loads. When loads due to other environmental conditions are taken into account, the sensitivity of global loads, i.e. the shear force and bending moment at the mudline, to changing nacelle yaw misalignment and blade pitch locking may not be as significant as the results shown in this subsection. This is particularly the case for those support structures for which wave loads are predominant.

- In the definition of load cases for the present case studies, the nacelle yaw misalignment (also called “yaw error”), for the abnormal turbine operating modes is taken as 30 degrees. All blades are assumed in the feathered position with the pitch angle of 90 degrees.

2.6 Case Studies – Monopile Support Structure

2.6.1 Summary of Model Parameters

The finite element model of the monopile support structure for the static and dynamic structural analysis is described in Section 2.3.3.1, where the equivalent monopile model for the FAST load analyses is also presented. The site conditions for the monopile case studies are summarized in Section 2.3.1. The turbine RNA and tower related parameters are given in 2.3.2.

Twenty load cases are used to evaluate the structural responses of the monopile support structure considering the effects of return period of environmental conditions, normal and abnormal turbine operating modes, wind and wave misalignment and site condition variations. These load cases are summarized in Table 2.35 along with various load components including wave loads on the support structure, aerodynamic loads on the turbine RNA, wind drag loads on the tower and wave slamming loads if breaking wave occurs. The modeling and analysis approach are described in Section 2.2.2

Since the FAST program does not account for the wind drag load on the tower, the wind load on the tower is calculated separately using the exponential wind shear law defined in Equation 2.2 for the extreme wind condition. The wind shape coefficient 0.5 (for a cylindrical section) is applied in this study. Figure 2.42 shows one of the profiles of the static wind drag loads on the monopile model. Table 2.33 summarizes all the relevant wind drag loads on the tower for different site conditions.

The wave conditions are given in Table 2.4 and Table 2.6, where the highlighted cells indicate that the wave breaking limit has been reached and therefore the breaking wave slamming load needs to be taken into account. For the monopile case studies, all but one site condition involves breaking wave. Nonlinear dynamic finite element analyses are performed to determine the representative base shear and overturning moment for global structural analysis. The wave slamming load is calculated according to IEC 61400-3 (2009). Figure 2.43 depicts the time history of wave slamming loads for different sites. The transient structural responses expressed in terms of mudline base shear forces and overturning moments are plotted in Figure 2.44 and Figure 2.45, respectively. The peak mudline base shear forces and overturning moments are summarized in Table 2.34.

Table 2.35 summarized structural loads originating from various sources relevant to the monopile case studies. The wave slamming loads included in Table 2.35 represent the peak mudline overturning moments with their associated base shear forces.

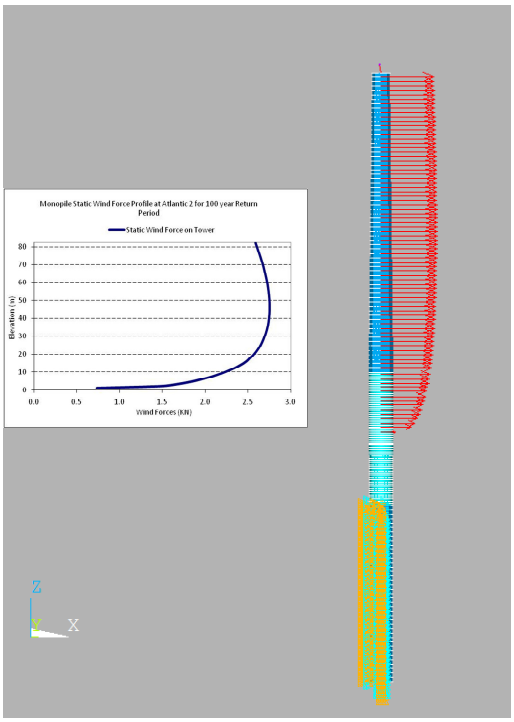

Figure 2.42 Static Wind Forces on the Monopile Support Structure

Table 2.33 Static Wind Forces on the Monopile Support Structure

Location	*Return Period*	*Water Depth*	*Eff. Depth (including Tide and Surge)*	*Mud to Hub*	*Elevation at Top of Tower*	*Elevation at Bottom of Tower*	*Wind Speed (1-hour) at Ref. 10 m*	*Total Static Wind Force on Tower*
	years	(m)	(m)	(m)	(m)	(m)	(m/s)	(kN)
Atlantic Region 2	100	13.7	15.6	100.6	82.6	14.6	32.9	210
Atlantic Region 3	100	13.7	16.6	100.6	81.6	13.6	40.2	315
GOM West Central	100	13.7	16.8	100.6	81.4	13.4	38.1	280
TX Site in GOM	100	13.7	16.8	100.6	81.4	13.4	34.7	230
Atlantic Region2	50	13.7	15.3	100.6	82.9	14.9	30.4	177
GOM West Central	50	13.7	16.3	100.6	81.9	13.9	34.3	225

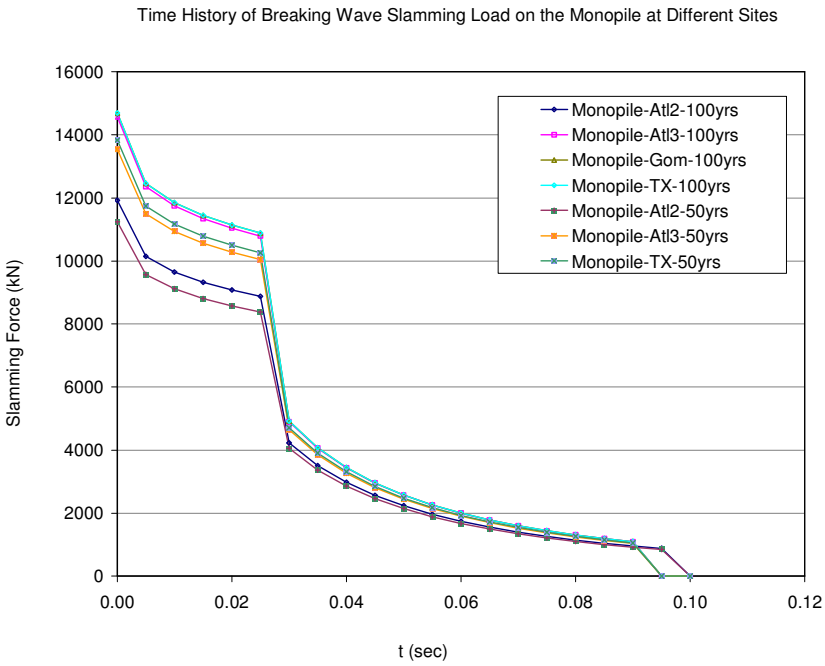

Figure 2.43 Time History of Breaking Wave Slamming Loads on the Monopile

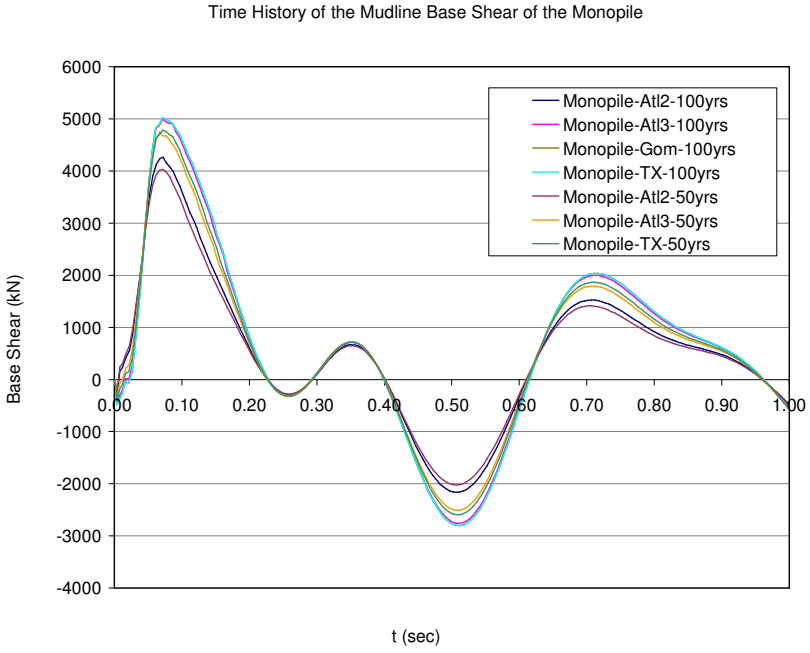

Figure 2.44 Mudline Base Shear Forces Due to Wave Slamming on the Monopile

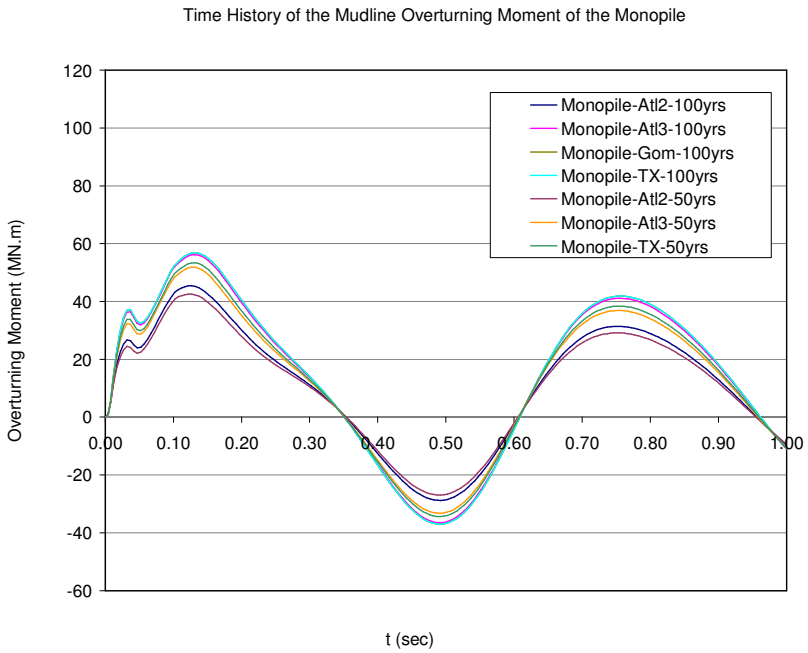

Figure 2.45 Mudline Overturning Moments Due to Wave Slamming on the Monopile

Table 2.34 Mudline Base Shear and Overturning Moment Due to Wave Slamming on the Monopile

Location	*Return Period*	*Effective Depth*	H_{max}	$H_{breaking}$	*Wave Celerity*	*Crest Elevation*	*Max. Base Shear at Mudline*	*Max. Overturning Moment at Mudline*
	years	(m)	(m)	(m)	(m/s)	(m)	(kN)	(MN.m)
Atlantic Region 2	100	15.6	18.2	11.6	11.9	9.4	4260	45.5
Atlantic Region 3	100	16.6	22.7	12.7	12.5	10.5	4992	56.2
GOM West Central	100	16.8	12.9	12.8	12.5	10.5	5023	56.8
TX Site in GOM	100	16.8	14.0	12.8	12.5	10.5	5023	56.8
Atlantic Region2	50	15.3	16.9	11.4	11.8	9.1	4032	42.5
Atlantic Region 2	50	15.3	16.9	11.4	11.8	9.1	4032	42.5
Atlantic Region 3	50	16.1	21.2	12.2	12.3	10.1	4752	51.9
TX Site in GOM	50	16.3	12.7	12.4	12.3	10.2	4786	53.4

Table 2.35 Summary of Structural Loads for the Monopile Case Studies

Case ID	*Structure Type*	*Location*	*Return Period*	*Wave & Wind Misalignment*	*Yaw Error*	*FAST - Turbine Base Shear at the Bottom of Tower*	*FAST - Turbine Overturning Moment at the Bottom of Tower*	*Base Shear at Mudline - Wind Force on Tower*	*Overturning Moment at Mudline - Wind Force on Tower*	*Base Shear at Mudline - Wave Slamming Force*	*Overturning Moment at Mudline - Wave Slamming Force*
				(deg)	(deg)	(kN)	(kN.m)	(kN)	(kN.m)	(kN)	(kN.m)
L1*	Monopile	ATL2	100	0	8	564	38649	210	15145	2753	45455
L2*	Monopile	ATL3	100	0	8	871	55389	315	19275	3513	56215
L3*	Monopile	GOM	100	0	8	851	49420	280	16538	3591	56846
L4*	Monopile	TX	100	0	8	680	37880	230	13584	3591	56846
L5*	Monopile	ATL3	100	-90	8	1164	91886	315	19275	3513	56215
L6*	Monopile	GOM	100	-30	8	1060	65419	280	16538	3591	56846
L7*	Monopile	GOM	100	-90	8	1190	80889	280	16538	3591	56846
L8*	Monopile	ATL2	100	0	30	1531	102806	210	15145	2753	45455
L9*	Monopile	ATL3	100	0	30	3057	210572	315	19275	3513	56215
L10*	Monopile	GOM	100	0	30	2344	155525	280	16538	3591	56846
L11*	Monopile	TX	100	0	30	1805	120656	230	13584	3591	56846
L12*	Monopile	ATL3	100	-90	30	3134	217189	315	19275	3513	56215
L13*	Monopile	GOM	100	-30	30	2436	161425	280	16538	3591	56846
L14*	Monopile	GOM	100	-90	30	2526	172560	280	16538	3591	56846
L39*	Monopile	ATL2	50	0	8	511	28000	177	11030	2662	42499
L40	Monopile	GOM	50	0	8	638	38215	225	13282	0	0
L41	Monopile	GOM	50	-30	8	745	50249	225	13282	0	0
L42*	Monopile	ATL2	50	0	30	1174	79005	177	11030	2662	42499
L43	Monopile	GOM	50	0	30	1746	115362	225	13282	0	0
L44	Monopile	GOM	50	-30	30	1849	121984	225	13282	0	0

Notes:

1. '*' mark in the Case ID column indicates that the breaking wave occurs.
2. ATL2 : Atlantic Region 2
3. ATL3 : Atlantic Region 3
4. GOM : GOM West Central Region
5. TX : Site Location in the GOM near the TX coast (NOAA NDBC Station 42035)

2.6.2 Monopile Case Study Results

Table 2.36 presents the maximum mudline overturning moment and its associated base shear force for each load case. It is assumed that the most unfavorable structural responses occur when the peak overturning moment is reached.

Table 2.36 also includes the maximum utilization ratio of the selected structural members as shown in Figure 2.46. The material yield strength is taken as 345 MPa. For comparison purpose, the strength design criteria in three different design guidelines, namely the ABS Guide (2011) (ABS-WSD), API-RP 2A-WSD (2007) (API-WSD) and IEC 61400-3 (2007)/ISO 19902 (2007) (IEC/ISO) are used for the calculation of the utilization ratio. It should be noted that

- ABS-WSD and API-WSD are the working stress design approach, which utilize the unfactored loads, whereas IEC/ISO follows the load and resistance factor design method, which requires the application of load factor. As an example, Table 2.37 shows the calculation sheet used in the member utilization check for load case L12.

- The design load case for the extreme storms defined in IEC 61400-3 refers to the 50-year return event. In the present study, both 50-year and 100-year return conditions are considered. Only the load factors specified in IEC 61400-3 are used in the utilization check using the IEC/ISO approach. These load factors are applied not only to the load cases for the 50-year return conditions but also those for the 100-year return conditions.

- The strength criterion defined in the API-WSD approach for the extreme design conditions is applied to both the normal and abnormal turbine operating modes while the support structures is under the 50-year return or 100-year return environmental conditions.

The following observations can be made from the monopile case study results given in Table 2.36. Further evaluation of the case study results through parametric comparisons are discussed in Section 2.9.

- The wave slamming load contributes a substantial portion of the total structural forces, while the wind turbine load contributes a significant portion of the total structure moment for Monopile structure. By comparing load case L12 with L13, it is observed that the member utilization ratio of the monopile support structure is predominantly controlled by the

overturning moment as both cases have comparative base shear forces while their overturning moments are quite different.

- For the abnormal load conditions with the 30 degree yaw misalignment, the utilization ratios calculated using the ABS-WSD approach agree well with those obtained by applying the extreme design criteria of the API-WSD approach. For the normal load conditions, however, the API-WSD approach under-predicts the utilization ratio, as it does not distinguish turbine's normal or abnormal operating modes.

- It is also observed that utilization ratios obtained using the ABS-WSD approach are fairly close (within 10% difference) to those based on the LRFD formulations given in the IEC/ISO approach for the same return period. In a few cases, however, the difference could reach around 15%. Further investigations reveal that the main difference is caused by the member strength criterion given by Eq. (13.3-8) in ISO 19902 (2007) rather than the definition of safety factors. It appears that the ISO 19902 adopted a less conservative criterion than that given in both the ABS Guide (ABS, 2011 [2.3]) and API RP 2A-WSD. It is also noted that this ISO criterion only applies when the ratio of the axial force of a member's acting axial force to its allowable axial force is less than 0.15.

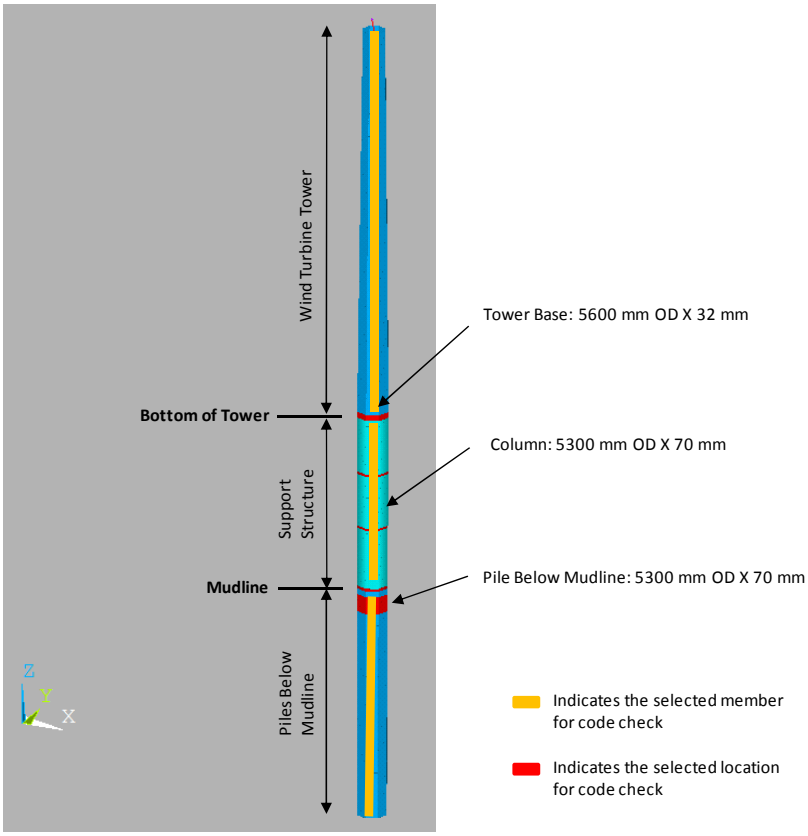

Figure 2.46 Monopile Member Size and Location for Utilization Ratio Calculation

Table 2.36 Structural Reponses and Utilization Check Results for the Monopile Support Structure

Case ID	*Structure Type*	*Location*	*Return Period*	*Wave & Wind Misalignment*	*Yaw Error*	*Total Base Shear at Mudline*	*Total Overturning Moment at Mudline*	*ABS Code Check (Max. UC)*	*API Code Check (Max. UC)*	*IEC/ISO Code Check (Max. UC)*
				(deg)	(deg)	(kN)	(MN.m)			
L1*	Monopile	ATL2	100	0	8	6921	154	0.46	0.38	0.42
L2*	Monopile	ATL3	100	0	8	8978	218	0.65	0.54	0.60
L3*	Monopile	GOM	100	0	8	9297	225	0.67	0.55	0.62
L4*	Monopile	TX	100	0	8	9188	217	0.65	0.54	0.60
L5*	Monopile	ATL3	100	-90	8	9691	282	0.83	0.69	0.77
L6*	Monopile	GOM	100	-30	8	9706	256	0.75	0.63	0.70
L7*	Monopile	GOM	100	-90	8	9979	275	0.81	0.67	0.76
L8*	Monopile	ATL2	100	0	30	7363	237	0.57	0.56	0.51
L9*	Monopile	ATL3	100	0	30	9821	407	0.97	0.96	0.88
L10*	Monopile	GOM	100	0	30	9843	342	0.82	0.81	0.74
L11*	Monopile	TX	100	0	30	9509	290	0.70	0.70	0.64
L12*	Monopile	ATL3	100	-90	30	11658	472	1.13	1.12	1.03
L13*	Monopile	GOM	100	-30	30	10792	383	0.92	0.92	0.84
L14*	Monopile	GOM	100	-90	30	11325	411	0.99	0.99	0.90
L39*	Monopile	ATL2	50	0	8	6474	142	0.43	0.36	0.40
L40	Monopile	GOM	50	0	8	4983	131	0.40	0.33	0.37
L41	Monopile	GOM	50	-30	8	5257	154	0.46	0.38	0.43
L42*	Monopile	ATL2	50	0	30	6670	195	0.48	0.48	0.43
L43	Monopile	GOM	50	0	30	5506	221	0.53	0.53	0.48
L44	Monopile	GOM	50	-30	30	6153	252	0.61	0.60	0.55

Notes:

1. '*' mark in the Case ID column indicates the breaking wave occurs.
2. IEC/ISO code check uses the load factors specified in IEC 61400-3 (2007) combined with the resistance factors and component strength criteria specified in ISO 19902 (2007)
3. ATL2 : Atlantic Region 2
4. ATL3 : Atlantic Region 3
5. GOM : GOM West Central Region
6. TX : Site Location in the GOM near the TX coast (NOAA NDBC Station 42035)

Table 2.37 Monopile Case L12 Member Utilization Ratio Check

Input Parameters	
E (Mpa)	210000
ABS / SF	1.25
API / AMOD	1.33
IEC/γ_f	1.1

Input Static Load Case	
Load Case	STL2

Input Geometry & Loads

Member property						Static Analysis (wave impact loading + wind forces on tower)						Transient Analysis (Fast turbine loading + wave loading + gravity)					
Location	D (m)	t (m)	k	L (m)	Fy (Mpa)	Axial Load, Fx_i (N)	Shear, Fy_i (N)	Shear, Fz_i (N)	Torsion, Mx_i (N.m)	Bending Moment, My_i (N.m)	Bending Moment, Mz_i (N.m)	Axial Load, Fx_i (N)	Shear, Fy_i (N)	Shear, Fz_i (N)	Torsion, Mx_i (N.m)	Bending Moment, My_i (N.m)	Bending Moment, Mz_i (N.m)
Column 4.7m above MSL	5.6	0.22	2	112.2	345	9.0E+03	-2.4E-13	-3.8E+06	5.3E-10	-2.2E+06	3.8E-12	-4.8E+06	-5.0E+06	-4.3E+05	-1.0E+05	2.9E+07	-2.6E+08
Column 4.9m below MSL	5.3	0.07	2	112.2	345	8.7E+03	-8.7E-14	-3.8E+06	5.3E-10	3.4E+07	3.3E-12	-4.4E+06	-6.6E+06	-4.3E+05	-1.0E+05	3.3E+07	-3.2E+08
Column at mudline	5.3	0.07	2	112.2	345	6.1E+03	-1.2E-14	-3.8E+06	5.3E-10	7.5E+07	4.0E-12	-3.0E+06	-7.8E+06	-4.3E+05	-1.0E+05	3.7E+07	-3.9E+08

Output (Utilization Ratio - ABS, API, IEC/ISO)			
	ABS	API	IEC/ISO
Column 4.7m above MSL	0.17	0.17	0.14
Column 4.9m below MSL	0.84	0.84	0.74
Column at mudline	1.10	1.10	0.99

Comparison	
API/ABS	ISO/ABS
102%	85%
99%	88%
99%	89%

Input Parameters	
E (Mpa)	210000
ABS / SF	1.25
API / AMOD	1.33
IEC/γ_f	1.1

Input Static Load Case	
Load Case	STL2

Input Geometry & Loads

Member property						Static Analysis (wave impact loading + wind forces on tower)						Transient Analysis (Fast turbine loading + wave loading + gravity)					
Location	D (m)	t (m)	k	L (m)	Fy (Mpa)	Axial Load, Fx_i (N)	Shear, Fy_i (N)	Shear, Fz_i (N)	Torsion, Mx_i (N.m)	Bending Moment, My_i (N.m)	Bending Moment, Mz_i (N.m)	Axial Load, Fx_i (N)	Shear, Fy_i (N)	Shear, Fz_i (N)	Torsion, Mx_i (N.m)	Bending Moment, My_i (N.m)	Bending Moment, Mz_i (N.m)
Bottom of tower	5.6	0.032	2	112.2	345	6.2E+02	2.2E-14	-2.7E+05	-3.8E-09	9.2E+06	2.0E-12	-5.5E+06	-1.0E+05	-8.6E+03	2.8E+04	-1.0E+06	-5.8E+06
pile below mudline	5.3	0.07	1	40.0	345	2.3E+02	-8.2E-12	3.9E+05	-1.0E-10	8.2E+07	-8.8E-12	-2.9E+06	1.0E+06	1.1E+06	-9.8E+04	3.6E+07	-4.1E+08
pile below mudline	5.3	0.07	1	40.0	345	1.8E+03	-6.0E-12	-9.4E+05	1.9E-09	8.2E+07	1.9E-13	-3.0E+06	-1.8E+06	7.1E+05	-1.0E+05	3.7E+07	-4.1E+08
pile below mudline	5.3	0.07	1	40.0	345	3.6E+03	-3.3E-12	-2.3E+06	4.1E-09	8.0E+07	6.8E-12	-3.0E+06	-4.7E+06	2.1E+05	-1.1E+05	3.8E+07	-4.0E+08

Output (Utilization Ratio - ABS, API, ISO)			
	ABS	API	IEC/ISO
Bottom of tower	0.17	0.17	-
pile below mudline	1.13	1.12	1.03
pile below mudline	1.13	1.12	1.03
pile below mudline	1.12	1.11	1.02

Comparison	
API/ABS	ISO/ABS
101%	-
99%	91%
99%	91%
99%	91%

2.7 Case Studies – Tripod Support Structure

2.7.1 Summary of Model Parameters

The finite element model of the tripod support structure for the static and dynamic structural analysis is described in Section 2.3.3.1, where the equivalent monopile model for the FAST load analyses is also presented. The site conditions for the tripod case studies are summarized in Section 2.3.1. The turbine RNA and tower related parameters are given in 2.3.2.

Eighteen load cases are defined for evaluating the structural responses of the tripod support structure subjected to various combinations of return periods of environmental conditions, normal and abnormal turbine operating modes, wind and wave misalignment and site locations. The load cases are summarized in Table 2.40. The modeling and analysis approach are described in Section 2.2.2

Similar to the monopile case studies, the static wind load on the tower is calculated using the exponential wind shear law defined in Equation 2.2 for the extreme wind condition. The wind shape coefficient 0.5 (for cylindrical section) is applied in this study. Figure 2.47 shows one of the profiles of the static wind drag loads on the monopile model. Table 2.38 summarizes the wind drag loads on the tower for different site conditions.

The wave conditions are given in Table 2.4 and Table 2.6, where the highlighted cells indicate that the wave breaking limit has been reached and therefore the breaking wave slamming load needs to be taken into account. For the tripod case studies, three site conditions involve a breaking wave, for which the nonlinear dynamic finite element analyses are performed to determine the transient responses of the tripod support structure. The wave slamming load is calculated according to IEC 61400-3 (2009). Figure 2.48 depicts the time history of wave slamming loads for different sites. The transient structural responses expressed in terms of mudline base shear forces and overturning moments are plotted in Figure 2.49 and Figure 2.50, respectively. The peak mudline base shear forces and overturning moments are listed in Table 2.39.

Table 2.40 summarized structural loads components relevant to the tripod case studies. Note that the wave slamming loads therein represent the peak mudline base shear forces with their associated mudline overturning moments.

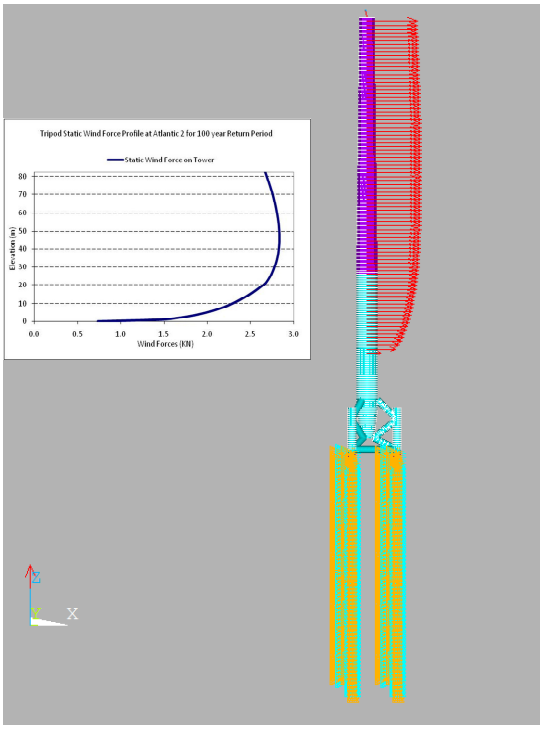

Figure 2.47 Static Wind Forces on the Tripod Support Structure

Table 2.38 Static Wind Forces on the Tripod Support Structure

Location	*Return Period*	*Water Depth*	*Eff. Depth (including Tide and Surge)*	*Mud to Hub*	*Elevation at Top of Tower*	*Elevation at Bottom of Tower*	*Wind Speed (1-hour) at Ref. 10 m*	*Total Static Wind Force on Tower*
	years	(m)	(m)	(m)	(m)	(m)	(m/s)	(kN)
Atlantic Region 2	100	24	25.9	117.6	89.3	21.3	32.9	233
Atlantic Region 3	100	24	26.9	117.6	88.3	20.3	40.2	351
GOM West Central	100	24	26.3	117.6	88.8	20.8	38.1	315
Atlantic Region 2	50	24	25.6	117.6	89.6	21.6	30.4	198
GOM West Central	50	24	26.0	117.6	89.2	21.2	34.3	255

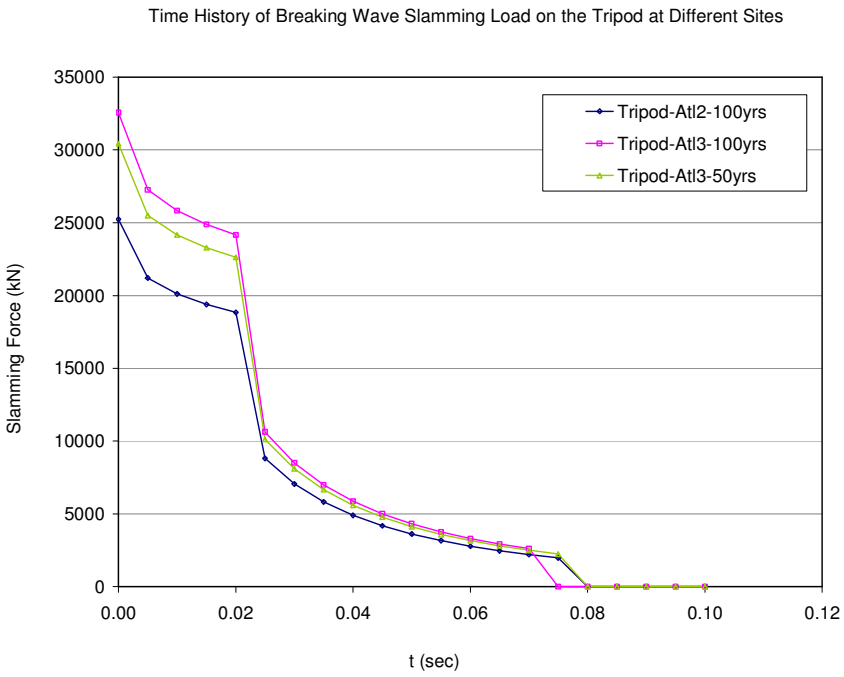

Figure 2.48 Time History of Breaking Wave Slamming Loads on the Tripod

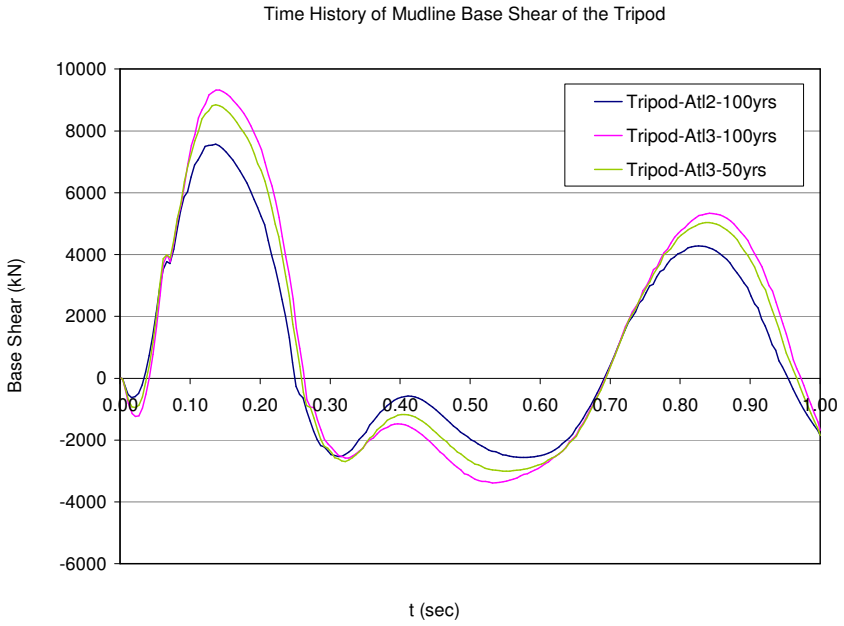

Figure 2.49 Mudline Base Shear Forces Due to Wave Slamming on the Tripod

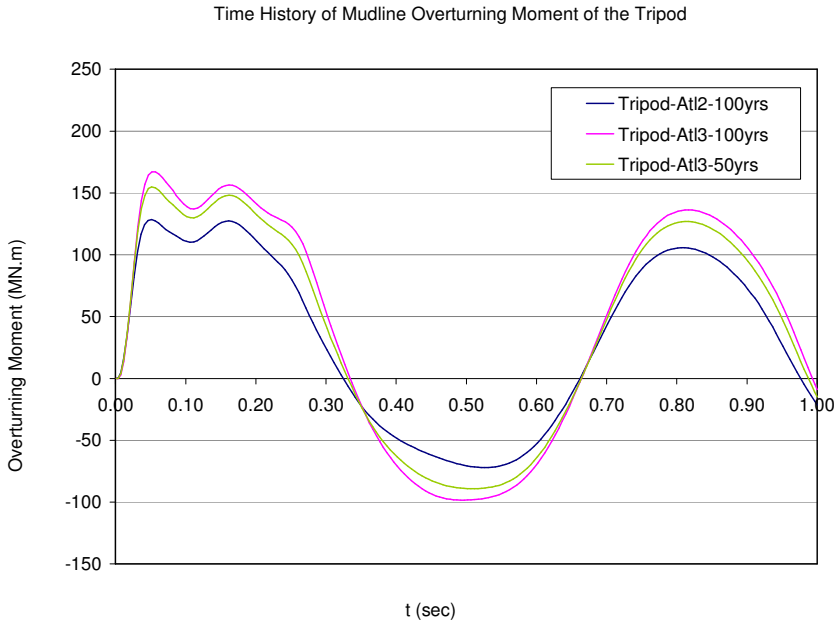

Figure 2.50 Mudline Overturning Moments Due to Wave Slamming on the Tripod

Table 2.39 Mudline Base Shear and Overturning Moment Due to Wave Slamming on the Monopile

Location	*Return Period*	*Effective Depth*	H_{max}	$H_{breaking}$	*Wave Celerity*	*Crest Elevation*	*Max. Base Shear at Mudline*	*Max. Overturning Moment at Mudline*
	years	(m)	(m)	(m)	(m/s)	(m)	(kN)	(MN.m)
Atlantic Region 2	100	25.9	18.2	17.7	14.5	13.4	7568	128.4
Atlantic Region 3	100	26.9	22.7	19.7	15.3	15.5	9320	167.1
Atlantic Region 3	50	26.4	21.2	19.1	15.1	14.9	8843	154.9

Table 2.40 Summary of Structural Loads for the Tripod Case Studies

Case ID	*Structure Type*	*Location*	*Return Period*	*Wave & Wind Misalignment*	*Yaw Error*	*FAST - Turbine Base Shear at the Bottom of Tower*	*FAST - Turbine Overturning Moment at the Bottom of Tower*	*Base Shear at Mudline - Wind Force on Tower*	*Overturning Moment at Mudline - Wind Force on Tower*	*Base Shear at Mudline - Wave Slamming Force*	*Overturning Moment at Mudline - Wave Slamming Force*
				(deg)	(deg)	(kN)	(kN.m)	(kN)	(kN.m)	(kN)	(kN.m)
L15*	Tripod	ATL2	100	0	8	782	34642	233	17250	7569	120100
L16*	Tripod	ATL3	100	0	8	2244	6888	351	24599	9320	147600
L17	Tripod	GOM	100	0	8	878	50037	315	20311	0	0
L18*	Tripod	ATL3	100	-90	8	1213	105772	351	24599	9320	147600
L19	Tripod	GOM	100	-30	8	1052	63717	315	20311	0	0
L20	Tripod	GOM	100	-90	8	1161	77171	315	20311	0	0
L21*	Tripod	ATL2	100	0	30	1553	98672	233	17250	7569	120100
L22*	Tripod	ATL3	100	0	30	5302	351765	351	24599	9320	147600
L23	Tripod	GOM	100	0	30	2706	177128	315	20311	0	0
L24*	Tripod	ATL3	100	-90	30	4193	282706	351	24599	9320	147600
L25	Tripod	GOM	100	-30	30	2764	180612	315	20311	0	0
L26	Tripod	GOM	100	-90	30	2873	190238	315	20311	0	0
L45	Tripod	ATL2	50	0	8	743	13991	198	11527	0	0
L46	Tripod	GOM	50	0	8	760	43763	255	15745	0	0
L47	Tripod	GOM	50	-30	8	872	50246	255	15745	0	0
L48	Tripod	ATL2	50	0	30	1053	39012	198	11527	0	0
L49	Tripod	GOM	50	0	30	1726	111238	255	15745	0	0
L50	Tripod	GOM	50	-30	30	1784	115231	255	15745	0	0

Notes:

1. '*' mark in the Case ID column indicates that the breaking wave occurs.
2. ATL2 : Atlantic Region 2
3. ATL3 : Atlantic Region 3
4. GOM : GOM West Central Region

2.7.2 Tripod Case Study Results

Table 2.40 presents the maximum mudline overturning moment and its associated base shear force for each load case. It is assumed that the most unfavorable structural responses occur when the peak overturning moment is reached.

Table 2.40 also includes the maximum utilization ratio of the selected structural members as shown in Figure 2.51. The material yield strength is taken as 345 MPa. Similar to the monopile case studies, three different design guidelines denoted as the ABS-WSD, API-WSD and IEC/ISO are used for the calculation of the utilization ratio. Table 2.41 shows the calculation sheets used in the member utilization check for load case L16, which has the maximum utilization ratio among all the load cases. Further evaluation of the case study results through parametric comparisons are discussed in Section 2.9.

A review of the tripod case study results given in Table 2.41 shows that

- Metocean conditions described in Section 2.3.1 shows that the Atlantic Region 3 (denoted as ATL3 in the table) has the highest wind speed among all site locations covered by the case studies. A further review of the FAST load analysis results reveal that exceptionally high responses are generated under the 100-year return wind and wave conditions in the Atlantic Region 3 due to a low frequency resonant component. It is also found that the structural dynamic analyses are unstable for load cases 22 and 24, where both cases are for 100-year return site conditions in the Atlantic Region 3 and with the turbine in the abnormal operating mode. It appears that the tripod support structure selected in the case studies is not a suitable design for the Atlantic Region 3.

- Similar to the finding obtained in the monopile case studies, the wave slamming load and turbine load contribute a significant portion of the total structural forces and moments.

- For the abnormal load conditions with 30 degree yaw misalignment, the utilization ratios calculated using the ABS-WSD approach agree well with those obtained by applying the extreme design criteria of the API-WSD approach. For the normal load conditions, however, the API-WSD approach under-predicts the utilization ratio because it does not distinguish turbine's normal or abnormal operating modes.

- The utilization ratios calculated based on the ABS-WSD approach also agree well with those based on the LRFD formulation in the IEC/ISO approach for both 100-year and 50-year return conditions. As concluded in Section 2.6.2 based on the utilization check for the monopile support structure, the main source of modest discrepancy is the difference in the utilization equations specified in ISO 19902 and the ABS guide.

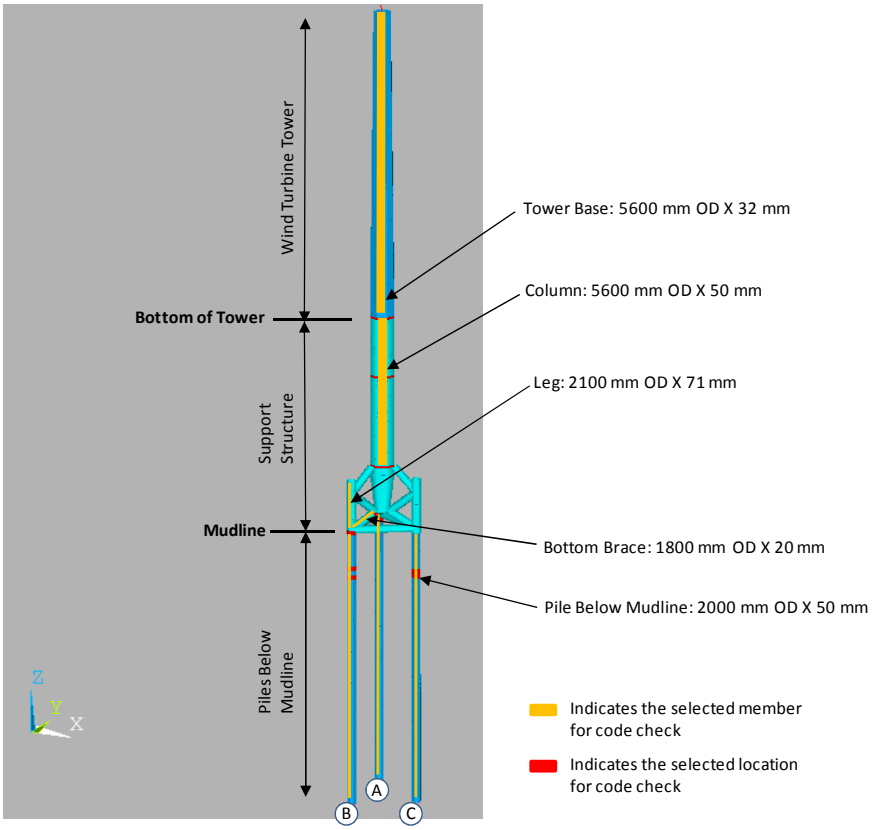

Figure 2.51 Tripod Member Size and Location for Utilization Ratio Calculation

Table 2.41 Structural Reponses and Utilization Check Results for the Tripod Support Structure

Case ID	*Structure Type*	*Location*	*Return Period*	*Wave & Wind Misalignment*	*Yaw Error*	*Total Base Shear at Mudline*	*Total Overturning Moment at Mudline*	*ABS Code Check (Max. UC)*	*API Code Check (Max. UC)*	*IEC/ISO Code Check (Max. UC)*
				(deg)	(deg)	(kN)	(MN.m)			
L15*	Tripod	ATL2	100	0	8	16681	372	0.80	0.65	0.77
L16*	Tripod	ATL3	100	0	8	23496	653	1.40	1.14	1.35
L17	Tripod	GOM	100	0	8	9712	253	0.50	0.41	0.49
L18*	Tripod	ATL3	100	-90	8	22477	598	1.11	0.92	1.02
L19	Tripod	GOM	100	-30	8	10074	288	0.48	0.39	0.46
L20	Tripod	GOM	100	-90	8	10311	311	0.52	0.42	0.50
L21*	Tripod	ATL2	100	0	30	16683	421	0.80	0.80	0.71
L22*	Tripod	ATL3	100	0	30	-	-	-	-	-
L23	Tripod	GOM	100	0	30	9987	390	0.74	0.74	0.66
L24*	Tripod	ATL3	100	-90	30	-	-	-	-	-
L25	Tripod	GOM	100	-30	30	11222	459	0.76	0.76	0.67
L26	Tripod	GOM	100	-90	30	12038	509	0.79	0.79	0.70
L45	Tripod	ATL2	50	0	8	8235	218	0.45	0.36	0.43
L46	Tripod	GOM	50	0	8	7912	188	0.38	0.31	0.36
L47	Tripod	GOM	50	-30	8	8311	225	0.37	0.30	0.35
L48	Tripod	ATL2	50	0	30	8435	248	0.40	0.39	0.38
L49	Tripod	GOM	50	0	30	8238	275	0.50	0.50	0.44
L50	Tripod	GOM	50	-30	30	8939	320	0.51	0.51	0.45

Notes:

1. '*' mark in the Case ID column indicates the breaking wave occurs.
2. IEC/ISO code check uses the load factors specified in IEC 61400-3 (2007) combined with the resistance factors and component strength criteria specified in ISO 19902 (2007)
3. ATL2 : Atlantic Region 2
4. ATL3 : Atlantic Region 3
5. GOM : GOM West Central Region

Table 2.42 Tripod Case L16 Member Utilization Ratio Check

Input Parameters	
E (Mpa)	210000
ABS / SF	1.5
API / AMOD	1.33
IEC/γ_f	1.35

Input Static Load Case	
Load Case	STL6

Input Geometry & Loads

Member property						Static Analysis (wave impact loading + wind forces on tower)						Transient Analysis (Fast turbine loading + wave loading + gravity)					
Location	D (m)	t (m)	k	L (m)	Fy (Mpa)	Axial Load, Fx_i (N)	Shear, Fy_i (N)	Shear, Fz_i (N)	Torsion, Mx_i (N.m)	Bending Moment, My_i (N.m)	Bending Moment, Mz_i (N.m)	Axial Load, Fx_i (N)	Shear, Fy_i (N)	Shear, Fz_i (N)	Torsion, Mx_i (N.m)	Bending Moment, My_i (N.m)	Bending Moment, Mz_i (N.m)
Column at connection of brace	5.6	0.07	2	101.2	345	1.5E+04	-2.7E-05	-9.7E+06	1.1E-08	3.7E+07	-6.8E-06	-1.6E+06	-4.9E+04	-9.9E+06	4.6E+04	3.2E+08	-8.7E+06
Column 7.1m below MSL	5.6	0.05	2	101.2	345	2.7E+03	-3.6E-11	-9.7E+06	1.1E-08	-1.6E+08	4.1E-09	-4.6E+06	-5.0E+04	-5.6E+06	4.6E+04	1.6E+08	-7.7E+06
Bottom brace at Leg A	1.8	0.02	0.8	6.9	345	3.9E+06	4.1E+05	3.5E+05	9.4E+05	1.8E+05	-1.8E+06	4.4E+06	4.0E+05	6.2E+05	1.1E+06	6.4E+05	-2.0E+06
Bottom brace at Leg B	1.8	0.02	0.8	6.9	345	3.9E+06	-4.1E+05	3.5E+05	-9.4E+05	1.8E+05	1.8E+06	4.4E+06	-4.0E+05	6.1E+05	-1.1E+06	6.0E+05	2.0E+06
Leg A at mudline	2.1	0.071	1	12.1	345	8.2E+06	-4.6E+05	-3.1E+06	1.4E+05	-7.5E+06	2.0E+06	2.2E+07	-5.3E+05	-4.5E+06	1.9E+05	-8.0E+06	1.7E+06
Leg B at mudline	2.1	0.071	1	12.1	345	8.2E+06	4.6E+05	-3.1E+06	-1.4E+05	-7.5E+06	-2.0E+06	2.1E+07	5.0E+05	-4.5E+06	-1.9E+05	-8.0E+06	-2.1E+06

Output (Utilization Ratio - ABS, API, ISO)			
	ABS	API	IEC/ISO
Column at connection of brace	0.88	0.73	0.81
Column 7.1m below MSL	1.18	0.98	1.08
Bottom brace at Leg A	0.65	0.54	0.61
Bottom brace at Leg B	0.66	0.54	0.61
Leg A at mudline	0.54	0.45	0.50
Leg B at mudline	0.53	0.44	0.49

Comparison	
API/ABS	ISO/ABS
83%	92%
83%	91%
83%	94%
83%	94%
83%	92%
83%	92%

Input Parameters	
E (Mpa)	210000
ABS / SF	1.5
API / AMOD	1.33
IEC/γ_f	1.35

Input Static Load Case	
Load Case	STL6

Input Geometry & Loads

Member property						Static Analysis (wave impact loading + wind forces on tower)						Transient Analysis (Fast turbine loading + wave loading + gravity)					
Location	D (m)	t (m)	k	L (m)	Fy (Mpa)	Axial Load, Fx_i (N)	Shear, Fy_i (N)	Shear, Fz_i (N)	Torsion, Mx_i (N.m)	Bending Moment, My_i (N.m)	Bending Moment, Mz_i (N.m)	Axial Load, Fx_i (N)	Shear, Fy_i (N)	Shear, Fz_i (N)	Torsion, Mx_i (N.m)	Bending Moment, My_i (N.m)	Bending Moment, Mz_i (N.m)
Bottom of tower	5.6	0.032	2	101.2	345	-5.4E+02	5.0E-12	-2.8E+05	-7.8E-11	9.4E+06	-3.7E-11	-5.5E+06	-2.3E+03	-7.6E+04	6.3E+02	2.8E+06	-1.3E+05
pile below mudline	2	0.05	1	60.0	345	-1.3E+07	2.3E-08	-3.2E+04	-5.1E-09	9.0E+06	-4.4E-08	-3.7E+07	1.6E+04	-1.6E+05	4.0E+03	1.8E+07	-8.6E+04
pile below mudline	2	0.05	1	60.0	345	-1.3E+07	2.4E-08	-4.5E+05	-5.8E-09	8.7E+06	-6.7E-08	-3.8E+07	1.7E+04	-7.4E+05	4.2E+03	1.7E+07	-1.0E+05
pile below mudline	2	0.05	1	60.0	345	6.3E+06	1.4E+04	1.7E+05	-8.7E+04	8.7E+06	3.4E+05	1.6E+07	1.1E+04	-7.3E+04	-1.2E+05	1.7E+07	3.8E+05
pile below mudline	2	0.05	1	60.0	345	6.8E+06	8.4E+04	-6.3E+05	-9.8E+04	8.3E+06	2.4E+05	1.7E+07	8.6E+04	-1.2E+06	-1.4E+05	1.6E+07	2.9E+05
pile below mudline	2	0.05	1	60.0	345	8.2E+06	-4.5E+05	-3.1E+06	1.3E+05	-6.0E+06	1.7E+06	2.2E+07	-5.2E+05	-4.4E+06	1.9E+05	-5.7E+06	1.4E+06

Output (Utilization Ratio - ABS, API, ISO)			
	ABS	API	IEC/ISO
Bottom of tower	0.16	0.14	-
pile below mudline	1.40	1.14	1.35
pile below mudline	1.40	1.14	1.35
pile below mudline	0.97	0.80	0.88
pile below mudline	0.95	0.78	0.87
pile below mudline	0.73	0.61	0.68

Comparison	
API/ABS	ISO/ABS
87%	-
81%	96%
81%	97%
83%	91%
83%	92%
83%	93%

2.8 Case Studies – Jacket Support Structure

2.8.1 Summary of Model Parameters

The finite element model of the jacket support structure for the static and dynamic structural analysis is described in Section 2.3.3.1, where the equivalent monopile model for the FAST load analyses is also presented. The site conditions for the jacket case studies are summarized in Section 2.3.1. The turbine RNA and tower related parameters are given in 2.3.2.

Eighteen load cases are defined for evaluating the structural responses of the jacket support structure subjected to various combinations of return period of environmental conditions, normal and abnormal turbine operating modes, wind and wave misalignment and site locations. The load cases are summarized in Table 2.44, where all the structural loads components relevant to the jacket case studies are included. The modeling and analysis approach are described in Section 2.2.2

Similar to the monopile case studies, the static wind load on the tower is calculated using the exponential wind shear law defined in Equation 2.2 for the extreme wind condition. The wind shape coefficient 0.5 (for cylindrical section) is applied in this study. Figure 2.52 shows one of the profiles of the static wind drag loads on the monopile model. Table 2.43 summarizes the wind drag loads on the tower under different site conditions.

The wave conditions are given in Table 2.4 and Table 2.6, which show that the breaking wave does not occur for the jacket cases.

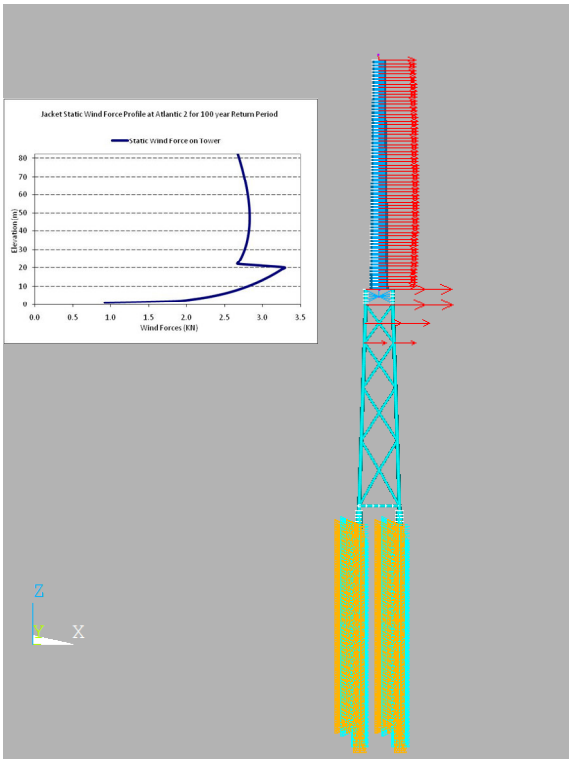

Figure 2.52 Static Wind Forces on the Jacket Support Structure

Table 2.43 Static Wind Forces on the Jacket Support Structure

Location	*Return Period*	*Water Depth*	*Eff. Depth (including Tide and Surge)*	*Mud to Hub*	*Elevation at Top of Tower*	*Elevation at Bottom of Tower*	*Wind Speed (1-hour) at Ref. 10 m*	*Total Static Wind Force on Tower*
	years	(m)	(m)	(m)	(m)	(m)	(m/s)	(kN)
Atlantic Region 2	100	47	48.9	140.6	89.3	21.3	32.9	245
Atlantic Region 3	100	47	49.9	140.6	88.3	20.3	40.2	367
GOM West Central	100	47	48.7	140.6	89.5	21.5	38.1	334
Atlantic Region 2	50	47	48.6	140.6	89.6	21.6	30.4	207
GOM West Central	50	47	48.5	140.6	89.7	21.7	34.3	268

Table 2.44 Summary of Structural Loads for the Jacket Case Studies

Case ID	*Structure Type*	*Location*	*Return Period*	*Wave & Wind Misalignment*	*Yaw Error*	*FAST - Turbine Base Shear at the Bottom of Tower*	*FAST - Turbine Overturning Moment at the Bottom of Tower*	*Base Shear at Mudline - Wind Force on Tower*	*Overturning Moment at Mudline - Wind Force on Tower*	*Base Shear at Mudline - Wave Slamming Force*	*Overturning Moment at Mudline - Wave Slamming Force*
				(deg)	(deg)	(kN)	(kN.m)	(kN)	(kN.m)	(kN)	(kN.m)
L27	Jacket	ATL2	100	0	8	629	15463	245	20692	0	0
L28	Jacket	ATL3	100	0	8	1087	40981	367	32760	0	0
L29	Jacket	GOM	100	0	8	807	51294	334	29347	0	0
L30	Jacket	ATL3	100	-90	8	1300	89972	367	32760	0	0
L31	Jacket	GOM	100	-30	8	878	55222	334	29347	0	0
L32	Jacket	GOM	100	-90	8	889	60413	334	29347	0	0
L33	Jacket	ATL2	100	0	30	896	31718	245	20692	0	0
L34	Jacket	ATL3	100	0	30	1589	72423	367	32760	0	0
L35	Jacket	GOM	100	0	30	1702	107795	334	29347	0	0
L36	Jacket	ATL3	100	-90	30	2017	133072	367	32760	0	0
L37	Jacket	GOM	100	-30	30	1726	110510	334	29347	0	0
L38	Jacket	GOM	100	-90	30	1655	107571	334	29347	0	0
L51	Jacket	ATL2	50	0	8	768	8674	207	19725	0	0
L52	Jacket	GOM	50	0	8	643	36925	268	25538	0	0
L53	Jacket	GOM	50	-30	8	722	41230	268	25538	0	0
L54	Jacket	ATL2	50	0	30	808	12661	207	19725	0	0
L55	Jacket	GOM	50	0	30	1290	79962	268	25538	0	0
L56	Jacket	GOM	50	-30	30	1330	84131	268	25538	0	0

Notes:

1. ATL2 : Atlantic Region 2
2. ATL3 : Atlantic Region 3
3. GOM : GOM West Central Region

2.8.2 Jacket Case Study Results

Table 2.45 presents the maximum mudline overturning moment and its associated base shear force for each load case. It is assumed that the most unfavorable structural responses occur when the peak overturning moment is reached.

Table 2.45 also includes the maximum utilization ratios of the selected structural members as shown in Figure 2.53. The material yield strength is taken as 345 MPa. Similar to the monopile case studies, three different design guidelines denoted as the ABS-WSD, API-WSD and IEC/ISO approaches are used for the calculation of the utilization ratio. Table 2.46 shows the calculation sheets used in the member utilization check for load case L28, which has the maximum utilization ratio among all the load cases. Further evaluation of the case study results through parametric comparisons are discussed in Section 2.9.

A review of the jacket case study results given in Table 2.45 shows that

- The wave load contributes a major portion of the total structural forces and moments of the jacket support structure.

- For the Atlantic Region 3 (ATL3), the values of maximum utilization ratio are all above 1.0 for the 100-year return conditions. This is within the expectation since the jacket is adapted from an optimized conceptual design based on the 50-year return conditions of a specific region in the North Sea.

- For the abnormal load conditions with 30 degree yaw misalignment, the utilization ratios calculated using the ABS-WSD approach agree well with those obtained by applying the extreme design criteria of the API-WSD approach. For the normal load conditions, however, the API-WSD approach under-predicts the utilization ratio because it does not distinguish turbine's normal or abnormal operating modes.

- The utilization ratios calculated based on the ABS-WSD approach agree well with those based on the LRFD formulation in the IEC/ISO approach for both 100-year and 50-year return conditions. As concluded in Section 2.6.2, the main source of modest discrepancy is the difference in the utilization equations specified in ISO 19902 and the ABS Guide.

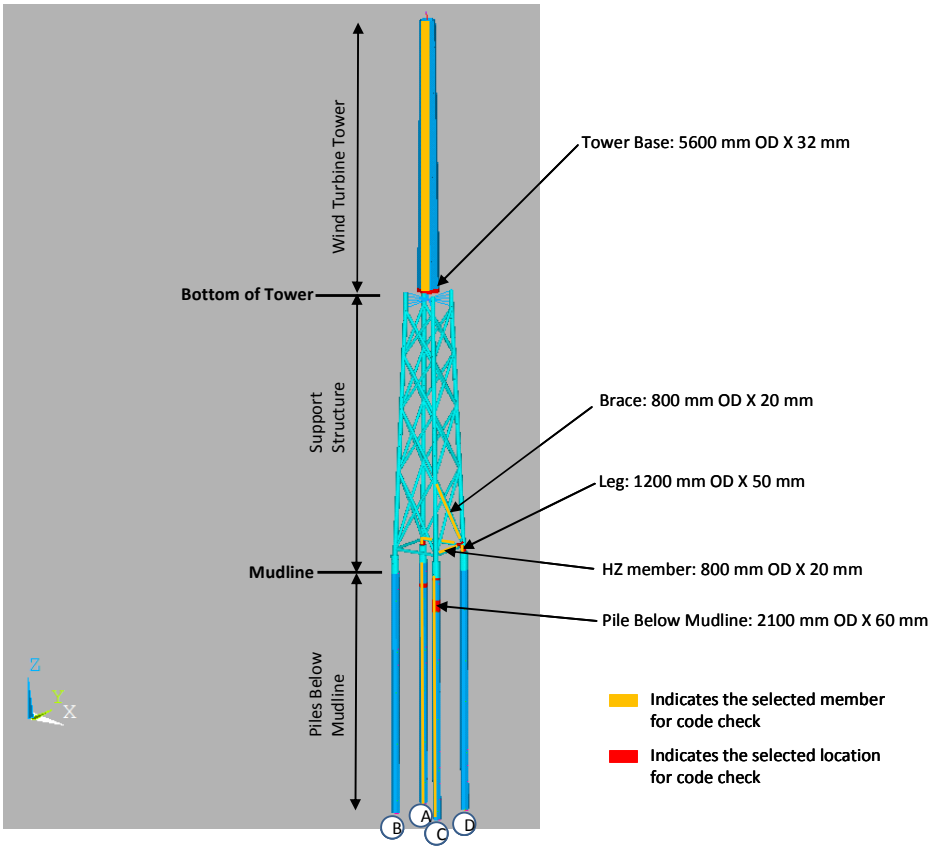

Figure 2.53 Jacket Member Size and Location for Utilization Ratio Calculation

Table 2.45 Structural Reponses and Utilization Check Results for the Jacket Support Structure

Case ID	*Structure Type*	*Location*	*Return Period*	*Wave & Wind Misalignment*	*Yaw Error*	*Total Base Shear at Mudline*	*Total Overturning Moment at Mudline*	*ABS Code Check (Max. UC)*	*API Code Check (Max. UC)*	*IEC/ISO Code Check (Max. UC)*
				(deg)	(deg)	(kN)	(MN.m)			
L27	Jacket	ATL2	100	0	8	9327	422	0.75	0.66	0.75
L28	Jacket	ATL3	100	0	8	15582	712	1.26	1.14	1.26
L29	Jacket	GOM	100	0	8	9847	407	0.71	0.60	0.66
L30	Jacket	ATL3	100	-90	8	15945	768	1.26	1.07	1.17
L31	Jacket	GOM	100	-30	8	10127	449	0.78	0.66	0.73
L32	Jacket	GOM	100	-90	8	10353	471	0.72	0.61	0.67
L33	Jacket	ATL2	100	0	30	9539	453	0.63	0.67	0.61
L34	Jacket	ATL3	100	0	30	15921	766	1.13	1.15	1.03
L35	Jacket	GOM	100	0	30	10231	487	0.71	0.72	0.65
L36	Jacket	ATL3	100	-90	30	16597	861	1.18	1.19	1.07
L37	Jacket	GOM	100	-30	30	10789	552	0.77	0.77	0.70
L38	Jacket	GOM	100	-90	30	11051	572	0.73	0.74	0.66
L51	Jacket	ATL2	50	0	8	7678	382	0.66	0.58	0.66
L52	Jacket	GOM	50	0	8	7875	335	0.55	0.48	0.55
L53	Jacket	GOM	50	-30	8	8084	366	0.60	0.50	0.56
L54	Jacket	ATL2	50	0	30	7716	388	0.55	0.58	0.53
L55	Jacket	GOM	50	0	30	8154	391	0.54	0.54	0.49
L56	Jacket	GOM	50	-30	30	8548	439	0.58	0.59	0.53

Notes:

1. IEC/ISO code check uses the load factors specified in IEC 61400-3 (2007) combined with the resistance factors and component strength criteria specified in ISO 19902 (2007)
2. ATL2 : Atlantic Region 2
3. ATL3 : Atlantic Region 3
4. GOM : GOM West Central Region

Table 2.46 Jacket Case L28 Member Utilization Ratio Check

Input Parameters	
E (Mpa)	210000
ABS / SF	1.5
API / AMOD	1.33
IEC/γ_f	1.35

Input Static Load Case	
Load Case	STL9

Input Geometry & Loads

Member property						Static Analysis (wave impact loading + wind forces on tower)						Transient Analysis (Fast turbine loading + wave loading + gravity)					
Location	D (m)	t (m)	k	L (m)	Fy (Mpa)	Axial Load, Fx_i (N)	Shear, Fy_i (N)	Shear, Fz_i (N)	Torsion, Mx_i (N.m)	Bending Moment, My_i (N.m)	Bending Moment, Mz_i (N.m)	Axial Load, Fx_i (N)	Shear, Fy_i (N)	Shear, Fz_i (N)	Torsion, Mx_i (N.m)	Bending Moment, My_i (N.m)	Bending Moment, Mz_i (N.m)
Brace from leg C to D at bot. elevation	0.8	0.02	0.9	22.5	345	-6.1E+04	-5.6E+01	-7.6E+02	-1.1E+03	5.2E+03	8.1E+02	-1.1E+06	9.0E+04	-1.8E+03	1.2E+05	9.0E+04	-1.7E+04
HZ from leg D to A at bot. elevation	0.8	0.02	1	11.9	345	-1.0E+03	-1.9E+02	-3.4E+03	-9.7E+02	2.0E+04	-1.1E+03	7.7E+04	-1.3E+04	-4.1E+05	-1.6E+04	2.5E+06	-8.0E+04
HZ from leg D to C at bot. elevation	0.8	0.02	1	11.9	345	7.7E+04	-3.1E+00	3.8E+00	6.9E-03	1.3E+03	1.4E+03	1.5E+06	3.8E+04	7.6E+02	-5.1E+03	4.2E+04	3.3E+04
Leg A at bottom elevation	1.2	0.05	1	15.1	345	1.4E+06	6.4E+04	2.2E+04	8.9E+03	4.7E+03	5.9E+04	2.6E+07	2.4E+06	1.9E+06	4.3E+05	-5.6E+06	6.5E+06
Leg D at bottom elevation	1.2	0.05	1	15.1	345	-1.4E+06	6.4E+04	-2.4E+04	8.9E+03	-2.9E+03	6.0E+04	-2.6E+07	2.7E+06	-1.8E+06	4.8E+05	5.5E+06	6.3E+06
Leg C at mudline	2.1	0.06	1	15.1	345	-1.4E+06	-2.4E+03	-9.3E+04	-1.0E+04	4.7E+05	-1.2E+04	-3.3E+07	-1.8E+05	-3.9E+06	-3.0E+05	1.4E+07	-1.0E+06

Output (Utilization Ratio - ABS, API, ISO)			
	ABS	API	IEC/ISO
Brace from leg C to D at bot. elevation	0.18	0.16	0.18
HZ from leg D to A at bot. elevation	0.98	0.81	0.88
HZ from leg D to C at bot. elevation	0.16	0.14	0.15
Leg A at bottom elevation	1.26	1.06	1.17
Leg D at bottom elevation	1.26	1.14	1.26
Leg C at mudline	0.63	0.54	0.65

Comparison	
API/ABS	ISO/ABS
85%	97%
82%	90%
83%	94%
84%	93%
91%	100%
86%	102%

Input Parameters	
E (Mpa)	210000
ABS / SF	1.5
API / AMOD	1.33
IEC/γ_f	1.35

Input Static Load Case	
Load Case	STL9

Input Geometry & Loads

Member property						Static Analysis (wave impact loading + wind forces on tower)						Transient Analysis (Fast turbine loading + wave loading + gravity)					
Location	D (m)	t (m)	k	L (m)	Fy (Mpa)	Axial Load, Fx_i (N)	Shear, Fy_i (N)	Shear, Fz_i (N)	Torsion, Mx_i (N.m)	Bending Moment, My_i (N.m)	Bending Moment, Mz_i (N.m)	Axial Load, Fx_i (N)	Shear, Fy_i (N)	Shear, Fz_i (N)	Torsion, Mx_i (N.m)	Bending Moment, My_i (N.m)	Bending Moment, Mz_i (N.m)
Bottom of tower	5.6	0.032	2	68.0	345	1.0E+02	-3.1E-05	-2.9E+05	-3.8E-09	1.0E+07	-1.2E-08	-5.5E+06	-9.3E+03	-3.8E+04	2.5E+03	5.9E+05	-5.1E+05
pile below mudline	2.1	0.06	1	60.0	345	1.2E+06	1.5E+02	3.7E+04	8.2E+03	-6.4E+05	-1.0E+04	2.3E+07	-9.3E+04	-1.5E+06	2.8E+05	-2.9E+07	-1.6E+06
pile below mudline	2.1	0.06	1	60.0	345	-1.2E+06	-1.2E+03	4.0E+04	-8.2E+03	-6.5E+05	-1.4E+04	-3.0E+07	-8.8E+04	-1.4E+06	-2.5E+05	-3.0E+07	-1.3E+06
pile below mudline	2.1	0.06	1	60.0	345	-1.2E+06	-1.2E+03	5.7E+04	-7.8E+03	-6.0E+05	-1.3E+04	-2.9E+07	-1.2E+05	-7.5E+05	-2.3E+05	-3.1E+07	-1.2E+06
pile below mudline	2.1	0.06	1	60.0	345	-1.2E+06	-1.2E+03	6.7E+04	-7.4E+03	-5.4E+05	-1.2E+04	-2.9E+07	-1.4E+05	-7.9E+04	-2.2E+05	-3.2E+07	-1.1E+06

Output (Utilization Ratio - ABS, API, ISO)			
	ABS	API	IEC/ISO
Bottom of tower	0.13	0.11	-
pile below mudline	0.83	0.69	0.76
pile below mudline	0.94	0.77	0.89
pile below mudline	0.95	0.78	0.90
pile below mudline	0.95	0.78	0.90

Comparison	
API/ABS	ISO/ABS
87%	-
83%	91%
82%	95%
82%	94%
82%	94%

2.9 Parametric Comparisons of Case Study Results

A parametric study is carried out to assess the correlations between the responses of turbine support structure and the main design parameters, which are considered critical in order to achieve a rational definition of design load cases for the hurricane conditions. The following parameters are included in the parametric study:

- Return period of design environmental conditions (Section 2.9.1)
- Normal and abnormal turbine operating modes (Section 2.9.2)
- Misalignment between wind and wave directions (Section 2.9.3)
- Type of support structures (Section 2.9.4)
- Site variations (Section 2.9.2)

2.9.1 Return Period of Environmental Conditions

One of most debated topics on adapting the IEC 61400-3 (2007) criteria for the US OCS is the return period of extreme storm conditions – whether it should be the direct adoption of the 50-year return period from IEC 61400-3 or the 100-year return period commonly applied to high consequence (L-1) hydrocarbon-related offshore structures. As indicated in Yu et al. (2011), the return period of the design environmental conditions should be determined from the perspective of an overall design approach (i.e. "a design recipe"). The present case studies are intended to provide a means of evaluating the effect of the return period of the design environmental conditions, in conjunction with other critical design parameters, on structural responses and the safety margin of an offshore wind turbine support structure.

Figure 2.54 through Figure 2.56 depict the ratio of the structural responses under the 100-year return environmental conditions to those calculated based on the 50-year return environmental conditions. Figure 2.56 is plotted using the results of utilization ratio check according to the ABS-WSD approach (see Section 2.6.2). The effect of turbine normal and abnormal operating modes, which are translated respectively to the yaw misalignment angle of 8 degrees and 30 degrees, is taken into account. The effect of site conditions in the Atlantic Region 2 (ATL2) and the GOM West Central region (GOM) (see Section 2.2.2.2) are also considered. The occurrence of breaking wave slamming is described in Table 2.47, which uses the wave conditions given in Table 2.4 and Table 2.6.

Table 2.47 Occurrence of Breaking Wave Slamming

	Monopile		Tripod		Jacket	
	50-Year	100-Year	50-Year	100-Year	50-Year	100-Year
Atlantic Region 2 (ATL2)	*	*	-	*	-	-
Atlantic Region 3 (ATL3)	*	*	*	*	-	-
GOM West Central (GOM)	-	*	-	-	-	-
TX Site in the GOM (TX)	*	*	-	-	-	-

Notes: * mark indicates the breaking wave slamming occurs.

The following observations are made from Figure 2.54 through Figure 2.56:

- In Figure 2.54, the mudline shear force ratio for "Monopile-GOM" and "Tripod-ATL2" are around 1.8 ~ 2.0, which means the magnitude of the mudline shear force under the 100-year return condition is nearly twice of that under the 50-year return conditions. This is mainly because the 100-year return conditions involve breaking wave slamming (see Table 2.47), while the 50-year return conditions do not. The slamming load appears to contribute approximately half of the total mudline shear forces in both cases. For the mudline overturning moment as shown in Figure 2.55, a similar observation can be made for "Tripod-ATL2" and "Monopile-GOM", although the values of the mudline overturning moment ratio are reduced to about 1.5 ~ 1.7. The reason for this reduction can be attributed to the fact that the slamming load is exerted near the water surface with a much shorter moment arm to the mudline than that for the turbine's aerodynamic loads.

- For "Monopile-ATL2", wave slamming occurs in both the 50-year and the 100-year cases. The relative increase in the responses due to the increase in the return period is about 20%. The relative changes in the mudline shear forces and overturning moments as well as the maximum utilization ratio share a similar trend.

- In Figure 2.55, the interaction between the return period and the yaw misalignment angle can be found in the case of "Tripod-GOM", "Jacket-ATL2" and "Jacket-GOM", where the slamming load is not present. A significant higher ratio for the 100-year to 50-year return mudline overturning moments for the yaw error of 30 degrees than that for the yaw error of 8 degrees indicates that the combined effect of strong hurricane wind and most unfavorable yaw misalignment can amplify the level of load increase. It is also noted that the jacket

support structure is less sensitive than the tripod support structure to yaw misalignment or to turbine operating modes.

- For "Jacket-ATL2" and "Jacket-GOM", the values of the ratio of 100-year to 50-year return mudline shear force and overturning moment are around 1.2 ~ 1.3, which are fairly close to what is normally found for jacket platforms designed to API RP 2A-WSD in the GOM. This observation suggests that the wave load on the jacket support structure is predominant over the aerodynamic load generated by the turbine. It also explains why the jacket support structure is relatively insensitive to the turbine operating modes.

- Figure 2.56 shows the ratio of the maximum member utilization ratio under the 100-year return conditions to that under the 50-year return conditions. The large values in the cases of "Monopile-GOM" and "Tripod-ATL2" are due to wave slamming, which occurs only under the 100-year return condition. It is also noted that the ratio for the "Tripod-GOM" case is 1.48 for the abnormal condition with the yaw error of 30 degrees. This is believed to be a result of the combined effect of strong hurricane wind and most unfavorable yaw misalignment that could amplify the level of load increase. With this magnitude of load increase, a member of optimized support structure designed to 50-year return conditions as according to IEC 61400-3, where the aggregated nominal safety margin for the abnormal condition is approximately 25%, may exceed the member's strength capacity after a 48% increase in loads under the 100-year return conditions.

- Figure 2.56 shows that the member responses in terms of utilization ratios correlate well with the global responses depicted in Figure 2.54 and Figure 2.55.

In addition to the relative change of structural responses with respect to the return period of site conditions discussed above, the actual magnitude of the responses of three support structures in ATL2 and GOM regions are provided in Figure 2.57 through Figure 2.59.

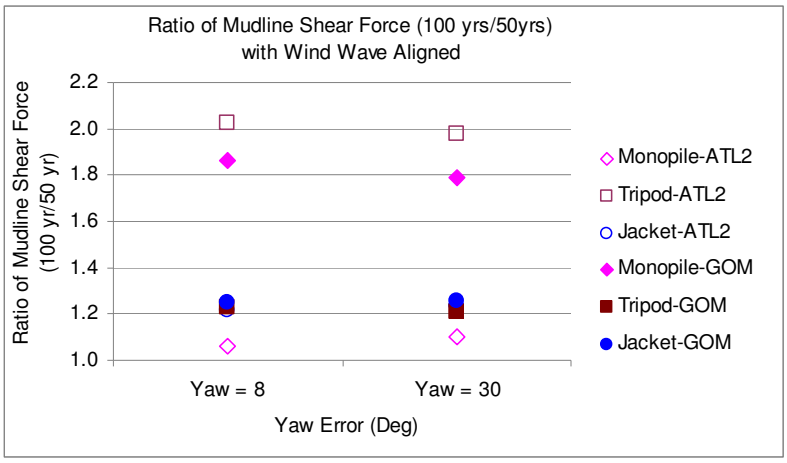

Figure 2.54 Ratio of 100-yr Return to 50-yr Return Mudline Shear Forces

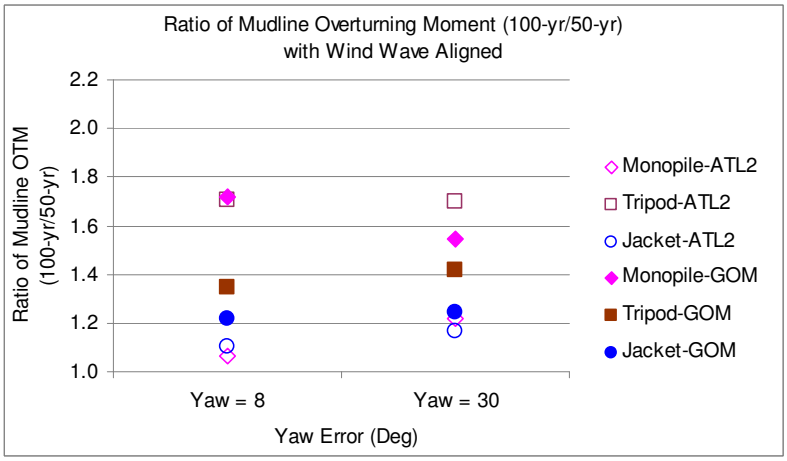

Figure 2.55 Ratio of 100-yr Return to 50-yr Return Mudline Overturning Moments

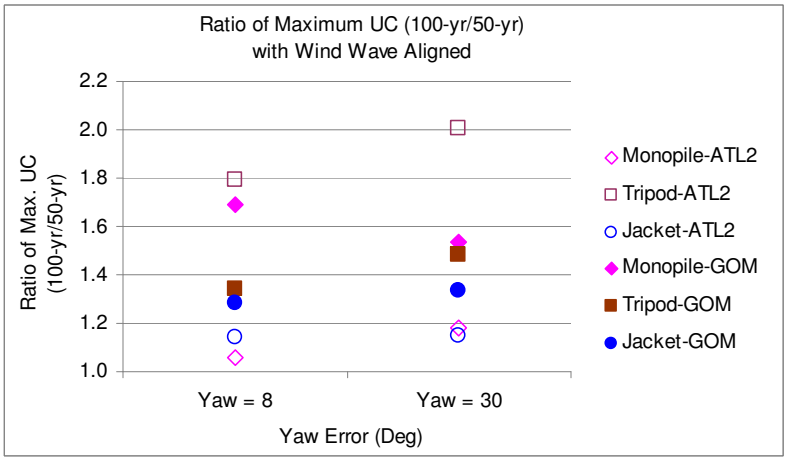

Figure 2.56 Ratio of 100-yr Return to 50-yr Return Maximum Utilization Ratios

Figure 2.57 illustrates the mudline shear forces and overturning moments for the monopile, tripod and jacket support structures in the ATL2 region. The significant increase in the mudline shear force and overturning moment in the tripod case under the 100-year return conditions is due to the wave slamming that does not occur under the 50-year return conditions. The plot also indicates that in terms of the mudline overturning moment, the monopile is the most sensitive to the yaw error while the jacket is the least.

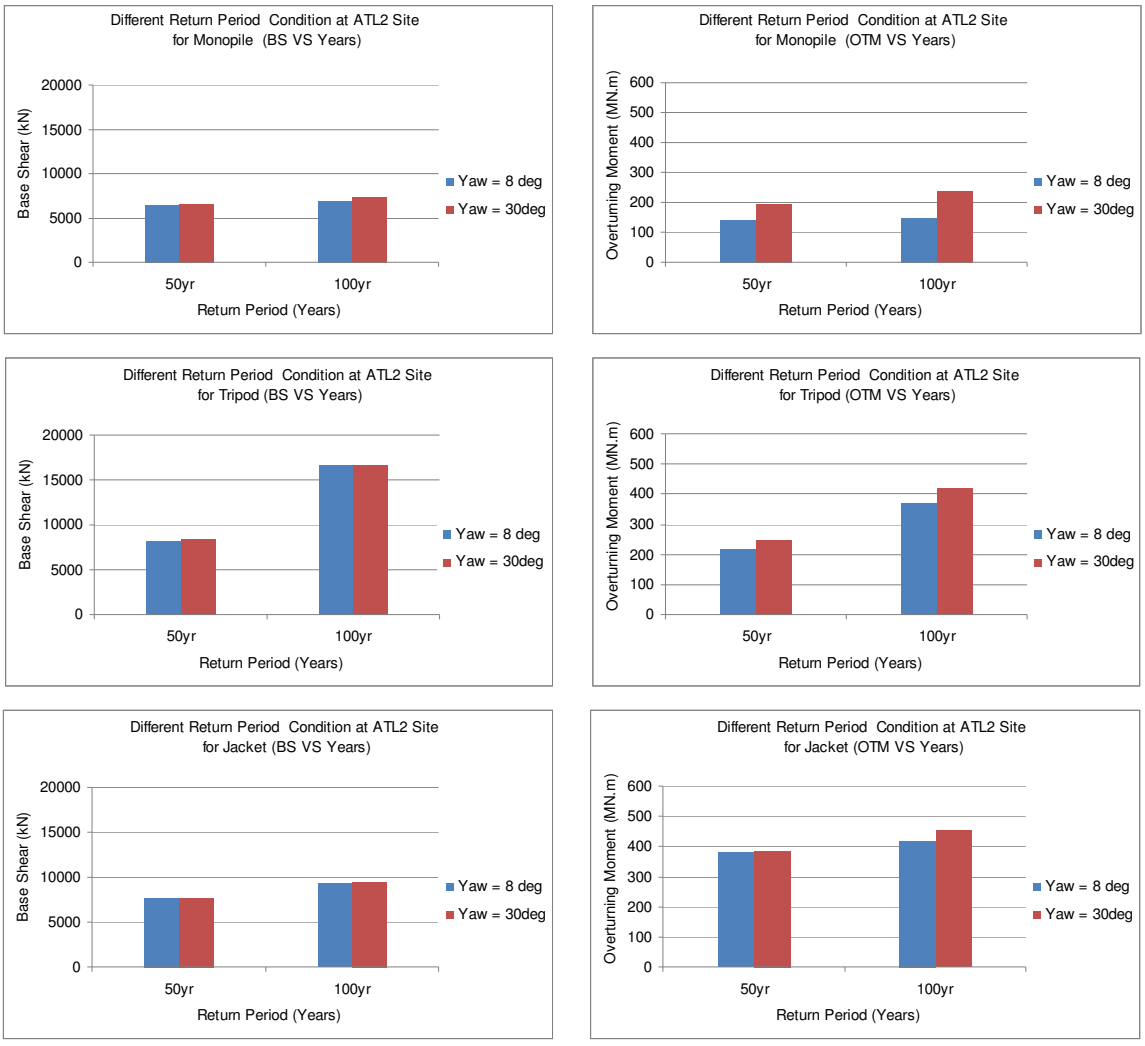

Mudline Shear Force **Mudline Overturning Moment**

Figure 2.57 Mudline Shear Forces and Overturning Moments (50-yr vs. 100-yr) in the ATL2 Region

Figure 2.58 depicts the mudline shear forces and overturning moments for the monopile, tripod and jacket support structures in the GOM region. Comparing to the mudline overturning moments plotted in Figure 2.57 for the ATL2 region, the support structures in the GOM region appear more sensitive to the return period for the case where no slamming occurs, or where slamming occurs for both 50-year and 100-year return conditions. This trend can also be seen in the Figure 2.54 through Figure 2.56. The main reason lies in the difference in the slope of the severity of environmental conditions versus the return period, or the so-call hazard curve. The GOM region is found to have a steeper slope than the ATL2 region.

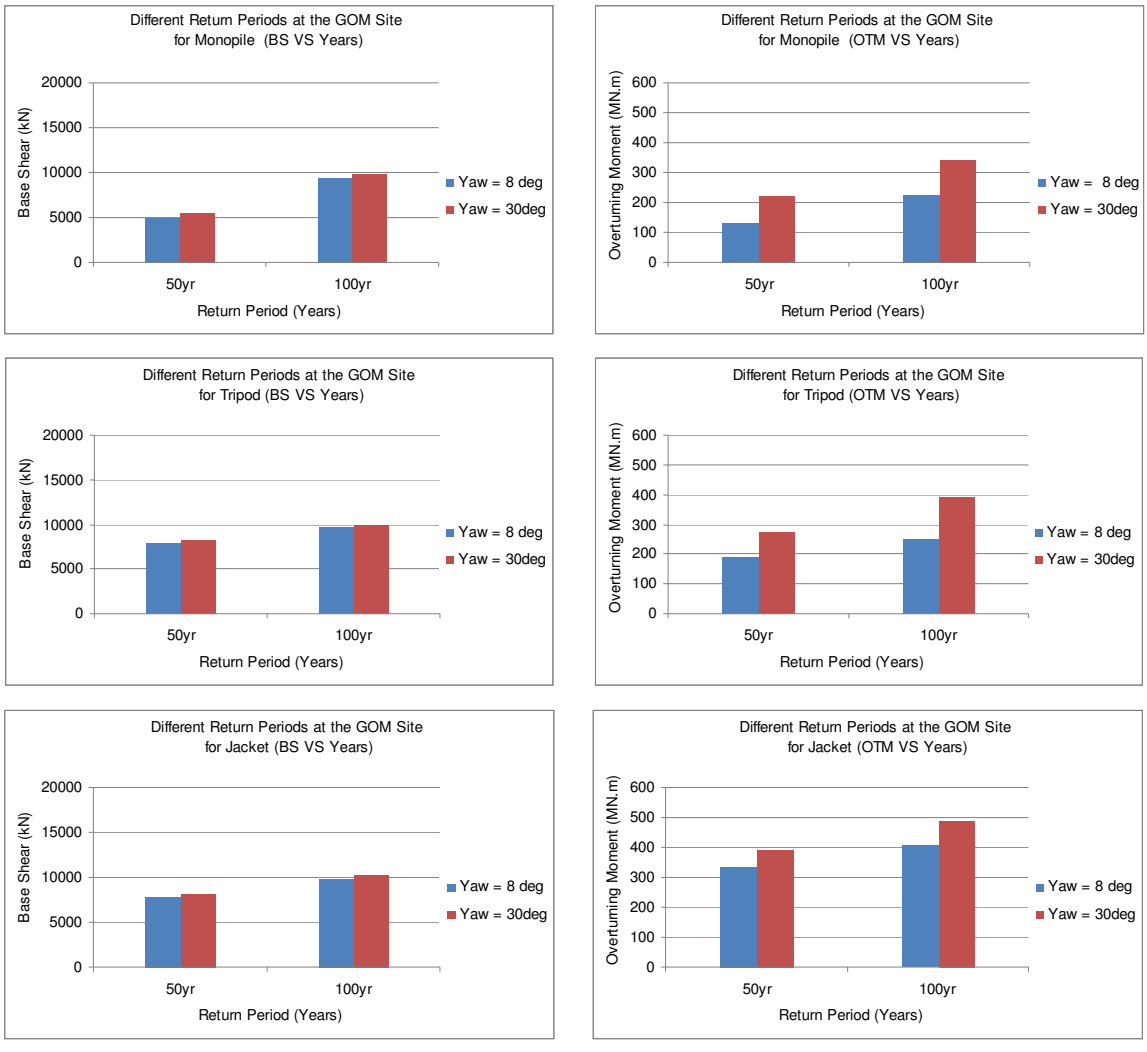

Figure 2.58 Mudline Shear Forces and Overturning Moments (50-yr vs. 100-yr) in the GOM Region

Figure 2.59 shows the maximum member utilization ratio for the monopile, tripod and jacket support structure in the ATL2 and GOM regions. Note that two different safety factors, i.e. 1.5 and 1.25 according to the ABS Guide (2011), are applied respectively to the normal turbine operating mode with the yaw misalignment of 8 degrees and the abnormal turbine operating mode with the yaw misalignment of 30 degrees. A significant increase from the 50-year return utilization ratio to the 100-year return utilization ratio can be found in the case of the tripod in the ATL2 region and the monopile in the GOM region due to the inclusion of slamming loads. An approximate 50% increase in the utilization ratio from 50-year return to 100-year return is also observed in the abnormal condition (Yaw = 30 deg) of the tripod in the GOM region, where the interaction of a strong wind and the yaw misalignment is a major cause of load increase.

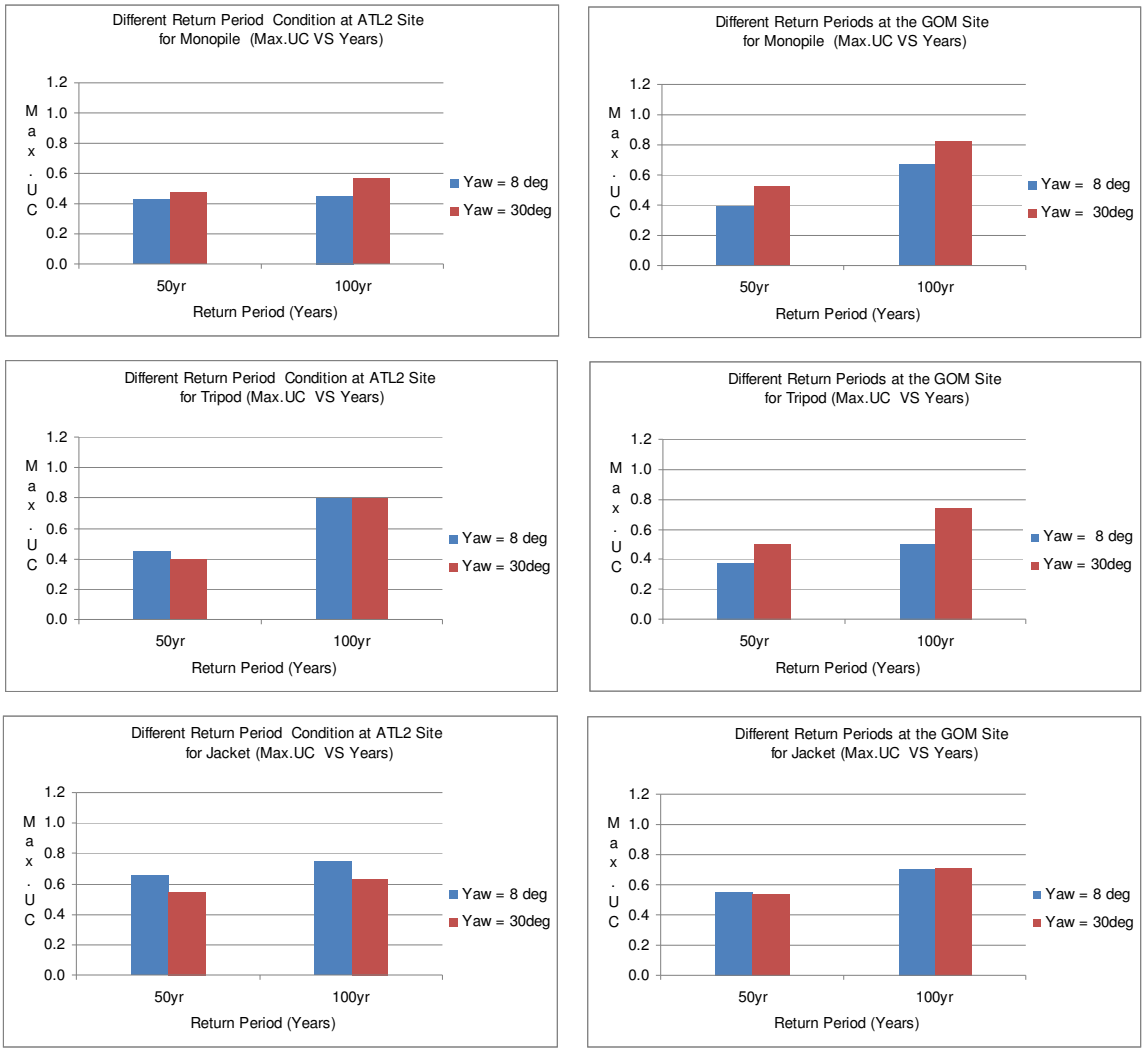

Atlantic Region 2 (ATL2) GOM West Central (GOM)

Figure 2.59 Utilization Ratios (50-yr vs. 100-yr) at the ATL2 and GOM Regions

2.9.2 Normal and Abnormal Turbine Operating Conditions

Turbine's control and safety systems play a significant role in regulating aerodynamic loads by adjusting blade pitch angle and nacelle yaw angle. This case study is focused on the effect of yaw misalignment on the global and member responses. The reference is made to Section 2.5.1 for the discussion of the effect of blade pitch locking.

Figure 2.60 reports the sensitivity of mudline shear force and overturning moment to the change of nacelle yaw misalignment when the turbine is subjected to 50-year return conditions. Figure 2.61 shows the results under 100-year return conditions.

It is shown that the mudline shear force is generally not too sensitive to yaw misalignment, regardless of the occurrence of wave slamming. It is also recalled that the result presented in Section 2.5.1 (see Figure 2.38), where only the aerodynamic loads under the 100-year return condition in the GOM West Central region is taken into account, shows the sensitivity of the mudline shear force to the yaw misalignment angle. However, the aerodynamic loads contribute only a small portion of the total mudline shear force. It is the wave load and slamming load, if applicable, that govern the mudline shear force.

For mudline overturning moment, however, aerodynamic loads play a more important role because of its acting moment arm to the mudline is much longer than that for other load types. The relative importance of aerodynamic load to the mudline overturning moment depends on the magnitude of wave-generated load, which is in turn closely tied to the type of support structure. The mudline overturning moment in response to the aerodynamic loads under the 100-year return condition in the GOM West Central region is shown in Figure 2.39. In the present case study, it is found that the hydrodynamic loads are predominant in the case of the jacket support structure, while the aerodynamic loads govern the monopile. The tripod support structure falls somewhere in between these two extremes. Figure 2.60 and Figure 2.61 further reveal that the jacket is least sensitive to the yaw misalignment while monopile shows a strong correlation. It is also found that the addition of wave slamming reduces the sensitivity of the mudline overturning moment to the yaw misalignment, while the increasing severity of hurricane environmental conditions, i.e. the higher return period, tends to amplify this sensitivity.

Figure 2.62 presents the maximum member utilization ratio for the monopile, tripod and jacket support structures. The results shown in the plot are based on the utilization check performed

using the working stress design criteria specified in the ABS Guide (2011) [2.2]. A safety factor of 1.5 is applied to the normal turbine operating mode with the yaw misalignment of 8 degrees, while 1.25 is applied to the abnormal turbine operating mode with the yaw misalignment of 30 degrees. It is shown that for the monopile support structure, the abnormal load case governs the design. For the jacket support structure, however, the normal load case prevails. The tripod support structure shows a mixed picture depending on the relative contribution from aerodynamic loads and hydrodynamic loads. Figure 2.62 appears to provide, to the extent of this study, a good justification of the strength criteria defined in the ABS Guide (2011), as the results of utilization check indicate a balanced pattern without the bias toward either normal or abnormal load cases.

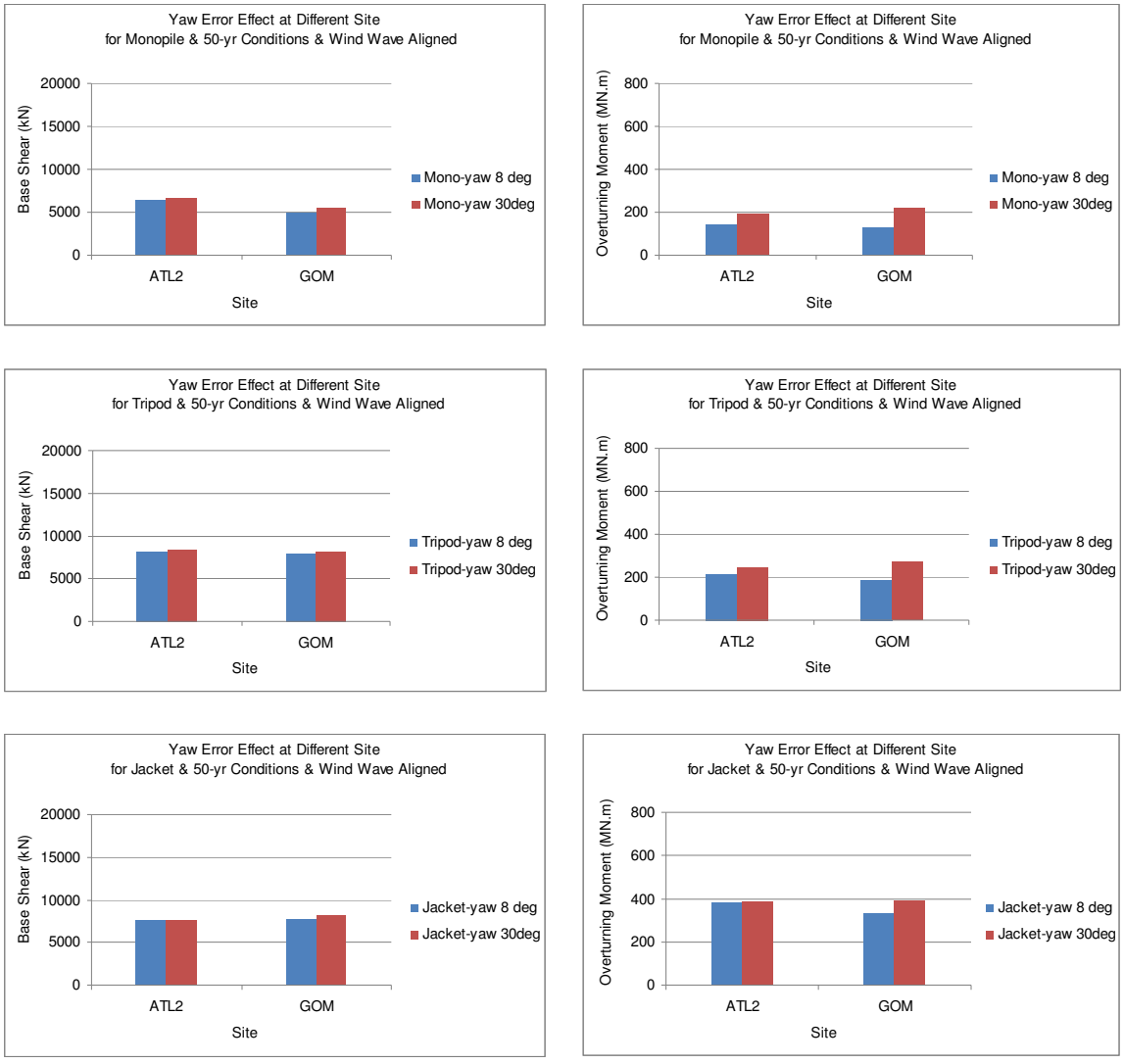

Figure 2.60 Mudline Shear Forces and Overturning Moments (Normal vs. Abnormal) under the 50-Year Return Conditions

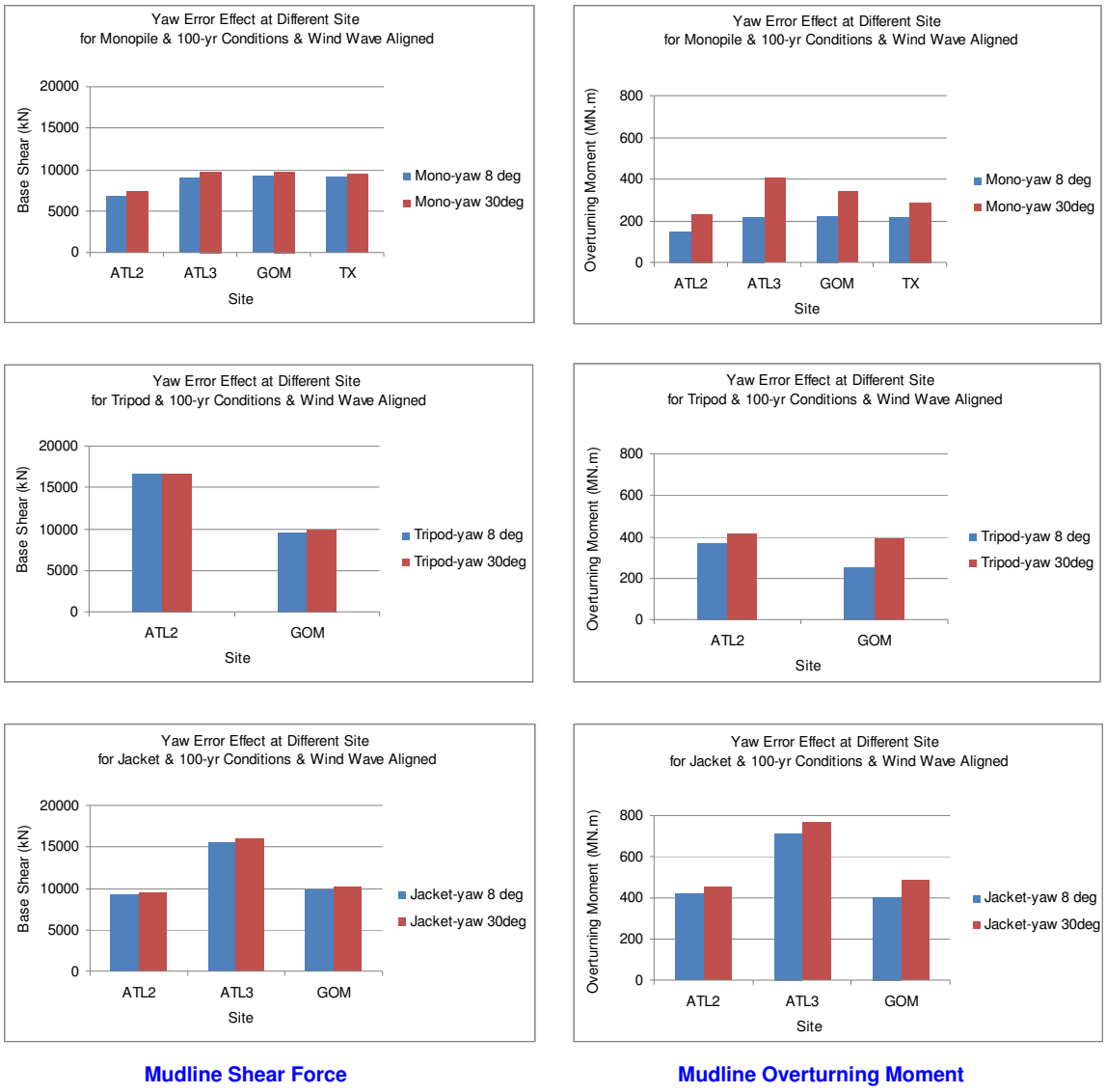

Mudline Shear Force **Mudline Overturning Moment**

Figure 2.61 Mudline Shear Forces and Overturning Moments (Normal vs. Abnormal) under the 100-Year Return Conditions

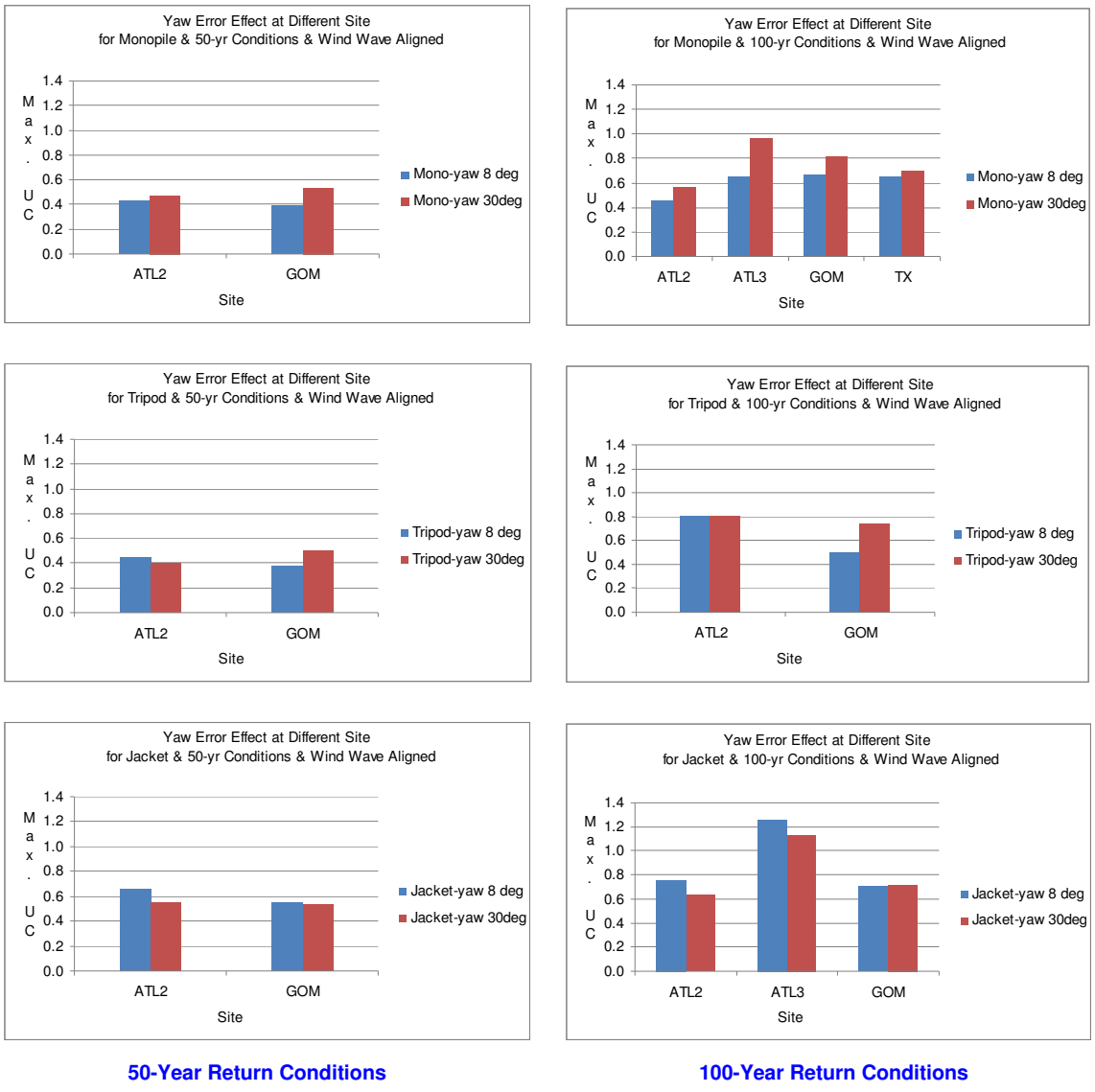

Figure 2.62 Member Utilization Ratios (Normal vs. Abnormal)

2.9.3 Wind and Wave Misalignment

The existing design guidelines typically require considering the misalignment of wave and wind directions up to ±30 degrees. As described in Section 2.1.2.2, however, waves in the region in front of the hurricane eye are roughly perpendicular to the local wind direction. The comparison made in this subsection is to assess the sensitivity of the structural responses to the misalignment between wind and wave directions.

Figure 2.63 through Figure 2.65 depict the shear forces and overturning moments at the tower base obtained from the FAST load simulation. The tower base is located above the maximum wave crest height and is defined as the interface between the turbine tower and the substructure. These tower base loads balance the aerodynamic loads and the inertia loads on the rotor nacelle assembly and the tower. It is shown that, in general, the misaligned wind and wave leads to higher tower base loads. Only for the case of the tripod under the 100-year return conditions in the ATL3 region, as shown in Figure 2.64, appears to be against this trend.

Figure 2.66 through Figure 2.68 report the 50-year and 100-year return mudline shear forces and overturning moments as well as the maximum utilization ratios calculated by the dynamic nonlinear finite element analysis. Three wind-wave misalignment angles including 0 (aligned), -30 degrees and -90 degrees are applied in the calculation. The resultant mudline shear forces and overturning moments demonstrate a consistent trend toward having the highest value under the -90-degree wind-wave misalignment. It is also found that the relative increase in the loads from the aligned case to the -30-degree misalignment case is generally larger than that from the -30-degree to the -90-degree misalignment.

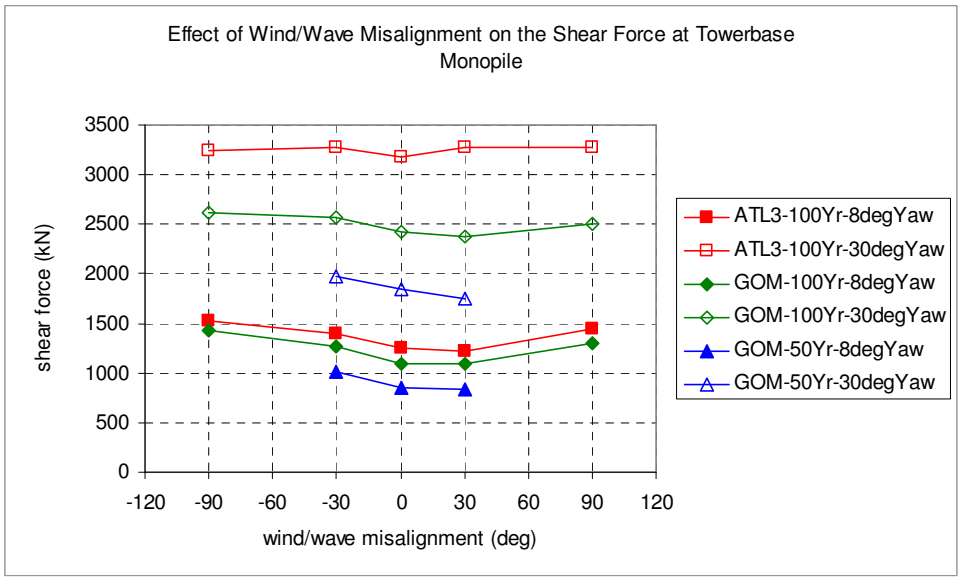

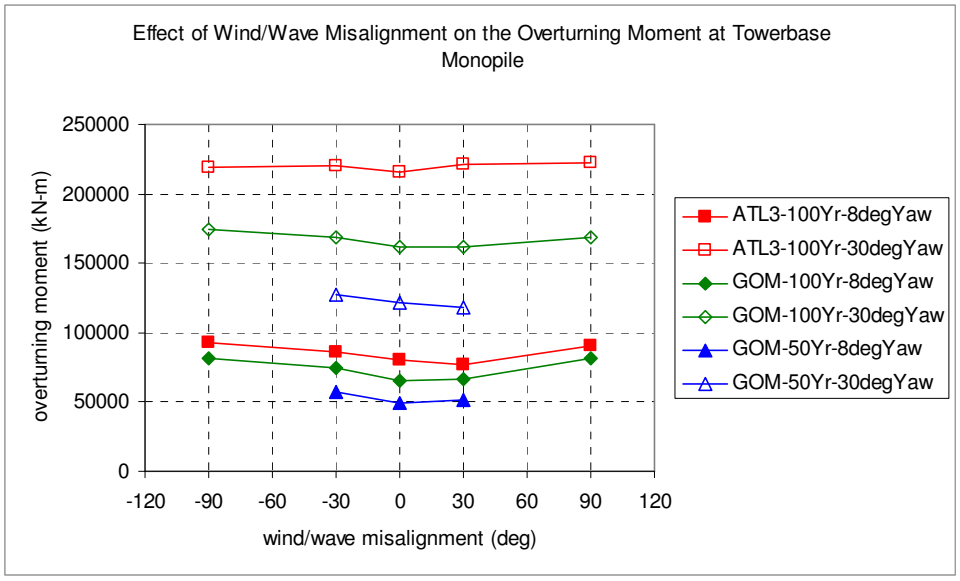

Figure 2.63 Turbine Tower Base Shear and Overturning Moment for the Monopile Case

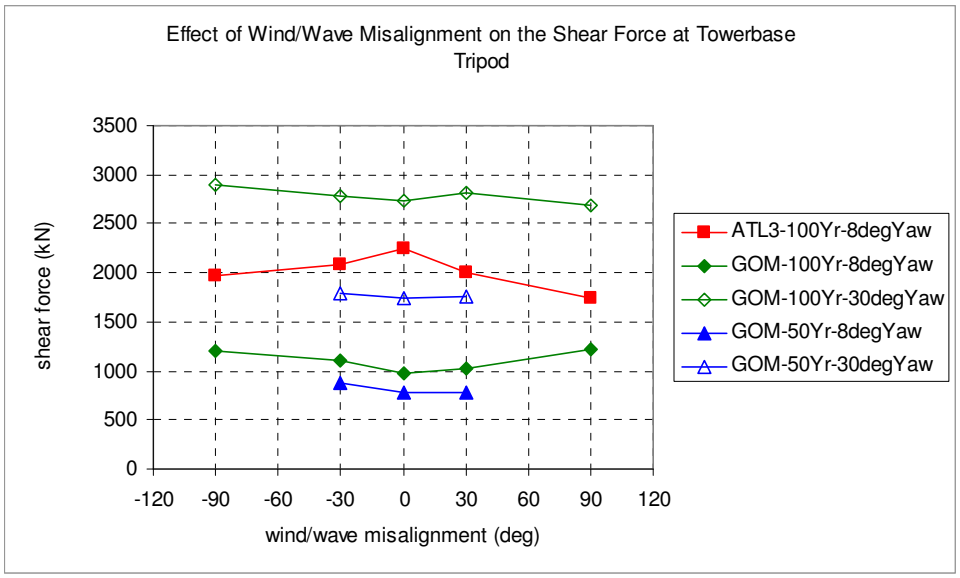

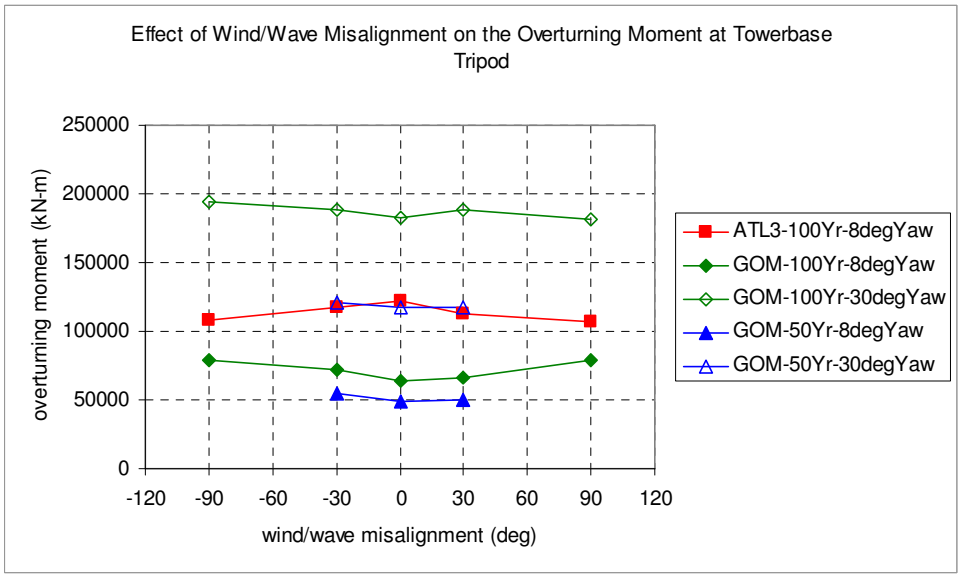

Figure 2.64 Turbine Tower Base Shear and Overturning Moment for the Tripod Case

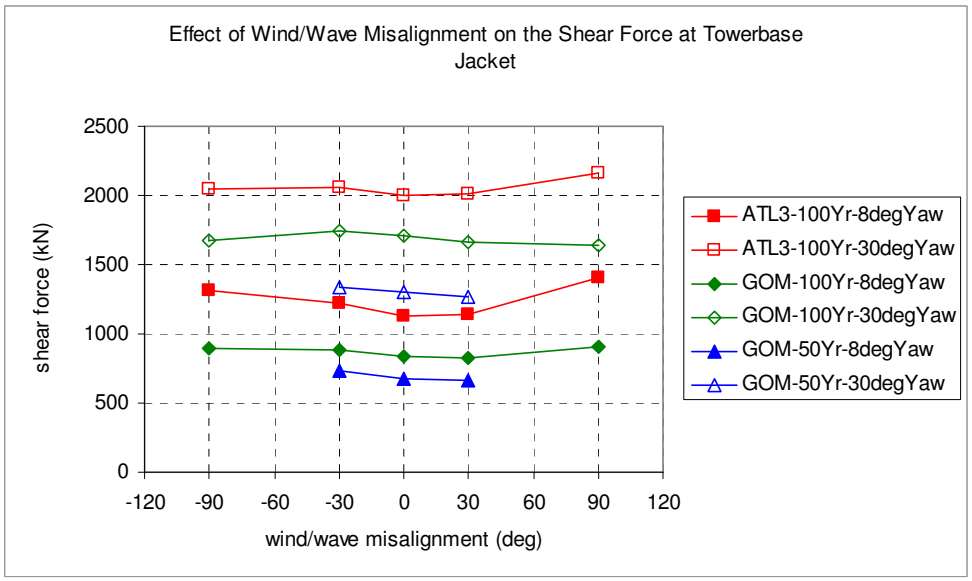

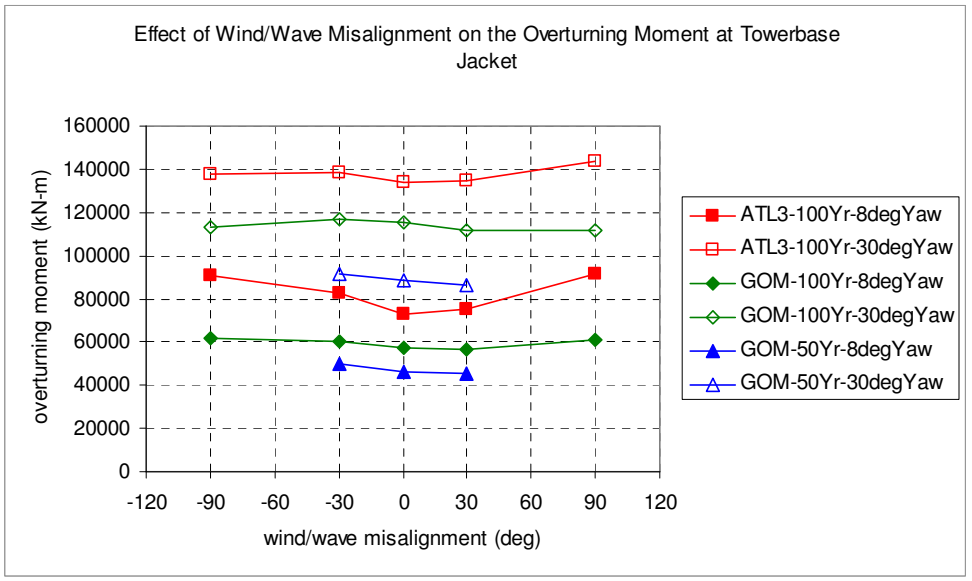

Figure 2.65 Turbine Tower Base Shear and Overturning Moment for the Jacket Case

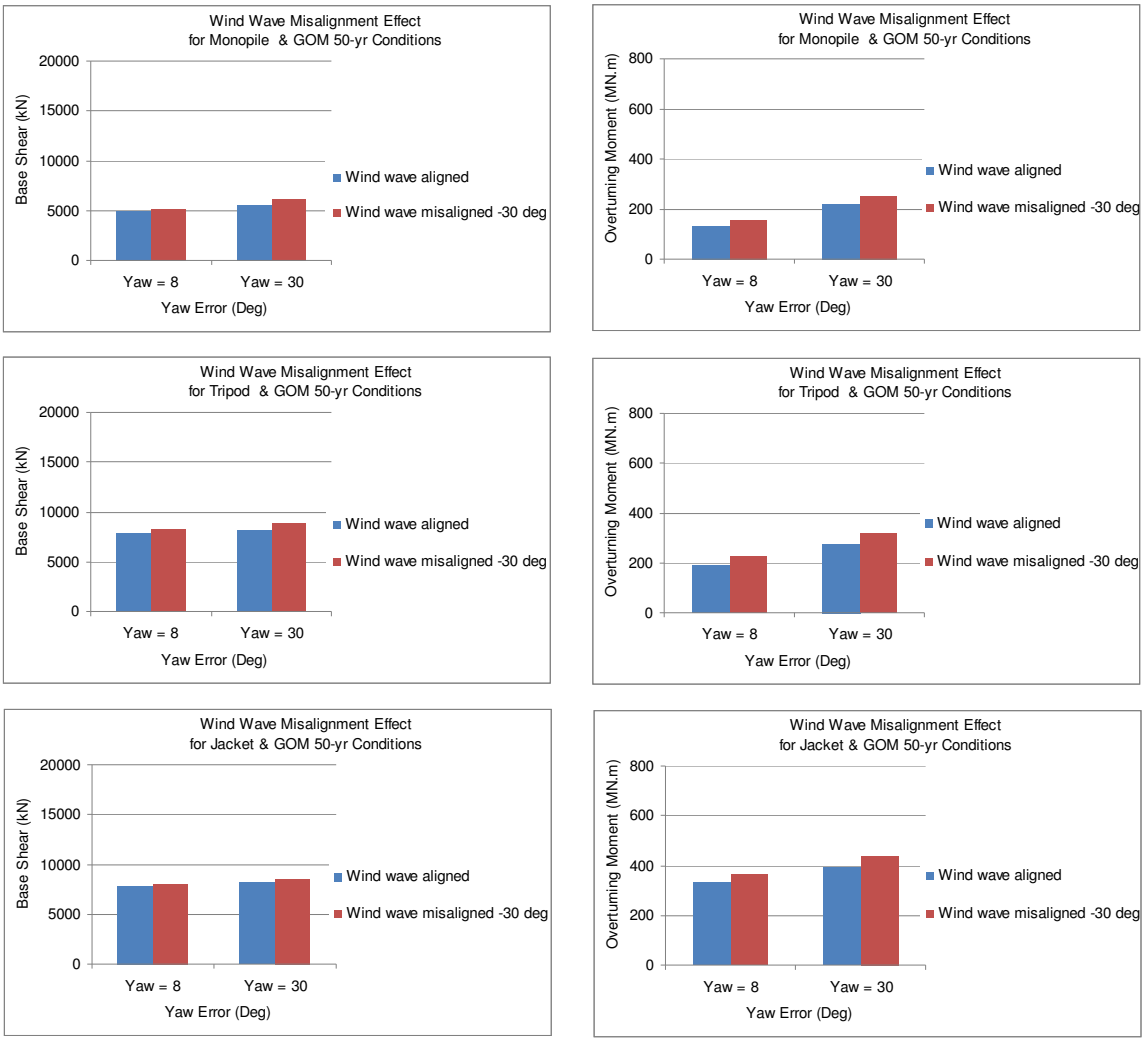

Mudline Shear Force **Mudline Overturning Moment**

Figure 2.66 Mudline Shear Forces and Overturning Moments vs. Wind-Wave Misalignment (under the 50-Year Return Conditions in the GOM West Central Region)

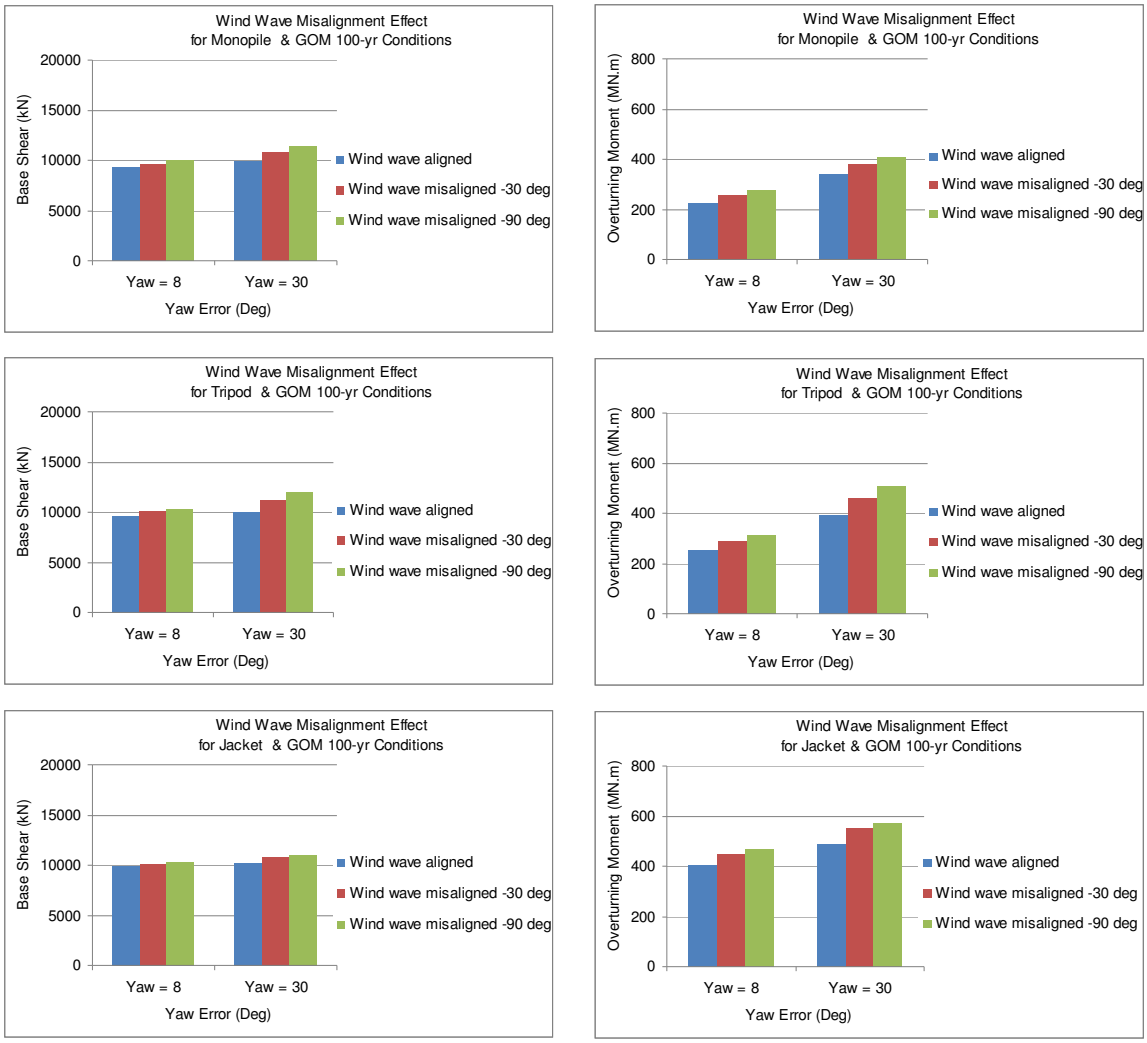

Figure 2.67 Mudline Shear Forces and Overturning Moments vs. Wind-Wave Misalignment (under the 100-Year Return Conditions in the GOM West Central Region)

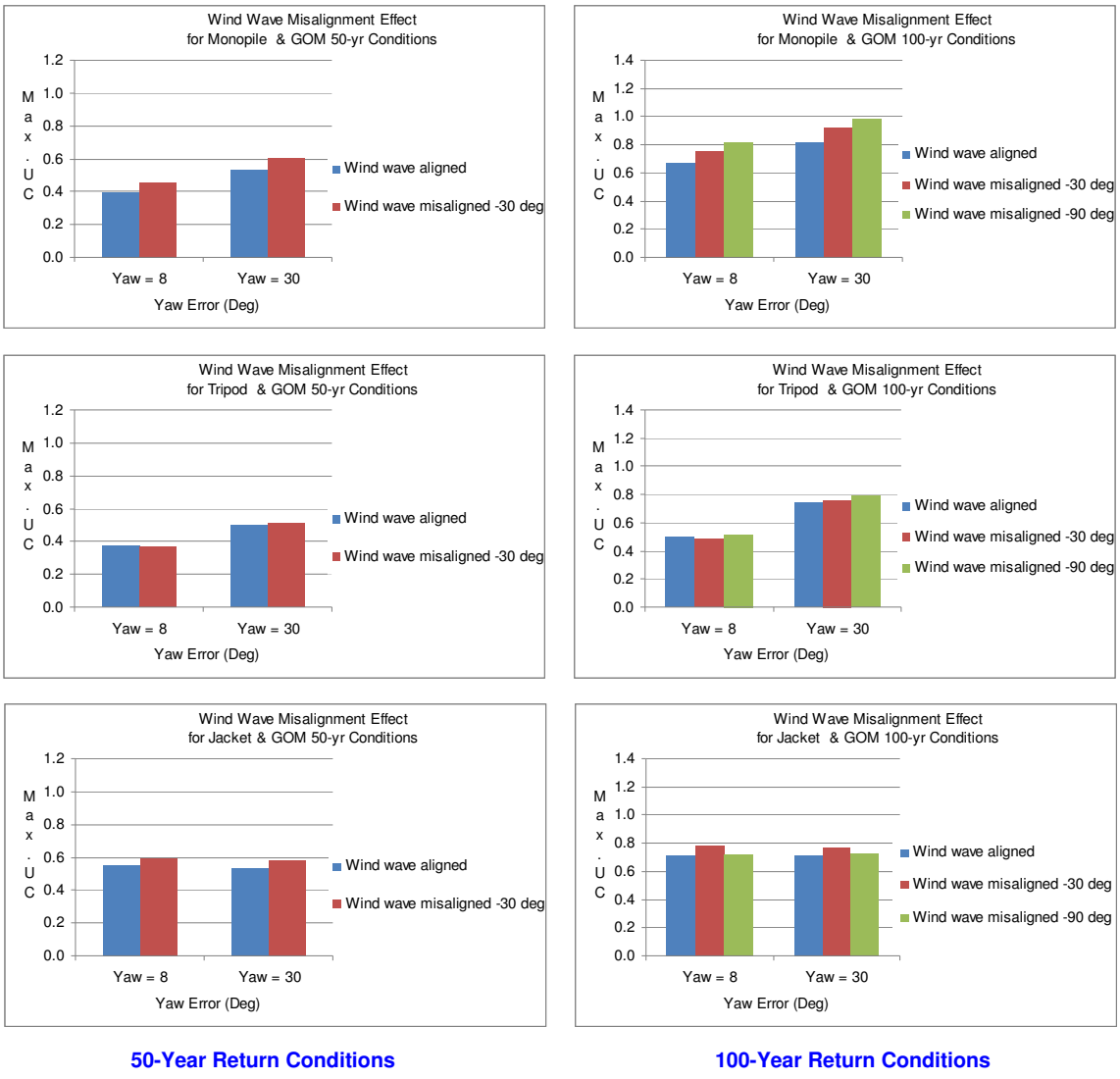

Figure 2.68 Member Utilization Ratios vs. Wind-Wave Misalignment (GOM West Central Region)

2.9.4 Type of Support Structures

The comparison is made in Figure 2.69 through Figure 2.71 of the global responses of the monopile, tripod and jacket support structures. The depth of the still water level for the monopile, tripod and jacket support structures are 13.7 m, 24 m and 47 m, respectively.

Figure 2.69 reports the mudline shear forces and overturning moments under the 50-year return and the 100-year return conditions in the ATL2 region. The following observations can be made:

- Under the 50-year return conditions, wave slamming occurs only to the monopile, where its mudline shear force is comparable to those applied to the tripod and jacket structures. As observed in Section 2.9.2, the major contributor to the mudline overturning moment is the hydrodynamic loads in the jacket case and the aerodynamic loads in the monopile case. The difference in the mudline overturning moment is also partially due to the difference in the water depth.

- Under the 100-year return conditions, wave slamming occurs to both the monopile and tripod support structures. The slamming loads exerted on the tripod generate a sharp increase in the mudline shear force and overturning moment. The mudline overturning moment becomes comparable to that of the jacket when the yaw misalignment angle is at 30 degrees, even if the water depth of the tripod case is about half of that of the jacket case. Note that the hub height is the same for both the tripod and the jacket supported turbines.

Figure 2.70 is plotted in a format similar to Figure 2.69, except that the site location is changed to the GOM region. It is found that:

- Under the 50-year return conditions, there is no wave slamming occurring to any support structure. The mudline shear force on the tripod is comparable to that on the jacket. The difference in the overturning moments on the tripod and jacket is mostly due to the effect of the water depth. Because of the lack of wave slamming, the monopile shows a lower level of mudline shear force compared to the one observed in the ATL2, even if the environmental conditions in the ATL2 are less severe than those in the GOM.

- Under the 100-year return conditions, the comparison of the mudline shear forces and overturning moments between the tripod and jacket shows a similar pattern to that under the 50-year return conditions. For the monopile, however, there is a significant increase in the

response due to the occurrence of wave slamming. The mudline shear force and overturning moment of the monopile case become comparable to those of the tripod.

Figure 2.71 compares the global responses of all three support structures subjected to the 100-year return conditions in the GOM and with the wind-wave misalignment of 0 degree (aligned), -30 degrees and -90 degrees. It is shown that

- All three support structures have the comparable level of mudline shear forces, where the wave slamming loads is taken into account for the monopile.
- With respect to the wind-wave misalignment, the comparison of mudline shear forces and overturning moment among three support structures shows a consistent pattern.

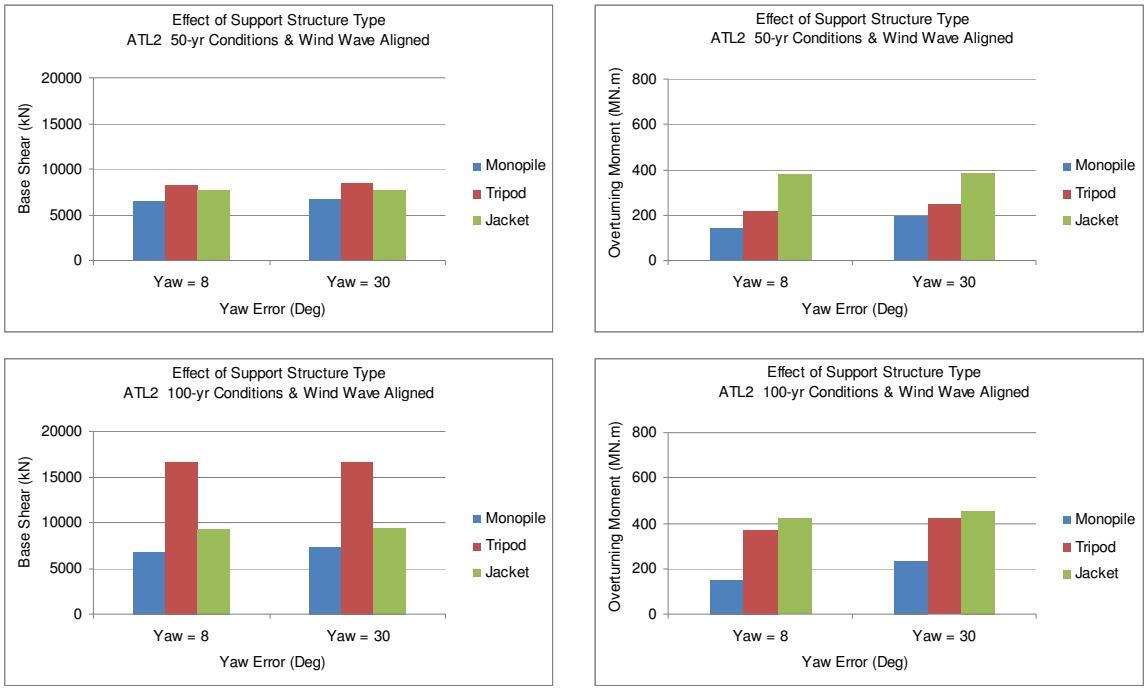

Mudline Shear Force **Mudline Overturning Moment**

Figure 2.69 Mudline Shear Forces and Overturning Moments (All Structures in ATL2)

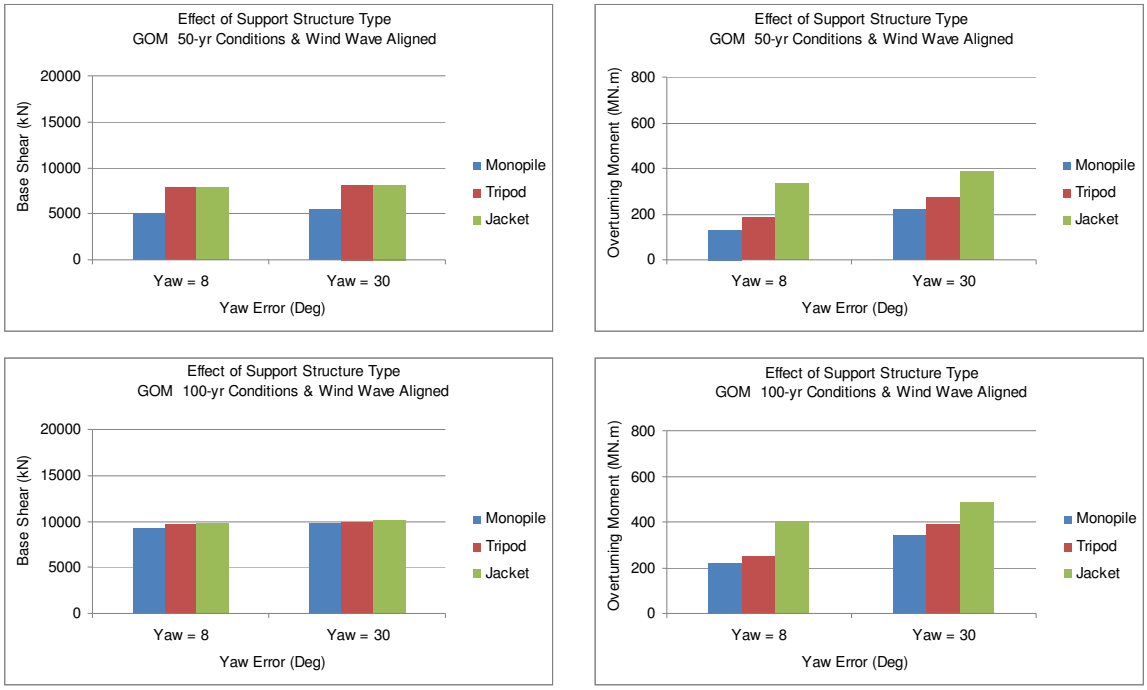

Mudline Shear Force **Mudline Overturning Moment**

Figure 2.70 Mudline Shear Forces and Overturning Moments (All Structures in GOM)

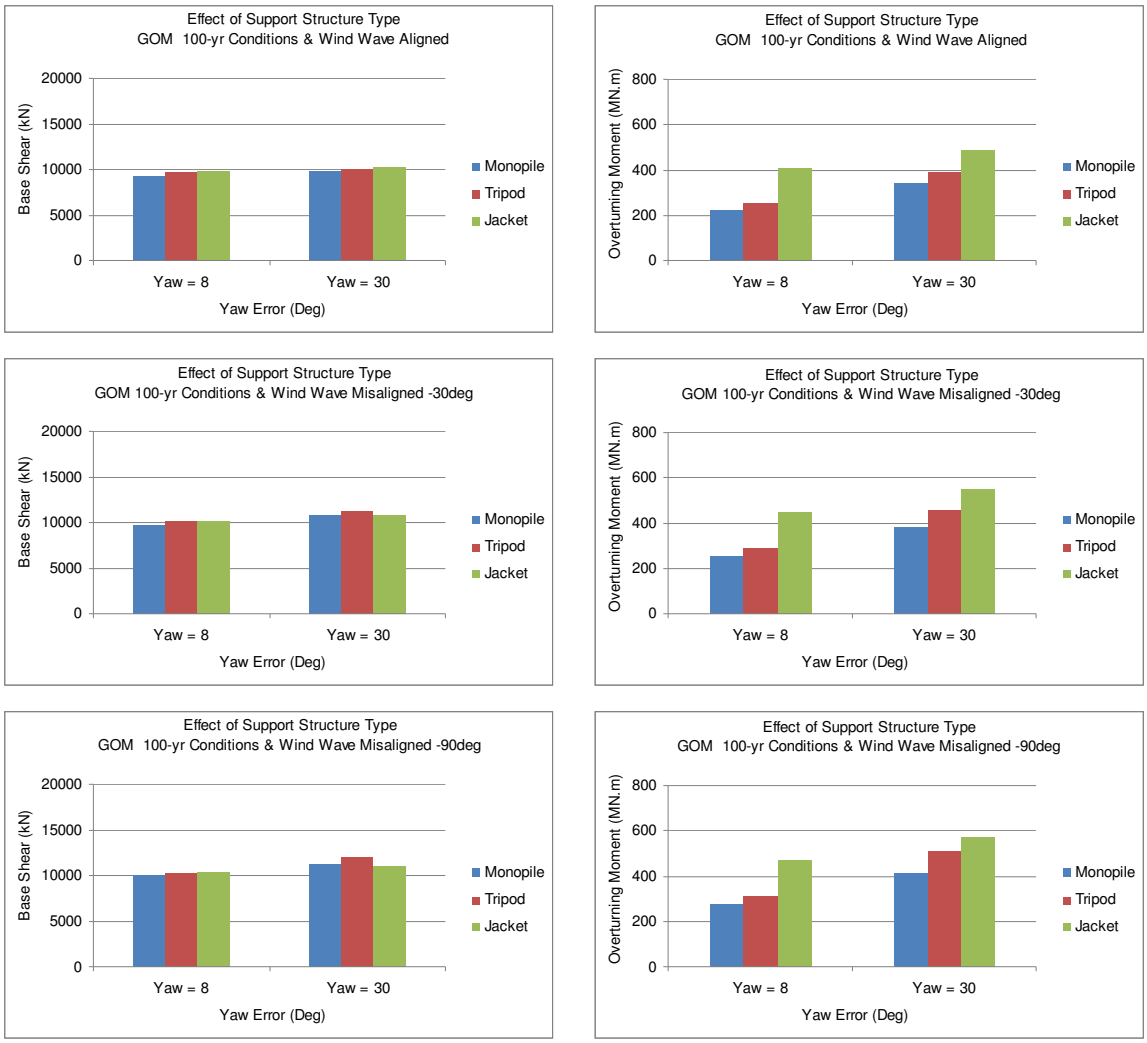

Figure 2.71 Mudline Shear Forces and Overturning Moments (All Structures under the 100-Year Return Conditions in the GOM with Various Wind-Wave Misalignments)

2.10 Conclusions and Recommendations

2.10.1 Hurricane Wind Models

The wind models recommended in IEC 61400-1 (2005) are primarily developed and calibrated using on-land wind measurements with the consideration of various terrain topologies. They are still considered applicable to a bottom-founded offshore wind farm sited in a coastal area, where onshore terrain effects can influence the characteristics of a turbulent wind field.

As observed in Section 2.4, the IEC wind model shows relatively higher power density in the high frequency range which covers the natural frequencies of bottom-founded turbine support structures and turbine blades. The API recommended wind model shows relatively lower turbulence intensity and has more energy in the lower frequency range. The API recommended model may be used for the bottom-founded support structure to be installed in "open ocean", where the effect of coastal topology and onshore roughness are negligible. The API recommended model is also believed to be a more reasonable choice for those floating support structures where low frequency responses are of great importance to the vessel stability, global motions and mooring system design.

It remains to be decided, however, as to under what condition the site location can be considered being in "open ocean". One example is given in the WMO guideline by Harper et al. 2009 [2.34], which defines that a site located beyond 20 km (12.5 miles) offshore as "at-sea", where the effect of coastal topology and onshore roughness may be assumed insignificant.

2.10.2 Design Criteria for Offshore Wind Turbines in Hurricane-Prone Regions

The state-of-the-art review and the case studies carried out in this project have identified or, in some cases, confirmed a number of unique features of offshore wind turbine responses. The following list summarizes the key findings that are critical for the development of strength design criteria for offshore wind turbines in hurricane-prone regions on the US OCS.

- The wind load generated by the aerodynamic response of turbine rotor can be a major, sometimes dominant, source of loads exerted to the support structure. The relative importance between aerodynamic loads and hydrodynamic loads to global responses is related to the type of support structures. The case studies carried out in this project show that

hydrodynamic loads are predominant in the case of the jacket support structure, while aerodynamic loads govern the global responses of the monopile. The tripod support structure behaves somewhere in between these two extremes. It is noted that the water depth can also influence the relative importance of the two load sources to the mudline overturning moment. The contribution from hydrodynamic loads to the mudline overturning moment increases with increasing water depth. On the other hand, the local responses of structural members could show a different dependence upon the two load sources. The location of an individual member in a support structure may determine its response characteristics.

- Turbine control and safety systems play a significant role in regulating the aerodynamic loads by adjusting the blade pitch angle and nacelle yaw angle. The sensitivity of the global responses of a support structure to the turbine operating modes is determined by the importance of aerodynamic loads relative to hydrodynamic loads. It is found that the addition of wave slamming reduces the sensitivity of the mudline overturning moment to the yaw misalignment, while the increasing severity of hurricane environmental conditions, i.e. the higher return period, tends to amplify this sensitivity.

- Because of the significance of turbine operating modes for the global and local structural responses, the definition of "Operating" and "Extreme" design criteria in API RP 2A-WSD (2007) using the return period of design environmental conditions is not directly applicable to offshore wind turbines. It is more appropriate to define the strength criteria based on the turbine operating modes rather than the severity of environmental conditions. Even though aerodynamic loads may not govern the global responses under certain circumstances, they may still be predominant for individual members, where the design code check equations and safety factors are to be applied.

- With the change to load modeling and the effect of wind turbine control and safety system, the slope of global loads (base shear and overturning moment) versus return period curve is different from those normally seen in the design of offshore oil and gas platforms. Applying the same design approach valid for offshore oil and gas platforms to offshore wind turbines will not result in the anticipated safety level. The case study results show that when the return period of environment condition is increased from 50 years to 100 years, the resultant global and local responses of a support structure could increase up to 100%. This is in a sharp contrast to a typical 20%~30% increase in the global responses for an offshore oil and

gas platform designed to API RP 2A-WSD (2007) in the Gulf of Mexico. According to API RP 2A-WSD (2007), 50-year return site specific environmental conditions should be used in the design of a medium consequence (L-2) platform. The actual capacity of a typical L-2 platform allows it to survive the hurricane on the US OCS with the return period higher than 100 years. The implied safety level in the IEC 61400-3 is the medium safety level, which is more or less similar to the medium consequence category defined in both API RP 2A-WSD (2007) and ISO 19902 (2007). It is expected therefore, that an offshore wind turbine support structure should at least survive a 100-year return hurricane with certain safety margins.

- Since the nominal safety margin implied in the IEC 61400-3 (2009) ultimate strength design criteria for the abnormal condition is approximately 25%, a member in an optimized support structure designed to the 50-year return extreme storm condition following IEC 61400-3 (2009) may exceed its strength capacity after up to 100% load increase from the 100-year return conditions. In other words, if the strength criteria and the design load case for extreme storms as specified in IEC 61400-3 (2007) are applied to hurricane-prone regions on the US OCS, the support structure may not be able to survive a 100-year return hurricane.

- Strong sensitivity of the structural responses to the return period of environmental conditions is found to be mainly caused by two scenarios: (1) wave slamming occurs in the 100-year return conditions, but not in 50-year return conditions, (2) nonlinear interaction between strong wind and yaw misalignment amplifies aerodynamic loads.

- Under the same extreme storm conditions with either 100-year or 50-year return, the results of member utilization check using the working stress design (WSD) strength criteria from the ABS Guide (2010) agree well with those calculated by the load and resistance design (LRFD) strength criteria specified in IEC 61400-3 (2009) in conjunction with ISO 19902 (2007). In this regard, the two sets of strength design criteria can be considered equivalent.

In order to account for the effect of the environmental conditions in hurricane-prone US waters, where the variation and, therefore, uncertainty of environmental conditions are much higher than those implied in the IEC 61400-3 (2009), the design requirement specified in IEC 61400-3 (2009) for the support structure of an offshore wind turbine has to be increased. This increased design requirement may be achieved by requiring a higher return period in the design load case, a larger safety factor in the strength design criteria, or the combination of both.

It is probably more appealing to adopt the same return period, i.e., 50 years, as required by IEC 61400-3 and increase the safety factor in the strength design criteria, with the intention to retain the existing design load case definitions in IEC 61400-3. However, the case study results reported in Section 2.9 indicate that the member utilization ratio could increase by anywhere from 5% to 100% when the return period of environmental conditions in the selected hurricane-prone regions on the US OCS is changed from 50 years to 100 years. This implies that in order to design an offshore wind turbine support structure that can survive a 100-year return storm, the load factor defined in IEC 61400-3 may need to be doubled. The problem is that enforcing a single safety factor for the entire US OCS would result in an over-stringent requirement to areas with fewer risks imposed by hurricanes or breaking wave slamming.

There is also a possibility of developing the regional safety factors such that the regional variations can be taken into account and therefore the conservativeness of applying a single safety factor can be reduced. However, this approach requires a significant amount of research to address the effect of the variations in regional environmental conditions, configurations of wind turbine support structure and foundation properties. To make the situation even more complex, the load factors in IEC 61400-3 (2009) are specified for the normal, abnormal and transportation/installation conditions, which are defined using the combination of turbine operating modes and external conditions.

An alternative approach is to increase the return period of extreme storm condition in the definition of design load cases.

- Previous studies as discussed in Section 2.1.4 have shown that applying the load factors specified in IEC 61400-3 (2009) in combination with the 100-year storm conditions in hurricane-prone regions on the US OCS can generate a design having the approximately same safety level as that of offshore wind turbines designed to IEC61400-3 and for the North Sea metocean conditions.

- Site variation of the occurrence probability of hurricane and breaking wave slamming can be taken into account by requiring the use of site-specific 100-year return environmental conditions in the design. The principle of “the higher the risk, the higher the safety margin” is achieved by increasing the return period from 50 years to 100 years.

- One argument often used to against using the 100-year return storm conditions is that it is currently not considered as a common practice of turbine manufacturers. There is a possibility, however, that the existing IEC61400-1 Class S could be refined to cover the change of return period. Note further that the increase in the load factor or safety factor as discussed above will also lead to the change of turbine design requirements, and therefore, the definition of standard turbine classes in IEC 61400-1, even if the 50-year return period is retained.

2.10.3 Recommendations

In summary, the recommended strength design criteria for the extreme storm conditions for a bottom-founded offshore wind turbine support structure to be deployed in hurricane-prone regions should include the following elements:

- The return period of site specific design environmental conditions should be 100 years.

- The difference between the normal and abnormal turbine operating conditions should be taken into account in the strength design criteria. Either LRFD strength criteria, as specified in IEC 61400-3 (2009) in conjunction with ISO 19902 (2007), or the WSD strength criteria, as specified in the ABS Guide (2010), may be applied.

- Wind models recommended in IEC 61400-1 (2005) should be used to generate the turbulent wind field as the input to aerodynamic load calculations. For those offshore wind turbines to be deployed in the open ocean with the minimum effect of coastal topology and onshore roughness, the wind model recommended in API Bulletin 2INT-MET (2007) and API RP 2A-WSD (2007) may be used as an alternative.

- Wind and wave misalignment should be considered within the range between -90 degrees and +90 degrees. Load calculations should be based on the misalignment angle that results in the highest load acting on the support structure.

- Both negative and positive storm surge should be considered in the design, particularly for those minimum support structures, such as monopiles and tripods. The negative storm surge increases the hub height wind speed and thus the aerodynamic loads. A negative storm surge

also increases the likelihood of wave breaking, hence slamming. The wave theory employed in the design should reflect the effect of water depth.

- Effect of the nacelle yaw misalignment relative to the incoming wind direction should be adequately considered in the design, particularly for those minimum support structures such as monopiles and tripods. In general, the yaw misalignment between -180 degrees and +180 degrees in combination with 100-year return site conditions should be considered as one of the abnormal load cases in the design. Load calculations should be based on the misalignment angle that results in the highest load acting on the support structure. The contribution of active or passive yaw control system may be taken into account in order to reduce the range of the yaw misalignment considered in the design, provided that the effectiveness of yaw control system at the intended site can be justified and an appropriate monitoring and maintenance program is implemented to maintain the effectiveness of the yaw control system during the service life of an offshore wind turbine. It may not be warranted to rely solely on a back-up power supply with a minimum capacity of 6 hours, as per IEC 61400-3 (2009), to mitigate the effect of yaw misalignment during a hurricane, particularly for the area that prolonged black-out could occur during and after a major hurricane.

- The aerodynamic loads generated by a wind turbine subjected to strong hurricane wind conditions should be determined by using recognized simulation software. If such a reliable source was not available, the Design Standard would have to specifically address the need to verify and calibrate such software for each design project.

3 Breaking Wave Slamming Loads

The main objectives of this task are to:

- Study the existing design method for offshore wind turbine support structures subjected to breaking wave slamming
- Evaluate the critical parameters governing the breaking wave slamming load
- Provide recommendations on the breaking wave load calculation for offshore wind turbines

Wave slamming, also called wave impact, remains a challenging technical area even though it has been studied for over 80 years since von Karman's pioneering work in 1920s [3.91]. Theoretically, the difficulty is due to the singularity of pressure and fluid velocity near the waterfront of the wetted surface. The pressure caused by wave slamming is also highly localized, non-stationary and time dependent. The duration of wave slamming typically lasts for about ten to several hundred milliseconds. It is therefore very difficult to have a consistent measurement of local slamming pressure. Experimental results of slamming pressures reported in the literature show significant scattering. The data scattering may be caused by different experimental setups, different numerical or theoretical models and the inherent uncertainties of slamming. Other characteristics, including air bubble, trapped air, acoustics, and nonlinearity and asymmetry of waves in shallow water, make the problem even more complicated.

Significant amount of research has been undertaken over the years on various subjects relevant to the wave slamming. It has been found that the wave slamming load is proportional to the square of slamming velocity of fluid particles hitting a structure's surface. Since breaking waves have the highest free surface water particle velocity compared to non-breaking and broken waves, they represent the most unfavorable wave slamming scenario that needs to be considered in design.

This study is aimed to evaluate the existing design methods and perform comparative studies using the published analytical slamming load models. Based on the results of the literature review and numerical analyses, recommendations are made on the design of circular cylinders subjected to the breaking wave slamming load. A circular cylinder can be either a slender tubular member or a large diameter circular pile or column.

The state-of-the-art review is reported in Section 3.1, where a number of analytical and numerical slamming load models as well as slamming experiments are discussed. Section 3.2 discusses the relative importance of various parameters that affect the calculation of wave slamming force. Section 3.3 presents the parametric analysis of four representative analytical slamming models. Dynamic finite element analyses are performed to examine the responses of a typical monopile support structure subjected to the wave slamming forces estimated using different models. The combined effect of soil conditions and structural damping ratio is evaluated. Section 3.4 provides the recommended approaches for calculating wave slamming forces on turbine structural members.

3.1 State-of-the-Art Review

The state-of-the-art review is carried out with the focus on the following topics:

- Mechanism of wave breaking
- Theoretical models, numerical simulation methods, experimental results and practical design guidelines relevant to breaking wave slamming loads

3.1.1 Breaking Waves

3.1.1.1 Wave Breaking Probability

Since the wave breaking is a strongly nonlinear process, the knowledge of wave breaking and its occurrence probability is mainly empirical. Reasonably consistent theoretical and phenomenological models have been developed and verified by field and laboratory measurements. A large number of publications do exist on breaking waves in both deep and shallow water. Only those published works that are relevant to the objectives of the present study are reviewed in this subsection. More literature can be found in the papers reviewed in this report. Among the issues emphasized in the present study is the increased percentage of wave breaking in shallow water.

An early study on the wave breaking in periodic waves dates back to Stokes. For wave breaking in irregular (random) waves, Battjes and Janssen (1978) [3.8] present a frequently referenced

work on the physical mechanisms of wave breaking and wave height dissipation in coastal areas. This theory is further developed by Thornton and Guza (1983) [3.87], who also present the shallow water field data on the Californian coast, where the measurements show a rapid depth-dependent increase in the percentage of breaking waves. It is found that the percentage of breaking waves in the measured data changes from about 10% in the deepest location to approximately 60% in the shallowest location. The predictions from the theoretical model described in the paper agree quite well with the field data. It is shown that asymptotically their formula predicts 100% breaking in very shallow conditions.

By extending their earlier work on the wave breaking in deep water (Banner et al., 2000 [3.7]), Babanin et al. (2001) [3.6] develop a different approach for predicting wave breaking in waters of constant depth. A common approach for the two depth ranges is developed by introducing a unified depth-dependent parameter. Data measured in the shallow water area of Australian Lake George show a good agreement with those predicted using the proposed approach. The authors also confirm the observations made by Thornton and Guza (1983) [3.87] that the maximum probability of breaking increases from about 10% in deep water to up to 60% in the shallowest conditions. This unified approach is developed further by Filipot et al. (2010) [3.31].

The probability of wave breaking for a specified water depth is also derived by Ochi (2003) [3.67], where the breaking point is defined as the moment when both the probability of breaking and the spectrum energy loss ratio reaches at least 0.1.

Several authors have studied the limiting wave height at a given water depth, among which Massel (1998) [3.59] provides a thorough review of various approaches and experimental data. In particular, an approach defining the breaking criterion using the maximum vertical fluid particle acceleration is explored. It is concluded that the ratio of maximum wave height H_{max} to the water depth d, H_{max}/d, should be 0.55. Other studies have indicated both lower and higher values than 0.55. The work has been followed up in e.g. Massel (2007) [3.60]. Further discussion is given in Section 3.2.3.2.

The relevance of the sea state steepness to the breaking wave slamming is studied by Stansberg (2011a) [3.80], where the results obtained from semisubmersible model tests in different sea states in deep water are compared. A sea state parameter is defined using a combination of the wave energy and steepness. A probabilistic analysis of the measurements shows that the local maximum slamming forces on a circular cylinder correlate fairly well with this parameter.

3.1.1.2 Breaking Wave Types

Breaking waves are typically classified into three different types including spilling, plunging, and surging breaking waves.

In spilling-type breaking waves, the wave crest is unstable and cascades down the wave front face, producing a foamy water surface. Spilling breaking waves normally occur on beaches with gentle slopes.

In plunging-type breaking waves, the crest curls over and forms a tunnel till it breaks and falls into the base of the wave. Plunging breaking waves normally occur where the slope of sea floor is moderately steep.

In surging breakers, the crest remains intact while the front face of the wave rolls onto the steep beach with minor breaking. Surging breaking waves normally occur on the beach where the sea floor slope is very steep.

Another type of breaking waves as referred in the Costal Engineering Manual (2008) [3.89] is the collapsing breaking waves. The crest of a collapsing breaking wave remains intact while the lower part of the wave front collapses and produces a highly turbulent water surface.

It has been found that the breaking wave type is correlated to the surf similarity parameter ξ_o, where ξ_o is a function of sea floor slope α and the square root of the wave steepness in deep water condition. An alternative definition of the surf similarity parameter, denoted as ξ_b, is referred in IEC 61400-3 (2009) [3.40], where ξ_b, is related to the breaking wave height.

$$\xi_0 = \frac{\tan\alpha}{\sqrt{H_0/L_0}} \quad \text{and} \quad \xi_b = \frac{\tan\alpha}{\sqrt{H_b/L_0}} \tag{3.1}$$

where H_0 denotes the wave height under the deep water condition; L_0 is the wave length under the deep water condition; H_b is the breaking wave height.

Table 3.1 shows the definition of breaking wave type according to IEC 61400-3 (2009) [3.40]. Costal Engineering Manual (2008) [3.89] published by the U.S. Army Corps of Engineers uses a slightly different threshold value, i.e. 0.5 instead of 0.45, to differentiate the spilling and plunging types of breaking waves.

It should be noted that Table 3.1 does not take into account the influence of the presence of structures, which may also affect the occurrence and type of breaking waves.

Table 3.1 Breaking Wave Types

Spilling	*Plunging*	*Surging*
$\xi_o < 0.45$	$0.45 < \xi_o < 3.3$	$3.3 < \xi_o$
$\xi_b < 0.4$	$0.4 < \xi_b < 2.0$	$2.0 < \xi_b$
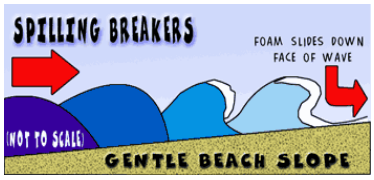	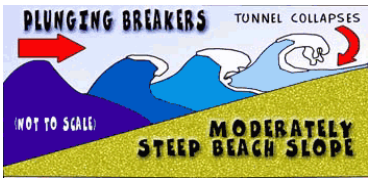	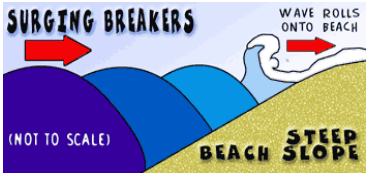

Note: The schematic plots of breaking waves are adapted from http://www.onr.navy.mil/focus/ocean/motion/waves2.htm

In general, the forces exerted by spilling and surging breaking wave can be approximated as quasi-static loads. It is the plunging breaking waves that can generate shock pressures with very high magnitude under certain conditions (IEC 61400-3, 2009 [3.40]; Costal Engineering Manual, 2008 [3.89]; Hubbell and Kulhawy, 1982 [3.38]; Wienke and Oumeraci, 2005) [3.98].

The large-scale model test conducted by Wienke (2001) [3.99] examine various wave breaking locations relative to the circular cylinder. It is observed that the plunging breaking wave occurring right in front of the circular cylinder generates the highest slamming forces.

For an undisturbed plunging breaking wave, the wave slamming force is an impulsive shock load. In less idealized ocean environments, however, various factors such as the three-dimensional shape of the sea surface, wave irregularities, the compressibility of air trapped between the structural member and free surface, the compressibility of water at beginning of slamming, the air bubbles near the free surface, and the size, shape and slope of surface subjected to slamming, may influence the intensity and time history of slamming force.

3.1.2 Analytical Slamming Load Models

The wave force on a slender cylinder can be described in the following equation:

$$F = F_D + F_I + F_S \tag{3.2}$$

where F is the hydrodynamic force vector per unit length along the member and normal to the axis of the member; F_D denotes the drag force vector per unit length; F_I denotes the inertia force vector per unit length, while F_S stands for the wave slamming force per unit length when wave slamming occurs.

The quasi-static force varies in time along with the water surface elevation. It is normally calculated by the Morison equation (Morison et al., 1950 [3.64] and Chakrabarti, 1987 [3.13]), while the slamming force is described by either von Karman (von Karman, 1929 [3.91]) or Wagner (Wagner, 1932 [3.92]) type of approach. The wave slamming force, also called the wave impact force, acts for a very short time relative to the wave period.

3.1.2.1 Morison Equation

The Morison equation describes the total wave force as the sum of the quasi-static inertial force and the drag force per unit length. The inertia force is assumed to be proportional to the fluid acceleration relative to the structural member. The drag force depends on the square of the fluid velocity relative to the structural member. The inertia and drag coefficients, which have to be empirically determined, are dependent on many parameters such as the Reynolds and Keulegan-Carpenter numbers, surface roughness ratio, structural configuration, etc. Reference is made to API RP 2A-WSD (2007) [3.3] for the recommended values of inertia and drag coefficients for the US OCS. The total force is determined by integrating the forces per unit length along the length of the cylinder.

For structures composed of members whose diameters are greater than 20% of the considered wave length or for structural configurations that may substantially alter the incident flow field, diffraction forces and the hydrodynamic interaction among structural members should be taken into account. In this case, the Morison equation is no longer valid. In order to calculate wave diffraction effects around a single circular cylinder, the solution provided by MacCamy and Fuchs (1954) [3.54], which is also discussed in IEC 61400-3 (2009) [3.40], may be used.

Some of the studies, especially among the earlier ones, focused on the global "quasi-static" wave slamming force defined within the framework of the Morison equation, disregarding rapidly varying dynamic slamming load components. The wave slamming load is approximated by an additional drag and in some cases inertia coefficients in the Morison equation. See NORSOK N-003 (2007) [3.65] and Sarpkaya (1978) [3.74] for examples. The drag and inertia coefficients are empirically derived by fitting measured data with the consideration of the dynamic amplification of structural member excited by wave slamming. Although this approach represents the simplest method to calculate the wave slamming load on a slender cylinder, its shortcoming is obvious because the fitted coefficients are associated with the dynamic characteristics of specific types of structure and therefore have to be used with cautions for general applications.

3.1.2.2 von Karman Type Slamming Load Models

One of the first attempts to solve for the slamming force on a body entering into water is performed by von Karman (1929) [3.91]. Since the complete hydrodynamic problem is very complex to solve, approximations must be made. In von Karman type slamming models, the airflow is considered not significant. Further, the effects of viscosity and surface tension are also negligible so that the irrotational flow of incompressible water can be assumed. Since the local flow acceleration is predominant relative to the gravitational acceleration when slamming occurs, gravity is also neglected. The total slamming force can then be written as:

$$F_S = \frac{dA}{dt}V \tag{3.3}$$

where A is the infinite-frequency added mass coefficient of the body in the slamming direction, while V is the relative velocity between water and the body. The value of A depends on the level of submergence. In the two dimensional case, the added mass calculation for the circular cylinder is simplified as a flat plate case, which yields:

$$A = \rho\frac{\pi}{2}c^2 \tag{3.4}$$

The length of c is measured between the two intersection points of the cylinder and the still water level (see Figure 3.1). By geometry it follows that:

$$c^2(t) = 2RVt - V^2t^2 \tag{3.5}$$

where R is the cylinder radius and the velocity V is assumed to be constant. This gives the following slamming force per unit length:

$$f_S = V\rho\frac{\pi}{2}\frac{dc^2(t)}{dt} = \pi\rho RV^2\left(1-\frac{V}{R}t\right) \tag{3.6}$$

where ρ is the water volume density. Since the wetted length c is defined from the still water level, von Karman type of methods neglect the so-called pile-up effect, i.e. the raise of the free surface elevation due to slamming.

By defining a slamming coefficient C_s, the above equation can be restated as follows:

$$f_S = \rho C_s RV^2 \quad \text{and} \quad C_s = \pi\left(1-\frac{V}{R}t\right) \tag{3.7}$$

The upper bound of slamming coefficient $C_s = \pi$ occurs at the moment when the cylinder hits the calm water surface.

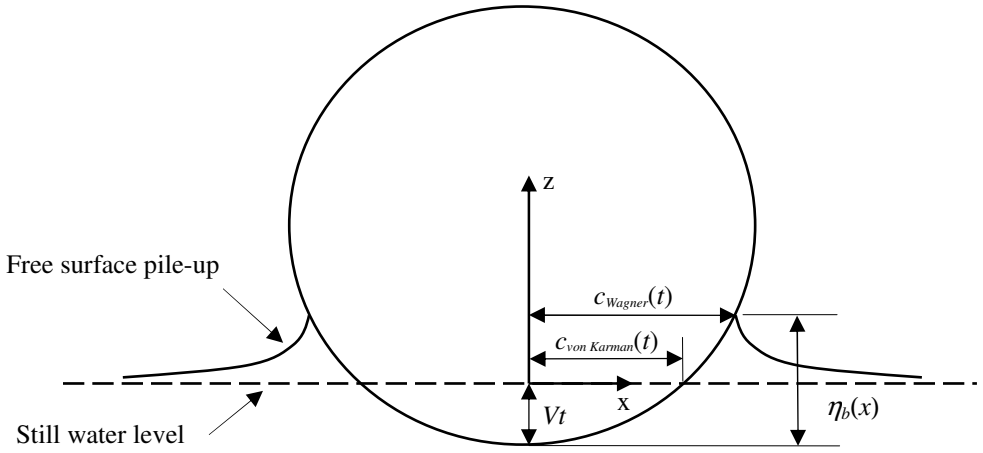

Figure 3.1 Definition of Parameters for Calculating Wave Slamming Forces

The von Karman approach is adopted by Goda et al. (1966) [3.36] and Tanimoto et al. (1986) [3.86] to estimate the wave slamming on vertical circular cylinders. Total slamming force F_S on cylindrical member due to breaking waves is obtained by:

$$F_S(t) = \lambda \eta_b \pi \rho V^2 R\left(1 - \frac{V}{R}t\right) = \lambda \eta_b f_S \tag{3.8}$$

where the coefficient λ, called the curling factor, describes the part of the surface elevation η_b of the breaker that contributes to the slamming; the term f_S on the right hand side denotes the force per unit length for circular cylinder, as defined in Equation (3.6). This equation is based on the assumption that the water front of a breaking wave over the height $\lambda\eta_b$ is vertical and moves at the wave phase velocity (celerity) V. Thus $\lambda\eta_b$ represents the height of the slamming area. Furthermore, Goda's approach assumes that the slamming force is equally distributed along the slamming area. Total slamming force can then be obtained using the strip theory with horizontal strips distributed along the cylinder's length.

3.1.2.3 Wagner Type Slamming Load Models

Due to the pile-up effect, the actual duration of slamming is shorter than that predicted by von Karman's theory while the actual maximum force is larger. The method developed by Wagner (1932) [3.92] takes into account the pile-up effect by assuming that the free surface elevation, η_b, relative to the bottom of the cylinder can be obtained by the time integration of the potential flow. This distance depends on the shape of the cylinder. With the time history of η_b, the length $c(t)$ of an imaginary flat plate can be found from the two intersection points between the cylinder and the free surface (see Figure 3.1). The wave slamming force is then obtained from Equation (3.4) following von Karman's method. To solve the resulting equation in relation to the plate length, the shape of the wetted body can be approximated by Taylor series:

$$\eta_b = R - \sqrt{R^2 - x^2} \approx \frac{1}{2R}x^2 + \frac{1}{8R^3}x^4 \tag{3.9}$$

For a small x value, only the first quadratic term of the series matters. This yields (Faltinsen, 1990 [3.28])

$$c^2(t) = 4RVt \tag{3.10}$$

The wetted length c from Wagner's theory is $\sqrt{2}$ times of that from von Karman's solution in Equation (3.5) at the beginning of slamming on calm water. The slamming force per unit length becomes:

$$f_S = V\rho\frac{\pi}{2}\frac{dc^2(t)}{dt} = 2\pi\rho RV^2 \tag{3.11}$$

The slamming force is time independent for this approximate parabolic shape and doubles the magnitude of the slamming force at the beginning of slamming obtained using von Karman's approach. Based on the same expression defined in Equation (3.7), the slamming force per unit length obtained using Wagner's theory becomes

$$f_S = \rho C_s RV^2 \quad \text{and} \quad C_s = 2\pi \tag{3.12}$$

The slamming coefficient $C_s = 2\pi$ occurs at the early stage of slamming for which only the first quadratic term in Equation (3.9) is taken into account.

Wienke (2001) [3.99] and Wienke and Oumeraci (2005) [3.98] indicate that the quadratic parabola representation gives a proper approximation only at the beginning of the slamming when x is small. Adding further terms of the series in Equation (3.9) will not substantially improve the accuracy, particularly when x is approaching R. In order to improve the approximation of the wetted surface of the cylinder, they introduced a polynomial stepwise function:

$$\begin{aligned} \eta_b &= \frac{1}{2R}x^2 \quad \text{for } 0 \le x \le \frac{R}{\sqrt{2}} \\ \eta_b &= \frac{1}{R^3}x^4 \quad \text{for } \frac{R}{\sqrt{2}} < x \le R \end{aligned} \tag{3.13}$$

This stepwise function gives a good approximation of the wetted surface of the cylinder at the beginning of slamming as described in Equation (3.9). When x approaches R, it also gives a better approximation of the wetted surface and improves the estimation of the slamming duration while providing a simple solution for the problem. The second segment yields the following wetted length c:

$$c^2(t) = \sqrt{\frac{8}{3}R^3Vt} \tag{3.14}$$

Wienke (2001) [3.99] uses the nonlinear Bernoulli equation without accounting for the gravitational part to estimate the pressure p_S as:

$$p_S = -\rho\frac{\partial\phi}{\partial t} - \frac{\rho}{2}(\nabla\phi\nabla\phi) + C(t) \tag{3.15}$$

where $C(t) = 1/2\rho V^2$ according to Wienke (2001) [3.99]. The upper limit x_0 of the integration corresponds to $p_S = 0$. This gives the following time dependent slamming force per unit length:

$$f_S(t) = 2\int_0^{x_0} p_S(x,t)dx = \rho V^2 \left(\frac{\pi}{u} - ar\tanh\left(\sqrt{1 - \frac{u^2}{4}} \right) \right) c \quad \text{where} \quad u = \frac{V}{dc/dt} \tag{3.16}$$

The total force can be calculated using the strip theory where horizontal strips are distributed along the cylinder's length as in Goda et al. (1966) [3.36].

When the mass of water hits the cylinder not normally but obliquely, the two-dimensional section of the cylinder has to be represented by an ellipse instead of a circular shape. Wienke (2001) [3.99] uses the same technique as the one for the case of vertical cylinder to derive the slamming force per unit length, except that the expansion series approximates an elliptic shape.

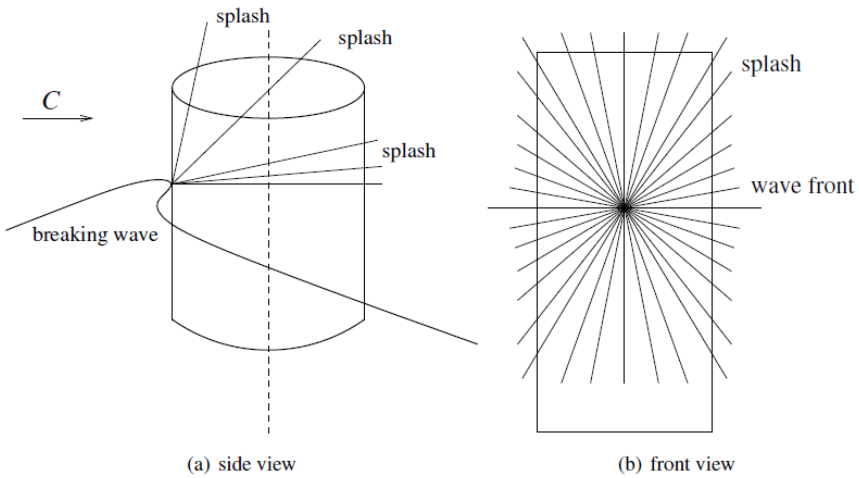

Figure 3.2 Splashing Pattern of Plunging Breaking Wave (IEC61400-3 Annex D)

During experiments with different inclination angles for the cylinder, Wienke (2001) [3.99] observes that the spreading of the water along the cylinder's surface takes place simultaneously on each horizontal section of the cylinder (see Figure 3.2). Starting at the wave slamming point on the cylinder, the splash is spreading radially in all directions and tangentially to the cylinder surface. Therefore, the pressure development is calculated by the above-described Wienke's two-dimensional model within cross-sectional planes along the spreading directions. In these planes, the cross section of the cylinder becomes elliptic. Wienke and Oumeraci (2005) [3.98] define the resulting total slamming force as in Goda et al. (1966) [3.36] by integrating the force per unit

length over the height of the slamming area $\lambda\eta_b$. Wienke and Oumeraci (2005) [3.98] derive the value of the curling factor λ from the maximum measured total slamming force, which occurs at the beginning of the slamming. The ratio of the measured maximum slamming force to the calculated slamming force per unit length f_S provides the height of the area of slamming $\lambda\eta_b$, where η_b is the maximum surface elevation of the breaking wave.

Comparing the total slamming force time history to those obtained using other theories, the Wienke model is slightly overestimated in the first segment and a slightly underestimated in the second one (see Figure 3.4). However, it is shown that the calculated slamming forces following the Wienke model expressed in Equation (3.16) agree well with experimental measurements (Wienke, 2001 [3.99]).

Armand and Cointe (1986) [3.4] develop another scheme using the method of matched asymptotic expansions where the perturbation parameter is defined as $\sqrt{VT/R}$ and T is the characteristic time scale of slamming. They divide the solution domain into an outer domain far from the water line and an inner domain, with the assumption that the outer solution near the singularity matches the inner solution at infinity. The first order solution of the asymptotic expansion gives C_s approximately equal to the theoretical value 2π from Wagner. The nonlinearity is taken into account by introducing the second order correction, which leads to a time variant solution of C_s. The second order solution appeared to agree well with the experiment results at the early stage of slamming, except for the small rising time observed at the beginning of slamming. However, it overestimates the slamming force when the penetration approximately goes beyond Vt/R=0.02.

3.1.2.4 Shallow Water Wave Kinematics

The analytical slamming load models as discussed in Section 3.1.2 requires the input of the water particle velocity at the free surface of a breaking wave. Theoretically, a wave breaks when the water particle velocity at the wave crest exceeds the wave celerity (phase velocity). It is reasonable to assume that the free surface water particle velocity (V) of a breaking wave is closely correlated to the wave celerity (u_c), which can be calculated using an appropriate analytical regular wave theory or numerical method.

Regular waves are often used to estimate the wave kinematics for so-called design waves. They can also be used to provide a simple estimation of wave kinematics based on the wave height, the

wave period and the water depth. Many efforts have been made to develop a diagram showing the applicability of the various regular wave theories. Le Mehaute (1969) [3.52] is the first to provide a classification diagram illustrating the applicability of the various regular wave theories according to the ratios $H/(gT^2)$ and $d/(gT^2)$, where H is the wave height, d is the water depth, and T is the equivalent deep water wave period, i.e. $gT^2 = 2\pi L$ where L denotes the wave length. This classification is developed further by several authors such as Dean and Dalrymple (1991) [3.22] and Chakrabarti (1987) [3.13]. Similar wave theory classifications have been adopted in various offshore structure design standards such as API RP 2A-WSD (2007) [3.3], ISO 19901-1 (2005) [3.41] and IEC 61400-3 (2009) [3.40].

To determine the shape of a wave, three length scales need to be considered: the wave height H, the wave length L, and the water depth d. Two important non-dimensional parameters can be written as

$$\mu = d/L \quad \text{and} \quad \delta = H/d \tag{3.17}$$

Depending on the magnitude of μ, two types of "wave theories" can be distinguished (Svendsen, 2006 [3.85], Mei, 1989 [3.61]):

- $\mu = O(1)$, i.e. in the order of 1

This case is related to a wave whose length is comparable to the water depth (finite water depth). Under this assumption, the only non-dimensional parameter that remains in the governing equations is $\delta\mu$, which is proportional to the commonly used wave slope $\varepsilon = ka$, where k is the wave number and a is the wave amplitude. This corresponds to the Stokes theory, in which ε is assumed to be small compared to 1.

For periodic (regular) waves, a fifth-order analytical solution is derived by Fenton (1985) [3.30]. A numerical method to calculate the coefficients of the Stokes expansion to any order is given in Schwartz (1974) [3.76] and Cokelet (1977) [3.19].

In shallow water, the Stokes expansion converges only for waves with infinitely small steepness, and therefore is not applicable. For finite water depth, higher order expansions are required comparing to the deep-water case. It is also observed that the convergence of the Stokes expansion is getting more difficult when higher order terms are included.

It should also be noted that in the perturbation expansion, the surface boundary conditions are defined at the still water level rather than on the actual water free surface. Therefore, the linear solutions are valid only up to the still water level. Stretching methods, such as Wheeler (1970) [3.96], have to be employed to calculate the velocity profile under the wave crest and above the still water level. Recent study by Stansberg et al. (2008) [3.82] show that the Wheeler method used with a linear input in deep water can significantly under-predict the maximum velocity beneath the wave crest.

The stream function theory developed by Dean (1974) [3.23] is a numerical solution to the governing equation. The stream function theory is extended by Dalrymple (1974) [3.21] to model waves on vertically sheared current. The expression of the Dean's stream function theory is based on the one obtained from the Stokes expansion. As a result, it also has convergence problems in the case of shallow water or when a wave approaches its breaking limit. In practice, an increasing number of terms are needed in the expansion series in order to obtain a correct wave profile and kinematics as the water depth decreases. The advantage of the stream function theory compared to Stokes analytical solutions is that it is much easier to compute the higher order solutions, which are necessary for steep waves in finite water depth. In addition, wave kinematics up to the free surface elevation can be directly solved by the stream function theory so that the stretching method required by Stokes theory is no longer needed.

- $\mu << 1$

This case corresponds to waves with a large characteristic length compared to the water depth (shallow water). Unlike the Stokes theory, the two small parameters, μ and δ, are no longer coupled. Depending on the relative magnitude of δ with respect to μ^2, three sub-cases can be defined according to the Ursell number (Ursell, 1953 [3.90]), which is defined as $U_r = \delta/\mu^2$.

– $U_r << 1$

In this case $\delta << \mu^2 << 1$, the wave height is infinitely small (linear wave theory in shallow water). This case is of little practical use.

– $U_r = O(1)$, i.e. in the order of 1

This case corresponds to long waves of moderate amplitude. It is often referred to as "long wave theory". It includes the Boussinesq-like wave models, which lead to the cnoidal and solitary wave theories. The main principles of all Boussinesq-like wave models are the shallow-water assumption, i.e. $\mu << 1$, and the elimination of the vertical coordinate from the governing equations. Although Boussinesq-like models are originally derived for shallow water, recent developments have extended their validity to deeper water (Clamond, 1999 [3.17]; Madsen et al., 2002 [3.55], 2003 [3.56]). For detailed reviews of the long wave theory, the reference is made to Svendsen (2006) [3.85], Dingemans (1997) [3.26] and Mei (1989) [3.61],

– $U_r >> 1$

This case, corresponding to long waves with large amplitude, is described by the so-called nonlinear shallow water equations, which have to be solved numerically.

3.1.3 Numerical Methods

The estimation of the wave load based on the Morison equation or von Karman and Wagner types of formulae requires the input of wave kinematics. Analytical wave theories show strong limitations when it comes to the description of steep and breaking waves, especially in finite water depth. Numerical methods may then constitute more accurate alternatives. There are two different approaches that numerical methods are employed to solve slamming problems:

- Fully numerical simulation of the wave-structure interaction can be used to predict the pressure distribution on a structure. The numerical integration of the pressure gives the wave load. The main advantage of this approach is that the wave diffraction is taken into account. However, this approach normally needs long CPU time and the numerical simulation may not be robust enough.

- Numerical methods can also be used to estimate the kinematics of steep and breaking waves without structure. The slamming forces are estimated by means of analytical load models such as Wagner's method in Rognebakke and Faltinsen (2000) [3.72]. The advantages of this approach are less CPU cost, the possibility to use larger time steps and better numerical robustness. It can also be combined with linear wave theory, where only the breaking wave

is calculated numerically (Marino et al., 2010a [3.57]). However, diffraction of the wave may not be fully accounted for and uncertainties regarding empirical coefficients in the slamming force model may be difficult to estimate.

Based on the assumptions made to describe the fluid flow, numerical methods can be divided into two main classes:

- Potential flow methods, which assume irrotational flow and neglected viscosity. If the fluid is treated as incompressible, the governing equation is the Laplace equation.

- Methods based on the general Navier-Stokes (NS) equations. An issue to be considered here is whether the viscous flow is laminar or turbulent. Neglecting the viscosity leads to the Euler equations. Vorticity, which may be created by wave breaking, can be captured by the Euler equations as well as by the Navier-Stokes equations.

According to the way the governing equations are discretized, one can also divide the methods into mesh-based methods and mesh-free methods.

3.1.3.1 Fully Non-linear Potential Flow Simulations

Ducrozet et al. (2010) [3.27] use the boundary element method (BEM) combined with mixed Eulerian-Lagrangian (MEL) method to study nonlinear diffraction by a cylinder in long waves in a domain with small finite depth. The numerically calculated wave run-up around the cylinder is compared to the experiments. A good agreement for the interaction of low steepness regular waves with the vertical cylinder is shown. The authors argue that the accuracy of the comparisons between the BEM-MEL method and experiments prove its ability to deal with highly nonlinear free surface flows.

Marino et al. (2010b) [3.58] present a numerical procedure to simulate extreme response of offshore wind turbines using BEM-MEL and a linear spectral approach. The latter makes it possible to define the irregular sea in each point of the space-time domain. A zero-crossing analysis defines the need for the BEM-MEL model for plunging breakers. If wave breaking does not occur, hydrodynamic loads are computed by using the standard Morison equation. If wave breaking occurs, the fully nonlinear wave simulator is called as many times as the number of accepted breakers. The fully nonlinear wave simulator delivers all the necessary kinematic parameters for the analytical slamming model proposed by Wienke and Oumeraci (2005) [3.98].

The advantage of this method is its computational efficiency with an improved accuracy for wave breaking. This method shows three times higher peak loads compared to the standard Morison linear wave approach.

Wang and Wu (2010) [3.93] show that a finite element method (FEM)-MEL method is able to describe fully nonlinear interactions between water waves and vertical cylinder arrays. Waves and hydrodynamic forces are calculated using the proposed approach for both bottom-mounted and truncated cylinders.

3.1.3.2 Volume of Fluid Method (VOF)

Mokrani et al. (2010) [3.62] use a Navier-Stokes (NS) VOF model to investigate the slamming force on a vertical wall and the related overtopping rate generated by a large plunging breaker. A breaking wave simulated with the NS-VOF model is validated against the BEM-MEL simulation. It is shown that the influence of the mesh resolution on the calculated pressure peak on the wall and the total force applied on the wall. The computed time history of the slamming force on the wall has a good accuracy compared to experimental data. Overtopping events generated after the slamming are also compared with experiments in this paper.

Corte and Grilli (2006) [3.20] present a numerical method to define the transient load on a cylindrical support structure. They use a BEM-MEL approach for extreme wave generation and the Finite Volume (FV) VOF model for the wave slamming process; the latter model being initialized using results of the former model. The free surface flow of the extreme wave around the cylinder is simulated in the FV-VOF model. The computational results of the FV-VOF method are compared through pressure time series to the analytic method of Wienke (2001) [3.99] (one-phase potential flow, constant fluid density) and to experimental results by Wienke (2001) [3.99] and Wienke and Oumeraci (2005) [3.98]. In all cases the maximum pressures computed with the FV-VOF method are smaller than those predicted by Wienke's method. The deviation is attributed to the averaged density used in the FV-VOF model in contrast to Wienke's potential flow approach. For later stages of the wave slamming, the FV-VOF model shows a good agreement with experimental results.

Bredmose and Jacobsen (2010) [3.10] use OpenFOAM to determine the slamming force by integrating the fluid pressure on the wetted cylinder wall. Forces are calculated using the Morison equation, where the physical velocity above the still water level is modified by Wheeler

stretching. The comparison of the forces shows that for the initial small waves the two methods give almost identical results. The force peaks of the main slamming are smaller in the Morison prediction compared to the CFD solution. The grid convergence study does not show large differences between using a coarse grid and a fine grid.

Pakozdi et al. (2011) [3.70] show that capturing the pressure evolution at a slamming event demands a very high spatial and temporal resolution, which is not necessary for the simulation of waves using a second-order implicit time integration scheme when the slamming is not of a concern.

3.1.3.3 Smoothed Particle Hydrodynamics (SPH)

Oger et al. (2010) [3.68] present a coupling between two codes, where BEM-MEL and SPH are sharing different tasks. A potential-theory based code is in charge of the global flow and SPH-flow is in charge of the local interactions simulations during the slamming in the vicinity of an impacted wall. The SPH calculations are restricted in a rectangular domain adjoining the wall. The compression of a gas pocket entrapped by a breaking wave onto a wall is also calculated using a two phases SPH fluid model. The first oscillation of the pocket is simulated in a very credible way according to experimental results obtained in different flume tanks.

3.1.3.4 Numerical Solution of the Wagner's Problem Coupled with Hydro-elasticity

Korobkin et al. (2006) [3.49] argue that the simplified theory of water slamming developed by Wagner is still the most advantageous for hydroelastic calculations. It is stated that

> *"First, this theory was designed for bodies with small deadrise angles, which are of primary concern from the point of view of hydroelasticity. Second, this theory was widely tested, so its strengths and weaknesses are well known. On the other hand, more advanced theories, including fully nonlinear models of potential flows with free boundaries, generally contain many technical and numerical 'tricks', which are incorporated, sometimes in an implicit way, with the aim of improving stability and performance of a solver. This can mean that sometimes a solution of more complex equations, which require sophisticated numerical schemes, is not necessarily more accurate than a solution of simplified equations, for which numerical calculations are more transparent and, moreover, a part of them can be performed analytically."*

Peseux et al. (2005) [3.71] numerically solve the three-dimensional Wagner problem using the finite element method. A numerical analysis is performed for both rigid and deformable structures. The fluid problem is represented in terms of a potential velocity formulation. A variational formulation together with a finite element method is adopted to solve the Wagner problem. A wetting correction is obtained through an iterative procedure. The numerical resolution is validated with simple problems, such as the water slamming problem of a two-dimensional wedge with small deadrise or an axis-symmetric cone. Good agreement between numerical and analytical results is achieved. The structural governing equations are solved using the finite element method. The fully coupled problem is then resolved with the same method. This formulation introduces a coupling matrix. The evaluation of its terms is checked for the sloshing problem in a tank with an elastic beam in the two-dimensional case and with an elastic plate in the three-dimensional case.

Korobkin et al. (2006) [3.49] combine a finite element method with the Wagner approach to develop an efficient numerical algorithm for the analysis of the interaction between a complex elastic structure and the liquid during slamming. Only the distribution of the velocity potential along the wetted part of the structure is required to compute the structural deflection and the bending stress distribution. This result is obvious within linear hydro-elasticity; however, the problem under consideration is nonlinear because the extent of the wetted part of the structure is a priori unknown. The decoupling of the hydrodynamic and structural analyses used in this reference is a generalized normal mode method. The generalization recognizes that the wetted area is unknown a priori and has to be determined together with the structural deflection. The hydrodynamic pressure is not evaluated and consequently the calculations of the velocity potential are reduced within the finite element method to the evaluation of the added mass matrix. The elements of the added mass matrix are analytically obtained and this makes the calculations of the structural response fast and efficient. Position and dimension of the contact region between the structure and the liquid are determined from the Wagner condition without additional assumptions. This condition is complicated and nonlinear, but it is shown that the Wagner condition is equivalent to a system of two ordinary differential equations for the coordinates of the contact points. Finally, the original coupled problem is reduced to a nonlinear system of ordinary differential equations for the displacements of the beam elements and the coordinates of the contact points. The system is integrated numerically by the fourth-order Runge-Kutta method. The analysis is valid for any blunt elastic structure entering water at moderate velocity.

The advantage of this method is that the coupling procedure is quite clear and the system of equations to integrate in time is of lower order (equal to the number of retained modes). The weakness may lie in the representation of very high slamming loads where the number of necessary modes increases, especially in the first few time instants.

An analysis of the elastic wedge entry problem is performed by Lu et al. (2000) [3.53]. In the paper, the hydrodynamic problem is solved based on the BEM together with the fully nonlinear free surface condition. The structural response is analyzed based on linear elastic theory using the FEM. The full fluid-structure interaction is included. The jet formed along the body surface is taken into account by introducing an extra jet-element. The finite element method is used to analyze the elastic response of the structure. The plates on both sides are divided into two-node finite elements. During water entry, the hydrodynamic pressure acting upon the wetted surface is obtained from Bernoulli's equation. When the pressure distribution acting upon the plates is found, the solution for the structural response can also be solved. In order to obtain the global coupled structural equilibrium equations, the nonlinear terms are linearized in Bernoulli's equation. The FEM for structural analysis and BEM for hydrodynamic analysis have identical element nodes on the wetted surface. The method presented in this paper can be extended for the three-dimensional slamming problem.

3.1.3.5 Boussinesq-based Modeling of Wave-Structure Interactions

Numerical Boussinesq methods can be used to compute loads on surface-piercing structures. They are particularly efficient for slender bodies, for which diffraction effects can be neglected, since a simple finite difference scheme on a rectangular grid can be used. This is done by Larsen et al. (2004) [3.51], who generated nonlinear irregular wave time series numerically without any structure and computed the resulting forces on offshore bottom-mounted wind turbines by means of an analytical model. This approach is also suggested in IEC 61400-3 (2009) [3.40].

Another possibility is to incorporate new boundary conditions around the structure in the Boussinesq numerical model and compute the resulting loads by directly integrating the pressure. In this case, some limitations caused by the grid resolution in the vicinity of the structure have to be considered. Existing resolution schemes used for Boussinesq wave-structure interactions include:

- Finite difference with a rectangular grid. This fast scheme is used by Fuhrman et al. (2005) [3.34] to compute the run-up on rectangular structures. It is not documented how good the estimation of wave forces can be for rectangular structures. This scheme may not be adapted to circular or more complex geometries.

- Finite difference with a curvilinear grid. This scheme is introduced by Wang et al. (1992) [3.95] for circular cylinders. They use an analytical coordinate transformation to map an initial rectangular grid to a grid that accounts for the contour of the circular cylinder. This resolution scheme is generalized to more complex geometries by Shi et al. (2001) [3.77], who compute nonlinear wave propagation in a circular channel as well as in the Ponce de Leon inlet.

- Finite elements with an unstructured mesh. There are a few attempts to integrate Boussinesq equations by means of a finite element scheme. This is done by e.g. Zhong and Wang (2009) [3.102] who use an unstructured triangular mesh to study the slamming loads on cylinder arrays. However, with this scheme, non-physical high-frequency oscillations have to be dealt with.

The following paragraphs give a short list of papers related to the study of wave-structure interactions by numerical Boussinesq models. Some wave run-up studies are also included to show the capabilities of Boussinesq-based methods, even though loads are not computed.

Wang et al. (1992) [3.95] consider the three-dimensional interaction between solitary waves and a surface-piercing circular cylinder. The system of Boussinesq equations used in the study is adapted from Wu (1981) [3.100]. It is weakly nonlinear and makes use of the layer-mean potential instead of the potential at the bottom. One should therefore expect that the water depth validity domain be restricted to shallow water. The numerical integration is performed by means of a finite-difference scheme. However, the difficulties in the modeling of the boundary conditions on the cylinder are considered by introducing a coordinate transformation that maps the cylinder surface back to a simple rectangular grid (curvilinear grid). The resulting force on the circular cylinder is obtained by integrating the pressure computed from the Bernoulli equation. The numerical solution is initialized with an analytical solitary wave as described in Section 3.1.3. No comparison with experimental data is included in this paper.

The previously mentioned study is pursued further in Wang and Jiang (1994) [3.94], where the interactions of solitary waves with pairs of cylinders, both in tandem and transversely arranged, are considered. As in Wang et al. (1992) [3.95], a curvilinear coordinate system is adopted to better describe the flow in the vicinity of the cylinders. In addition, a more general double-grid resolution scheme is implemented. The first kind of grid is uniform and rectangular, whereas the second one is circular and matches the geometry of each cylinder. The solution is matched simply by using interpolation. Time series of the estimated global forces on the cylinders are presented without comparison with experimental data.

Bingham et al. (2004) [3.9] and Fuhrman et al. (2005) [3.34] apply the Boussinesq numerical model derived in Madsen et al. (2002) [3.55] and Madsen et al. (2003) [3.56] to study run-up and diffraction of regular waves by a rectangular surface-piercing structure. Although the resulting force is not computed, it could be done in practice through pressure integration. The integration of the Boussinesq equations, which in this case are also valid in deep water, is performed using a finite difference scheme. This work is pursued further in Fuhrman and Madsen (2008) [3.32], who included a moving wet-dry boundary algorithm to estimate the run-up around a conical island. Comparisons with surface elevation measurements from Molin et al. (2005) [3.63] show very good agreement. More details regarding the method can also be found in Fuhrman (2004) [3.33].

Jamois et al. (2006) [3.46] study the nonlinear wave run-up on bottom-mounted and surface-piercing rectangular structures and compare the results from their Boussinesq numerical model to experiments. They re-formulate the method developed by Madsen et al. (2003) [3.56] in terms of the velocity potential instead of horizontal velocities. The total number of unknowns is reduced from 7 to 5, which increases the computational efficiency. In addition, the numerical stability of the method seems to be improved, especially when dealing with structures with sharp corners. However, the domain of validity for the water depth is reduced to $kd \leq 4$, where k is the wave number and d is the water depth, with an accuracy of about 3% for the wave kinematics. They use a finite difference integration scheme with a uniform rectangular grid, which is adapted to the geometry of the surface-piercing structure. The grid is chosen to avoid the corners of the rectangular structure, where the potential flow solution shows singularities. The latter are still responsible for high-frequency numerical noise, which has to be filtered out. The experimental results used for comparisons involved regular waves generated in a 16 m by 28 m offshore wave tank as described in Molin et al. (2005) [3.63]. Several wave steepness and relative wave

directions are investigated. A good quantitative agreement is obtained between the numerical and experimental results for the nonlinear wave run-up, even for steep waves.

In a recent paper by Zhong and Wang (2009) [3.102], the nonlinear interaction between shallow water waves and cylindrical structures are modeled using a finite element integration method. The Boussinesq equations used in the study are those from Wu (1981) [3.100] so that the model is valid in shallow water only. The depth-averaged velocity vector is used to relax the z-dependency in the equations and the mass conservation (Laplace equation) is consequently fulfilled exactly. The finite element scheme makes it possible to use unstructured triangular meshes to discretize the fluid around relatively complex structures as cylinder arrays. However, spurious numerical oscillations have to be damped out artificially in order to stabilize the finite element integration scheme. Forces due to the interaction of a solitary wave with a circular cylinder and an array of four circular cylinders are estimated by pressure integration for several wave slopes. Comparison with experimental measurements from Yates and Wang (1994) [3.101] show a fairly good agreement with regard to the surface elevation but the numerically computed forces are overestimated, especially for steep waves.

3.1.4 Slamming Experiments

The determination of slamming loads from steep and breaking waves is theoretically very complex. Hence, experiments are crucial for the validation of theories, numerical methods and software tools. In some cases, slamming loads are also directly estimated using model testing.

Due to the random nature of slamming loads, which exhibit a particularly large statistical scattering, measuring slamming loads is challenging work. There is a rich collection of literature on model test measurements of local and global loads on fixed vertical cylinders and similar structures in non-breaking as well as breaking waves. Experimental activities are reported both from the offshore engineering and the coastal engineering communities. The experiment set-ups cover deep, intermediate and shallow water conditions. This section provides a review of relevant slamming experiments.

Most of the referenced experiments apply breaking waves generated either by focusing on summation of many harmonic components, or by breaking of regular waves due to a shoal. Only a few of them apply waves breaking randomly in an irregular wave field. Some of the early

studies measure the "quasi-static" global force without considering the time varying slamming component. The slamming force is modeled within the framework of the Morison equation. Additional drag and inertia coefficients are obtained through data fitting to match the experimental results.

In the original papers, most of the results are given either in normalized scales or in model scale. For comparison and reference purposes, whenever physical values are addressed, they are scaled up to a full scale corresponding to a breaking wave height of about 15 m – 20 m and a crest height of about 10 m – 15 m, using Froude's law. Diameters or cross-sections of the tubular structure members correspond typically to the range 4 m – 15 m.

3.1.4.1 Local Wave Slamming Loads on Circular Cylinders

For general circular cylinders with a radius R, the peripherally integrated force per unit height, as defined in Equation (3.7), takes the following expression:

$$f_S = \rho C_s R V^2 \tag{3.18}$$

f_S is sometimes referred to as the line force, or the sectional force. This equation is used to estimate the equivalent slamming coefficient for a given measurement of slamming force.

For the local effect on small area of circular cylinders, the equation of local pressure p_S is in the similar form as that of the slamming pressure on a flat plate.

$$p_S(x) = \frac{2\rho R V^2}{(c^2 - x^2)^{1/2}} = \frac{1}{2}\rho C_{s,Local} V^2 \qquad \text{for } |x| < c(t) \tag{3.19}$$

where the local slamming coefficient $C_{s,Local}$ is a function of x and c (see Figure 3.1). Based on Wagner's slamming load model described in Section 3.1.2.3, the wetted surface length c is determined by Equation (3.10) such that

$$C_{s,Local}(x) = \frac{4R}{(c^2 - x^2)^{1/2}} = 4 \cdot \left(\frac{4Vt}{R} - \left(\frac{x}{R} \right)^2 \right)^{-1/2} \qquad \text{for } |x| < c(t) = 2\sqrt{VRt} \tag{3.20}$$

This local pressure coefficient can be used to compare with the experimental measurements. Theoretically, the local pressure coefficient is infinite at the immediate vicinity of $|x| = c(t)$ as defined in Equation (3.20). However, the measured slamming pressure is always finite. This

discrepancy is partially due to the incorrect boundary conditions on the free surface at the immediate vicinity of $|x|=c(t)$. The potential flow solution around a flat plate, represented by Equation (3.20), gives an infinite vertical velocity at the plate edges, while in the case of circular cylinder slamming test, the velocity around the front of the wetted surface is almost horizontal and resembles a horizontal jet flow. The physics is apparently not well modeled near $|x|=c(t)$. On the other hand, experimental errors are also possible, given that the maximum slamming pressure strongly depends on the area over which the pressure is measured. In this sense, the experimental value is an averaged pressure over a small but finite area while the theoretical pressure is over an infinitesimal area.

A commonly used reference is the experimental fitting done by Campbell and Weynberg (1980) [3.11]. They find that for a horizontal cylinder penetrating a water surface the local slamming coefficient $C_{s,Local}$ takes a maximum value of 5.15 at the initial penetration stage, and reduces during the penetration. The observed local slamming coefficients along the wetted surface also appear fairly close to those predicted by Equation (3.20).

Chaplin et al. (1992) [3.16] report a set of three experiments carried out at different model scales. Both regular and breaking waves are considered for circular bottom-mounted cylinders in finite water. The scales correspond to 1:8, 1:32 and 1:160, respectively, determined by matching a full-scale crest height of about 15m and celerity of 17 m/s. Full-scale cylinder diameters then correspond to 4 m, 5.1 m and 4 m, and the water depth corresponds to 40 m. Local pressures (measured by small pressure cells), global forces, wave elevation and wave particle velocities are measured. Breaking waves are mainly made by focused wave groups or similar techniques, while some tests are performed with breaking on a sloped bed. The highest local pressures reported correspond to around 300 kPa - 600 kPa at full scale that lead to the local slamming coefficients $C_{s,Local}$ around 2 ~ 4. The results are lower than those obtained from other experiments reviewed herein. One possible explanation could be that the actual probes might not have been hit by the most intense part (tongue) of plunging wave. The actual size of the pressure sensors, which is not given in their report, is another uncertain factor.

Chan et al. (1995) [3.15] perform a similar experiment with a fixed circular cylinder in a small scale, corresponding to 1:80 when it is compared with full scale crest height of 15m and celerity of 17 m/s. Deep-water plunging breakers are generated by a focusing wave technique similar to that in Chan and Melville (1988) [3.14]. Local pressure cells covering very small areas are used.

They report extreme local pressures corresponding to $C_{s,Local}$ about 30 - 90 in the worst condition. These are very high values partially because they are local quantities over very small areas and are subjected to large statistical uncertainties and spatial variations, which are also addressed in the paper through repeated experiments. The slamming duration is very short, with the extreme cases showing around 3 ms at full scale. The experiment also shows a significant sensitivity to the position of the breaking point relative to the cylinder; the largest pressures occur when the wave starts to break just on the cylinder wall. Air cushion effects are also discussed in the paper.

Wienke and Oumeraci (2005) [3.98] carry out a large set of breaking wave experiments with circular cylinders of diameter corresponding to 5m at full scale in the large Hannover wave tank (GWK). The cylinders are fixed in both vertical and inclined positions relative to the calm water surface. The largest slamming load in breaking waves is observed in vertical position. Scaled up by 8:1, the crest height is about 15 m, the celerity is about 17 m/s, and the water depth is 32 m. Plunging breakers are generated by focused Gaussian wave packets. Local pressures, total forces, wave elevation and particle velocities are measured. The tests are in many respects similar to those by Chaplin et al. (1992) [3.16] as described above, while the maxima in the local pressure field seem to be better captured in this experiment. Extreme local pressures (from pressure cells) up to 12 MPa at full scale are observed, corresponding to a slamming coefficient $C_{s,Local}$ about 70 – 80, which is similar to the smaller scale experiment by Chan et al. (1995) [3.15]. The effect of relative position of the breaking point is also studied in the paper.

Suyuthi and Haver (2009) [3.84] report two different wave basin experiments with a semisubmersible (with rectangular columns) and a TLP (with circular columns). Wave slamming forces on platform columns in steep irregular waves are measured using the force panels of area size 11 m^2 and 6 m^2, respectively, at full scale, which allow deriving the pressures averaged over the area of the force panel rather than local pressures. The model scale is 1:55. A probabilistic approach, including a large number of 3-hour storm wave realizations (seed numbers), is used in the study. It is likely that most of the observed slamming events are due to breaking wave events. For 10,000-year storm conditions in the North Sea the spatially averaged extreme pressure levels are 2.6 MPa and 3.0 MPa at full scale for the semisubmersible and the TLP, respectively, at 90% fractile levels. With the estimated extreme particle velocities given in the paper as 17.7 m/s and 18.3 m/s, the spatially averaged slamming coefficients $C_{s,Local}$ is estimated to be 16.7 and 18, respectively. In a later paper (Clauss et al., 2010 [3.18]) the velocities are revised to be in a range

between 16 m/s and 25 m/s in both cases, and the slamming coefficients are therefore lower than the above values (slightly higher than 10).

Roos et al. (2010) [3.73] test a scaled model of a gravity-based structure with a caisson and four circular columns. Slamming is measured by means of a vertical array of small force cells with area 2.25 m^2 at full scale. The water depth is 82.5 m. A model scale of 1:100 is applied. The presence of the large caisson may be considered to be similar to a distinct shallow water shoal. Tests in a 10,000-year North Sea irregular wave condition are reported. As described in Suyuthi and Haver (2009) [3.84] above, the model is tested in a number of 3-hour realizations for robust extreme value estimation, and 90% fractile level extremes are derived. Spatially averaged extreme pressures are found to be up to 3.5 MPa, which is larger than the averaged pressures for the two platforms reported by Suyuthi and Haver (2009) [3.84]. The difference may be due to using smaller force cells in this case.

Stansberg (2011b) [3.81] analyzes data from 1:40 and 1:125 experiments under the deep water condition with breaking wave loads on a fixed column with rectangular cross section. Breaking waves are generated by a focusing wave technique as well as by random groups. Crest height is about 17 m, and the celerity is about 18 m/s – 19 m/s. Maximum particle velocities estimated from a CFD study are about 25 m/s. Local pressures are measured by a 7×7 square array covering 19 m^2 at full scale, located in the area of the plunging wave attack. Total forces are also measured by a force cell of the same area, and it is verified that they agree well to the average pressure derived from the pressure array. The most extreme measured local pressures in the 1:40 tests are around 4 MPa – 5 MPa at full scale, while the scatter between repeated measurements is high. Maximum spatially averaged pressures over 19 m^2 are typically around 2 MPa. In the 1:125 scaled tests, several tests show similar values, while some measurements show particularly high values of 25 MPa locally and with a spatial average around 10 MPa. These latter observations are made after a slight deliberate adjustment of the column position, with its front just at the starting point of the breaking, while such accurate adjustment and iterations are not possible in the 1:40 tests. Thus the 1:125 tests show that the results are very sensitive to the accurate relative position of the column. This observation is also made in several other studies. The very high pressure level indicates that repeated measurements are necessary before a final conclusion can be made from an experiment.

Arntsen et al. (2011) [3.5] measure the vertical force profile from breaking waves on a fixed cylinder located on a shoal using several ring force transducers located vertically on the cylinder. Regular waves breaking on the shoal are generated. After scaling the results by 70:1, the crest height is about 17.5m, the celerity is about 20 m/s, and the shoal depth is 28 m. The transducers have a natural frequency in the range of 250 Hz - 900 Hz (model scale). Hence, the dynamic effects have to be removed by deconvolution. The vertical profile shows a distinct peak around 13 m above the still water level similar to observations from other studies. From the measured forces and by using Equation (3.18), the slamming coefficient C_s is found to be 4.27.

3.1.4.2 Global Force Measurements and Quasi-Static Approach

In addition to the very rapid and localized slamming loads from steep and breaking waves, the global loads generated by the wave slamming on a cylinder are also of great interest.

A number of publications (see e.g. Wiegel, 1982 [3.97]; Tanimoto et al., 1986 [3.86]; Wienke, 2001 [3.99]; Irschik et al., 2004 [3.44]; Wienke and Oumeraci, 2005 [3.98]) have reported measurements of global (depth-integrated) forces and moments on a vertical cylinder, which is either bottom-hinged with a stiff spring force sensor system or hanging "freely" using two connection points. In both cases the set-up corresponds to an almost fixed condition due to the use of a stiff force spring sensor system. The natural period of the global system is clearly longer than that of the excitation force, and therefore the force may be considered as quasi-static in that respect. Still the measured forces are influenced by dynamic resonance effects due to system characteristics, and should usually be considered as system response forces rather than direct excitation forces. The natural period of the system plays a critical role and should be properly taken into account. The effect from the time varying characteristics of the slamming force on the resulting force has been investigated by Tanimoto et al. (1986) [3.86], Wienke (2001) [3.99], Irschik et al., (2004) [3.44].

Another important factor for the total load is the fraction, also called the curling factor γ, of the crest height which impacts on the circular cylinder and can be considered having a vertical front with a very high, uniform particle velocity. The experimental results show large scattering of the value of γ. Depending on the inclination of cylinder relative to the still water surface, the estimated mean values of γ is between 0.2 and 0.8 (Wiegel, 1982 [3.97]; Tanimoto et al., 1986 [3.86]; Irschik et al., 2004 [3.44]; Wienke and Oumeraci, 2005 [3.98]).

Existence of high frequency ringing vibrations on vertical cylinders in steep and energetic waves is a relatively recent observation from model tests. The excitation is related to higher-order wave load effects (Tanimoto et al., (1986) [3.86]; Stansberg et al., (1995) [3.83], Krokstad et al. (1998) [3.50]). The ringing phenomenon may become an issue for wind turbine support structures subjected to passing steep waves.

Chakrabarti et al. (1997) [3.12] estimated drag and inertial coefficients from model tests in breaking waves with current. In the case of waves only, a drag coefficient of 1.4 is estimated, while in the case of waves with current the drag coefficient is reduced to around 1.0. The inertia forces accounted for only about 5% – 10% of the total force, and coefficient estimates are therefore quite uncertain. In Tørum (1989) [3.88], local time-invariant drag and inertia coefficients, C_D and C_M are derived at various vertical levels on a cylinder, from steep regular wave measurements. Similar analyses are made from measurements in breaking waves (Kjeldsen et al., 1986 [3.48]). It is observed that the total forces, as well as the inertia coefficient C_M, increases significantly above the mean water level and can reach up to around 6 at the crest surface.

3.1.4.3 Spatial and Temporal Average of Local Slamming Pressure

Slamming of energetic breaking waves is found to exert high local pressures over a very small area (typically corresponding to 0.1 m^2 or less at full scale). In some studies, the local peak pressure is found to correspond to around 20 MPa at full scale. The slamming peak pressure is also associated with a very short duration in the range of 2 ms – 10 ms. The highest peak normally comes with the shortest duration and the sharpest spatial distribution. The instantaneous spatial distribution often shows strong local effects, especially in the vertical direction since the waves are unidirectional. Meanwhile, the statistical scattering between repeated measurements is also very high, probably related to the random nature of the actual peak event and its location. These pressure levels, as well as the scattering, are confirmed by a number of independent experiments using cylindrical columns, rectangular columns and vertical walls.

On the other hand, those randomly fluctuating shock pressures are not directly relevant to design. It is the pressure averaged over a larger area and with a longer duration that should be taken into account. The measurements made on spatially averaged pressures show clearly lower pressure levels, with maxima typically up to around 2 MPa – 3 MPa. The random scattering is also reduced while the acting time duration is increased.

3.1.4.4 Effects of Water Depth

The literature survey could not determine whether or not the water depth will influence the slamming loads significantly, as long as the wave kinematics is the same. It has not been found that slamming coefficients should depend on the water depth. This is in accordance with the statement made in Oumeraci et al. (1992) [3.69] that the main difference between the wave slamming in deep and shallow water is found in the wave characteristics, while the slamming physics itself may not be very different. Nevertheless, it does not automatically mean that there is no such effect, since slamming measurements are subject to large statistical uncertainties.

The water depth will, however, influence the wave characteristics. In shallow water, the celerity is reduced, the local steepness is increased, and the occurrence probability of breaking and very steep waves will increase. Breaking wave particle velocity measurements in finite water indicate that maximum free-surface values are close to the celerity (Chaplin et al. (1992) [3.16], Irschik et al. (2002) [3.45]).

3.1.4.5 Free Surface Particle Velocity

In breaking waves, the water particle velocity V at free surface is often assumed to be equal to the wave celerity u_c. This is empirically found to be a reasonable choice as seen from many reported velocity measurements (Chaplin et al., 1992 [3.16], Wienke (2001) [3.99], Irschik et al., (2002) [3.45], Wienke and Oumeraci (2005) [3.98]). Experiments are performed in finite to shallow water. Most of the test runs reported are conducted at a relatively large scale (around 1:10 or similar).

It is also reasonable to believe that the real maximum particle velocity in breaking waves exceeds the phase velocity, since this is one of the basic criteria for breaking to occur. This is reflected in the DNV recommendation (2010a) [3.24], where $V = 1.2u_c$ is taken for undisturbed waves and the breaking wave height are defined as the most probable highest values for a given return period. Numerical and experimental studies reported by Stansberg (2011b) [3.81] show that a factor of 1.2 may be a reasonable choice. However, there are other sources, such as Ochi and Tsai (1984) [3.66], stating that the breaking wave particle velocity is lower than or approximately equal to the wave celerity.

The discrepancy in the measurement of breaking wave particle velocity may be partly due to different breaking wave experiment setups. It may also, in principle, be caused by uncertainties

connected with measurements. For example, the vertical variation in the particle velocity under a breaking wave is very large, and the measured velocity can be very sensitive to the actual vertical sampling location.

It is difficult, on the basis of various observations and suggestions in the literature, to make a firm recommendation on which factor should be used along with the wave celerity to define the maximum water particle velocity in a breaking wave. To the extent of the literature review carried out in this report, however, it appears that 1.0 or higher should be applied to the plunging breaking wave slamming on vertical circular cylinders.

3.1.5 Existing Design Guidelines

There are several design standards dealing with the prediction of design slamming loads from wave breaking on vertical or horizontal cylinders. They are mostly referring to the simplified and empirical engineering modeling discussed in Section 3.1.2. The conventional format as defined in Equation (3.7) for the slamming force per unit length, f_S, and Equation (3.19) for the local slamming pressure, p_S, is summarized below:

$$f_S = \rho C_s R V^2 \tag{3.21}$$

$$p_S(x) = \frac{1}{2} \rho C_{s,Local} V^2 \tag{3.22}$$

In this subsection, some of commonly known standards are briefly reviewed in alphabetical order. For more details, the readers are referred to the original publications.

ABS (2010a) [3.1] defines an equation for calculating wave slamming (impact) pressure on stiffened flat plates and slender tubular members. The formula is expressed in a typical format that is convenient for the calculation of structural scantling. A pressure distribution factor is defined to take into account spatial averaging of local slamming pressures for flat panels, stiffeners and girders in a stiffened shell with a rectangular or circular cross-section. For slender tubular members, the slamming local pressure is required to be applied on the width of member, i.e. $2R$, and from the still water level to the maximum wave crest height of design sea state. In deep water and with definition of free surface water particle velocity V=0.77u_c following Ochi and Tsai (1984) [3.66], the slamming pressure equation defined in ABS (2010a) [3.1] for slender

tubular members can be reformatted according to Equation (3.21) and (3.22), which lead to the slamming coefficient $C_s = C_{s,Local} = \pi$. The celerity u_c is associated with the design sea state with 100-year return period.

API RP 2A-WSD (2007) [3.3] and ISO 19902 (2007) [3.42] address the slamming force per unit length (or height) on a slender tubular member using the same approach. Both recommend using Equation (3.21) with a slamming coefficient between $C_s = 0.5\pi - 1.7\pi$, depending on the rise time and natural frequency as considered by Sarpkaya (1978) [3.74]. The reference is also made to Sarpkaya and Isaacson (1981) [3.75].

DNV (2010a,b) [3.24] [3.25] recommends for vertical slender cylinders, the slamming force per unit height is given by Equation (3.21) with a slamming coefficient up to 5.15 following Campbell and Weynberg, 1980 [3.11] for smooth circular cylinders. The free-surface particle velocity of breaking waves is defined as 1.2 times of the celerity u_c of the most probable highest breaking wave with a given return period. The most probable highest breaking wave height is taken as 1.4 times of the most probable significant wave height with the same return period.

GL (2005) [3.35], IEC 61400-3 (2009) [3.40] and ISO 21650 (2007) [3.43] adopt the approach developed by Wienke (2001) [3.99] and Wienke and Oumeraci (2005) [3.98], whose model is introduced in Section 3.1.2.3. Shallow water is explicitly considered in this slamming load model.

The primary concern about the wave slamming for offshore wind turbines is the slamming force exerted on monopile foundations, which are vertically oriented, large diameter circular cylinders. For those more complex offshore wind turbine support structures, such as jackets, the wave slamming should also be considered for the design of horizontal members. A number of guidelines, such as API RP 2A-WSD (2007) [3.3] and ISO 19902 (2007) [3.42], are available for the local design of horizontal members of oil and gas platforms and can be used for the application to similar members of an offshore wind turbine support structure. NORSOK N-003 (2007) [3.65] takes a different approach than API and ISO by considering the slamming force as the Morison type of drag loads. It recommends using a minimum drag coefficient of 3 along with a dynamic amplification factor of at least 2, unless the dynamic response analysis can justify a smaller dynamic amplification effect. If the time history of wave slamming on a horizontal circular cylinder is considered important, an approach developed by Kaplan (1992) [3.47] may be applied.

Table 3.2 provides a brief comparison of commonly used design guidelines for wave slamming loads. Further comparisons of the typical slamming load models as well as the responses of the monopile wind turbine support structures subjected to the slamming loads predicted by those models are presented in Section 3.3.

Table 3.2 Commonly Used Design Guidelines for Wave Slamming Loads

Slamming Load Model	*IEC 61400-3 (2009)* *ISO 21650 (2007)* *GL (2005)* *ABS (2010b)*	*DNV (2010a,b)*	*ABS (2010a)*	*API RP 2A-WSD (2007)* *ISO 19902 (2007)*
Analytical Model	Wienke-Oumeraci	Campbell-Weynberg	Ochi-Tasi	Sarpkaya
Load Type	Dynamic	Dynamic	Quasi-static load for determining scantling of tubular members, plates, stiffeners and girders in splash zone	Quasi-static load for local structural sizing of horizontal members in the splash zone
Slamming Coefficient (C_s)	• Time variant • 2π at t=0 for force per unit length	• Time variant • 5.15 at t=0 for force per unit length	• π for global forces per unit length on slender members	• 0.5π~1.7π for force per unit length • π for dynamic analysis and 5.5 otherwise
Wave Particle Velocity (V)	Wave celerity, u_c	$1.2u_c$ and breaking wave height H_b may be calculated H_b=$1.4H_s$ (significant wave height) at a given return period	$0.77u_c$ and breaking wave height H_b=$1.86H_s$ in deep water. H_s is associated with 100-year return design sea state.	Water particle velocity normal to the member axis at impact
Area Subjected to Slamming Load	A curling factor is defined for plunging breaking waves acting on vertical/inclined tubular members. Local pressure is to be applied to the width of a tubular member.	Local pressure is assumed on a sector of 45° with a height of $0.2H_b$ in the range of still water level and wave crest height.	Slamming force per unit length is to be applied on the width of tubular member and from the still water level to the maximum design wave crest height.	No guidance

3.2 Parameter Study

3.2.1 Wave Related Parameters

This section lists the wave and structure related parameters that are of significance for the estimation of wave slamming loads. For each of these parameters, related physical phenomena or parameters are provided. A number of physical relations important to the breaking waves are summarized in Section 3.2.3. The Reynolds number is not listed here since viscosity is considered insignificant for the wave slamming problem. Similarly, the Keulegan-Carpenter number (API RP 2A-WSD, 2007 [3.3]) is also omitted. It is related to the relative importance of the drag and inertia terms in the Morison equation, which corresponds to the quasi-static part of wave force, but is not directly related to the dynamic slamming component, as formulated in Section 3.1.2.

3.2.1.1 Water Depth

- Breaking Limit. The wave breaking limit introduced by Miche (see Section 3.2.3.2) gives the maximum wave slope as a function of the ratio of the water depth to the wave length. The lower the water depth, the lower the slope limit for breaking waves. Consequently, wave breaking occurs more often in shallower water.

- Dispersion Relation. The water depth directly influences the dispersion relation, i.e. the relation between the wave frequency ω and the wave length L. Consequently, the wave celerity, or phase velocity also depends on the water depth. The lower the water depth, the slower the phase velocity will be. For breaking waves, the maximum horizontal water particle velocity is about the same as the wave celerity. Therefore, the maximum horizontal water particle velocity, which is typically taken as the slamming velocity, also decreases with lowering water depth.

- Ursell Number. The Ursell number, which is related to the validity of the Stokes and long wave theories, depends on the water depth. See also Section 3.2.3.3.

- Non-linearity. For long wave theory, such as Boussinesq-type models, one of the two small parameters of the perturbation expansion is the ratio of the water depth d to the wave length L. As the water depth increases, the non-linearity in these models increase, and therefore linear solutions become invalid.

3.2.1.2 Wave Height

- Wave Kinematics. According to linear wave theory, the water particle velocity and acceleration are proportional to the wave height. Higher waves will thus result in larger wave loads, including drag and inertia components, as well as slamming loads.

- Wave Steepness. The wave height is directly related to the wave steepness, which is the ratio of wave height to wave length.

- Area of Slamming. For breaking waves, the higher the wave height, the larger the area of slamming on the structure (Wienke and Oumeraci, 2005 [3.98]). Therefore, higher waves contribute to larger slamming loads.

- Ursell Number. The Ursell number, which is related to the validity of the Stokes and long wave theories, depends on the wave height. See also Section 3.2.3.3.

3.2.1.3 Wave Period

The wave period is directly related to the wave length through the dispersion relation given in Section 3.2.3.1.

- Wave Kinematics. According to linear wave theory, the fluid particle velocity is proportional to the inverse of the wave period T, and the particle acceleration is proportional to T^2. Longer waves will thus provide smaller wave loads.

- Breaking Limit. The wave breaking limit introduced by Miche gives the maximum wave slope as a function of the ratio of the water depth to the wave length, which is directly related to the wave period. See also Section 3.2.3.2.

- Wave Steepness. The wave period is directly related to the wave steepness, which is the ratio of wave height to wave length.

- Diffraction Effects. Diffraction effects for a surface-piercing circular member become significant when the ratio of its diameter to the incident wave length exceeds 1/5. See also Section 3.2.3.4.

- Ursell Number. The Ursell number, which is related to the validity of the Stokes and long waves theories, depends on the wave length and therefore on the wave period. See also Section 3.2.3.3.

3.2.1.4 Wave Steepness

The wave steepness, which is defined as the ratio of the wave height to the wave length, is used as a small perturbation parameter in the perturbation expansion in both Stokes' and long wave theories. With large steepness values, the wave geometric and kinematic properties deviate from those predicted by linear wave theory. In practice, the larger the particle velocities and accelerations, the higher will be wave crests and therefore larger local steepness will be observed. For irregular waves, a characteristic steepness S_p can be defined using the significant wave height H_s and the spectral peak period T_p such that $S_p = 2\pi H_s/(gT_p^2)$, where g is the acceleration of gravity.

3.2.2 Structure Related Parameters

3.2.2.1 Diameter

- Diffraction Effects. Diffraction effects (see also Section 3.2.3.3) for a surface-piercing circular member become significant when the ratio of its diameter to the wave length exceeds 1/5. The larger the circular member, the stronger the diffraction effects.

3.2.2.2 Inclination

- Relative Angle between the slamming surface and the direction of water particle velocity. The inclination of the circular cylinder will change the relative angle between slamming surface and the water particle velocity, and therefore will change the magnitude of the slamming loads.

- Area of Slamming. The area of slamming increases with the inclination of a circular cylinder towards an incident breaking wave. Wienke and Oumeraci (2005) [3.98] obtained a maximum slamming load on a vertical circular cylinder at an inclination of 25 degrees towards the incident breaking waves, although this result is based on a limited number of breaking wave realizations.

3.2.2.3 Characteristic Structure Area for Pressure Integration

For slamming loads, owing to significant scattering of the localized pressure distribution, the pressure averaged over a given surface area of a circular cylinder decreases with the size of this area. The size of characteristic area, over which the pressure distribution is averaged or measured, has to be taken into account.

3.2.2.4 Characteristic Structural Dynamic Response Properties

Structural dynamic response properties, such as natural periods and modal shapes, coupled with the intensity and time variant nature of slamming loads, will determine the dynamic responses of a structure subjected to slamming loads. Significant dynamic responses could be excited not only in local structural members where the slamming load is applied but also in the global structure.

3.2.3 Some Important Physical Relationships

3.2.3.1 Dispersion Relation

In finite water depth d and according to the linear Stokes theory, the dispersion relation becomes

$$\left(\frac{2\pi}{T}\right)^2 = gk\tanh(kd) \tag{3.23}$$

where T is the wave period, k ($=2\pi/L$) the wave number, L the wave length and g the acceleration of gravity. The wave celerity (phase velocity), u_c, is given by

$$u_c = \omega / k \quad \text{with} \quad \omega = 2\pi / T \tag{3.24}$$

In deep water, the dispersion relation may be simplified to

$$L = gT^2 / 2\pi \tag{3.25}$$

and the wave celerity $u_c = gT/2\pi$.

3.2.3.2 Breaking Limit

The breaking wave limit given by Miche (see Chakrabarti, 1987) is

$$\frac{H}{L} = 0.142\tanh(kd) \tag{3.26}$$

where H is the wave height, L the wave length, k (=$2\pi/L$) the wave number and d the water depth. The limiting steepness of the breaking waves decreases with the water depth. In deep water the limiting steepness H/L approaches to a constant of 0.142. In shallow water, the limiting wave height is about H=0.78d for the flat seabed, although the limiting height in shallow water increases with increasing seabed slope (Costal Engineering Manual (2008) [3.89]).

Lower values of the breaking wave height have been observed in irregular waves where breaking could occur over a large area as individual wave components reach their breaking limit. A commonly cited breaking wave limit height is the modified Miche criterion (see Costal Engineering Manual (2008) [3.89], Ochi, (2003) [3.67]):

$$\frac{H_{m0}}{L} = 0.1\tanh(kd) \tag{3.27}$$

where H_{m0} is the zero-moment wave height. In shallow water with flat seabed, H_{m0}=0.55d (see also Section 3.1.1.1).

3.2.3.3 Ursell Number

The Ursell number (U_r) is given by

$$U_r = HL^2/d^3 \tag{3.28}$$

where H is the wave height, L the wave length and d the water depth. In the case when $U_r < 26$ and waves have moderate steepness, the Stokes theory is applicable.

3.2.3.4 Diffraction Effect

When the diameter of a surface-piercing cylinder is small compared to the length of incoming waves, the wave field is altered by the presence of the cylinder. When the diameter of the cylinder becomes larger, the incoming waves will be diffracted. In this case, wave properties such as the surface elevation or the kinematics are more difficult to estimate since the diffracted wave pattern has to be counted. According to API RP 2A-WSD (2007) [3.3], a tubular member with diameter D can be considered as hydrodynamically transparent, i.e. diffraction effects can be neglected, when the member diameter does not exceed one fifth of the incident wave length.

3.3 Comparative Study of Analytical Breaking Wave Slamming Load Models

Four analytical models that represent typical approaches to formulate the slamming load have undergone further evaluation in this section. Direct load model comparisons are performed by comparing the predicted magnitude and time variation of slamming loads. Dynamic responses are calculated for a typical monopile support structure subjected to the slamming loads predicted by the four models. The effect of structural damping ratio and soil stiffness, which affect monopile's natural frequencies and modal shapes, are also evaluated.

3.3.1 Analytical Models Used in the Comparative Study

3.3.1.1 Wienke Model

The background of Wienke model has been discussed in Section 3.1.2.3. Following the notations used in Annex D of IEC 61400-3 (2009) [3.40], the total slamming force F_I is defined as:

- For $0 \le t \le \dfrac{R}{8V\cos\gamma}$,

$$F_I = \lambda \eta_b \rho_{water} R V^2 \cos^2\gamma \left(2\pi - 2\sqrt{\frac{V\cos\gamma}{R}t} \times ar\tanh\sqrt{1-\frac{V\cos\gamma}{4R}t} \right) \tag{3.29}$$

- For $\dfrac{3R}{32V\cos\gamma} \le t' \le \dfrac{12R}{32V\cos\gamma}$ with $t' = t - \dfrac{R}{32V\cos\gamma}$,

$$F_I = \lambda \eta_b \rho_{water} R V^2 \cos^2\gamma \left(\pi\sqrt{\frac{1}{6\dfrac{V\cos\gamma}{R}t'}} - \sqrt[4]{\frac{8}{3}\frac{V\cos\gamma}{R}t'} \times ar\tanh\sqrt{1-\frac{V\cos\gamma}{4R}t'\sqrt{6\frac{V\cos\gamma}{R}t'}} \right) \tag{3.30}$$

The slamming coefficient C_s is determined by

$$C_s = F_I / \lambda \eta_b \rho_{water} R V^2 \tag{3.31}$$

The total duration of the slamming T is given by:

$$T = \frac{13R}{32V\cos\gamma} \tag{3.32}$$

where ρ_{water} is the density of water; V is the free surface water particle velocity which is assumed equal to the wave celerity C; H_b is the wave height at the breaking location; η_b is the maximum elevation of the free surface (crest height); R is the radius of circular cylinder; λ is the curling factor, which is approximately taken as 0.5 for a vertical cylinder; γ ($0^o \leq \gamma < 90^o$) is the angle between the wave direction and the direction normal to cylinder's axis; $\cos\gamma = 1$ is for wave breaking at a vertical cylinder while $\cos\gamma < 1$ is for an over-curling breaking wave front hitting a vertical cylinder, or wave breaking at an inclined cylinder.

Figure 3.3, which is adapted from IEC 61400-3 (2009) [3.40], depicts a schematic illustration of the parameters referred in the equations above.

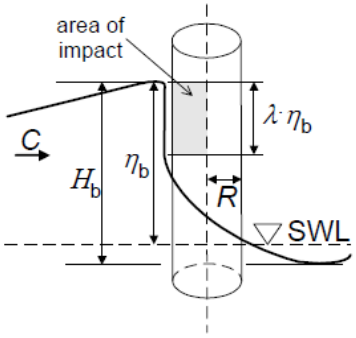

Figure 3.3 Breaking Wave Slamming Load on a Circular Cylinder (IEC 61400-3, 2009)

3.3.1.2 Campbell-Weynberg Model

The Campbell-Weynberg model (DNV, 2010a [3.24]) is based on the model test by Campbell and Weynberg (1980) [3.11] with the horizontal circular cylinders entering into calm water at various constant downward velocities. The curve fitting of test results follows the slamming force per unit length, f_S, as defined in Equation (3.7), such that

$$f_S = \rho C_s R V^2 \qquad C_s = 5.15\left(\frac{2R}{2R+19s} + \frac{0.107s}{2R}\right) \tag{3.33}$$

where ρ is the water density; V is the free surface water particle velocity; R is the radius of circular cylinder; s (=Vt) is the penetration depth. The equation of C_s is valid up to the moment of full submergence (i.e. $s \leq 2R$). Once the cylinder is fully submerged, C_s=0.8. When calculating the slamming force due to a plunging breaking wave on a vertical cylinder, DNV (2010a) [3.24]

recommends the same slamming time duration as defined by Wienke i.e. T=13R/32V, which is much shorter than the time for reaching full submergence. The change (truncation) of this slamming load history could significantly reduce the magnitude of global response of the cylinder as shown in Section 3.3.2

In the present comparative study presented in Section 3.3.2, the water particle velocity is assumed the same as the wave celerity (see Section 3.1.4.5). Curling factor λ, which is not defined in the original Campbell-Weynberg model, is assumed to be 0.5.

3.3.1.3 Goda Model

The Goda model (Goda, 1966 [3.36]; Tanimoto et al., 1986 [3.86]) is based on the von Karman model, which predicts lower C_s (=π) at the beginning of the slamming. The time history of C_s is obtained by including the second order term in the calculation of the length of wetted surface. The slamming force per unit length, f_S, is given as:

$$f_S = \rho C_s R V^2 \quad \text{and} \quad C_s = \pi\left(1 - \frac{V}{R}t\right) \tag{3.34}$$

where ρ is the water density; V is the free surface water particle velocity; R is the radius of circular cylinder. The time history of C_s is a linear function of time and valid till the full submergence of the cylinder.

Goda, et al. (1966) [3.36] derived the curling factor λ=0.4. More recent study by Tanimoto, et al. (1986) [3.86], who extend the application of Goda's model to inclined cylinders, and by Wienke (2001) [3.99], who applies the approach similar to Goda's to derive the curling factor, shows that λ=0.5 is a more reasonable choice for a vertical circular cylinder, i.e. $t \le 2R/V$.

3.3.1.4 Armand-Cointe Model

The Armand-Cointe model (Armand and Cointe, 1986 [3.4]) represents one of the efforts of developing a more accurate approximation of the water pile-up (free surface) by including higher order terms into Wagner's theory. The slamming force per unit length, f_S, is given as:

$$f_S = \rho C_s R V^2 \quad \text{and} \quad C_s = 2\pi - \left(4.72 - \ln\left(\frac{V}{R}t\right)\right)\sqrt{\frac{V}{R}t} \tag{3.35}$$

where ρ is the water density; V is the free surface water particle velocity; R is the radius of circular cylinder. The time history of C_s is a linear function of time. The solution is the second order solution of the asymptotic expansion. Armand and Cointe (1986) [3.4] show that the solution appears to provide a good estimation when Vt/R is small.

Curling factor λ is not defined in the original Armand-Cointe model and is assumed to be 0.5 in the present comparative study.

3.3.2 Comparative Study Results

Nonlinear transient analysis is performed to evaluate the structural responses of a monopile support structure subjected to the wave slamming loads calculated using the models summarized in Section 3.3.1.

The monopile support structure model defined in Section 2.3.3.1 is used in the comparative study. The 100-year return wave conditions in the GOM West Central regions (see Table 2.6) are applied in the analysis, where the wave celerity is 12.51 m/s, the breaking wave height is 12.75 m, and the maximum wave crest height is 10.47 m. The area on the monopile subjected to the breaking wave slamming is determined following Wienke's approach as illustrated in Figure 3.3. A curling factor of 0.5 is applied.

Figure 3.4 depicts the time history of slamming force calculated using the four slamming load models given in Section 3.3.1. Two time durations for the Campbell-Weynberg model are included in the plot. The first starts at the beginning of contact and ends at the moment of reaching full submergence, as the model is originally intended. The second assumes the same slamming duration as that of the Wienke model (see 3.3.1.2).

Figure 3.5 and Figure 3.6 present the time histories of the mudline shear forces and the overturning moments, respectively, calculated by the nonlinear transient finite element analysis. The soil is assumed to be stiff clay and the 1% structural damping is applied. It is shown that

- The slamming time duration can greatly affect the maximum structural responses. Even though the slamming force in the Goda model is on the lower bound ($C_s=\pi$ following von Karman's approach) at the early stage of slamming, the over-stretched time history produces

higher global responses than the Wienke model, which assumes $C_s=2\pi$ at the beginning of slamming following Wagner's approach.

- The responses obtained using the Campbell-Weynberg model and the Wienke model agree relatively well. For the truncated Campbell-Weynberg, the slamming time duration is assumed to be the same as that of the Wienke model and is much shorter than the time required to reach full submerge.

- As indicated in Section 3.3.1.4, the accuracy of the Armand-Cointe model up to the second order improves the solution of original Wagner's model, but can still over-predict the slamming load when *Vt*/*R* is not small.

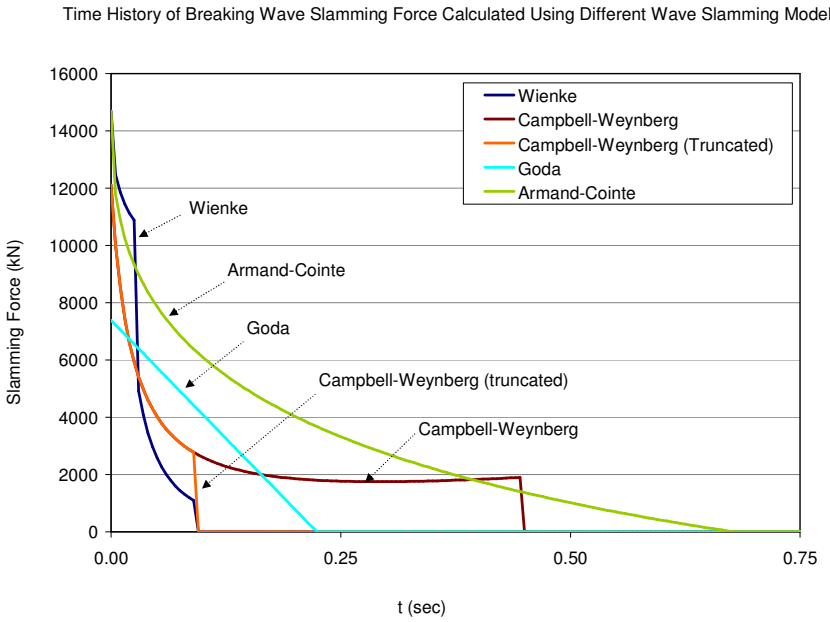

Figure 3.4 Wave Slamming Load of Four Different Models

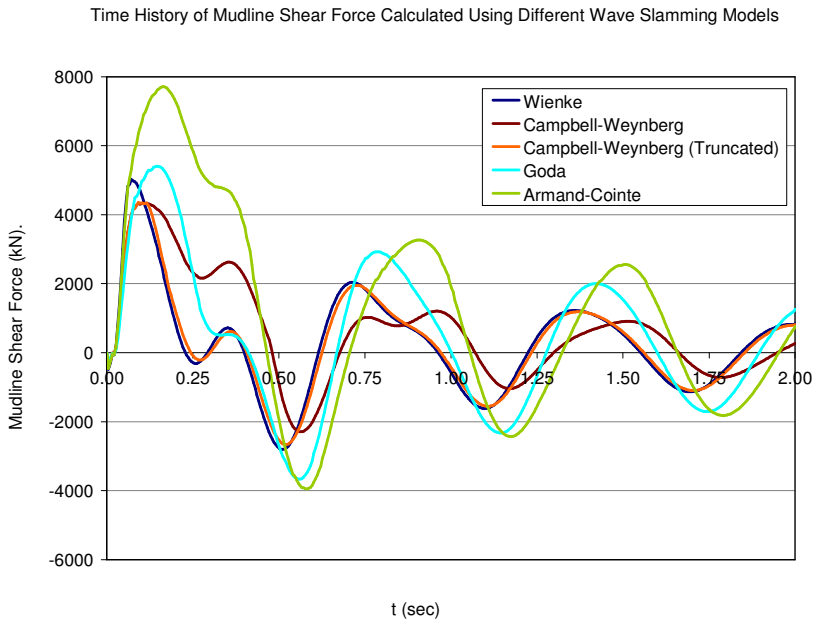

Figure 3.5 Time History of Mudline Shear Forces

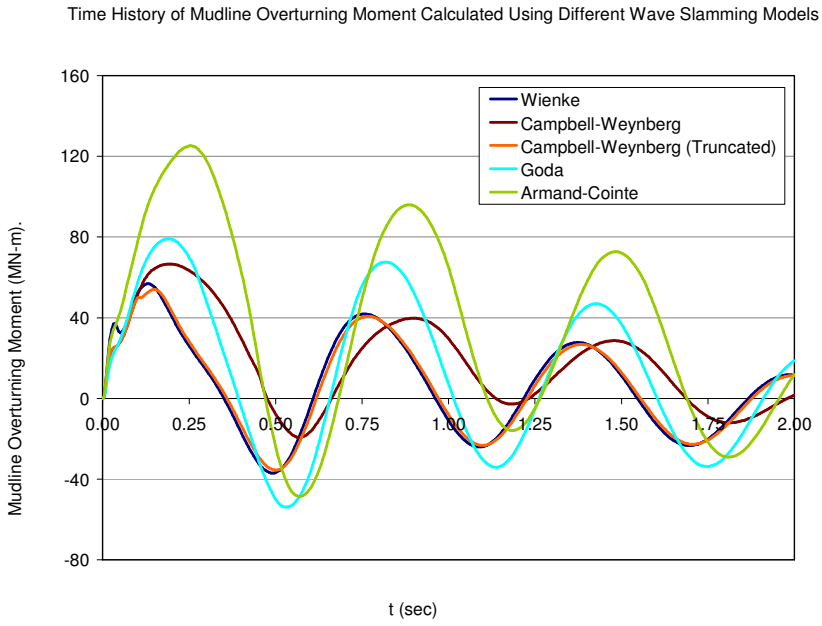

Figure 3.6 Time History of Mudline Bending Moments

Further comparison is made between the Wienke model and the truncated Campbell-Weynberg model for the monopile support structure having various combinations of soil conditions and structural damping ratio. The definition of analysis local cases is given in Table 3.3. Figure 3.7 depicts the undrained shear strength of the stiff and soft soil conditions considered in the analysis.

The maximum mudline shear forces and overturning moments are summarized in Table 3.4. Figure 3.8 and Figure 3.9 are the time series of mudline shear forces calculated using the Wienke and the truncated Campbell-Weynberg model, respectively, while Figure 3.10 and Figure 3.11 show the plots of the time series of mudline overturning moments. The following observations can be made based on the calculation results.

- The slamming loads following the Wienke model consistently result in higher maximum global responses of the monopile support structure.

- In the case where a typical 1% structural damping ratio is applied to the monopile support structure, the global responses due to the slamming loads calculated by the two models are fairly close. The relative difference is about 15% for the mudline shear force and 5% for the mudline overturning moment.

- When the damping ratio is increase to 3%, which may be considered as an upper bound of the damping ratio of a monopile, the time series of global responses show quite significant transient effects at the beginning of the slamming. The differences in the global responses associated with the two slamming load models are scattered between approximately 2% and 24%.

Table 3.3 Load Case Definition for the Wave Slamming Comparison

Load Case	*Slamming Load Model*	*Damping Ratio*	*Soil Type*
Case 1	Wienke	1%	Stiff soil
Case 2	Wienke	3%	Stiff soil
Case 3	Wienke	1%	Soft soil
Case 4	Wienke	3%	Soft soil
Case 5	Truncated Campbell-Weynberg	1%	Stiff soil
Case 6	Truncated Campbell-Weynberg	3%	Stiff soil
Case 7	Truncated Campbell-Weynberg	1%	Soft soil
Case 8	Truncated Campbell-Weynberg	3%	Soft soil

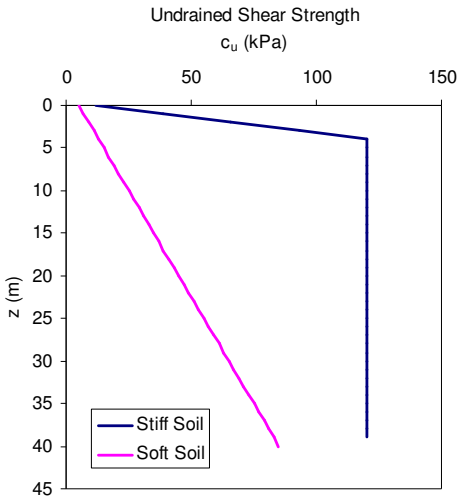

Figure 3.7 Undrained Shear Strength for Stiff and Soft Soil

Table 3.4 Maximum Slamming Responses at the Mudline Calculated Using the Wienke Model and the Truncated Campbell-Weynberg Model

Damping Ratio	*Soil Type*	*Mudline Shear Force (kN)*		*Mudline Bending Momnet (MN.m)*	
		Wienke Model	*Truncated Campbell-Weynberg Model*	*Wienke Model*	*Truncated Campbell-Weynberg Model*
1%	Stiff soil	5023	4346	56.8	53.9
3%	Stiff soil	4208	3432	52.3	52.2
1%	Soft soil	3543	3344	39.0	37.1
3%	Soft soil	3987	3043	35.7	30.0

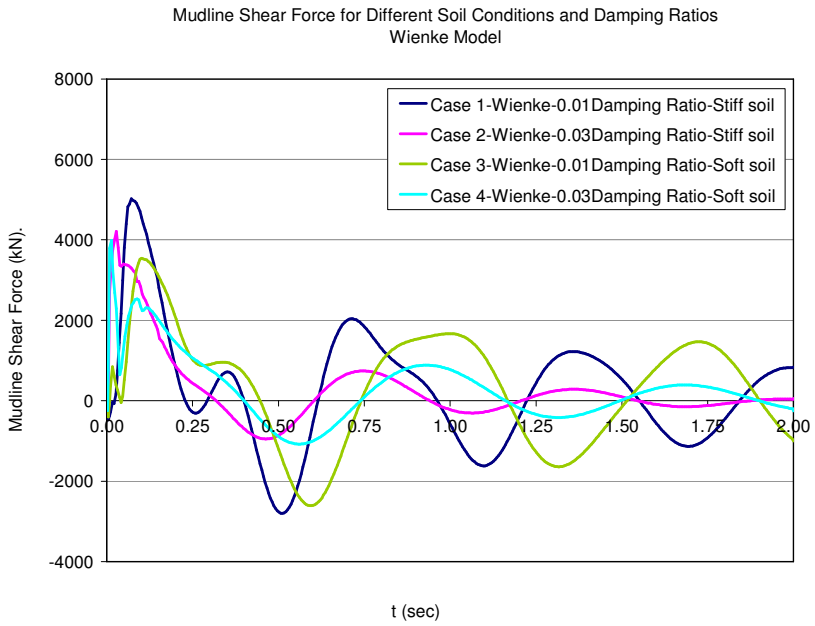

Figure 3.8 Mudline Shear Forces Calculated Using the Wienke Model

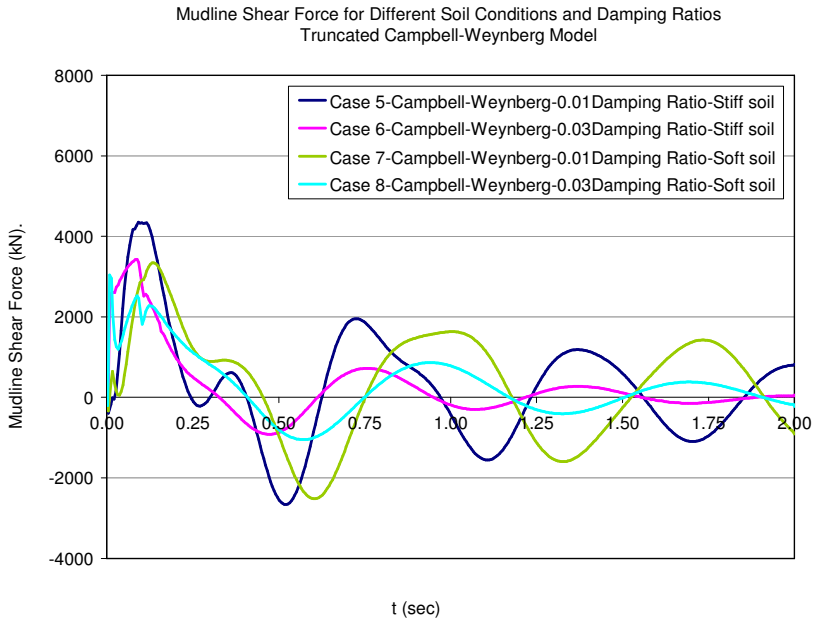

Figure 3.9 Mudline Shear Forces Calculated Using the Truncated Campbell-Weynberg Model

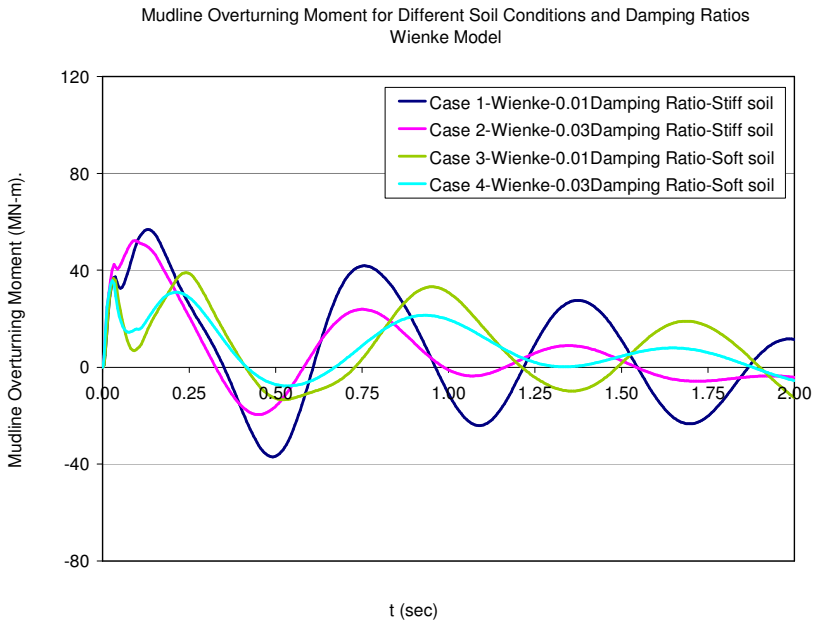

Figure 3.10 Mudline Bending Moments Calculated Using the Wienke Model

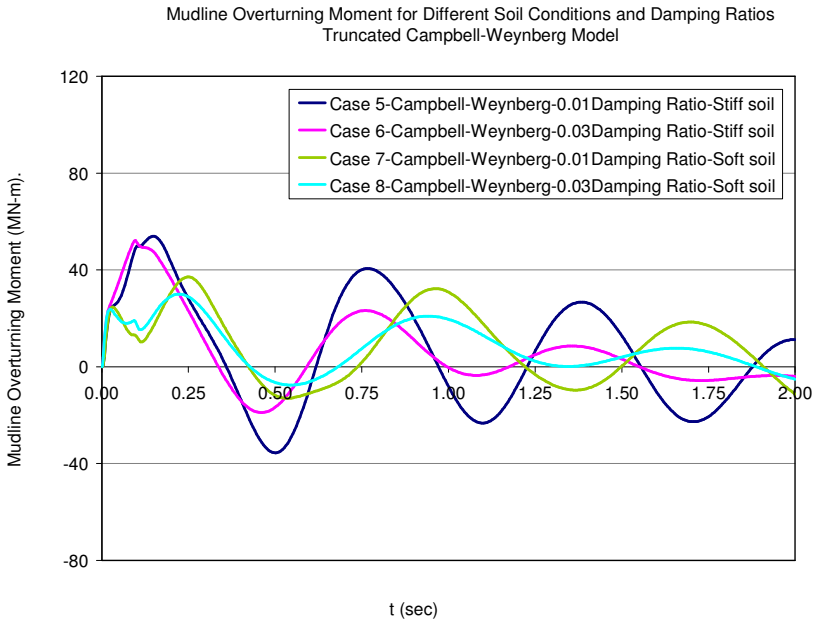

Figure 3.11 Mudline Bending Moments Calculated Using the Truncated Campbell-Weynberg Model

3.4 Conclusions and Recommendations

An accurate prediction of the breaking wave slamming load on a vertical circular cylinder is very complex due to the highly nonlinear nature of slamming. Empirical knowledge from model tests, as well as full scale measurements, is still critically important. Simplified analytical models using empirical coefficients are commonly used in the design of wind turbine support structures. Uncertainties are largely related to the slamming coefficient, the free-surface particle velocity in the crest and the spatial and temporal distribution of the slamming load.

In recent studies, a variety of sophisticated numerical methods and software have been developed. Fully nonlinear models or Navier-Stokes (CFD) solvers are in most cases needed for solving the wave slamming problem. The most important research area includes models for strongly nonlinear waves as well as for the resulting slamming loads on structures. CFD itself or in combination with other methods appears to be a very promising path, while the methods based on the potential theory are unable to predict wave breaking. Still, the prediction of very steep and near-breaking events by the potential theory can also be useful in many cases.

The literature review discusses a number of promising fully nonlinear and CFD numerical approaches and results. However, it appears that while future improvements will probably change the picture, the software is still not accurate and robust enough as a standalone tool for the wave slamming simulation. They do, however, provide useful information that can augment the results obtained from simplified tools and experiments. A significant amount of work is still needed for improving numerical algorithms and also for validating against qualified experimental data. This is a very challenging task partially because of the difficulties in having a consistent interpretation of wave slamming measurements. The need for significant computer resources for CFD analysis also remains an issue.

Experimental data from many model tests on breaking wave slamming have been reviewed, representing different types of experimental set-ups and breaking wave conditions as well as model scales ranging from 1:8 – 1:160. Local pressure measurements using sensors of varying sizes, ranging from pressure probes covering typically full-scale areas of 0.1 m^2 – 1 m^2 to force panels of 5 m^2 – 20 m^2, have been reviewed. Deep, intermediate and shallow water conditions have been considered. For comparison reasons, all data have been scaled up to full scale to model a breaking wave with a typical crest height between 12 m and 17 m along with a free-surface maximum celerity around 17 m/s – 19 m/s. For use in other conditions, results might be scaled

differently. Comparisons have also been made by using normalized data in the form of slamming coefficients.

The literature review has shown that the different measurements give a fairly consistent observation, although more or less different test conditions and model scales are used. Several sources report extreme local ("point") pressures with the magnitude up to 20 MPa at full scale in the given wave conditions. Those measurements of peak local pressures almost always come with large statistical scattering among repeated measurements and also vary significantly in space. The most extreme measurements are connected with very short durations around a few milliseconds. Measurements of spatially averaged pressures over larger areas show lower magnitudes with longer durations.

It is noted that the random scattering is also present in the spatially averaged pressures, although the scattering is somewhat lower than that of local pressures. With respect to structural design it is more relevant to consider the spatially averaged values than the very unstable local pressures. The area for averaging (smoothing) local slamming pressures is dependent upon the actual application and structural details.

The effects on breaking wave slamming going from deep to finite and shallow water seem to be mainly related to the differences in the steep wave characteristics, and not so much to the slamming physics itself when the same wave kinematics is assumed. This observation confirms the finding by Oumeraci et al. (1992) [3.69].

It has not been found, on the basis of the literature reviewed in this study, that slamming coefficients should depend on water depth. However, this does not mean that there is no such effect, simply because slamming measurements are subject to such large statistical uncertainties that the dependency on water depth may be overwhelmed by data scattering. In addition to the model tests, a number of relevant numerical wave models have also been identified. Some of them make use of an extended Boussinesq approach. No clear observation of the effect of the water depth on the slamming physics has so far been made.

However, water depth clearly influences the wave properties. When the water depth approaches the finite and shallow regimes, the celerity is reduced, the local steepness is increased, and the occurrence probability of breaking and very steep waves increases. A detailed knowledge of the irregular steep wave kinematics and breaking at any water depth is essential to a reliable

prediction model. Measurements in finite water indicate that the maximum particle velocity on the free surface of a breaking wave is closely related to the wave celerity.

With respect to the prediction and probability of wave breaking, there are several probabilistic and physical models that have been proposed based on theoretical analyses combined with observations from field and laboratory measurements. Both deep water and finite/shallow conditions have been addressed. An increased probability of breaking with decreasing water depth is expressed in some of the models. The direct influence of the actual breaking probability on the resulting wave slamming loads needs further study.

For practical applications in structural design, simple, but well calibrated analytical slamming load models have shown their unique advantage over more sophisticated numerical simulations and model testing. Based on the findings garnered to the extent of this study, it is believed that the Wienke model stands out as the latest development for calculating slamming forces on vertical and inclined circular cylinders.

The Wienke model starts with the Wagner's approach and is calibrated by a series of well organized large-scale model tests, in which the global responses that are more relevant to the design of turbine support structures subjected to wave slamming are measured in addition to local pressures. The averaging of local pressure measurement is taken into account by defining a curling factor that determines the size of the area subjected to the slamming of breaking wave front. The effect of inclination of cylinder relative to the still water line is one of modeling parameters in the model tests. The effect of inclination on the curling factor is also evaluated. Various wave breaking scenarios are tested and analyzed and shallow water conditions are specifically considered. The observations confirm that the plunging wave breaking right in front of the cylinder generates the highest slamming loads. The observations also lead to a better understanding of spray pattern of water particles during the slamming.

The Wienke model is an analytical model in a simple, easy-to-implement format. It has been referenced in a number of design standards such as IEC 61400-3 Annex D (2009) [3.40], GL (2009) [3.35] and ABS (2010) [3.2] for offshore wind turbines and also in ISO 21650 Annex G (2007) [3.43] for applications to costal structures.

The Campbell-Weynberg model may still be considered as an acceptable alternative for calculating the slamming forces on vertical circular cylinders. However, this model needs to be

used along with the curling factors and slamming duration such as those obtained in Wienke's study. As exemplified in the comparative study, the "net" effect of wave slamming on structural responses is determined not only by the slamming coefficient and water particle velocity but the realistic representation of the spatial and temporal distribution of the slamming process. These four factors must be considered collectively in assessing the validity of a wave slamming load model.

4 Summary

This project is focused on two subjects that are critical to the design of offshore wind farms on the US OCS. The first is the governing load cases and load effects for wind turbines subjected to hurricane environmental conditions on the US OCS. The second is the evaluation of breaking wave slamming load models applicable to the design of offshore wind turbine support structures.

The key findings and the recommended design practices are provided in Section 2.10 for the hurricane design criteria and Section 3.4 for the breaking wave slamming load models. Although the applicability of the conclusions drawn in this report may be limited to the extent of the site conditions, the types of support structures and the wind turbine used in the case studies, efforts have been made to choose representative data and designs.

In addition to what has been accomplished in this project, the following subjects relevant to the present study are believed to be of great importance and recommended for further studies.

- **Turbulent Wind Model**

Although numerous studies have been carried out to simulate the hurricane turbulent wind field, hurricane wind field modeling remains a challenging technical area. The model recommended in API RP 2A-WSD (2007), as well as in API Bulletin 2INT MET (2007) and ISO 19902 (2007), is based on the measurement of offshore wind conditions near Norwegian coast. It has been used extensively by the offshore oil and gas industry for the design of topside structures and station keeping systems. IEC 61400-3 (2009) refers to IEC 61400-1 (2005) for the turbulent wind models that are developed mostly considering on-land wind measurements for the terrain with small surface roughness. Some studies have been performed to compare various turbulent wind models, but no clear recommendation has been made. This study evaluates the responses of a typical offshore wind turbine subjected to the turbulent wind field generated using two representative turbulent wind models. The results show significant discrepancy that could greatly affect the strength and particularly fatigue design. More studies are desirable to gain further understanding of the hurricane wind modeling as well as its applicability to the offshore wind turbine design.

- **Foundation Model**

This project does not cover the effect of foundation variations on the response characteristics of an offshore wind turbine support structure. Soil properties of stiff clay are assumed in the case studies. The interaction between soil and pile foundation is based on the guidelines of API RP 2A-WSD (2007). It is noted that the applicability of the design criteria specified in API RP 2A-WSD (2007) to large diameter pile foundations remains an undetermined area. Long term foundation degradation due to the high frequency cyclic loading and seabed scour is another important and potentially critical design issue for which further research is needed.

- **Offshore Wind Turbine Analysis Procedures and Software Tools**

The load and response analysis for offshore wind turbines should consider complex interactions among aerodynamic loads, hydrodynamic loads, actions of turbine safety and control systems, structural dynamic responses and soil foundation reactions. The sophistication of the analysis for offshore wind turbines calls for establishing rational analysis procedures that can appropriately take into account the unique load and response characteristics of offshore wind turbines. The development of such analysis procedures is partially dependent upon the capability of simulation software tools. The U.S. Department of Energy is currently sponsoring the development of next-generation simulation tools for both bottom founded and floating offshore wind turbines, with the primary focus on software capability enhancements and software validations. It is believed that the development and validation of offshore wind turbine analysis procedures on the basis of the latest simulation capabilities is equally important.

- **Validation of Slamming Load Model**

Few field measurements of wave slamming loads and resultant structural responses are available in the public domain. Various slamming load models have been developed and calibrated using the scaled model tests. This is based on the assumption that the scaling would not significantly change the characteristics of slamming, although wave slamming is a strong nonlinear random process. It is desirable, however, to use field measurement data to verify and possibly further improve wave slamming load models. Since the wave slamming occurs along with other ocean environmental conditions such as waves, surges and currents, the field measurements can provide valuable information for verifying the assumption of linear superposition of hydrodynamic loads

from various sources. The field measurement is preferred to make in typical offshore wind farms. Both metocean and structural responses need to be measured concurrently.

References for Section 2

2.1 Alves, J.G.M, Tolman, H.L. and Chao, Y., 2004 Hurricane -Generated Wind-Wave Research at NOAA/NCEP. 8th International Workshop on Wave Hindcasting and Forecasting, Turtle Bay, Hawaii, Paper G3

2.2 American Bureau of Shipping (ABS), 2010. Guide for Building and Classing Offshore Wind Turbine Installations.

2.3 American Bureau of Shipping (ABS), 2011. Guide for Buckling and Ultimate Strength Assessment for Offshore Structures.

2.4 American Petroleum Institute (API), 2007. API Bulletin 2INT-MET, Interim Guidance on Hurricane Conditions in the Gulf of Mexico

2.5 American Petroleum Institute (API), 2007. API RP 2A-WSD: Recommended Practice for Planning Designing and Constructing Fixed Offshore structures – Working Stress Design, 21st Edition (with Errata and Supplement in 2002, 2005 and 2007).

2.6 American Society of Civil Engineers (ASCE), 2010. Minimum Design Loads for Buildings and Other Structures (ASCE 7-10),

2.7 Andersen, O. J. and Lovseth, J., 2006. The Frøya Database and Maritime Boundary Layer Wind Description. Marine Structures, 19 (2-3): 173-192.

2.8 Argyriadis, K., 2003. Recommendations for Design of Offshore Wind Turbines - External Conditions, State of the Art. Report for RECOFF, Germanischer Lloyd, Hamburg, Germany.

2.9 Ashuri, T. and Zaaijer, M.B., 2007. Review of Design Concepts, Methods, and Considerations of Offshore Wind Turbines. European Offshore Wind Conference, Berlin, Germany.

2.10 Barth, S. and Peinke, J., 2007. Intermittence and Scale Separation above the North Sea. 2007 European Wind Energy Conference, Milan, Italy

2.11 Berek, E.P., Cooper, C.K., Driver, D.B., Heideman, J.C., Mitchell, D.A., Stear, J.D. and Vogel, M.J., 2007, Development of Revised GoM Metocean Hurricane Conditions for Reference by API Recommended Practices. Offshore Technology Conference, Houston, TX, Paper No. OTC 18903.

2.12 Black, P.G., Buchan, S.J. and Cohen, R.L., 1999. The Tropical Cyclone Eyewall Mesovortex: A Physical Mechanism Explaining Extreme Peak Gust Occurrence in TC Olivia, Offshore Technology Conference, Houston, Texas, 3–6 May, 1999, paper No. OTC 10792.

2.13 Bouws, E., Gunther, H., Rosenthal, W. and Vincent, C.L., 1985. Similarity of the Wind Wave Spectrum in Finite Depth Water: 1. Spectral Form. J. Geophys. Res., 90(C1): 975-86.

2.14 Buchan, S.J., Black, P.G. and Cohen, R.L., 1999. The Impact of Tropical Cyclone Olivia on Australia's Northwest Shelf, Offshore Technology Conference, Houston, Texas, Paper No. OTC 10791.

2.15 Buhl, M.L. and Manjock, A., 2006. A Comparison of Wind Turbine Aeroelastic Codes Used for Certification, National Renewable Energy Laboratory, Golden, CO, Report Number: NREL/CP-500-39113.

2.16 Clausen, N., Candelaria, A., Gjerding, S., Hernando, S., Norgard, P., Ott, S. and Tarp-Johansen, 2007. Wind Farms in Regions Exposed to Tropical Cyclones. 2007 European Wind Energy Conference, Milan, Italy

2.17 Clausen, N., Ott, S., Tarp-Johansen, N. 2006a. ASEAN Wind 2005 Design of Wind Turbines in Typhoon Area. Riso National Laboratory, Roskilde, Denmark.

2.18 Clausen, N., Ott, S., Tarp-Johansen, N., Norgard, P., Larsen, X., Pagalilawan, E. and Hernando, S., 2006b. Design of Wind Turbines in an Area with Tropical Cyclones. 2006 European Wind Energy Conference, Athens, Greece.

2.19 Danish Energy Agency, 2001. Recommendation for Technical Approval of Offshore Wind Turbines.

2.20 Dean, R. G., 1974. Evaluation and Development of Water Wave Theories for Engineering Application, Special Report No. 1, U. S. Army Corps of Engineers, Coastal Engineering Research Center. Fort Belvoir, VA.

2.21 Det Norske Veritas (DNV), 2010a. OS-J101 Design of Offshore Wind Turbine Structures.

2.22 Det Norske Veritas (DNV), 2010b. RP-C205 Environmental Conditions and Environmental Loads.

2.23 Dvorak, V., 1975. Tropical Cyclone Intensity Analysis and Forecasting from Satellite Image. Monthly Weather Review, 103: 420–430.

2.24 Elkinton, C.N., Rogers, A.L., Manwell, J.F., McGowan, J.G, and Lueck, M., 2004. Influences of Offshore Environmental Conditions on Wind Shear Profile Parameters in Nantucket Sound. Proc. World Renewable Energy Congress, Denver CO.

2.25 Engineering Sciences Data Unit (ESDU), 1982. Strong Winds in the Atmospheric Boundary Layer, Part 1: Mean Hourly Wind Speed, Item No. 82026, London.

2.26 Engineering Sciences Data Unit (ESDU), 1983. Strong Winds in the Atmospheric Boundary Layer, Part 2: Discrete Gust Speeds," Item No.83045, London.

2.27 Fabian, V., Wojciech, P. and Kaufer, D., 2011. Description of a Basic Model of the "UpWind Reference Jacket" for Code Comparison in the OC4 Project under IEA Wind Annex 30.

2.28 Frandsen, S., Tarp-Johansen, N.J. Norton, E. Argyriadis, K., Bulder, B. and Rossis, K., 2005. Recommendations for Design of Offshore Wind Turbines. Final Technical Report. Risø National Laboratory, Roskilde, Denmark.

2.29 Garciano, L. E. O. and Koike, T., 2007. A Proposed Typhoon Resistant Design of a Wind Turbine Tower in the Phillipines. International Journal of Japanese Society of Civil Engineers, 63(2), 181-189.

2.30 Garciano, L. E. O., Koike, T., 2010. New Reference Wind Speed for Wind Turbines in Typhoon-prone Areas in the Philippines. J. Struct. Engrg. Volume 136, Issue 4, pp. 463-467 (April 2010)

2.31 German Federal Maritime and Hydrographic Agency (BSH), 2007. Standard Design of Offshore Wind Turbines.

2.32 Germanischer Lloyd (GL), 2005. Guideline for the Certification of Offshore Wind Turbines.

2.33 Giammanco, I.M., Schroeder, J.L., Hirth, B.D., 2007. Hurricane Ivan Deployment Summary. Wind Science and Engineering Research Center, Texas Tech University, Lubbock, Texas

2.34 Harper, B.A., Kepert, J.D. and Ginger, J.D., 2009. Guidelines for Converting Between Various Wind Averaging Periods in Tropical Cyclone Conditions, World Meteorological

Organization (WMO) Sixth Tropical Cyclone RSMCs/TCWCs Technical Coordination Meeting, Brisbane, Australia, November 2-5, 2009

2.35 Holland, G.J., An analytic model of the wind and pressure profiles in hurricanes, Monthly Weather Review, 108 (1980) 1212-1218.

2.36 Hsu, S.A., 2008. Estimating 3-second and Maximum Instantaneous Gusts from 1-minute Wind during a Hurricane. Electronic Journal of Structural Engineering, 77-79.

2.37 International Electrotechnical Commission (IEC), 2005. IEC 61400-1: Wind turbines – Part 1: Design Requirements, 3rd Edition.

2.38 International Electrotechnical Commission (IEC), 2005. IEC 61400-1 Ed.3: Wind turbines – Part 1: Design Requirements.

2.39 International Electrotechnical Commission (IEC), 2009. IEC 61400-3: Wind turbines – Part 3: Design Requirements for Offshore Wind Turbines, 1st Edition.

2.40 International Electrotechnical Commission (IEC), 2009. IEC 61400-3 Ed.1: Wind turbines – Part 3: Design Requirements for Offshore Wind Turbines.

2.41 International Organization for Standardization (ISO), 2005. ISO 19901-1: Petroleum and natural gas industries - Specific requirements for offshore structures Part 1: Metocean design and operating considerations. Geneva, Switzerland.

2.42 International Organization for Standardization (ISO), 2007. ISO 19902: Petroleum and natural gas industries - Fixed Steel Offshore Structures. Geneva, Switzerland.

2.43 Ishihara, T., Yamaguchi, A., Takahara, K., Mekaru, T. and S. Matsuura, S., 2005. An Analysis of Damaged Wind Turbines by Typhoon Maemi in 2003. The Sixth Asia-Pacific Conference on Wind Engineering, 2005, Seoul, Korea.

2.44 Jha, A., Dolan, D. Musial, W. and Smith, C., 2009. On Hurricane Risk to Offshore Wind Turbines in US Waters. Offshore Technology Conference, Houston, Texas, Paper No. OTC 20811.

2.45 Jonkman, J. and Musial, W., 2010. Final Technical Report for Subtask 2: The Offshore Code Comparison Collaboration (OC3), IEA Wind Task 23 Offshore Wind Technology and Deployment. International Energy Agency, Paris, France.

2.46 Jonkman, J.M. and Buhl, M.L., 2005. FAST User's Guide. National Renewable Energy Laboratory, Golden, Colorado, Report No. NREL/TP-500-38230.

2.47 Jonkman, J.M., Butterfield, S., Musial, W. and Scott, G., 2009. Definition of a 5-MW Reference Wind Turbine for Offshore System Development. National Renewable Energy Laboratory, Golden, Colorado, Report No. NREL/TP-500-38060

2.48 Kogaki, T., 2010. IEA WIND ANNEX XI Topical Expert Meeting #64 on Wind Conditions for Wind Turbine Design, Tokyo, Japan

2.49 Langreder, W. and Højstrup, J., 2007. Going to Extremes: A Parametric Study on Peak-Over-Threshold and Other Methods. 2007 European Wind Energy Conference, Milan, Italy

2.50 Mann, J., Ott, S., Jorgensen, B.H. and Frank, H.P., 2002, WAsP Engineering 2000, Risø National Laboratory, Roskilde, Denmark. Report No: Risø–R–1356.

2.51 Manwell, J.F., Rogers, A.L., McGowan, J.G, and Elkinton, C.N., 2004. Characterization of the External Conditions for the Design of Offshore Wind Energy Systems in the United States. Proc. of the AIAA/ASME Wind Energy Symposium, Reno, NV.

2.52 Meilan, A. and Tsouroukdissian, A.R., 2010. Development and Adaptation of Wind Turbines to Typhoons and Earthquakes Conditions. Proc. Association of the Electricity Supply Industry of East Asia and the Western Pacific.

2.53 MMI Engineering Inc., 2009. Comparative Study of OWTG Standards. Comparative Study of Offshore Wind Turbine Standards JIP Report.

2.54 National Oceanic & Atmospheric Administration, NCEP/NCAR Reanalysis Project. http://www.cpc.ncep.noaa.gov/products/wesley/reanalysis.html

2.55 National Oceanic & Atmospheric Administration, NOAA WAVEWATCH III. http://polar.ncep.noaa.gov/waves/

2.56 Oceanweather, Inc. http://www.oceanweather.com/metocean/index.html

2.57 Ochi, M. K. and Shin, Y. S., 1988. Wind Turbulent Spectra for Design Consideration of Offshore Structures, Offshore Technology Conference (OTC), Houston, Texas, Paper No. OTC 5736.

2.58 Ochi, M.K., 2003. Hurricane-Generated Seas. Elsevier Ocean Engineering Book Series (Volume 8), Elsevier Ltd. Oxford, UK.

2.59 Okazaki, T. Watabe, H. and Ishihara, T., 2005. Development of Typhoon Simulation Technique- Toward Estimation of Typhoon Risk in Japan, The Fourth European & African Conference on Wind Engineering, Prague, 11-15 July, 2005, Paper No. 167IV

2.60 Ott, S., 2006. Extreme Winds in the Western North Pacific. Risø National Laboratory, Roskilde, Denmark, Report No. Risø-R-1544.

2.61 Paulsen, B.M. and Schroeder, J.L., 2005. An Examination of Tropical and Extratropical Gust Factors and the Associated Wind Speed Histograms. Journal of Applied Meteorology, 44, 270-280

2.62 Saigal, R., Dolan, Der Kiureghaian, A. Camp, T. and Smith, C., 2007. Comparison of Design Guidelines for Offshore Wind Energy Systems. Offshore Technology Conference, Houston, Texas, Paper No. OTC 18984.

2.63 Sharples, M., 2010, Structure, Equipment and Systems for Offshore Wind Farms on the OCS, Part 2 - Commentary. Minerals Management Service Department of the Interior, MMS TA&R Project No. 633.

2.64 Stewart, S.W 2008. U.S. Offshore Extreme Wind Analysis Based on Hurricane Return Probabilities. The Pennsylvania Wind Energy Symposium: Power for the Future, Penn State Applied Research Laboratory, November, 2008.

2.65 Stewart, S.W., Shelton, S.M. and Hunt, M.H., 2010. Impact of Hurricanes on Offshore Wind Development. AWEA North America Offshore Wind Conference, Poster Session, Atlantic City, NJ.

2.66 Takahara, K., Mekaru, T., Shinjo, F., Ishihara, T., Yamaguchi, A. and S. Matsuura, S., 2004. Damages of Wind Turbine on Miyakojima Island by Typhoon Maemi in 2003. Proc. of 2004 European Wind Energy Conference and Exhibition.

2.67 Tarp-Johansen, N.J., 2005. Partial Safety Factors and Characteristic Values for Combined Extreme Wind and Wave Load Effects. ASME Journal of Solar Energy Engineering, 127, 242-252.

2.68 Tarp-Johansen, N.J., Manwell, J.F. and McGowan, J., 2006. Application of Design Standards to the Design of Wind Turbines in the US. Offshore Technology Conference, Houston, Texas, Paper No. OTC 18359.

2.69 Tolman, H.L., Alves, J.G.M and Chao, Y., 2004. Operational Forecasting of Wind-Generated Waves by Hurricane Isabel at NCEP. AMS Weather and Forecasting, 20, 544-557

2.70 Transportation Research Board, Structural Integrity of Offshore Wind Turbines: Oversight of Design, Fabrication, and Installation. Special Report 305, Committee on Offshore Wind Energy Turbine Structural and Operating Safety, Transportation Research Board, Washington, D.C.

2.71 U.S. Army Corps of Engineers, 2008. Coastal Engineering Manual - Part II. Engineering Manual 1110-2-1100, Washington, D.C.

2.72 U.S. Army Corps of Engineers. Wave Information Studies (WIS) Project. http://frf.usace.army.mil/wis2010

2.73 University of Florida, Florida Coastal Monitoring Program (FCMP). http://fcmp.ce.ufl.edu/

2.74 US Department of Interior, 30 CFR Part 285, 2009. Renewable Energy Alternate Uses of Existing Facilities on the Outer Continental Shelf.

2.75 Vickery, P.J. and Skerlj, P., 2005. Hurricane Gust Factors Revisited, ASCE Journal of Structural Engineering, 131(5), 825-832

2.76 Vickery, P.J., Masters, F.J., Powell, M.D. and Wadhera, D., 2007. Hurricane Hazard Modeling: The Past, Present and Future, ICWE12 Cairns, Australia 2007

2.77 Vickery, P.J., Skerlj, P.F., Steckley, A.C. and Twisdale, L.A., 2004. Hurricane Wind Field Model for Use in Hurricane Simulations, Journal of Structural Engineering, 126(10), 1203-1221

2.78 Wright, C. W., Walsh, E. J., Vandemark, E. J., Krabill, W. B., Garcia, A. W., Houston, S. H, Powell, M. D., Black, P. G. and Marks, F. D., 2001. Directional Wave Spectrum Spatial Variation in the Open Ocean, Journal of Physical Oceanography, 31: 2472- 2488.

2.79 Wu, C., Taylor, A.A, Chen, J. and Shaffer, W.A., 2003. Tropical Cyclone Forcing of Ocean Surface Waves, the Fifth Conference on Coastal Atmospheric and Oceanic Prediction and Processes, Seattle, Washington.

2.80 Yamasita, A. and Sekita, K., 2004. Analysis of the Fatigue Damage on the Offshore Wind Turbines Exposed to Wind and Wave Loads within the Typhoon Area. ASME 2004 23rd International Conference on Offshore Mechanics and Arctic Engineering (OMAE2004), June 20–25, 2004, Vancouver, British Columbia, Canada, Paper no. OMAE2004-51347

2.81 Young, I. R., 1999. Wind Generated Ocean Waves. Elsevier Ocean Engineering Book Series (Volume 2), Elsevier Ltd. Oxford, UK.

2.82 Young, I. R., 2006. Directional Spectra of Hurricane Wind Waves, J. Geophys. Res., 111

2.83 Young, I., 1988. Parametric Hurricane Prediction Model, ASCE Journal of Waterway, Port, Coastal, and Ocean Engineering, 114(5), 637-652

2.84 Young, I., 2003. A Review of the Sea State Generated by Hurricanes, Journal of Marine Structures, 16(3), 201-218.

2.85 Yu, B., 2007. Surface Mean Flow and Turbulence Structure in Tropical Cyclone Winds. PhD Thesis, Florida International University, Miami, Florida.

2.86 Yu, Q., Samuelsson, L. and Tan, P., 2011. Design Considerations for Offshore Wind Turbines in US Waters - the American Way. Offshore Technology Conference (OTC), Houston, Texas, Paper No. OTC 21870.

References for Section 3

3.1 American Bureau of Shipping (ABS), 2010a. Guide for Building and Classing Floating Production Installations.

3.2 American Bureau of Shipping (ABS), 2010b. Guide for Building and Classing Offshore Wind Turbine Installations.

3.3 American Petroleum Institute (API), 2007. API RP 2A-WSD: Recommended Practice for Planning Designing and Constructing Fixed Offshore structures – Working Stress Design, 21st Edition (with Errata and Supplement in 2002, 2005 and 2007).

3.4 Armand, J.L. and Cointe R., 1986. Hydrodynamic Impact Analysis of a Cylinder. The 5th Offshore Mechanics and Arctic Engineering (OMAE) Conference, Tokyo, Japan.

3.5 Arntsen, Ø., Ros, X., and Tørum, A., 2011. Impact Forces on a Vertical Pile from Plunging Breaking Waves. In Coastal Structures 2011, Yokohama, Japan.

3.6 Babanin, A., Young, I., and Banner, M., 2001. Breaking Probabilities for Dominant Surface Waves on Water of Finite Depth. J. Geophys. Res., 106:11659–11676.

3.7 Banner, M., Babanin, A., and Young, I., 2000. Breaking Probability for Dominant Waves on the Sea Surface. J. Phys. Oceanogr., 30:3145–3160.

3.8 Battjes, J. A. and Janssen, J. F. M., 1978. Energy Loss and Set-up due to Breaking of Random Waves. In 16th Int. Conf. on Coastal Engineering (ICCE), ASCE, page 569.

3.9 Bingham, H., Fuhrman, D. R., Jamois, E., and Kimmoun, O., 2004. Nonlinear Wave Interaction with Bottom-mounted Structures by a High-order Boussinesq Method. In International Workshop on Water Waves and Floating Bodies Proceedings.

3.10 Bredmose, H. and Jacobsen, N. G., 2010. Breaking Wave Impacts on Offshore Wind Turbine Foundations: Focused Wave Groups and CFD. In Proceedings of the ASME 2010 29th International Conference on Ocean, Offshore and Arctic Engineering (OMAE), Shanghai, China.

3.11 Campbell, I. and Weynberg, P. A., 1980. Measurement of Parameters Affecting Slamming. Technology Reports 440, Southampton University: Wolfson Unit for Marine Technology.

3.12 Chakrabarti, S. K., Kriebel, D., and Berek, E., 1997. Forces on a Single Pile Caisson in Breaking Waves and Current. Applied Ocean Research, 19(2):113–140.

3.13 Chakrabarti, S., 1987. Hydrodynamics of Offshore Structures. WIT Press.

3.14 Chan, E. and Melville, W., 1988. Deep-water Plunging Wave Pressures on a Vertical Plane Wall. In Roy. Soc. London, No. 417 A, pages 95–131.

3.15 Chan, E.-S., Cheong, H.-F., and Tan, B.-C., 1995. Laboratory Study of Plunging Wave Impacts on Vertical Cylinders. Coastal Engineering, 25:87–107.

3.16 Chaplin, J., Flintham, T., Greated, C., and Skyner, D., 1992. Breaking Wave Forces on a Vertical Cylinder. Report 90 324, Health and Safety Executive, London, UK.

3.17 Clamond, D., 1999. Steady Finite-amplitude Waves on a Horizontal Seabed of Arbitrary Depth. Journal of Fluid Mechanics, 398:45–60.

3.18 Clauss, G. F., Haver, S. K., and Strach, M., 2010. Breaking Wave Impacts on Platform Columns - Stochastic Analysis and DNV Recommended Practice. In Proceedings of the ASME 2010 29th International Conference on Ocean, Offshore and Arctic Engineering (OMAE), Shanghai, China.

3.19 Cokelet, E., 1977. Steep Gravity Waves in Water of Arbitrary Uniform Depth. Philosophical Transactions of the Royal Society. London, 386:179–206.

3.20 Corte, C. and Grilli, S. T., 2006. Numerical Modeling of Extreme Wave Slamming on Cylindrical Offshore Support Structures. In Proceedings of the Sixteenth (2006) International Offshore and Polar Engineering Conference, pages 394–401, San Francisco, California, USA.

3.21 Dalrymple, R. A., 1974. A Finite Amplitude Wave on a Linear Shear Current. J. Geophys. Res., 79:4498–4505.

3.22 Dean, R. and Dalrymple, R. A., 1991. Water Wave Mechanics for Engineers and Scientists. World Scientific Pub Co Inc.

3.23 Dean, R. G., 1974. Evaluation and Development of Water Wave Theories for Engineering Application, Special Report No. 1, U. S. Army Corps of Engineers, Coastal Engineering Research Center. Fort Belvoir, VA.

3.24 Det Norske Veritas (DNV), 2010a. OS-J101 Design of Offshore Wind Turbine Structures.

3.25 Det Norske Veritas (DNV), 2010b. RP-C205 Environmental Conditions and Environmental Loads.

3.26 Dingemans, M., 1997. Water Wave Propagation over Uneven Bottoms, volume 13. World Scientific.

3.27 Ducrozet, G., Bingham, H. B., Engsig-Karup, A. P., and Ferrant, P., 2010. High-Order Finite Difference Solution for 3d Nonlinear Wave-Structure Interaction. In 9th International Conference on Hydrodynamics, pages 225–230.

3.28 Faltinsen, O. M., 1990. Sea Loads on Ships and Offshore Structures. Cambridge Ocean Technology Series. Cambridge University Press.

3.29 Faltinsen, O., Newman, J., and Vinje, T., 1995. Nonlinear Wave Loads on a Slender Vertical Cylinder. J. Fluid Mech., 289:179–198.

3.30 Fenton, J., 1985. A Fifth-Order Stokes Theory for Steady Waves. Journal of Waterway, Port, Coastal and Ocean Engineering, 111:216–234.

3.31 Filipot, J. F., Ardhuin, F., and Babanin, A. V., 2010. A Unified Deep-to-Shallow Water Wavebreaking Probability Parameterization. J. Geophys. Res., 115:C04022.

3.32 Fuhrman, D., R. and Madsen, P., 2008. Simulation of Nonlinear Wave Run-up with a High-Order Boussinesq Model. Coastal Engineering, 55:139–154.

3.33 Fuhrman, D., R., 2004. Numerical Solutions of Boussinesq Equations for Fully Nonlinear and Extremely Dispersive Water Waves. PhD thesis, Technical University of Denmark.

3.34 Fuhrman, D., R., Bingham, H., B., and Madsen, P., A., 2005. Nonlinear Wave-Structure Interactions with a High-Order Boussinesq Model. Coastal Engineering, 52:655–672.

3.35 Germanischer Lloyd (GL), 2005. Guideline for the Certification of Offshore Wind Turbines.

3.36 Goda, Y., Haranaka, S., and Kitahata, M., 1966. Study of Impulsive Breaking Wave Forces on Piles. Report of Port and Harbor Research Institute, 5(6): 1–30. Concept also in English language in Watanabe, A. and Horikawa, K., 1974): Breaking Wave Forces on Large Diameter Cell. Proc. 14th Intern. Conf. on Coastal Eng. pp 1741-1760.

3.37 Groenendijk, H.W., 1998. Shallow Foreshore Wave Height Statistics. Master's Thesis, Section of Fluid Mechanics, Faculty of Civil Engineering and Geosciences, Delft University of Technology, Delft, The Netherlands.

3.38 Hubbell, W.D. and Kulhawy, F.H., 1982. Costal Structures Handbook Series – Environmental Loads. New York Sea Grant Institute, Albany, NY.

3.39 International Electrotechnical Commission (IEC), 2005. IEC 61400-1: Wind Turbines – Part 1: Design Requirements, 3rd Edition.

3.40 International Electrotechnical Commission (IEC), 2009. IEC 61400-3: Wind Turbines – Part 3: Design Requirements for Offshore Wind Turbines, 1st Edition.

3.41 International Organization for Standardization (ISO), 2005. ISO 19901-1: Petroleum and Natural Gas Industries - Specific Requirements for Offshore Structures Part 1: Metocean Design and Operating Considerations. Geneva, Switzerland.

3.42 International Organization for Standardization (ISO), 2007. ISO 19902: Petroleum and Natural Gas Industries - Fixed Steel Offshore Structures. Geneva, Switzerland.

3.43 International Organization for Standardization (ISO), 2007. ISO 21650: Actions from Waves and Currents on Coastal Structures. Geneva, Switzerland.

3.44 Irschik, K., Sparboom, U. and Oumeraci, H., 2004. Breaking Wave Loads on a Slender Pile in Shallow Water. Proceedings of the 29th International Conference on Coastal Engineering (ICCE), Lisbon, Portugal.

3.45 Irschik, K., Sparboom, U., and Oumeraci, H., 2002. Breaking Wave Characteristics for the Loading of a Slender Pile. In ASCE, editor, Proceedings 28th International Conference Coastal Engineering (ICCE), volume 2, pages 1341–1352, Cardiff, U.K.

3.46 Jamois, E., Fuhrman, D., Bingham, H., and Molin, B., 2006. A Numerical Study of Nonlinear Wave Run-Up on A Vertical Plate. Coastal Engineering, 53:929–945.

3.47 Kaplan, P., 1992. Wave Impact Forces on Offshore Structures: Re-Examination and New Interpretation. Offshore Technology Conference, Houston, Texas, Paper No. OTC 6814.

3.48 Kjeldsen, S., Torum, A., and Dean, R., 1986. Wave Forces on Vertical Piles Caused by 2 And 3 Dimensional Breaking Waves. In 20th Int. Conf. Coastal Eng., Taipei, pages 1929–1942. ASCE.

3.49 Korobkin, A., Gueret, R., and Malenica, S., 2006. Hydroelastic Coupling of Beam Finite Element Model with Wagner Theory of Water Impact. Journal of Fluids and Structures, 22(4): 493 – 504.

3.50 Krokstad, J. R., Stansberg, C. T., Nestegaard, A., and Marthinsen, T., 1998. A New Nonslender Ringing Load Approach Verified Against Experiments. Journal of Offshore Mechanics and Arctic Engineering, 120:20–29.

3.51 Larsen, S., Gravesen, H., Sørensen, S., Jørgensen, L., and Vølund, P., 2004. Wind and Wave Loads to Borkum Riffgrund Offshore Wind Farm. In European Wind Energy Conference.

3.52 Le Mehaute, B., 1969. An Introduction to Hydrodynamics and Water Waves. Springer.

3.53 Lu, C. H., He, Y. S., and Wu, G. X., 2000. Coupled Analysis of Nonlinear Interaction Between Fluid and Structure During Impact. Journal of Fluids and Structures, 14(1): 127 – 146.

3.54 MacCamy, R. C. and Fuchs, R. A., 1954. Wave Forces in Piers: A Diffraction Theory. Technical Memorandum 69, Beach Erosion Board, US Navy Corps of Engineers.

3.55 Madsen, P., Bingham, H., and Liu, H., 2002. A New Boussinesq Method for Fully Nonlinear Waves from Shallow to Deep Water. Journal of Fluid Mechanics, 462:1–30.

3.56 Madsen, P., Bingham, H., and Schaffer, H. A., 2003. Boussinesq-Type Formulations for Fully Nonlinear and Extremely Dispersive Water Waves: Derivation and Analysis. Proc. R. Soc. London. A, 459:1075–1104.

3.57 Marino, E., Borri, C., and Peil, U., 2010a. A Fully Nonlinear Wave Model to Account for Breaking Wave Impact Loads on Offshore Wind Turbines. Journal of Wind Engineering and Industrial Aerodynamics.

3.58 Marino, E., Borri, C., and Peil, U., 2010b. Offshore Wind Turbines: A Wind-Fully Nonlinear Waves Integrated Model. In the Fifth International Symposium on Computational Wind Engineering (CWE2010).

3.59 Massel, S. R., 1998. The Limiting Wave Height in Wind-Induced Waves Train. Ocean Engineering, 25:735–752.

3.60 Massel, S. R., 2007. Ocean Waves Breaking and Marine Aerosol Fluxes. Springer.

3.61 Mei, C. C., 1989. The Applied Dynamics of Ocean Surface Waves. Advanced Series on Ocean Engineering, Volume 1.

3.62 Mokrani, C., Abadie, S., Grilli, S., and Zibouche, K., 2010. Numerical Simulation of The Impact of a Plunging Breaker on a Vertical Structure and Subsequent over Topping Event Using a Navier-Stokes VOF Model. In Proceedings of the Twentieth (2010) International Offshore and Polar Engineering Conference, pages 729–736, Beijing, China.

3.63 Molin, B., Remy, F., Kimmoun, O., and Jamois, E., 2005. The Role of Tertiary Wave Interactions in Wave-Body Problems. J. Fluid Mech, 528:323–354.

3.64 Morison, J. R., Brien, M. P. O., Johnson, J. W., and Shaaf, S., 1950. The Forces Exerted by Surface Waves on Piles. Journal of Petroleum Technology, Petroleum Transactions, AIME 189:149–154.

3.65 NORSOK Standard N-003, 2007. Actions and Action Effects, Edition 2. Standards Norway, Lysaker, Norway.

3.66 Ochi, M. K. and Tsai, C. H., 1984. Prediction of Impact Pressure Induced by Breaking Waves on Vertical Cylinders in Random Seas. Applied Ocean Research, 6(3): 157–165.

3.67 Ochi, M.K., 2003. Hurricane-Generated Seas. Elsevier Ocean Engineering Book Series (Volume 8), Elsevier Ltd. Oxford, UK.

3.68 Oger, G., Guilcher, P.-M., Jacquin, E., Brosset, L., Grenier, N., and Touze, D. L., 2010. Simulations of Liquid Impacts Using a Two-Fluid Parallel SPH Model. In 5th international SPHERIC workshop, pages 76–82, Manchester, UK. SPHERIC.

3.69 Oumeraci, H., Partenscky, H. W., and Tautenhain, E., 1992. Breaking Wave Loads on Vertical Gravity Structures. In Proceedings of the Second (1992) International Offshore and Polar Engineering Conference, pages 532–539, San Francisco, CA, USA.

3.70 Pakozdi, C., Kendon, T. E., and Stansberg, C. T., 2011. Breaking Wave Impact on a Platform Column: An Introductory CFD Study. In Proceedings of Proceedings of the ASME 2011 30th International Conference on Ocean, Offshore and Arctic Engineering, Rotterdam, The Netherlands.

3.71 Peseux, B., Gornet, L., and Donguy, B., 2005. Hydrodynamic Impact: Numerical and Experimental Investigations. Journal of Fluids and Structures, 21(3): 277 – 303. Marine and Aeronautical Fluid-Structure Interactions - Marine Acoustics.

3.72 Rognebakke, O. and Faltinsen, O., 2000. Damping of Sloshing due to Tank Roof Impact. In 15th International Workshop on Water Waves and Floating Bodies.

3.73 Roos, J., Swan, C., and Haver, S., 2010. Wave Impacts on the Column of a Gravity Based Structure. In Proceedings of the ASME 2010 29th International Conference on Ocean, Offshore and Arctic Engineering.

3.74 Sarpkaya, T., 1978. Wave Impact Loads on Cylinders. In Proc., Offshore Technology Conference, Houston, TX, Paper No. OTC 3065.

3.75 Sarpkaya, T., and Isaacson, M., Mechanics of Wave Forces on Offshore Structures, Van Nostrand Reinhold, New York, 1981.

3.76 Schwartz, L., 1974. Computer Extension and Analytic Continuation of Stokes' Expansion for Gravity Waves. Journal of Fluid Mechanics, 62:553–578.

3.77 Shi, F., Dalrymple, R., Kirby, J., Chen, Q., and Kennedy, A., 2001. A Fully Nonlinear Boussinesq Model in Generalized Curvilinear Coordinates. Coastal Eng., 42:337–358.

3.78 Soemantri, D., 2010. Comparison of Numerically Predicted Response and Measured Response for Jacket Structures. Master's Thesis, Department of Marine Technology, Norwegian University of Science and Technology, Trondheim, Norway.

3.79 Stansberg, C. T., 1997. Ringing Loads from Experiments with Cylinders of Different Diameters - An Empirical Study. In Proc., BOSS '97, Delft, the Netherlands.

3.80 Stansberg, C. T., 2011a. Characteristics of Steep Second-Order Waves in Finite and Shallow Water. Proceedings of the ASME 30th International Conference on Ocean, Offshore and Arctic Engineering OMAE2011-50219.

3.81 Stansberg, C. T., 2011b. Wave Impact Loads JIP Phase 2: Task 4. Wave Slamming on Columns in Deep Water. MARINTEK Report 580158.04.01, MARINTEK Sintef, Trondheim, Norway.

3.82 Stansberg, C. T., Gudmestad, O., and Haver, S. K., 2008. Kinematics under Extreme Waves. Journal of Offshore Mechanics and Arctic Engineering, 130(2).

3.83 Stansberg, C. T., Huse, E., Krokstad, J., and Lehn, E., 1995. Experimental Study of Non-Linear Loads on Vertical Cylinders in Steep Random Waves. In Proceedings of the Fifth International Offshore and Polar Engineering Conference, volume 3, pages 75–82, The Hague, The Netherlands.

3.84 Suyuthi, A. and Haver, S. K., 2009. Extreme Loads due to Wave Breaking against Platform Column. In Proceedings of the Nineteenth International Offshore and Polar Engineering Conference.

3.85 Svendsen, I. A., 2006. Introduction to Nearshore Hydrodynamics. Advanced Series on Ocean Engineering, Volume 24.

3.86 Tanimoto, K., Takahashi, S, Kaneko, T. and Shiota, K., 1986. Impact Force of Breaking Waves on an Inclined Pile. The 5th Offshore Mechanics and Arctic Engineering (OMAE) Conference, Tokyo, Japan.

3.87 Thornton, E. and Guza, R., 1983. Transformation of Wave Height Distribution. J. Geophys. Res., 88(C10): 5925–5938.

3.88 Tørum, A., 1989. Wave Forces on Pile in Surface Zone. Journal of Waterway, Port, Coastal and Ocean Engineering, 115(4): 547–565.

3.89 U.S. Army Corps of Engineers, 2008. Coastal Engineering Manual - Part II. Engineering Manual 1110-2-1100, Washington, D.C.

3.90 Ursell, F., 1953. The Long-Wave Paradox in the Theory of Gravity Waves. Proceedings of the Cambridge Philosophical Society, 49: 685–694.

3.91 von Karman, T., 1929. The Impact of Seaplane Floats during Landing. Technical Note 321, NACA, Washington.

3.92 Wagner, H. 1931, Landing of Seaplane, Technical Note 622, NACA, Washington

3.93 Wang, C. and Wu, G. X., 2010. Interactions between Fully Nonlinear Water Waves and Cylinder Arrays in a Wave Tank. Ocean Engineering, 37: 400–417.

3.94 Wang, K. and Jiang, L., 1994. Solitary Wave Interactions with an Array of Two Vertical Cylinders. Applied Ocean Research, 15: 337–350.

3.95 Wang, K., Wu, T., and Yates, G., 1992. Three-Dimensional Scattering of Solitary Waves by Vertical Cylinder. Journal of Waterway, Port, Coastal and Ocean Engineering, 118(5): 551–566.

3.96 Wheeler, J., 1970. Method for Calculating Forces Produced by Irregular Waves. J. Petroleum Tech., 249: 359–367.

3.97 Wiegel, R.L. 1982. Forces Induced by Breakers on Piles, Proceedings of the 18th International Conference on Coastal Engineering (ICCE), Cape Town, South Africa.

3.98 Wienke, J. and Oumeraci, H., 2005. Breaking Wave Impact Force on a Vertical and Inclined Slender Pile - Theoretical and Large-Scale Model Investigations. Coastal Engineering, 52:435–462.

3.99 Wienke, J., 2001. Druckschlagbelastung auf Schlanke Zylindrische Bauwerke durch Brechende Wellen. PhD thesis, Technischen Universitat Carolo-Wilhelmina zu Braunschweig, Germany.

3.100 Wu, T., 1981. Long Waves on Ocean and Coastal Waters. J. Eng. Mech. Div., ASCE), 107:501–522.

3.101 Yates, G. and Wang, K., 1994. Solitary Wave Scattering by a Vertical Cylinder: Experimental Study. In International offshore and polar engineering conference, Vol. 3, Osaka, Japan, volume 3, pages 118–124.

3.102 Zhong, Z. and Wang, K., 2009. Modeling Fully Nonlinear Shallow-Water Waves and Their Interactions with Cylindrical Structures. Computers and Fluids, 38:1018–1025.

Appendix A Abbreviations

ABS	American Bureau of Shipping
API	American Petroleum Institute
ATL2	Atlantic Coast Region 2
ATL3	Atlantic Coast Region 3
BOEMRE	Bureau of Ocean Energy Management, Regulation, and Enforcement
DNV	Det Norske Veritas
GL	Germanischer Lloyd
GOM	Gulf of Mexico
IEC	International Electrotechnical Commission
ISO	International Organization for Standardization
LRFD	Load and Resistance Factor Design
NOAA	National Oceanic and Atmospheric Administration
NREL	National Renewable Energy Laboratory
OCS	Outer Continental Shelf
RNA	Rotor Nacelle Assembly
USACE	US Army Corps of Engineers
WSD	Working Stress Design

Appendix B Terms and Definitions

1. *Crest Height*: Wave surface elevation measured relative to the Still Water Level

2. *Cyclone:* An atmospheric closed circulation rotating counter-clockwise in the Northern Hemisphere and clockwise in the Southern Hemisphere

3. *Extra-tropical Cyclone*: A synoptic-scale Cyclone of any intensity for which the primary energy source is baroclinic, that is, results from the temperature contrast between warm and cold air masses

4. *Foundation:* Structural and/or geotechnical component which is located on and beneath the sea floor and transfers the loads acting on the structure into the sea bed

5. *Gust:* Brief rise and fall in wind speed lasting less than 1 minute

6. *Hub Height:* Height of the center of the swept area of a wind turbine rotor above the Mean Sea Level

7. *Hurricane:* A Tropical Cyclone in which the maximum 1-minute average wind speed at 10 m (33 ft) above the surface is 119 km/hr (64 kt or 74 mph) or higher. The term *hurricane* is used for Northern Hemisphere tropical cyclones east of the International Dateline to the Greenwich Meridian. The term *typhoon* is used for Pacific tropical cyclones north of the Equator west of the International Dateline.

8. *Mean Sea Level (Mean Still Water Level):* Average level of the sea over a period long enough to remove variations due to waves, tides and storm surges

9. *Mean Wind Speed:* Statistical mean value of the instantaneous wind speed over a specified time interval

10. *Offshore Wind Farm:* A group of Offshore Wind Turbines installed at an offshore site

11. *Offshore Wind Turbine:* An Offshore Wind Turbine consists of a Rotor-Nacelle Assembly and its Support Structure

12. *Omni-directional (Wind, Waves or Currents):* Acting in all directions

13. *Parked:* Condition of a wind turbine that is either in a Standstill or an Idling condition, depending on the design of the wind turbine

14. *Return Period:* A return period is an average time duration between occurrences of an event or of a particular value being exceeded. A return period in years is equal to the reciprocal of the annual probability of exceedance of an event or of a particular value of a random parameter such as wind speed, wave height or sea elevation.

15. *Rotor-Nacelle Assembly (RNA):* A Rotor-Nacelle Assembly of a horizontal axis wind turbine, carried by the Support Structure, consists of the rotor components, including blades, hub, shaft, and spinner, and the nacelle, a housing which contains the mainframe, generator frame, drive train components, electrical generator components, wind turbine control and protection components and other elements on top of the Tower.

16. *Still Water Level (SWL):* An abstract water level typically defined as the sum of the highest astronomical level and the positive storm surge excluding variations due to waves

17. *Substructure:* Structure component which extends upward from the sea floor and connects the Foundation to the Tower

18. *Support Structure:* A Support Structure of offshore wind turbine is a site dependent offshore structure, supported by or attached to the sea floor. The design of the Support Structure is based on foundation and long term environmental conditions at a particular installation site where it is intended to remain. The sea floor attachment afforded to the Support Structure may be obtained by pilings, direct bearing, or other types of foundation. A Support Structure consists of the Tower, Substructure, and Foundation.

19. *Sustained Wind Speed:* Time-averaged wind speed with an averaging duration of 1 minute or longer

20. *Tower:* Structure component which extends upward from somewhere above the Mean Sea Level and connects the Substructure to the Rotor-Nacelle assembly

21. *Tropical Cyclone:* A warm-core non-frontal synoptic-scale Cyclone, originating over tropical or subtropical waters, with organized deep convection and a closed surface wind circulation about a well-defined center.

22. *Tropical Storm:* A Tropical Cyclone in which the maximum 1-minute average wind speed at 10 m (33 ft) above the surface ranges from 63 km/hr (34 kt or 39 mph) to 118 km/hr (63 kt or 73 mph).

23. *Turbulence Intensity:* Ratio of the wind speed standard deviation to the mean wind speed, determined from the same set of measured data samples of wind speed, and taken over a specified period of time

24. *Water Depth:* Vertical distance between the sea floor and Still Water Level

25. *Wind Profile (Wind Shear Law):* Mathematical expression for assumed wind speed variation with height above Still Water Level

26. *Yaw Misalignment:* Horizontal deviation of the wind turbine rotor axis from the wind direction